



AFRL-OSR-VA-TR-2014-0246

Electrosprayed Heavy Ion and Nanodrop Beams for Surface Engineering

M Gamero-Castano
UNIVERSITY OF CALIFORNIA IRVINE

09/17/2014
Final Report

DISTRIBUTION A: Distribution approved for public release.

Air Force Research Laboratory
AF Office Of Scientific Research (AFOSR)/ RTE
Arlington, Virginia 22203
Air Force Materiel Command

REPORT DOCUMENTATION PAGE				<i>Form Approved</i> OMB No. 0704-0188	
Public reporting burden for this collection of information is estimated to average 1 hour per response, including the time for reviewing instructions, searching existing data sources, gathering and maintaining the data needed, and completing and reviewing this collection of information. Send comments regarding this burden estimate or any other aspect of this collection of information, including suggestions for reducing this burden to Department of Defense, Washington Headquarters Services, Directorate for Information Operations and Reports (0704-0188), 1215 Jefferson Davis Highway, Suite 1204, Arlington, VA 22202-4302. Respondents should be aware that notwithstanding any other provision of law, no person shall be subject to any penalty for failing to comply with a collection of information if it does not display a currently valid OMB control number. PLEASE DO NOT RETURN YOUR FORM TO THE ABOVE ADDRESS.					
1. REPORT DATE (DD-MM-YYYY)		2. REPORT TYPE		3. DATES COVERED (From - To)	
4. TITLE AND SUBTITLE				5a. CONTRACT NUMBER	
				5b. GRANT NUMBER	
				5c. PROGRAM ELEMENT NUMBER	
6. AUTHOR(S)				5d. PROJECT NUMBER	
				5e. TASK NUMBER	
				5f. WORK UNIT NUMBER	
7. PERFORMING ORGANIZATION NAME(S) AND ADDRESS(ES)				8. PERFORMING ORGANIZATION REPORT NUMBER	
9. SPONSORING / MONITORING AGENCY NAME(S) AND ADDRESS(ES)				10. SPONSOR/MONITOR'S ACRONYM(S)	
				11. SPONSOR/MONITOR'S REPORT NUMBER(S)	
12. DISTRIBUTION / AVAILABILITY STATEMENT					
13. SUPPLEMENTARY NOTES					
14. ABSTRACT					
15. SUBJECT TERMS					
16. SECURITY CLASSIFICATION OF:			17. LIMITATION OF ABSTRACT	18. NUMBER OF PAGES	19a. NAME OF RESPONSIBLE PERSON
a. REPORT	b. ABSTRACT	c. THIS PAGE			19b. TELEPHONE NUMBER (include area code)

Electrosprayed Heavy Ion and Nanodrop Beams for Surface Engineering and Electrical Propulsion

Air Force Office of Scientific Research

Award # FA9550-11-1-0308

Final Report

Index

Abstract	2
Experimental characterization and modeling of electrospray beams	3
Characterization of typical thruster surfaces bombarded by nanodroplets and modeling of nanodroplet impact.	11
Fundamental study of the generation of nanoparticles and evaluation of chemical monopropellants for use in electrospray thrusters	41
Fundamental research on ionic liquid ion sources	46
References	65
Appendix. Copies of publications	70

Abstract

In this project we have investigated the generation, interaction and energetic impact of electrosprayed nanodroplets and molecular ions, covering continuously the projectile size range from 1 nm up to hundreds of nm. The 1-20 nm size range is of great interest to achieve variable specific impulse (I_{sp}) from 100 s to >1000 s in drop-based electrical propulsion, while pure molecular ion emission enables higher I_{sp} . The resulting knowledge is directly applicable to electrospray thrusters/electric propulsion (achievement of improved and variable I_{sp} , maximization of thrust, power density and propulsive efficiency, quantification of the lifetime of electrospray thrusters), and will lead to new opportunities in other fields such as MEMS and IC fabrication (broad-beam and focused-beam nanodroplet and ion sources for high speed beam milling and microfabrication, reactive nanodroplet and ion etching, polishing of large and curved mirrors), surface processing (patterning of crystalline surfaces with amorphous layers, patterning of a textured surface with controllable roughness, strengthening of materials for increased thruster life, microscopy), and secondary ion mass spectrometry (SIMS) of organic surfaces. The goals of this project were to gain a detailed, first-principles understanding of the production of nanoprojectiles, the extraction of their beams, their interaction with surfaces, and the investigation of the propulsive and surface processing applications outlined above.

The specific research problems tackled during this project and accomplishments include: the development of a basic electrospray beam model, and measurements of the spreading of the beam at varying temperature; the experimental characterization and typical thruster surfaces bombarded by electrosprayed nanodroplets, and a molecular dynamics study of the physics of nanodroplet impact; the extension of the minimum size of electrosprayed nanodroplets, and the exploration of energetic propellants for propulsion and sputtering; and molecular dynamics simulations of the fragmentation and emission of ions from ionic liquids.

1. Experimental Characterization and Modeling of Electrospray Beams.

The goal of this line of research is to develop a modeling tool for reproducing the geometry of an electrospray beam as a function of beam current, extracting electrode geometry and electrode potentials. This model could be used, for example, to determine the operational range (i.e. beam flow rates and extraction potentials) of a given thruster geometry; or for the optimal design of the thruster geometry. In parallel to the modeling effort, it is essential to experimentally characterize electrospray beams emitted by a source of known geometry for the following three reasons: a) it gives insights on how to construct the model; b) it provides parameters of the beam such as the particles' specific charge distribution, initial velocity and breakup position, etc. which are inputs to the model; and c) it makes it possible to compare experimental and model results, and hence validate the model. We will describe first the experimental characterization of EMI-Im beams at varying emitter temperature, and continue with a description of the beam model and beam calculations.

Figure 1.1 shows the experimental setup used to characterize the EMI-Im beams. Two time of flight collectors and a retarding potential analyzers mounted on an XYZ stage are used to characterize the beams, electrosprayed from a single emitter/extractor source. The temperature of the emitter can be varied and controlled with an electrical heater, a thermocouple and a commercial digital controller. A good understanding of how the beam spreads is needed to assess its interaction with spacecraft surfaces, and to design the accelerating electrodes of the thruster. Furthermore, electrospray thrusters must operate within a temperature range

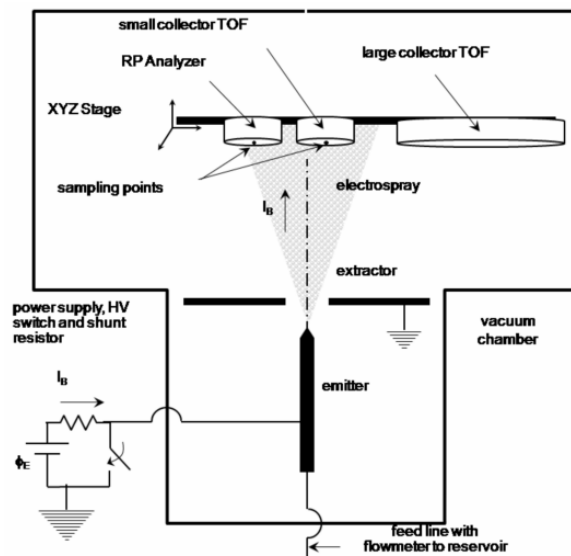


Figure 1.1. Experimental setup to characterize EMI-Im beams.

defined by mission specifications. With this arrangement we measure beam profiles and particle composition inside the beam as a function of position, mass flow rate and working temperature.

Figure 1.2 shows several beam profiles, at different emitter temperatures. The profiles are recorded by the retarding potential analyzer operated without a potential barrier, and moving along a plane perpendicular to the beam axis located 0.102 m downstream from the emission point. Note that the profiles are rather axisymmetric, due to the accurate construction of the electrospray source. The retarding potential and time of flight of particles along any point in the profiles can be determined with the RPA and small collector TOF detector shown in Fig. 1.1.

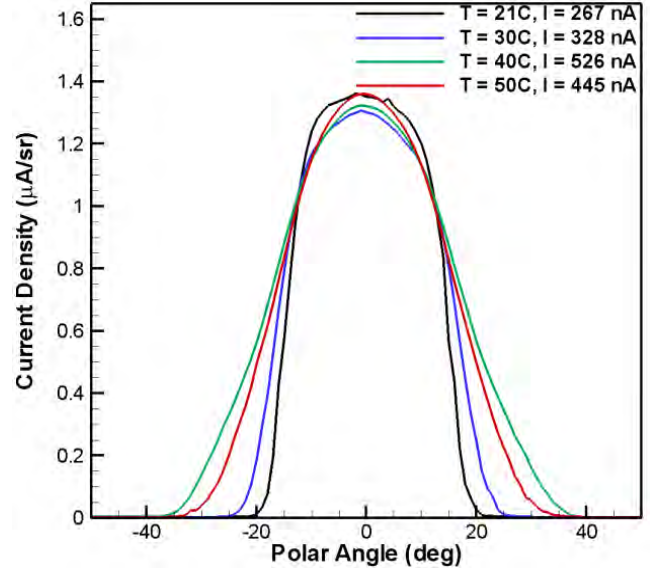


Figure 1.2. Beam profiles at different working temperatures and beam currents.

Figure 1.3 shows TOF curves for beams with similar currents and at two representative emitter temperatures, 21C and 50C. The voltage difference between the emitter and the extractor is 1608 V in all cases. The spectra resolve the ion and droplet populations of the beam, and show how the ion fraction increases with temperature. This is to be expected because ion evaporation is enhanced at increasing temperature. More interestingly, the average velocity (and therefore the specific charge $\frac{q}{m} = \frac{1}{2} \frac{v^2}{V_{ACC}}$)

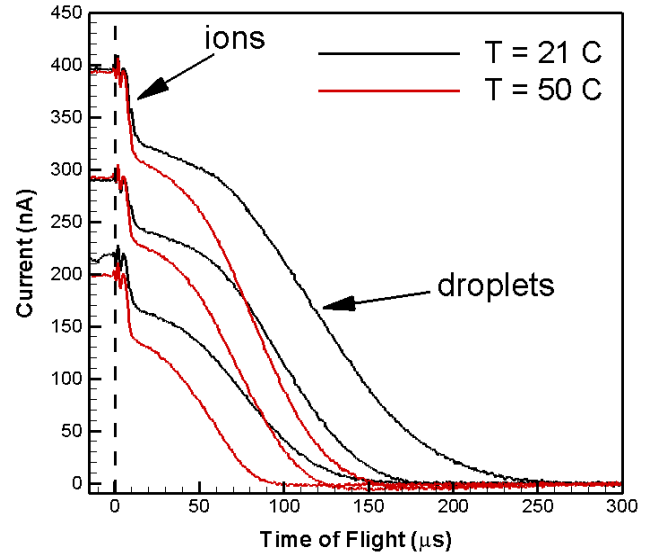


Figure 1.3. TOF curves for several beam currents and two emitter temperatures.

$\frac{q}{m} = \frac{1}{2} \frac{v^2}{V_{ACC}}$) of the droplets increases with temperature at constant beam current. This trend is due to the significant increase of the electrical conductivity of Emi-Im with temperature,¹ and the known dependence of the droplets' specific charge on the electrical conductivity, $\frac{q}{m} \sim \sqrt{\frac{\gamma K}{\rho \dot{m}}}$.

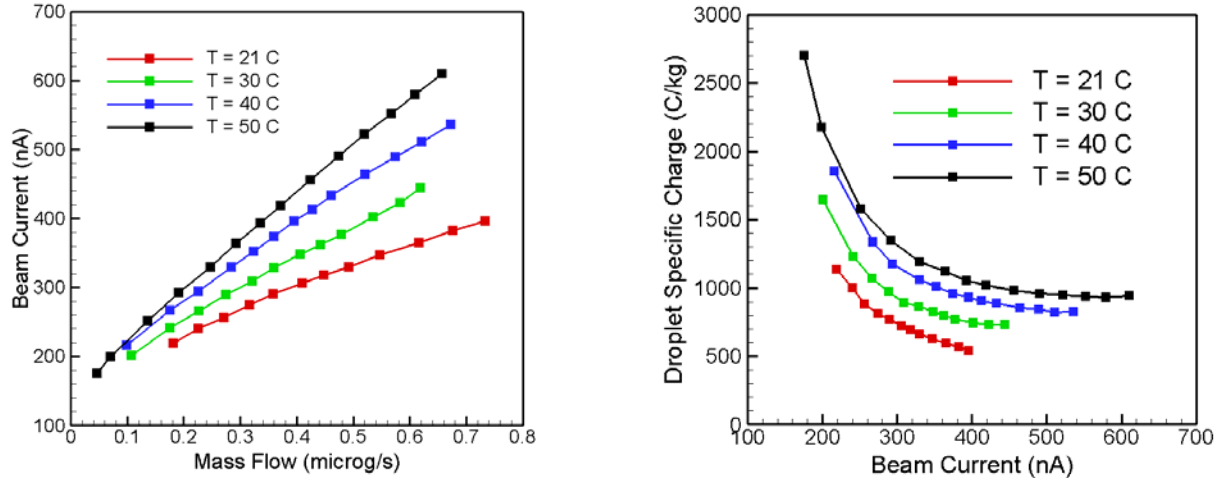


Figure 1.4. Beam current vs. mass flow rate, and average droplet specific charge vs. beam current, for several emitter temperatures.

These curves, properly integrated, provide the beam mass flow rate, thrust and Isp .

Figure 1.4 shows the dependence between beam current and mass flow rate, and the dependence between droplets' average specific charge and beam current, at temperatures of 21, 30, 40 and 50C. The mass flow rate is computed by integrating the TOF curve

$$\dot{m} = \int_0^{\infty} \frac{2V_{ACC}(t)}{L^2} t^2 I' dt,$$

while the average specific charge is defined as the specific charge associated with the time of flight at 50% of the droplet current. Again, because of the significant increase of the electrical conductivity with temperature, the beam current increases with temperature at constant mass

flow rate, $I_B \sim \sqrt{\frac{\gamma K \dot{m}}{\rho}}$. Figure 1.4 places the beam current in the abscissa instead of the mass

flow rate because the current is the easiest beam parameter to measure (both in the lab and

during thruster operation), and therefore it is the parameter used to monitor and control the performance of the thruster. Note that, at constant beam current, the average specific charge varies significantly in the temperature range considered, increasing approximately two-fold between 21C and 50C.

Figure 1.5 shows the thrust, specific impulse and propulsive efficiency as functions of the beam current and temperature. These parameters are computed with formulae:

$$T = \int_0^\infty \frac{2V_{ACC}(t)}{L^2} t I' dt \quad I_{SP} = \frac{T}{g_0 \dot{m}} \quad \eta_T = \frac{T^2}{2 \dot{m} V_{ACC} I_B}$$

The emitter potential of 1608 V applied in the experiments is used as acceleration voltage. Both the thrust and the specific impulse change substantially at constant beam current, as the emitter temperature varies. These variations of key propulsive parameters must be taken into account by the thruster operator, who will typically track the beam current and the emitter potential to infer thruster performance and control it. The variation of thrusting efficiency with temperature is less significant, the slightly reduction with temperature being due to the increasing ionic fraction and the associated reduction of efficiency caused by the larger polidispersity of exhaust velocities. The existence of an efficiency maximum at constant temperature is due to the increasing ionic

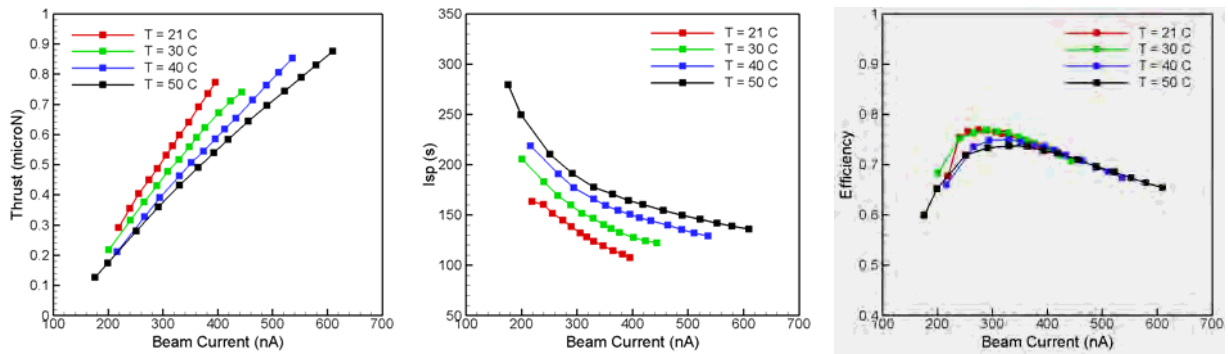


Figure 1.5. Thrust, specific impulse and thrusting efficiency as functions of beam current and emitter temperature.

fraction at decreasing beam current, and the increasing droplet velocity dispersion at increasing beam current (see TOF curves in Fig. 1.3).

The dependence of the propulsive parameters on emitter temperature is significant but not critical in the studied range, because although it affects the performance of the thruster it does not prevent its operation. On the other hand the effect of temperature on the broadening of the beam is potentially more alarming, because the interception by the extracting electrodes of an unexpected broader beam will cause the failure of the thruster. Figure 1.7 shows beam

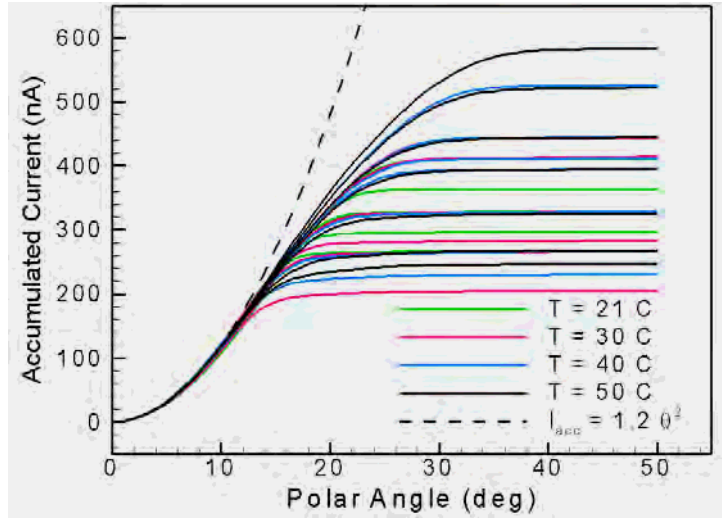


Figure 1.7. Current accumulated between the axis and a given polar angle, as a function of the beam current and emitter temperature.

profiles as a function of beam current and emitter temperature, this time in the form of the beam current accumulated between the axis and a value of the polar angle. Any given curve starts following a *universal* trend (initially parabolic) which continues for most of its polar angle range, and finally asymptotes to a constant value. The profiles are surprisingly identical for beams of equal current, regardless of the emitter temperature. These curves indicate that a) beams with identical beam currents have the same geometry, regardless of the emitter temperature; and b) the current density in the core of the beam is only a function of the polar angle, and does not depend on the specific charge of the droplets. Since the specific charge and the initial velocity of the droplets play important roles in the differential equations describing the trajectories of the droplets, and the specific charge of droplets changes substantially with emitter temperature at constant beam current, the universal trend observed in Fig. 1.7 is rather puzzling. So far, we do not have a satisfactory explanation for this unexpected behavior.

The beam model is based on the integration of particle trajectories defining the surface envelopes containing a fraction of the beam particles. The particles in the beam are divided into discrete groups of identical particles (same specific charge and diameter), and carrying a

fraction of the total beam current. To make this partition knowledge of the particles' specific charge distribution is required; in our case we measure this distribution using time of flight and retarding potential spectrometry. The envelope of each particle group is then computed by integrating the equation of motion of a particle flying along the envelope. The electric field acting on this particle is the superposition of the electric field induced by the electrodes (and computed by a commercial program solving Laplace equation), and the electric field induced by the sum of the volumetric charge densities contained by each envelop. A detailed description of this model can be found in Ref[2]. The main novelties of the new model are: 1) we now compute the space charge field by solving Poisson's equation for the volumetric charge distribution associated with the envelopes, rather than using an approximate analytical field. This change improves the accuracy of the electric field and therefore the computed structure of the beam; 2) we now construct the model for a beam typical of electrospray thrusters (in particular for a beam of the ionic liquid EMI-Im), rather than for a beam of large droplets with low specific charge and I_{sp} .

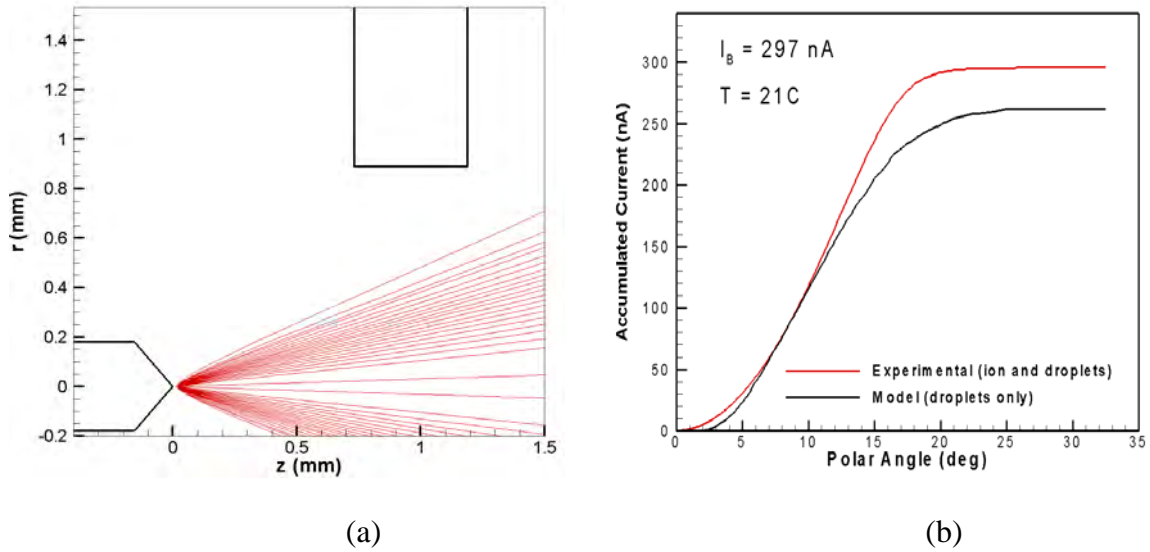


Figure 1.8. (a) Electrospray source geometry and particle trajectories obtained with the model; (b) comparison between experimental and model beam accumulated current vs. polar angle.

Figure 1.8(a) shows the geometry of emitter and extractor electrodes used in the model (and in the experiments), together with particle trajectories obtained with the beam model. In this

simulation the beam was divided into 80 particle groups, yielding 80 envelopes. The figure shows some of the envelopes, including the most outer one. Once the envelopes are computed, and since each one carries a known fraction of the beam current, the current carried by the beam between the axis and a given polar angle can be computed. This function (experimental and model) is plotted in Fig. 1.8(b). The model reproduces rather well the overall shape and the angular extend of the accumulated current function. The total current is smaller in the model because we track droplets and not ions (which in this case carry 17% of the total beam current). However we know from the experimental characterization that the ion population is located in the core of the beam, while the droplets appear throughout the angular range of the beam. Thus the maximum polar angle at which droplets are observed is the maximum angle of the beam; they are seen to coincide in Fig. 1.8(b).

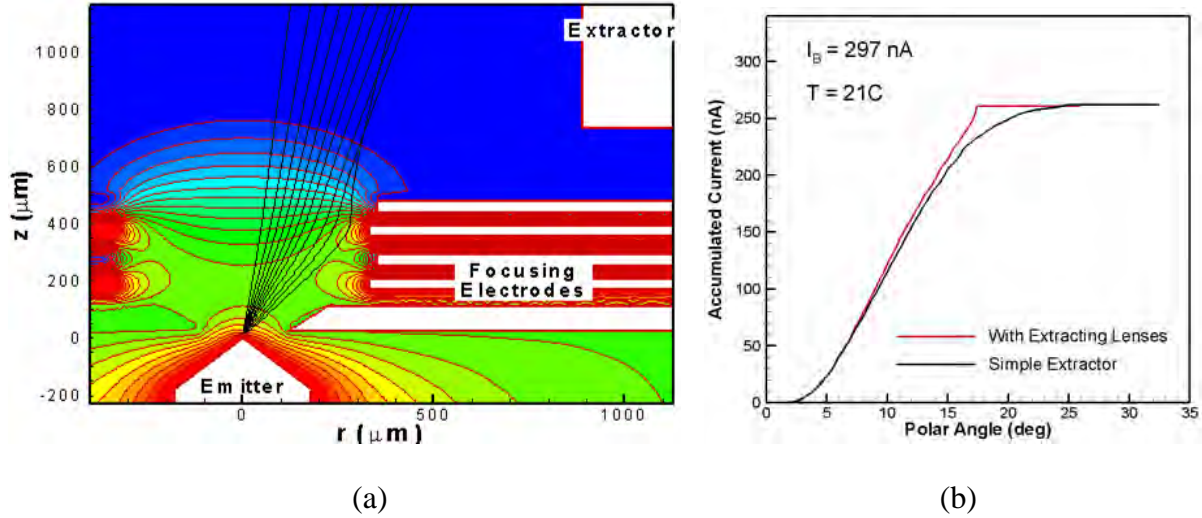


Figure 1.9. (a) Focusing extractor design for reducing the expansion of EMI-Im beams; (b) accumulated beam current vs. polar angle, for a simple extractor geometry, and the focusing geometry in (a).

After the knowledge gained with the experimental characterization of EMI-Im beams and the solution of the beam model, the natural next step in this line of research is the determination of optimum thruster electrode geometries, i.e. designs that maximize thrust density while avoiding beam impingement. Our plan was to use the model to guide the design of single emitter sources, which would then be microfabricated and tested in the lab. Figure 1.9 (a) illustrates how we could use the beam model to improve the design of extracting electrodes. In this case we are

simulating a 297 nA beam at room temperature, in a geometry featuring several sequential extractors with different electric potentials. After variation of the extractor geometry and potential values, we found the geometry in Fig. 1.9 (a) which significantly reduces the spreading of the beam, as shown in Fig 1.9 (b). Unfortunately we did not have the time nor the resources to continue the work on this problem.

2. Characterization of Typical Thruster Surfaces Bombarded by Nanodroplets and Modeling of Nanodroplet Impact.

We have investigated the impact of energetic nanodroplets on a variety of surfaces, with the goal of understanding the erosion patterns on the surfaces of spacecrafts operating electrospray thrusters. In particular, we have characterized the phenomenology of nanodroplet bombardment on a variety of single-crystal semiconductors including silicon, indium arsenide, indium phosphide, germanium, gallium arsenide, gallium antimonide, gallium nitride and silicon carbide; studied the role of the liquid's composition on the sputtering of silicon; study the effect of liquid composition on a variety of substrates such as Si, GaN, SiC and GaAs; and modeled the impact of a nanodroplet on Si to determine the physics behind the sputtering and the amorphization of thin surface layers. This work has produced the following publications and articles currently under review, which are attached in this document as an appendix:

- F. Saiz, R. Borrajo-Pelaez, and M. Gamero-Castaño, “Atomistic modeling of the sputtering of silicon by electrosprayed nanodroplets”, *Journal of Applied Physics*, 116, 054303 (2014).
- R. Borrajo-Pelaez, E. Grustan-Gutierrez, and M. Gamero-Castaño, “Sputtering of Si, SiC, InAs, InP, Ge, GaAs, GaSb, and GaN by electrosprayed nanodroplets”, *Journal of Applied Physics*, 114, 184304 (2013).
- F. Saiz, R. Borrajo-Pelaez, and M. Gamero-Castaño, “The Influence of the Projectile's Velocity and Diameter on the Amorphization of Silicon by Electrosprayed Nanodroplets”, *Journal of Applied Physics* 114, 034304 (2013)
- F. Saiz, M. Gamero Castaño, “Amorphization of silicon induced by nanodroplet impact: A molecular dynamics study”, *Journal of Applied Physics*, 112(5), 054302/1-6 (2012).
- R. Borrajo-Pelaez and M. Gamero-Castaño, “The Effect of the Molecular Mass on the Sputtering by Electrosprayed Nanodroplets”, Submitted to *Applied Surface Science*.

- M. Gamero-Castaño, A. Torrents, R. Borrajo-Pelaez, J.G. Zheng, “Amorphization of Hard Crystalline Materials by Electrosprayed Nanodroplet Impact”, Submitted to Applied Surface Science.

2.1 Experimental characterization of the sputtering of Si, SiC, InAs, InP, Ge, GaAs, GaSb and GaN by electrosprayed nanodroplets of the ionic liquid EMI-Im.

The size of the projectile has important effects on how an ion beam interacts with a target, and extending the range of this parameter beyond atomic dimensions offers opportunities in both research and technological applications. For example, the size of gas cluster ions and their relatively low specific charge compared to atomic ions are credited with the high sputtering yields, dense energy deposition and shallow surface damage typical of cluster ion beams;³ large projectile sizes are correlated with the ability to desorb large molecules in secondary ion mass spectrometry;^{4,5,6} and the theoretical study of the energetic impact of cluster ions and larger nanoparticles has become a problem of interest.⁷ Gas cluster ions are the largest projectiles available but, due to their low charging level (one elementary charge), their effective diameters are limited to a few nanometers (e.g. a large Ar_{2000}^+ gas cluster ion has a diameter of 5.6 nm). This absence of an appropriate particle source has hindered the experimental research with larger projectiles and the development of applications benefitting from them, an obstacle that has now been removed by the introduction of energetic beams of electrosprayed nanodroplets.⁸

The electrohydrodynamic atomization of dielectric liquids in the cone-jet mode produces sprays of charged droplets with narrow size distributions.⁹ The average diameter of the droplets is controlled between a few nanometers and macroscopic dimensions by adjusting the flow rate and the physical properties of the liquid and, since many dielectric liquids are readily electrosprayed in vacuum, electrohydrodynamic atomization can be used as a source for nanoparticle beams. Besides enabling research and technological applications in a previously unavailable projectile size range, the electrospray source has some advantageous properties: being a point source its beamlets can be electrostatically focused into submicrometric spots; MEMS techniques can be used to fabricate sources with dense emitter arrays for broad beam

applications; and the chemical composition of the projectile can be varied -to combine physical sputtering with chemical effects. The introduction by Fernandez de la Mora of ionic liquids as ideal fluids for electrospraying in vacuum has been an important factor in the development of the field.¹⁰ The low vapor pressures and high electrical conductivities of ionic liquids, combined with the very large number of chemical compounds available, has stimulated the research of ionic liquid-based electrospraying for electric propulsion,¹¹ secondary ion mass spectrometry,¹² and ion and nanodroplet beams.^{8,13}

We have characterized the damage caused by energetic beams of electrosprayed nanodroplets striking the surfaces of single-crystal semiconductors including Si, SiC, InAs, InP, Ge, GaAs, GaSb and GaN. The sputtering yield (number of atoms ejected per projectile's molecule), sputtering rate and surface roughness are measured as functions of the beam acceleration potential. The maximum values of the sputtering yields range between 1.9 and 2.2 for the technological important but difficult to etch SiC and GaN respectively, and 4.5 for Ge. The maximum sputtering rates for the non-optimized beam flux conditions used in our experiments vary between 409 nm/min for SiC and 2381 nm/min for GaSb. The maximum sputtering rate for GaN is 630 nm/min. Surface roughness increases modestly with acceleration voltage, staying within 2 nm and 20 nm for all beamlet acceleration potentials and materials except Si. At intermediate acceleration potentials the surface of Si is formed by craters orders of magnitude larger than the projectiles, yielding surface roughness in excess of 60 nm. The effect of projectile dose is studied in the case of Si. This parameter is correlated with the formation of the large craters typical of Si, which suggests that the accumulation of damage following consecutive impacts plays an important role in the interaction between beamlet and target.

Figure 2.1 shows photographs of the Si, SiC and Ge targets bombarded at several acceleration potentials, and surface profiles for the Si target. In all cases the beamlet carves a flat circular depression surrounded by a deeper ditch. The diameter of these macroscopic craters decreases at increasing acceleration voltage because the axial electric field between the extractor and the target, being proportional to acceleration voltage, reduces the polar angle of the particle trajectories exiting the extractor orifice. Typical crater diameters for low and high acceleration potentials are 1 mm and 0.3 mm respectively. The depth of the craters augments with acceleration voltage because of the positive correlation between sputtering yield and molecular

kinetic energy, and the reduction of the crater area at increasing acceleration potential. For example, the depths of the Si, SiC and Ge targets are 0.9, 0.7 and 5.6 μm at 14.6 kV acceleration voltage, V_A , and 3.7, 5.8 and 22.4 μm at $V_A = 24.6$ kV. Besides these trends common to all target materials there are noticeable differences between the Si surfaces in one hand, and the surfaces of SiC and Ge (all other semiconductors behave like SiC and Ge). First, the Si craters are surrounded by substantial deposits in the form of circular iridescent rings forming a Newton color series, which are much less visible in other materials. These and similar experiments with other liquids suggest that the projectile's imide group has an affinity for forming charged compounds with the sputtered Si, which are pushed back to the target by the electric field.

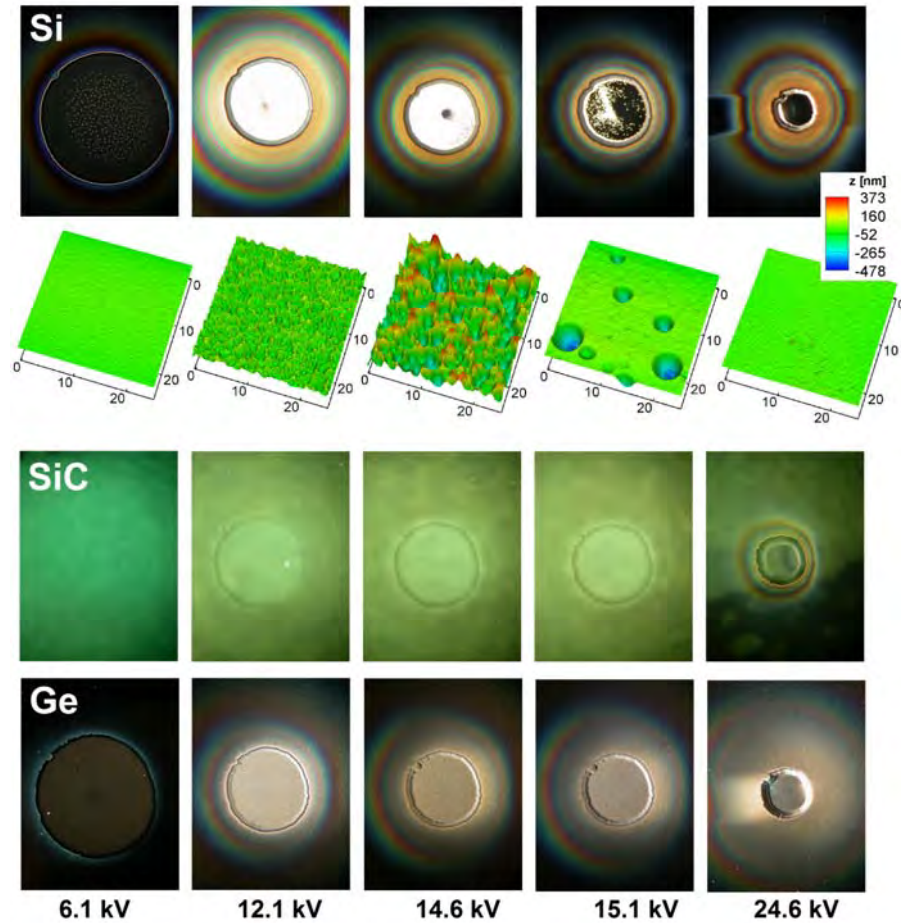


Figure 2.1. Photographs of Si, SiC and Ge targets struck by the beamlet during 600 s, at varying acceleration potential. The Si photographs are complemented with atomic force microscopy of the bombarded surfaces.

The roughness of the surfaces is also markedly different. The atomic force microscope AFM profiles for Si show surfaces covered by micrometric craters with sizes that increase with the acceleration voltage up to 15 kV. These craters are large, e.g. the typical diameter and depth at $V_A=14.6$ kV are 2-3 μm and 0.5 μm respectively, orders of magnitude larger than the average diameter of the nanodroplets. These micrometric and intertwined craters produce very rough surfaces, which manifest in the photographs at 12.1 kV and 14.6 kV by the high scattering of light (the photographed samples are illuminated at a glancing angle). At still higher acceleration potential the surface of Si becomes specular, and is occasionally dotted by very large, isolated craters. The surfaces of all other materials also exhibit craters but these are significantly smaller, and their sizes and density do not vary with the acceleration voltage as much as in Si.

Figure 2.2 plots the roughness of the surfaces struck by the beamlet. The roughness of Si increases sharply with acceleration voltage, reaching a maximum value of 69 nm at 14.6 kV; at higher acceleration voltage the surface becomes much smoother. The roughness of all other materials increases slowly with acceleration voltage and, in some cases, levels off or slightly decreases at the highest acceleration voltages; the values are substantially lower than the peak roughness for Si. Note that germanium also follows this monotonic trend, despite being a material closely related to silicon. The maximum roughness for GaN, GaAs, GaSb, InP, InAs, Ge and SiC are 12.7, 11.7, 19.5, 8.1, 7.9, 17.5 and 11.2 nm respectively. The AFM profiles in Fig. 2.3 shows the patterns of impacts behind the surface roughness of different materials, and the singular behavior of Si. The surfaces of GaN, SiC and Ge in the bottom row are typical of all semiconductors other than Si: the surfaces have small indentations with diameters of the order of 0.1 μm and depths of a few tens of nanometers, and which must be the dimples left by individual droplets impacting on the surface. The Si targets also display this pattern of small indentations, but at acceleration voltages between 10.1 kV and 15.1 kV these small marks are superimposed over an additional pattern of much larger craters, which dominate the surface roughness. Each large crater must be produced by the single impact of a projectile that is not much larger than the average droplet (2 orders of magnitude smaller than the large craters): we have never detected large droplets in these beams despite a thoroughly investigation with an induction charge detector; and large droplets, far exceeding the Rayleigh charge limit at the required specific charge, would be unstable.

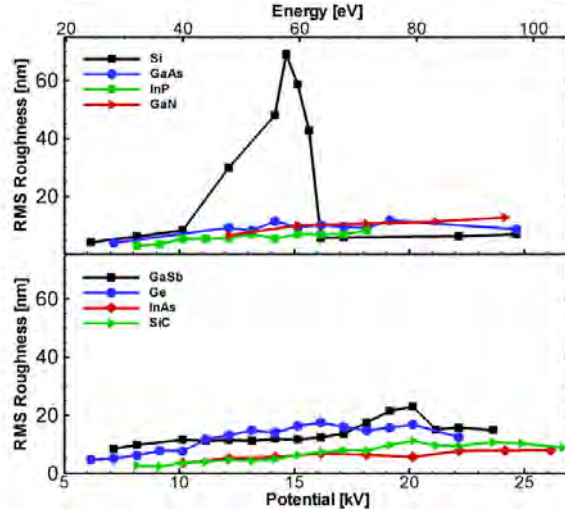


Figure 2.2. Roughness of the bombarded samples as a function of acceleration potential. Silicon behaves differently from all other materials.

Figure 2.4 shows sputtering yields as a function of acceleration voltage, and projectile's molecular kinetic energy. The sputtering yields increase monotonically with molecular energy, leveling off at approximately 70 eV in most materials. The yields for GaAs, InAs and GaSb decrease slightly at the highest acceleration voltages. The maximum sputtering yields for Si, GaN, GaAs, GaSb, InP, InAs, Ge and SiC are 2.2, 2.2, 4.2, 4.1, 4.1, 3.6, 4.5 and 1.9 respectively. These values are similar to the maximum sputtering yields of atomic projectiles, and significantly higher than those of gas cluster ions. For instance, the sputtering yields of Si and SiC bombarded by atomic argon at normal incidence and 500 eV are 0.4 and 0.8; and the sputtering yields of Si and SiC struck by gas cluster ions at 20 kV acceleration potential are 0.008 and 0.013. As in the case of the surface roughness, the dependence of the sputtering yield on acceleration voltage differs significantly between Si and other materials. Rather than increasing monotonically with acceleration voltage, the sputtering yield of Si first increases with acceleration voltage, peaks at 12.1 kV, and abruptly decreases at 14.6 kV to remain nearly constant thereafter. The sharp drop in sputtering yield coincides with the drop in surface roughness. Figure 2.4 also shows that SiC and GaN have substantially higher threshold energies for sputtering than all other semiconductors, which could be expected from the exceptionally high thermal, mechanical and chemical stability of these two compounds.

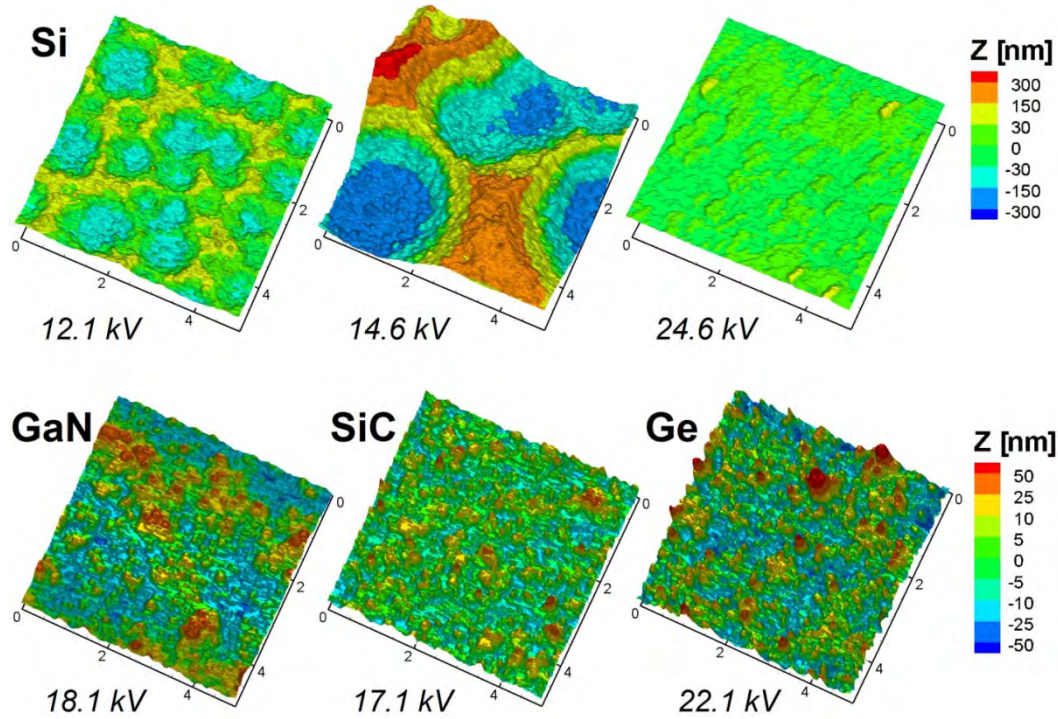


Figure 2.3. Atomic force microscope measurements of Si, GaN, SiC and Ge samples. The impacts of individual droplets produce a pattern of small indentations in all surfaces. In addition, a very few number of impacts produce large craters in Si at acceleration potentials between 10 kV and 15 kV.

Figure 2.5 shows sputtering rates, a figure of merit which, being proportional to the particle flux, depends on factors such as beam focusing, emitter density, etc. In our experiments the flux is only a function of the acceleration voltage, making it possible to compare the sputtering rates on different targets at constant acceleration voltage. The sputtering rate increases monotonically with acceleration voltage because both the particle flux and the sputtering yield increase with this parameter. The sputtering rates for Ge, GaSb and GaAs at 20 kV exceed 1000 nm/min, a value typical of reactive ion etching and orders of magnitude higher than what is achievable with ion beam milling. The maximum sputtering rates for SiC and GaN, 410 and 630 nm/min, are similar to the best rates possible with reactive ion etching (970 nm/min for SiC, 1300

nm/min for GaN), and significantly higher than the rates associated with the more comparable ion beam milling technique (below 10 nm/min for GaN).

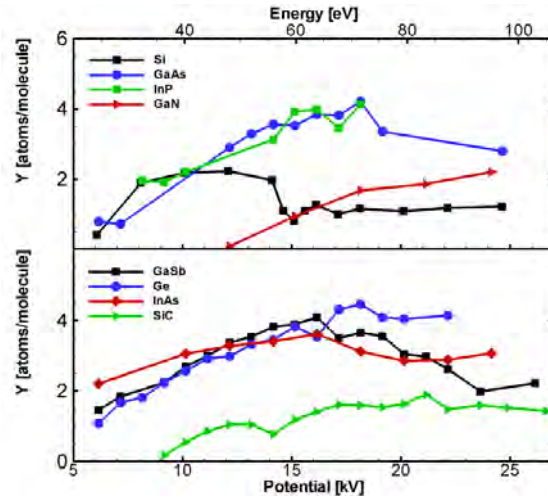


Figure 2.4. Sputtering yields as a function of acceleration potential. The maximum sputtering yields of all semiconductors are comparable. The maximum values between 2 and 4 atoms per projectile's molecule are substantially higher than those of gas cluster ions at similar acceleration potentials.

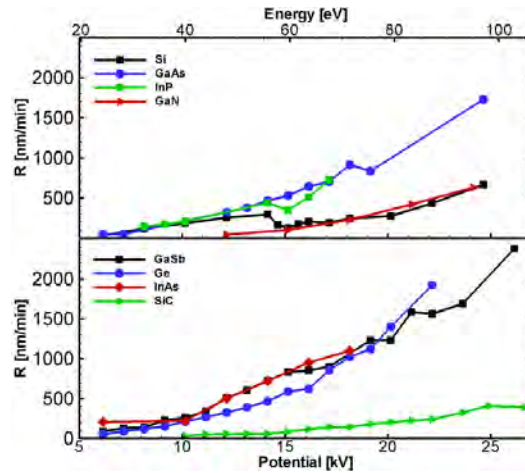


Figure 2.5. Sputtering rates versus acceleration potential. The sputtering rates in these experiments are similar to the values yielded by reactive ion etching, and orders of magnitude higher than in the comparable ion beam milling process.

The effect of the projectile dose on the damage exacted on Si is further illustrated in Fig. 2.6. In these experiments the beamlet strikes a spot during a period which is varied between 10 s and 600 s. The projectile dose is proportional to this time. The experiments are done at 12.1 kV and 18.1 kV acceleration potentials, to produce conditions that cause intertwined microscopic craters with high surface roughness and a smooth specular surface, respectively (see Fig. 2). The droplet number fluxes are estimated at $3.8 \times 10^{15} \text{ m}^{-2}\text{s}^{-1}$ and $7.3 \times 10^{15} \text{ m}^{-2}\text{s}^{-1}$ and, with an average droplet diameter of 27 nm, it takes about 0.47 s and 0.25 s for the beamlet to uniformly strike the surface with at least one impact. The photographed samples are illuminated along the line of sight and, since a rough surface scatters light effectively in all directions, the rougher the surface the darker the bombarded area appears. The photographs and the associated plots show how the surface roughness for the 12.1 kV beamlet increases with dose until it saturates at an exposure time of approximately 300 s, i.e. the formation of the large craters typical of Si requires exceeding a critical projectile dose. Conversely the roughness caused by the 18.1 kV beamlet, and the sputtering yields for either acceleration voltage, do not depend on the projectile dose. These results suggest a link between the accumulation of damage induced by consecutive impacts, and the formation of the very large craters characteristic of Si, which dominate the surface roughness when present. Also, at high enough projectile energy, the impact modifies the surface in such a way that this accumulation effect disappears. Furthermore, since the ejection of Si from these large craters does not have a significant contribution to the sputtering yield, the frequency at which the large craters form must be much lower than the rate at which the projectiles impact.

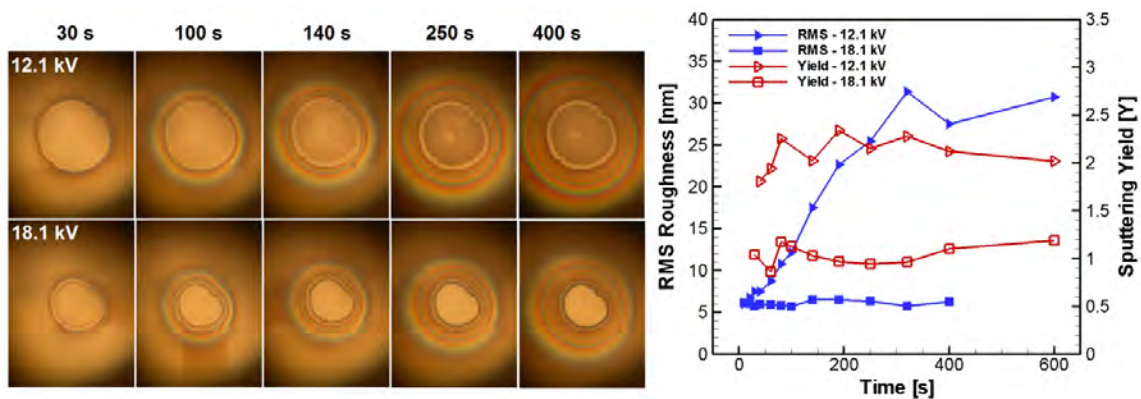


Figure 2.6. The effect of projectile dose on the surface roughness and sputtering yield of Si, at 12.1 kV and 18.1 kV beamlet acceleration potentials.

2.2 Molecular dynamics simulations of nanodroplet impact, physics of amorphization

The hypervelocity impact of electrosprayed nanodroplets on single-crystal silicon amorphatizes a thin layer of the target. Molecular Dynamics simulations have shown that the amorphization results from the melting of the material surrounding the impact interface, followed by an ultrafast quenching that prevents recrystallization. In the following paragraphs we discuss the roles played by the projectile's diameter and velocity on the amorphization phenomena, and compare the simulation results with experimental measurements of a bombarded silicon target. In the range of projectile diameter and impact velocity studied (diameter between 5 and 30 nm, and velocity between 1 and 6 km/s), the projectile velocity plays a more relevant role than its diameter. A significant amorphous layer begins to develop at a velocity near 3 km/s, its thickness rapidly increasing with velocity until it plateaus at about 4 km/s. The reduction of the melting temperature with pressure combined with the conversion of kinetic energy into thermal energy are responsible for the melting of silicon starting at an impact velocity of 3 km/s. Once the conditions inducing amorphatization are reached, the volume of the generated amorphous phase scales linearly with both the kinetic energy and the volume of the projectile.

Figure 2.7 illustrates the evolution of the projectile and the silicon target following the impact of a 20 nm drop at 6 km/s. Each panel shows a slice of atoms in the axis of impact, has a thickness of 0.86 nm, and atoms are colored according to a temperature scale. The projectile penetrates into the substrate producing a crater that reaches a maximum depth of 14 nm at 10 ps, and which stabilizes at a depth of 10.2 nm and diameter of 17.1 nm after several oscillations lasting approximately 35 ps. As the momentum of the projectile's molecules is transferred to the substrate, approximately 97% of its kinetic energy is dissipated within 7.6 ps from impact. During this time the dissipation is localized in the surrounding area near the crater, increasing the temperature of this region above the melting point (see Fig. 2.7.c). This area melts and, due to its very small volume and efficient heat conduction, quenches at a rate near 15.3×10^{12} K/s. At this cooling rate the liquid phase does not have sufficient time to recrystallize, undergoing a glass transition around 60 ps.

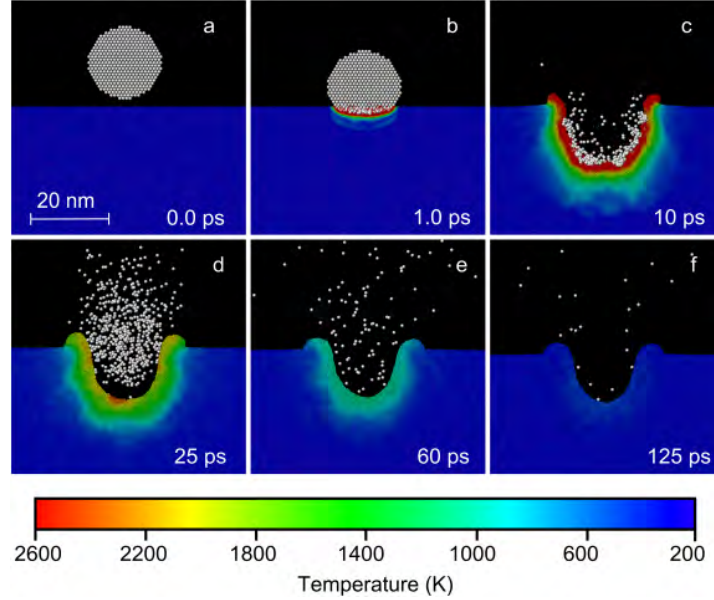


Figure 2.7. Impact of a 20 nm projectile at 6 km/s, showing the evolution of the crater and the temperature field in the slab.

The panels in Fig. 2.8 show the impact region at the conclusion of the simulations for projectiles with several diameters and velocities. Silicon atoms are colored in red, yellow, and blue to indicate their final phase and phase evolution: red atoms are in the amorphous phase at the end of the simulation; blue atoms are in the crystalline phase at the end of the simulation; yellow atoms are in the crystalline phase at the end of the simulation, but were in the amorphous phase at some previous time. Panels (a) to (d) show the effect of projectile diameter at an impact velocity of 6 km/s. The impacts produce craters with depths similar to the droplet diameters, and which become more spherical at increasing droplet diameter. At 6 km/s all projectiles amorphatize a substantial layer surrounding the crater, with average thickness ranging between 2.2 nm and 10.1 nm for the 5 nm and 30 nm droplets respectively. Panels (e) and (f) are for the 30 nm droplet and velocities of 2.0 and 3.5 km/s. At these lower velocities the impact produces shallow indentations, and only the first few layers of atoms are rearranged away from the crystalline lattice. In all cases we observe groups of atoms that at some point following the impact were in a non-crystalline phase, and which eventually recover the crystalline structure (atoms depicted in yellow). These atoms are located in the interface between the final

amorphous and crystalline domains, in regions that during the compression were deformed enough to lose long-range order for a brief period of time but did not melt.

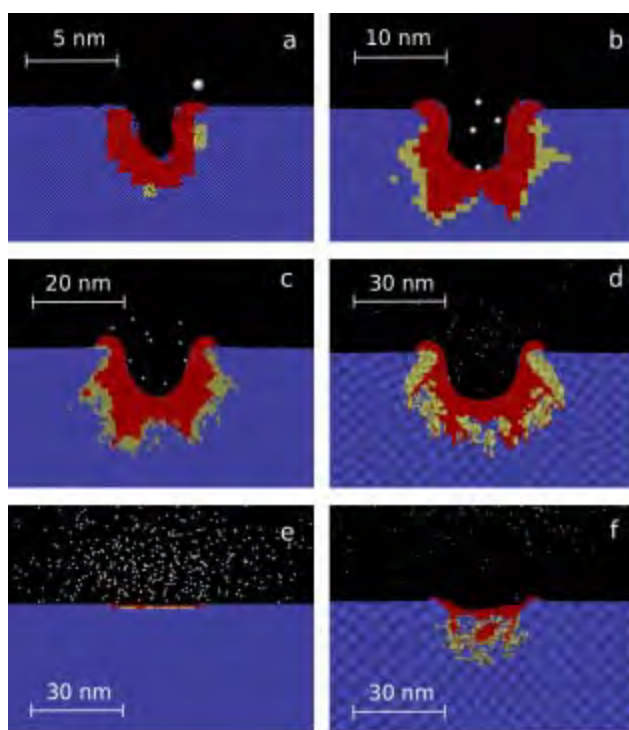


Figure 2.8. Cross-sectional images at the end of simulation. Panels (a), (b), (c) and (d) are for projectile diameters of 5 nm, 10 nm, 20 nm, and 30 nm, at impact velocity of 6 km/s. Panels (e) and (f) are for the 30 nm droplet at 2.0 km/s and 3.5 km/s. Projectile molecules are depicted in white; blue atoms represent the Si crystalline phase; red atoms represent amorphous Si areas; yellow atoms represent crystalline areas that at some previous time were in the amorphous phase.

The amorphization of a silicon layer is also observed in nanodroplet impact experiments. Figure 2.9 shows cross sectional TEM images of samples bombarded at average velocities of (a) 3.00 km/s, (b) 3.45 km/s, and (c) 4.94 km/s. The spotted regions are platinum layers deposited for protection of the surface during sample processing; crystalline Si shows in the higher magnification images as regions with geometric fringe patterns, and as a dark, homogeneous area at the lowest magnification; and amorphous Si appears as a distinct lighter band sandwiched between the Pt and crystalline Si. The impacts do not significantly alter the crystalline structure at the lowest velocity, and produce amorphous layers at the intermediate and largest velocities. The average thickness of the amorphous layer is 3.5 nm at 3.45 km/s, and

25 nm at 4.94 km/s. At 3.45 km/s the amorphous layer is relatively parallel to the original surface, while it deforms at increasing velocity producing larger amorphous pockets connected by thinner amorphous sections. The increasing surface roughness with impact velocity is consistent with the simulations in figures 2.8(d), 2.8(e) and 2.8(f), which show how the impact at 2.5 km/s barely modifies the surface of the target, the impact at 3.5 km/s produces a shallow indentation with a thin amorphous layer, and the impact at 6.0 km/s produces a large crater surrounded by an irregular and thick amorphous layer.

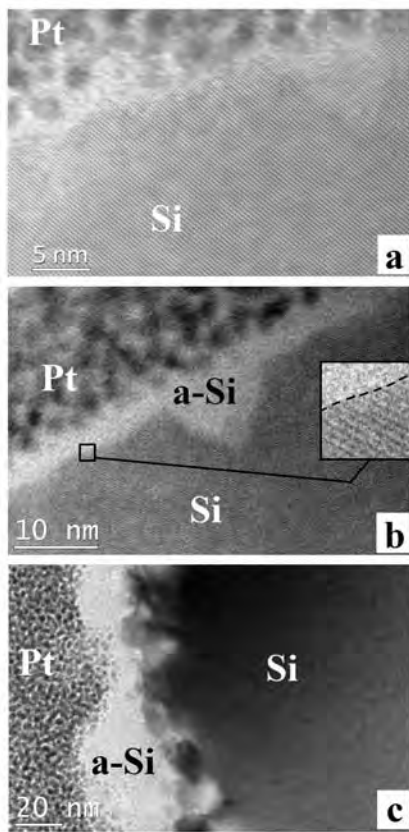


Figure 2.9. TEM images of samples bombarded by nanodroplets with acceleration voltages of (a) 4.65 kV, (b) 6.15 kV, and (c) 12.55 kV, and associated impact velocities of 3.00 km/s, 3.45 km/s and 4.94 km/s. The nanodrops do not significantly alter the crystalline structure at the lowest velocity, and produce amorphous layers at the intermediate and largest velocities

Figure 2.10 shows the dependence of the thickness and volume of the amorphous layer on the projectile's velocity and diameter. Thickness and volume are normalized with the diameter of the projectile and its volume, while a second horizontal axis displays the projectile's molecular kinetic energy. The thickness of the amorphous layer is a small fraction of the projectile's diameter for velocities under 3 km/s, it increases to a fraction between 0.29 and 0.34 at 4 km/s, and remains approximately constant at higher velocities. The normalized volume of the amorphous phase is also negligible for impact velocities below 3 km/s, and increases almost linearly with the molecular energy at velocities higher than 3 km/s. The simulations thus indicate that although low velocity impacts randomize the atomic positions in the initial atomic layers of the target, a threshold velocity of approximately 3 km/s is needed to extend the amorphization to atoms that are not in direct contact with the projectile. Furthermore, when the amorphization is significant, the thickness and volume of the amorphous phase scale linearly with the diameter and volume of the projectile. In addition to the simulation results, Fig. 2.10(a) also displays the thickness of the amorphous layers produced by the beamlet of electrosprayed nanodroplets (average diameter of 26 nm). The experimental curve matches well the MD simulations: it exhibits a threshold velocity between 3 km/s and 3.45 km/s for triggering the appearance of significant amorphization; and shows how the thickness of the amorphous layer increases with impact velocity before settling to a constant value. This constant value is twice as large as what is reproduced by the simulations, a disparity that may be related to the different impact conditions in the experiments: there is a natural variability in the diameter of the electrosprayed droplets; and the surface of the target in the experiments is modified by multiple impacts, with some four droplets typically hitting an area equal to the droplet's cross section. The modeling of the actual, multiple impact problem is not trivial because a large number of impacts must be simulated to condition the target. For example, for the 5 and 30 nm projectiles and the targets' dimensions used in this study, we would need to simulate 216 and 96 impacts respectively, randomly distributed throughout the target, to reach the experimental projectile dose (our CPU time for simulating a single impact by a 30 nm droplet exceeds 24 hours). In addition, although the SW potential reproduces well the solid and liquid phases of silicon and therefore captures the high pressure melting and the onset of amorphization during quenching, it

replicates less accurately the properties of the amorphous phase, and an alternative potential must be used instead to model it.

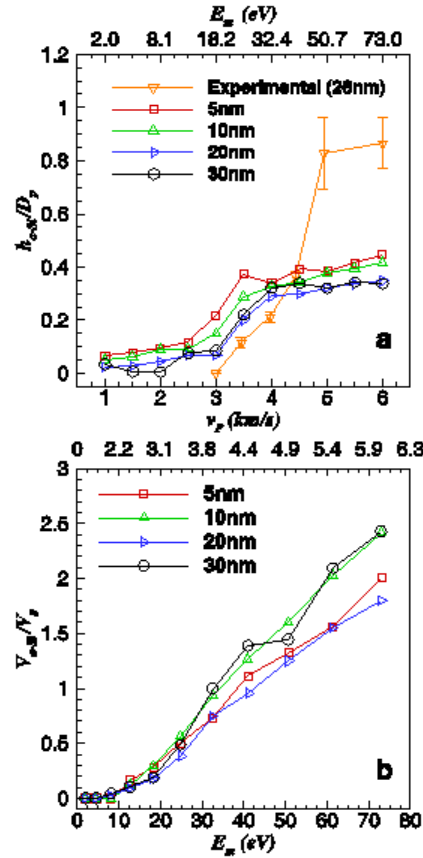


Figure 2.10. Thickness of the simulated and experimental amorphous layers, ha-Si, and volume of the simulated amorphous layers, Va-Si, versus projectile diameter and velocity (or equivalently molecular energy). Thickness and volume are normalized with the diameter and volume of the projectile.

During the impact a fraction of the initial kinetic energy of the projectile is deposited into the target increasing the potential and kinetic energy of the silicon atoms, while the projectile atoms bouncing back from the surface retain the remaining fraction. Furthermore, the kinetic energy of the atoms in the substrate can be decomposed into thermal and translational components by dividing the target into adjacent cubical volumes (we use a side of 1.69 nm, i.e. three Si unit cell side lengths), computing the average velocity of the atoms for each volume, and subtracting this average velocity to obtain the temperature .

The thermal and translational energies of the target are the sum over all cubical volumes. Figure 2.11 shows the fraction of the projectile's energy transferred to the target, as well as the fraction converted into target's thermal energy, as functions of projectile diameter and velocity. Since the thermal energy and the total energy of the target evolve with time, Fig. 2.11 plots their maximum values. The diameter of the projectile does not have a significant effect on the total fraction, and has a small influence in the fraction converted into thermal energy (the smaller the diameter the higher the conversion). On the other hand the velocity plays a significant role: a mere 15% of the projectile energy is transferred at 1 km/s, of which an average of 7% is in the form of thermal energy; both fractions increase with projectile velocity, reaching 70% and 18% respectively at 3 km/s; and at velocities beyond 3 km/s the transferred energy fraction increases asymptotically to a value of 95%, while the fraction converted into thermal energy remains approximately constant at 22 %. These results indicate that for impact velocities below 3 km/s the temperature of the silicon region surrounding the impact increases with the fraction of energy that is transferred. At still higher velocities and as the temperature exceeds the melting point of silicon, the resulting phase change becomes an efficient mechanism for absorbing the energy of the projectile at relatively constant temperature.

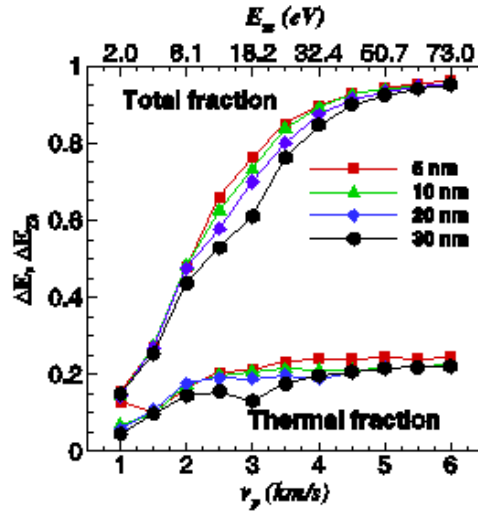


Figure 2.11. Total fraction of the projectile's kinetic energy transferred to the target, ΔE_t , and fraction that is converted into thermal energy, ΔE_{Th} , as functions of the projectile's velocity and diameter.

Since the interactions between liquid molecules, and between liquid molecules and Si atoms, are modeled with a crude two-body ZBL potential, it is worth considering whether the use of a more accurate full atom force field for the interaction between droplet atoms, and between droplet and silicon atoms, would significantly change how much energy of the projectile is transferred to the target. Although we cannot answer this question directly (the number of atoms in the projectiles is too large to consider a full atom force field), we think that the picture described in the previous paragraph is essentially correct. This opinion is based on: the very large kinetic energy of the projectiles' molecules (e.g. 18.2 eV at 3.0 km/s, 73.0 eV at 6.0 km/s); the comparatively very small value of the ionic bond energy in the molecules of the ionic liquid (a large fraction of the anions and cations are already dissociated at room temperature, and a small fraction of the projectile energy would be needed to dissociate the remaining molecules); and the unlikely generalized decomposition of the covalent bonds joining the atoms in the ions.

Both experiments and simulations show that substantial amorphization only occurs when the impact velocity exceeds a value of approximately 3.0 km/s. The sharp onset of amorphization at this threshold velocity results from the sudden convergence of the temperature and the melting point in the area surrounding the impact. This rapid convergence is caused by the simultaneous increase of the temperature and the reduction of the melting point at increasing impact velocity. To illustrate this Fig. 2.12 shows the evolution of the temperature, pressure, melting point and atomic coordination number near the impact interface, for a 10 nm projectile and four impact velocities. A spherical control volume with a radius of 1.08 nm, containing 280 Si atoms, and centered in the axis of impact 1.2 nm below the surface, is used to compute the thermodynamic paths. All charts show a pressure pulse following the impact with a lag of approximately 1 ps, and with a peak value (4.33 GPa, 6.20 GPa, 10.6 GPa, and 11.23 GPa) correlated with the stagnation pressure of the projectile (3.04 GPa, 4.75 GPa, 6.84 GPa, and 9.31 GPa). The melting point of Si decreases at increasing hydrostatic pressure, and its evolution in Fig. 12 is estimated by inserting the pressure of the control volume in the known relation for the melting curve $T_m(P_H)$. Thus, the impact reduces the melting point from 1685 K to minima of 1475 K, 1332 K, 897 K, and 887 K at increasing impact velocity. At the same time dissipation and the peak

temperature of the control volume increase with impact velocity. Figure 2.12 illustrates how these two trends sharply reduce the minimum gap between melting point and substrate temperature, finally bringing the temperature above the melting point during an extended period at a velocity of 3.0 km/s. The melting of the solid phase beyond this threshold velocity is most evident in the shift of the coordination number from 4 to a value near 6.5.

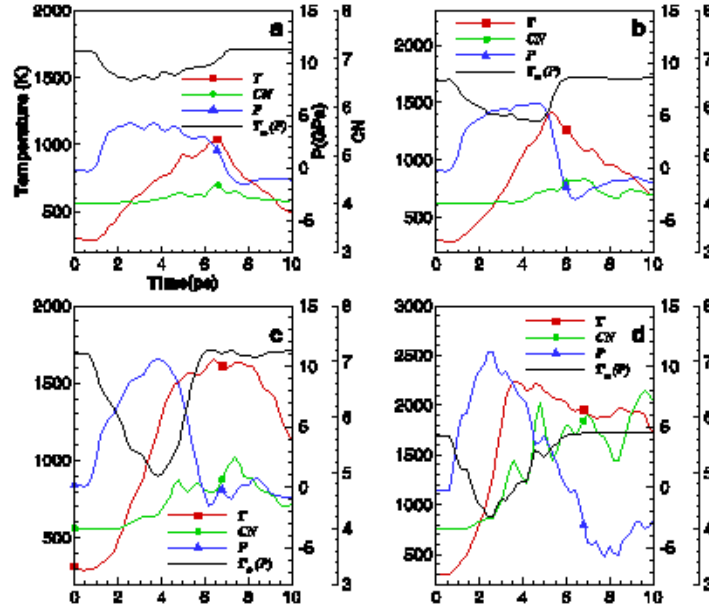


Figure 2.12. Evolution of the temperature, coordination number, pressure, and melting point below the surface of impact for the 10 nm projectile at velocities of (a) 2 km/s, (b) 2.5 km/s, (c) 3 km/s, d) 3.5 km/s.

2.3 Molecular dynamics simulations of nanodroplet impact, physics of sputtering

Physical sputtering is a fundamental phenomenon with a wide range of applications in surface engineering and surface elemental analysis. Although sputtering by light particles is well understood on the basis of Sigmund's collision cascade linear model,¹⁴ this theory underestimates the sputtering by larger projectiles like heavy atoms, molecular ions and gas cluster ions.^{15,16} Instead, other mechanisms such as thermal spikes caused by high density

collision cascades and thermal evaporation are known to control the sputtering by these larger projectiles.^{17,18} The former is a prototypical non-equilibrium process, while the latter is formulated within the confines of partial thermodynamic equilibrium.

The dependence of the sputtering yield on the nuclearity of molecular and gas cluster ions is superlinear (e.g. the sputtering yield of an cluster ion made of n argon atoms is higher than n times the sputtering yield of an argon atom having the same impact velocity as the cluster) and,¹⁹ as a result of the sputtering yield enhancement, the use of these large projectiles has proliferated and become an active area of research in ion beams.²⁰ Besides enhanced sputtering the impact phenomenology exhibits unique characteristics such as shallow implantation, surface smoothing, the ability to desorb intact macromolecules, etc. making large projectiles especially interesting for surface engineering and secondary ion mass spectrometry.^{21,22} These advantageous properties are associated with the short penetration range of a massive projectile, which transfers its kinetic energy and momentum within a thin surface layer. Dissipation is then concentrated in a small volume of the target, resulting on high energy densities and the maximization of the number of atoms that can overcome the surface binding potential.

The beneficial features of molecular and gas cluster ions are correlated with their size.²³ Until recently gas cluster ions were the largest projectiles available for ion beams, their low charging level limiting effective diameters to a few nanometers. This obstacle has disappeared with the introduction of electrosprayed nanodroplets, which are readily generated with sizes ranging from a few nanometers to tens of microns. Energetic electrosprays of glycerol droplets were used in the past to clean surfaces and for secondary ion mass spectrometry,^{24,25} but only recently electrosprayed nanodroplets were proven to be efficient sputtering projectiles.²⁶ The origin of this development can be traced to advancements in the theory of electrohydrodynamic atomization,²⁷ which provided a path for the electrospraying of monodisperse and controllable beams of highly charged nanodroplets.²⁸ Despite the experimental demonstration of nanodroplet sputtering the associated physics are not yet understood, motivating the present molecular dynamics simulations. More specifically this article models the impact of a nanodroplet of the ionic liquid 1-ethyl-3-methylimidazolium bis(trifluoromethylsulfonyl) imide,²⁹ Emi-Im, on a

[100] single-crystal silicon target, and resolves the sputtering mechanisms and the effects of the diameter and the velocity of the projectile on the sputtering yield.

The molecular dynamics technique is frequently used to study sputtering by molecular and gas cluster ions because of the accuracy of interacting potentials, and the detailed information on the positions and interactions of all projectile and target atoms. Molecular dynamics has been used to determine the sputtering mechanisms of small nanoprojectiles;³⁰ surface amorphization and smoothing;³¹ the transition from atomistic to macroscopic behavior exhibited in the collisions of nanoprojectiles;³² the effect of the interaction potential of the target's atoms on the sputtering yield,³³ etc.

We use the open-source program LAMMPS to simulate the impact of a nanodroplet on a [100] silicon wafer.^{34,35} The droplet is built as an hexagonal-closed-packaging arrangement of spheres with masses of 391.31 amu. Each sphere represents a molecule of the ionic liquid Emi-Im, a material that we have used extensively in experiments.³⁶ The radius of the spheres is set to 0.42 nm to match the density of the liquid, 1520 kg/m³. The parametrical range of the simulations includes projectile diameters of 5, 10, 20, and 30 nm, and impact velocities between 1 and 6 km/s. The forces between silicon atoms are modeled with the Stillinger-Weber (SW) potential,³⁷ while the universal Ziegler-Biersack-Littmark potential is used for the interaction between the projectile's molecules, and between the projectile's molecules and Si atoms.³⁸ This simple, two-body repulsive potential does not reproduce chemical interactions during the impact, nor does it take into account the internal degrees of freedom of the molecule which is in any case modeled as one large pseudo atom. The ZBL potential has the following form:

$$U(r) = \frac{Z_1 Z_2 e^2}{4\pi\epsilon_0 r} \varphi(r)$$

where Z_1 and Z_2 are the atomic numbers of the interacting particles ($Z = 198$ for Emi-Im, computed as the aggregate atomic numbers of its atoms), r is the interatomic distance, and $\varphi(r)$ is the screening potential function approximated by

$$\varphi(r) = \sum_{i=1}^4 a_i e^{-b_i r / a_U}$$

with coefficients $a_1 = 0.1818$, $a_2 = 0.5099$, $a_3 = 0.2802$, $a_4 = 0.02817$, $b_1 = 3.2$, $b_2 = 0.9423$, $b_3 = 0.4028$, $b_4 = 0.2016$. a_U is defined as

$$a_U = \frac{0.8854 a_B}{Z_1^{0.23} + Z_2^{0.23}}$$

where a_B is the Bohr radius (0.539177 Å). The cutoff distance for the interactions between molecule-molecule and silicon-molecule is set to 0.803 nm, i.e. at 95% of the diameter of the Emi-Im molecule. The equations of motion of the constitutive particles are integrated with a timestep of 1 fs, for long enough times to capture all atom ejections (all run times exceed 30 ps). We will frequently refer to the temperature field in the target when analyzing the simulations. Regardless of whether partial thermodynamic equilibrium is reached, a pseudo local *temperature* can always be defined at a point as the average of the kinetic energies of N atoms enclosed in a spherical control volume centered at that point:

$$T = \frac{m \sum_{i=1}^N (\mathbf{v}^i - \langle \mathbf{v}^i \rangle)^2}{3k_B N}$$

where k_B is the Boltzmann's constant, m is the mass of a silicon atom, and \mathbf{v}^i is the velocity vector of the i -atom. We will also refer to the thermal energy of an atom, defined as $3 k_B T/2$ where the temperature is evaluated at the position of the atom.

Thermal spikes caused by high density collision cascades and thermal evaporation are the dominant sputtering mechanisms for molecular and gas cluster ions, and we expect them to control sputtering by nanodroplets as well. The energy distributions of the atoms sputtered by these two mechanisms are:

$$F_C(E) = \frac{2UE}{(E+U)^3}, \text{ and} \quad (5)$$

$$F_{Th}(E) = \frac{E}{(k_B T)^2} \exp\left(-\frac{E}{k_B T}\right) \quad (6)$$

where E is the kinetic energy of the ejected atom, U is the surface binding energy, and T refers to the temperature of the surface from which atoms are evaporated. When comparing the simulation data to these two expressions we will approximate the surface binding energy by the standard enthalpy of formation of Si(g), $h_f^0 = 4.67$ eV,³⁹ and use the critical temperature of silicon as an upper limit for the temperature of the evaporating surface, $T_{cr} = 7925$ K (or 0.68 eV).⁴⁰

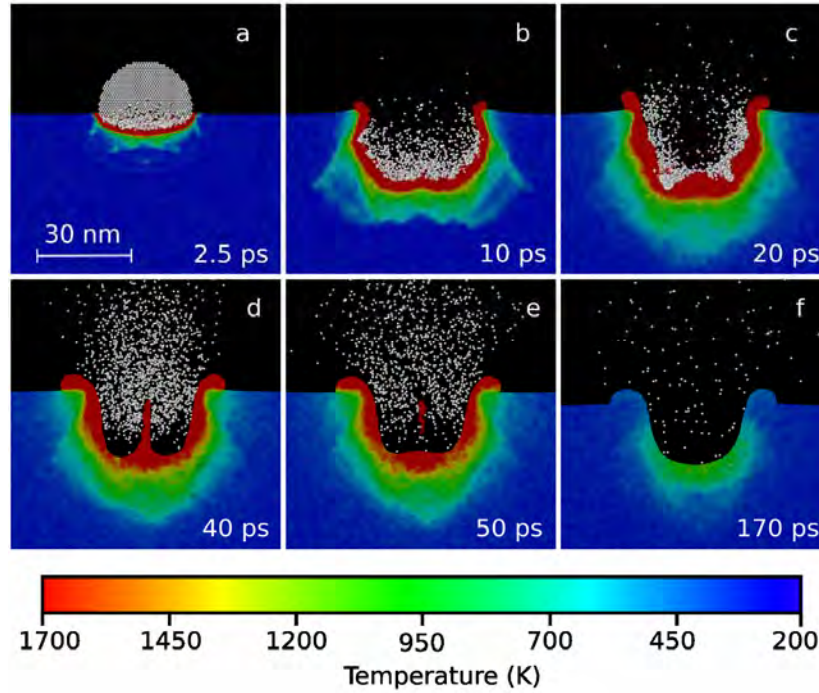


Figure 2.13. Impact of 30 nm droplet at 6 km/s. The cross sections include the axis of impact, and show the temperature field in the target. A total of 10,805 Si single atoms are sputtered.

Figures 2.13 to 2.17 illustrate a typical impact, in this case a 30 nm droplet with a velocity of 6 km/s. Figure 2.13 shows the evolution of a thin cross section of the target and projectile including the axis of impact. The molecules of the projectile are shown in white, while the color

graduation of the target renders the temperature field. At 6 km/s the projectile has enough energy to penetrate the target a distance comparable to its diameter, leaving behind a crater. As the projectile penetrates a fraction of its kinetic energy is dissipated into a thin layer of silicon generating temperatures well above the melting point (which at 1 atm has a value of 1685 K), and a substantial region melts and remains liquid for several picoseconds. This phase transition is facilitated by the reduction of the silicon's melting point with pressure.⁴¹ While the center of the crater reaches its maximum depth of 22.7 nm at 14 ps and begins to unload thereafter, a fraction of the projectile's molecules continues penetrating forming two lobes around the axis of the impact. The higher pressure in the lobes pushes a jet of fluid upward, which at 48 ps breaks apart from the target as two large conglomerates of 411 and 1337 Si atoms. These axial uplifts are also observed during the impact of macroprojectiles,⁴² and appear in our simulations at projectile diameters and velocities of, and exceeding, 20 nm and 5.5 km/s. The surface of the crater stabilizes at about 100 ps, while the temperature field continues its equilibration with the thermal bath. In addition to the conglomerates of 411 and 1337 atoms, 10,805 Si single atoms escape from the target, most of them during the first few picoseconds.

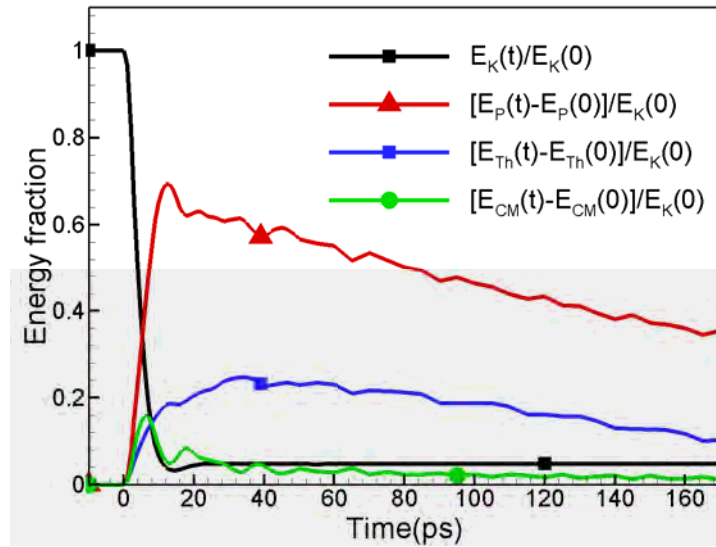


Figure 2.14. Impact of 30 nm droplet at 6 km/s: evolution of the projectile's kinetic energy, $E_K(t)$, and the target's potential $E_P(t)$, thermal $E_{Th}(t)$, and kinetic energy of the average velocity field $E_{CM}(t)$. All energies are normalized with the initial kinetic energy of the projectile and, in the case of the target's, offset with their initial values.

Figure 2.14 illustrates how the kinetic energy of the projectile, $E_K(t)$, is transferred to the target and converted into thermal and potential energies, $E_{Th}(t)$ and $E_P(t)$, and kinetic energy of the average velocity field, $E_{CM}(t)$. The energies in Fig. 2.14 are offset with their initial values and normalized with the initial kinetic energy of the projectile. The impact is characterized by a brief period of intense collisionality, the projectile losing 93.4% of its kinetic energy within 10 ps. By this time 16.6%, 65.1% and 8.9% of the projectile's energy have been transferred to the target in the form of thermal, potential and average kinetic energies respectively. The molecules of the projectile retain only 4.8% of their initial kinetic energy as they recoil out of the target. The thermal energy continues increasing after the projectile stops transferring energy to the target, due to the dissipation of the average velocity field and across the shock wave moving away from the impact. By the end of the simulation 49.6% of the kinetic energy of the projectile is transferred away from the slab by the thermostat, while 35.4% remains in it as potential energy mostly associated with the formation of the amorphous phase surrounding the impact, and 10.2% as an increase of thermal energy with respect to the initial state.³⁵

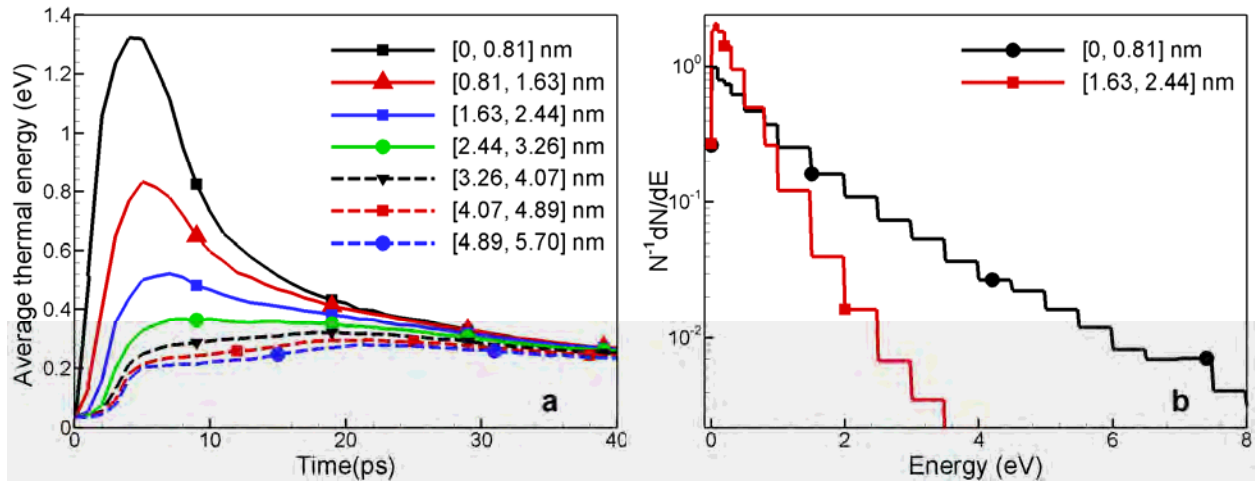


Figure 2.15. Impact of 30 nm droplet at 6 km/s: (a) evolution of the atomic average thermal energy as a function of distance from the surface of the crater; (b) distributions of thermal energy for the atoms positioned within [0, 0.81] nm and [1.63, 2.44] nm from the

surface of the crater; 4.50% and 0.067% of the atoms exceed the surface binding energy of 4.67 eV, respectively.

The density of thermal energy near the surface is more relevant to sputtering than the total value deposited in the target because, due to the lack of penetration of the projectile's molecules, it is the energetic state of the outermost silicon atoms what drives sputtering. Figure 2.15(a) shows the average thermal energy of the atoms located within a thin layer surrounding the crater, as a function of both time and distance from the surface of the crater. The average energy of the outermost atoms peaks 4 ps after the impact, at a value of 1.33 eV. For reference, if the atoms were in equilibrium the associated temperature would be 10280 K, i.e. well above the critical temperature. The average thermal energy decreases rapidly with distance from the surface, and at depths exceeding 3 nm the position of the energy maximum shifts towards the 20-30 picosecond window due to diffusion from the outermost atoms towards the bulk. Note that the large gradients of thermal energy are significantly reduced within this time window, suggesting that the surface approaches partial thermal equilibrium at about 25 ps. Figure 2.15(b) shows the distribution of thermal energy for the atoms in the [0, 0.81] nm and [1.63, 2.44] nm layers, at 4 ps. 4.50% of the atoms in the outermost layer have energies exceeding the surface binding energy of 4.67 eV, while the same fraction in the [1.63, 2.44] nm layer is only 0.067%. Clearly the fraction of atoms that are likely to be ejected is significant in the first atomic layer, and decreases rapidly with distance from the crater's surface.

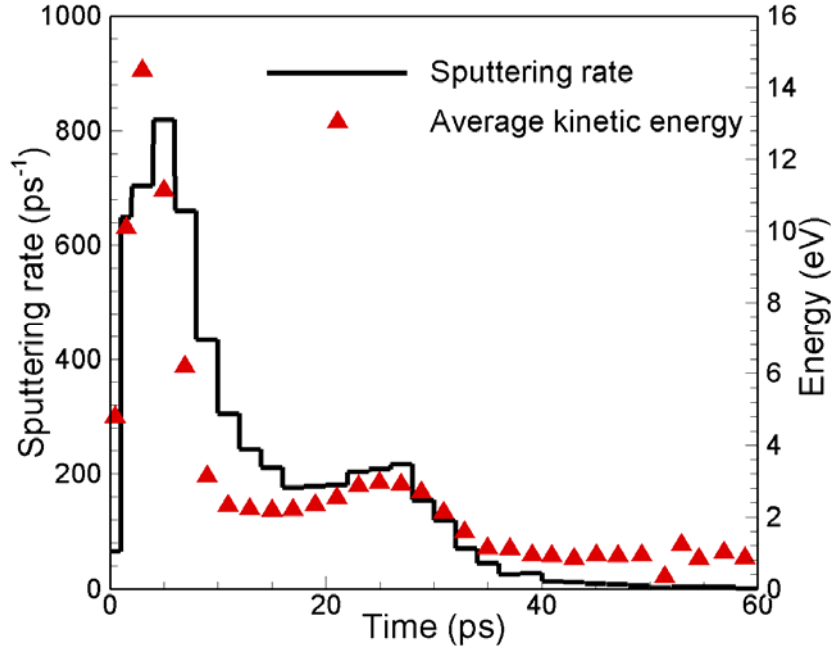


Figure 2.16. Impact of 30 nm droplet at 6 km/s: sputtering rate and average kinetic energy of the sputtered atoms over time.

Figure 2.16 shows the rate at which single Si atoms are sputtered and the average kinetic energy of the ejecta as a function of time, for the 30 nm and 6 km/s projectile. The sputtering rate has a bimodal distribution with a dominant peak associated with the collisional phase of the impact, and a lower second peak centered at 27 ps and coinciding with the onset of partial thermal equilibrium observed in Fig. 2.15(a). The total number of sputtered atoms is 10,805, with 55.1% of them being ejected within the initial 10 ps. The average kinetic energy of these atoms is high: for example, 13.0% of the sputtered atoms are released between 2 and 4 ps with an average kinetic energy of 14.5 eV. If the ejected atoms followed the thermal evaporation distribution (6), the associated temperature would be 84,000 K. This value, which would correspond to the temperature of the surface from which the atoms are evaporated, greatly exceeds the critical temperature of silicon and therefore a sputtering mechanism other than thermal evaporation must be controlling the ejection of these energetic atoms. Furthermore, the profiles in Fig. 2.15(a) suggest that the surface is far from partial thermodynamic equilibrium during these early stages. On the other hand, 2.53% of the atoms are ejected 35 ps after the impact, at a time when

the collisions between projectile molecules and target atoms have long subsided (see Fig. 2.14). The average kinetic energy of these atoms is 0.91 eV, and the corresponding temperature for a thermal evaporation distribution is 5,275 K, a value more in sync with the target's temperature field and which makes thermal evaporation the likely sputtering mechanism at these latter times.

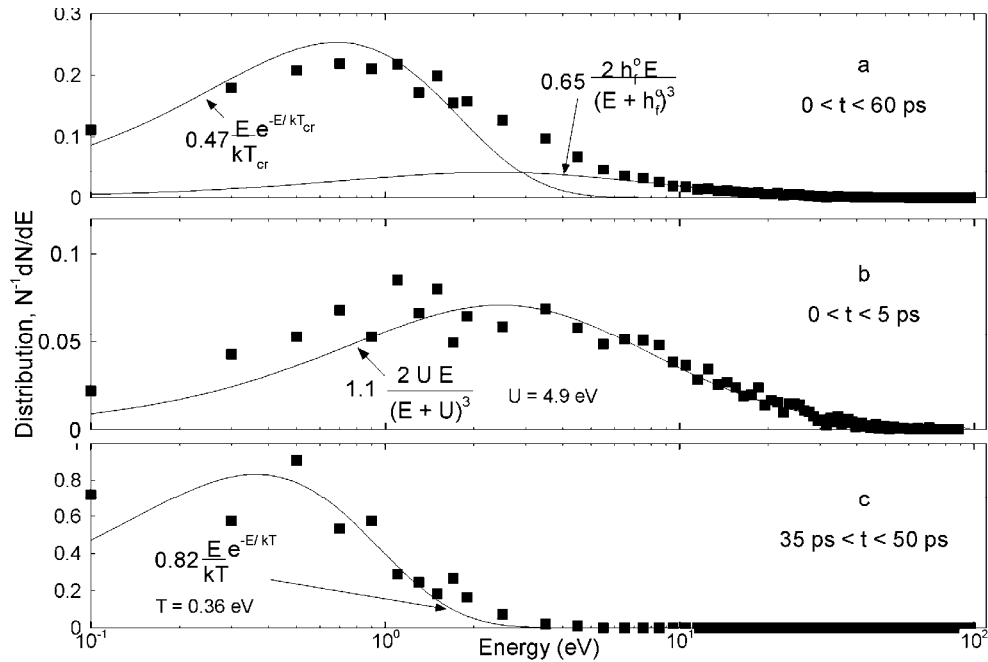


Figure 2.17. Impact of 30 nm droplet at 6 km/s: kinetic energy distributions of atoms sputtered in three different periods: (a) within 0 and 60 ps; (b) within 0 and 5 ps; and (c) within 35 and 50 ps. Collision cascades dominate the sputtering during the initial phase of the impact, while atoms are evaporated at latter times.

The energy distributions in Fig. 2.17 provide a better deconvolution of the sputtering mechanisms. The distributions are for atoms ejected within three different periods: (a) the overall interval of 60 ps including all sputtered atoms; (b) the initial interval between 0 and 5 ps characterized by intense collisionality; and (c) a period between 35 and 50 ps in which the geometry of the crater has become stationary, there is local thermodynamic equilibrium, and the temperature field relaxes towards the temperature of the bath. The overall distribution (a) decays slowly at high energies, similarly to the E^{-2} decay of collisional sputtering, ruling out thermal evaporation as the only acting mechanism. Conversely the significant fraction of atoms at low energies is indicative of thermal evaporation, and prevents a good overall fitting to the collision

cascade model. Since it is apparent that both mechanisms are contributing to the overall sputtering we fit the data to a collision cascade model with a value of h_f^0 for the surface binding energy, and to a thermal evaporation function with the maximum possible temperature $T = T_{cr}$, to estimate the relative importance of each mechanism. The fittings, shown in Fig. 5(a), suggest that about 65% of the sputtered atoms are ejected by collision cascades, and that a maximum of 47% of the atoms can be evaporated. The distribution in Fig. 2.17(b) follows more closely the collisional sputtering scenario, the interaction between projectile and target being most intense during this initial period of the impact. In this case we fit the distribution to a collisional model with two free parameters, the surface binding energy and a proportionality constant, obtaining values of 4.9 eV and 1.1 respectively. The fitting yields a good physical value for U and slightly over predicts the area of the distribution, suggesting that collision cascades is indeed the sputtering mechanism acting in the early stages of the impact. Finally, to probe thermal sputtering we use the energy distribution of atoms emitted between 35 and 50 ps, a period characterized by the absence of direct interaction between the projectile and the target. In this case a fitting to the evaporation model yields a temperature of 0.36 eV (4200 K) and a distribution that accounts for 82% of the atoms. The temperature of the fitting is significantly lower than the critical temperature of Si, but higher than the temperature of the crater's surface. However it is worth pointing out that the temperature is not constant nor homogeneous, but varies over time and location in the crater's surface, and therefore the fitting of the actual distribution to the thermal evaporation model with a unique temperature is inappropriate. In any case, the sharp drop of the distribution at increasing energy, its Gaussian shape and the concentration of particles at relatively low energies are indicative of thermal sputtering during this late stage of the process.

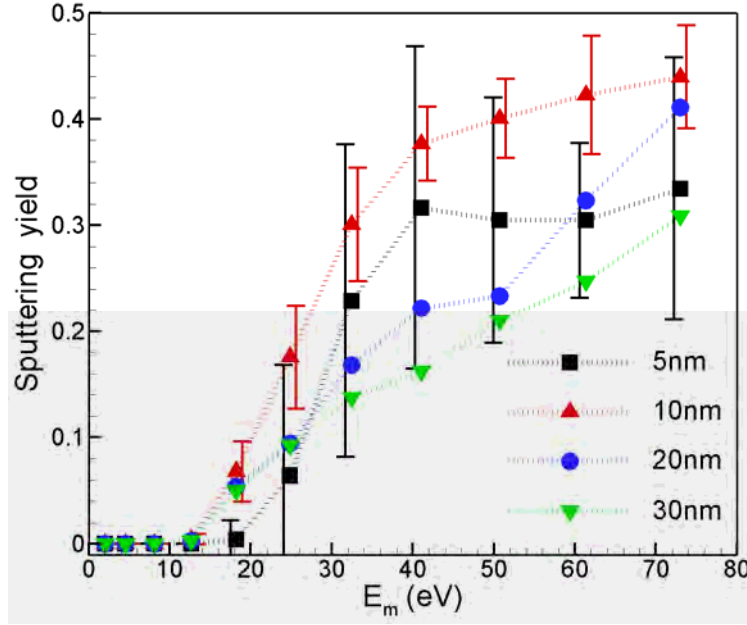


Figure 2.18. Sputtering yield as a function of molecular kinetic energy and droplet diameter. The error bars for the smaller projectiles are indicative of the randomness of the sputtering yield associated with the arbitrariness of the initial atomic configurations.

Figure 2.18 shows the sputtering yield (average number of Si atoms ejected per projectile's molecule) as a function of the projectile's size and molecular kinetic energy. One half of the error bars for the 5 nm and 10 nm projectiles represents the standard deviations of the sputtering yield for 10 simulations, each one calculated with a different set of initial conditions for the target atoms and the point of impact. The ratio between the standard deviations and the sputtering yields average to 0.62 and 0.14 for the 5 nm and the 10 nm projectiles respectively. The fast reduction of the variation of the sputtering yield at increasing projectile diameter makes it unnecessary to simulate the much more computationally expensive impacts of the 20 and 30 nm projectiles with multiple initial conditions. The emission of Si atoms starts between 2.5 and 3.0 km/s (12.7 and 18.3 eV), a range that coincides with the beginning of the melting of the target's surface.⁴³ Above this threshold the sputtering yield increases monotonically with the kinetic energy of the projectile, almost linearly for the 20 and 30 nm projectiles, reaching an average value of 0.37 at 73 eV. The sputtering yield at constant impact velocity is maximum for

the 10 nm projectile, and decreases with diameter for the 20 and 30 nm projectiles. The main reason for this is the backscattering of ejected Si atoms by collisions with molecules of the nanodroplet and other sputtered Si atoms, and the redeposition of some of the backscattered atoms. For example, for the 30 nm projectile impacting at 6 km/s we count a total of 32,470 Si atoms having at some time a coordination number of zero, i.e. which at some point are detached from the target. But only 10,805 of them escape away from the target and are counted as sputtered atoms; the rest, i.e. more than twice the final number of sputtered atoms, come back to the surface of the crater because either their escape trajectories intersects it, or because they are backscattered. This reduction of the sputtering yield increases with projectile diameter as the length of the region with a high density of Emi-Im molecules and which the ejected Si atom must cross, and therefore the likelihood for backscattering, is proportional to the diameter of the projectile. The experimental sputtering yields at the highest studied energies are about a factor of 2 larger than in our simulations.³⁶ The difference between the experimental and numerical results may be due to several reasons: first, the experimental data are generated by a beam of nanodroplets with a distribution of diameters and velocities, which introduces uncertainty in the comparison; and secondly, the simulations consider the impact of a single projectile on a perfect Si surface, while the experimental data are the result of multiple impacts on the same target area. It is likely that the state of the surface left after each impact in the experiments (a thin layer surrounding the crater melts and quenches to form an amorphous phase, probably generating a zone with high stresses) is weaker and conducive to the formation and propagation of cracks, or to other phenomena that favors sputtering and which are not accounted for in our isolated impact simulations.

3. Fundamental Study of the Generation of Nanoparticles and Evaluation of Chemical Monopropellants for Use in Electrospray Thrusters.

The research described in this section was executed by the group of Prof. Fernández de la Mora. It involves contributions from graduate students Juan Fernandez Garcia and Roberto Alonso Matilla, as well as Prof. J. Fernandez de la Mora.

3.1 Production of nanodrops going down to 1-2 nm in diameter.

This task is relevant to the proposed study on the dependence of drop erosion of targets as a function of projectile size. The dimensions of electrospray drops may be reduced continuously from microns down to a range widely believed to be of about 10 nm. Smaller drops could in principle be created from sufficiently conducting liquids if the usual electrospraying scaling laws remained valid down to arbitrarily small sizes. However, these laws cease to apply when the jet becomes narrow enough for electric fields in the range of 1 V/nm to arise. This happens at electrical conductivities of about 1 S/m. At higher conductivities substantial ion currents start evaporating from the liquid tip. This then alters radically the behavior of the spray, precluding in most cases the controlled production of drops with diameters smaller than 10 nm. In recent STTR work (AFOSR FA9550-09-C-0178 to Alameda Applied Sciences) the Yale group discovered that the ionic liquid ethylammonium nitrate (EAN) binds its own individual charges far more strongly than any other ionic liquid previously studied. As a result, it has an unusually low tendency to evaporate ions, and could be expected to be capable of producing much smaller drops than any other known material. This possibility is however precluded by the relatively high viscosity of EAN, which limits the maximal conductivity and the smallest drop size achievable. We reasoned that the mixtures of EAN with neutral solvents of lower viscosity would enable substantially higher electrical conductivities than possible in pure EAN. This we found to be indeed the case in mixtures of EAN with sulfolane (SF). Remarkably, the previously

observed exceptionally strong binding of the EAN ions to pure EAN was equally applicable to SF/EAN mixtures, which led to the ability to produce unprecedentedly small drop sizes. The radical advantages of these mixtures for electrical propulsion have been discussed in Yale's reports to Alameda Applied Sciences relating to AFOSR FA9550-09-C-0178. Here we discuss their comparable implications on projectile size control for erosion studies.

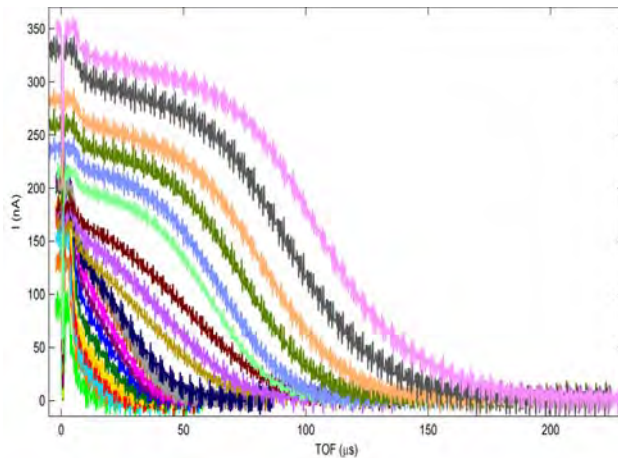


Figure 3.1. Time of flight curves for 50/50 (vol) EAN/SF in positive polarity for several propellant flow rates Q . Distance extractor-collector $L=154\text{mm}$.

Figure 3.1 shows time of flight curves resulting from plotting the spray current $I(t)$ received at a collector electrode after a time t following interrupting the spray. Downward steps of the current taking place at small times correspond to the short arrival time of small and fast drops, while longer times are associated to the larger flight times of larger and slower drops. All the curves show a contribution from very fast particles with flight times below $10\text{ }\mu\text{s}$, corresponding to evaporated ions. This feature is most prominent on the curves most to the left, also showing a broader peak of nanodrops moving almost as fast as the ions. The size of these drops can be precisely controlled down to diameters which we estimate as surely smaller than 2 nm . We have therefore developed a splendid new source of nanodrops covering continuously the size range from tens of nanometers down to almost one nanometer. With this tool it now becomes possible to cover essentially the full range of projectile sizes, from molecular dimensions up to the larger projectiles previously developed by the UCI group.

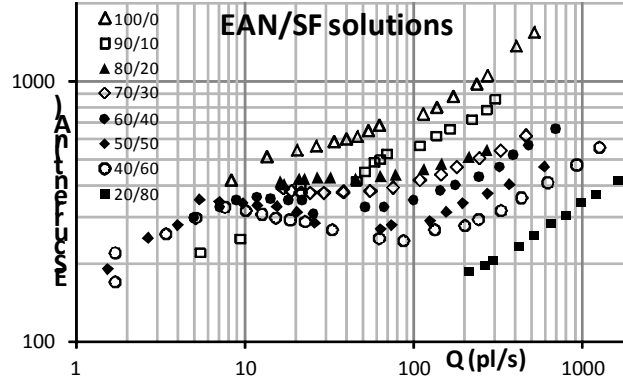


Figure 3.2. Electro spray (ES) current vs. propellant flow rate Q for EAN/SF (vol/vol) mixtures in positive polarity.

Some insights on how drastically smaller these drops are compared to prior studies can be obtained by following in Figure 3.2 the dependence of the spray current I versus liquid flow rate Q as a function of the volume fraction of EAN/SF. The least conducting solution (20/80 EAN/SF) has an $I(Q)$ behavior typical of the droplet mode, with a monotonic variation close to $I \sim Q^{1/2}$ (dashed line). The other solutions behave similarly at high Q , but exhibit a rather different $I(Q)$ trend at lower Q , and extend drastically their lowest flow rate Q_{min} . The latter effect is rather singular, as Q_{min} shifts by about two orders of magnitude from the 20/80 to the 40/60 solution. Exploring the evolution between the two rather disparate performances arising at EAN concentrations between 20% and 40% would have been instructive, but this was not investigated. The 40/60, 50/50 and 60/40 blends exhibit a minimum and maximum (min/max) in the current, with the magnitude of the peak decreasing in the last one, and the min/max structure turning into an inflexion for IL concentrations of 70% and higher. The maximum current achieved increases monotonically with increasing EAN, providing a substantial increase in consumed power per Taylor cone. However, the performance deteriorates at increasing EAN concentrations, and is considerably poorer for the pure salt (even though it is still far better in the drop mode for pure EAN than for alternative neat IL propellants). The smallest values of Q_{min} are obtained in the 40/60 and 50/50 mixtures (to some extent also the 60/40 solution).

These are the optimal concentrations from the point of view of achieving both the smallest drops, and the widest range of mean drop sizes.

3. 2 Identification ionic liquids oxidizing ILs for dual electrical/chemical propulsion and target erosion by controlled deposition of internal energy.

Like the previous one, success in this task would have considerable advantages for both the propulsive as well as the hypervelocity impact studies contemplated in our program. The identification of an energetic ionic liquid with good electrospray performance would open the path for dual propulsion, where the same propellant could be accelerated either electrically or chemically, depending on the thrust level needed (though at the cost of greatly reduced *Isp*). The Air Force has already developed energetic ionic liquids based on HAN formulations. These formulations have been tested at Yale after removal of their small water content, and have interesting characteristics as electrical propellants. However, they are much inferior to EAN/SF mixtures in their ability to produce a wide range of drop sizes for variable *Isp* propulsion. For target bombardment our proposal noted the interest to control both drop size and the amount of chemical power (internal energy) rather than the more readily controlled kinetic energy of the projectile. Therefore, it seemed necessary to develop new materials for this task.

3.2.1: Attempts based on mixtures of EAN. The natural candidate was EAN, given its excellent electrospraying performance (just discussed), and its substantial chemical energy (considerably smaller however than that of HAN). We had originally proposed to develop mixtures of EAN with other oxidizing salts in order to widen the range of internal energies available, both for propulsion and for erosion. We have as a result studied the miscibility of EAN with a variety of other oxidizing salts based primarily on nitrates. Surprisingly given the expected affinity between one nitrate and another, none of the many inorganic nitrates tested were miscible with EAN. Although these explorations have been fruitless, our original proposal of studying erosion by combined release of internal and chemical energy can still be pursued with pure EAN, which is sufficiently energetic to be ignitable as a pure substance (as shown in unpublished work by Professor Richard Yetter), whence a nanodrop of pure EAN would surely ignite on high velocity impact against a target.

3.2.2: New possibilities based on EAN ferrofluid. In recent discussions with Professor Brad King, we have learned that his collaborators from N. Zealand have developed a ferrofluid based on EAN mixed with iron oxide nanoparticles. This development has a number of promising implications both in electrical propulsion (currently pursued by Prof. King) as well as in the development of new types of hypervelocity projectiles: First, because the magnetic nanoparticles are very small (5-8 nm diameter), they offer for the first time the possibility to study target bombardment with hard nanosized solid materials (iron oxide) accelerated to hypervelocities. Second, at high impact energies, some the oxygen in the iron oxide nanoparticles suspended in the EAN ferrofluid might conceivably be liberated and become available for a more energetic release of internal energy than from pure EAN. These enticing ideas are now beginning to develop, and have not yet been tested in the laboratory.

4. Fundamental Research on Ionic Liquid Ion Sources.

This line of research was executed by the MIT group lead by Prof. Lozano. Molecular dynamics simulations are used to explore electrospray thrusters on a scale that cannot be seen with experiments.

4.1 Solvated Ion Fragmentation Background

The emissions from an ionic mode electrospray are typically comprised not only of individual ions, but also of small clusters, known as solvated ions. These solvated ions typically consist of an ion with attached neutral clusters. For example, when operating in ionic mode with positive polarity and the liquid EMI-BF₄, the beam consists of (EMI-BF₄)_n EMI⁺. For many liquids, the beam contains mostly of $n = 0$ ions (known as monomers) and $n = 1$ ions (known as dimers).^{44,45, 46} The $n = 0$ fraction is typically between 30% and 50%. A small proportion of $n = 3$ ions are also found. For more complex liquids, such as EMI-Beti and C₅MI-FAP, somewhat higher proportions of $n = 3$ and even $n = 4$ ions are found,^{47,48} but the largest constituents of the beam are still $n = 0$ and particularly $n = 1$.

After extraction, these solvated ions can fragment, typically forming neutrals and ions with lower n . This process is illustrated for a dimer (and $n = 2$ solvated ion) in Fig. 4.1. When fragmentation occurs after the ion has been completely emitted from the thruster, there is no impact on performance. However, fragmentation that occurs while the ion is still accelerating can significantly affect efficiency and specific impulse, as the neutral clusters formed during fragmentation cannot be accelerated by the electric field; if this fragmentation occurs before the neutrals have reached high speed, they drift out of the thruster slowly and provide only a negligible contribution to thrust, although this is partially compensated by the increased speed of the monomer ion product, which accelerates faster at lower mass. An understanding of the factors affecting fragmentation is therefore important when selecting a particular ionic liquid as the propellant.

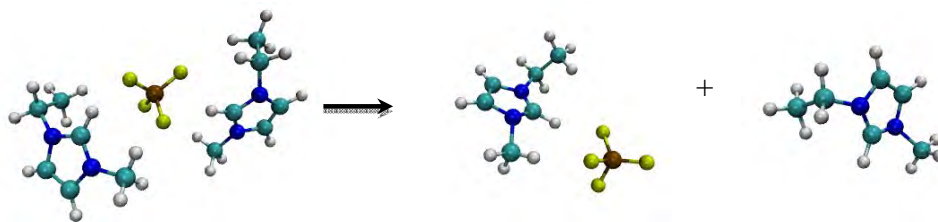


Figure 4.1. The ion fragmentation process illustrated for a positive dimer emitted from the liquid EMI-BF₄. The dimer on the left has +1 charge and fragments into a cation-anion pair with zero net charge and a cation monomer with +1 charge. The neutral pair can no longer be accelerated by the electric field and hence fragmentation is a cause of inefficiency if it occurs before the dimer is fully emitted from the thruster.

An additional factor affecting efficiency is polydispersity; this refers to the different sizes of ions present in the beam. When a given amount of energy is available for accelerating particles to provide thrust, it is always most efficient to use that energy to accelerate particles to the same size. The presence of ions with various different n therefore causes efficiency losses because different mass implies different speed. Furthermore, fragmentation contributes to the distribution of particle sizes and so also affects these polydispersity losses.

Simulating Fragmentation with Molecular Dynamics

To understand the effects of fragmentation, large numbers of solvated ions needed to be simulated. However, it was not possible to use only full emission simulations for this, as the computational expense would have been too great - the number of solvated ions emitted during a simulation is relatively low, even after many days of computational time. As a result of this problem, it was necessary to instead directly generate a large number of samples of solvated ions.

These random samples must include both coordinates and velocities for all atoms. This set of coordinates and velocities determines the internal energy of the ion. Although generation of large numbers of solvated ions from droplet emission was not practical, emitted ions seen in

droplet emission simulations can nevertheless be used to identify a reasonable range of internal energies, which can then be used as realistic target energies for the generation of sample coordinates and velocities.

An approach to generating consistent random velocities and coordinates for a given target energy still needs to be described. There is no analytic method for generating consistent velocities and coordinates in a complex non-linear system; instead, the typical approach used in molecular dynamics is as follows: coordinates are chosen, the resulting potential energy is calculated, and then the remaining energy is assigned in the form of kinetic energy randomly distributed among the atoms. The system is finally allowed to relax to an equilibrium state in which the coordinates and velocities are consistent.

This standard approach is unfortunately not suitable when generating initial conditions for simulations intended to reveal an event, as in this case when solvated ions are prone to fragmentation. This is because the ions may fragment during the equilibration process. A compromise approach used in this work is to equilibrate the ions at a target temperature instead of a target energy; more specifically, an NVT simulation is used instead of an NVE simulation. This is a well-developed process, as it is far more common for simulations in general to have an initial temperature target instead of an initial energy target. The NVT approach prevents fragmentation because fragmenting ions have high velocities as they move apart; these velocities appear in the temperature calculation, resulting in a high value. However, the temperature cannot reach a high value in an NVT simulation because it is being regulated (effectively, the system is modeled as being situated next to a heat sink that acts as a thermostat) and so ions are thereby prevented from moving apart fragmentation events are suppressed.

Having settled on NVT simulations for initial condition generation, it was then necessary to decide on a target temperature. This was done by trial and error to find a temperature that give an equilibrium internal energy close to that desired; each sample now had a slightly different internal energy, but the distribution of energies over a large number of samples was confirmed to always be in a narrow range around the desired energy.

The final information required was the initial conditions for the NVT simulation. For this, coordinates of stable solvated ions from a full emission simulation were used. Although the

same coordinates were used for each sample, the initialization to random velocities resulted in independent samples at the end of the NVT initialization simulations.

An Explanation of Fragmentation Physics

The work performed in this section was previously reported in the 2012 Annual Review, but it is necessary to comment again briefly to place more recent work in context. Initially, the ionic liquid EMI-BF₄ was used. 10,000 samples of negative dimers were generated at each of a variety of energies; each energy level was chosen from the range of energies seen in emissions from a full droplet simulation. For each energy level, some simulations were performed without an external electric field and others used a constant external electric field in the vicinity of 1.5 V/nm, which is an approximation to the electric field strength found at the surface of a Taylor cone. This model is unrealistic because the field remains constant here, whereas it decreases with distance according to an approximately inverse square root relationship in a physical system. This is however not a significant limiting factor because the impact of the electric field can be seen immediately in all cases and not just at long times. This can also be seen as the worst case for the impact of an electric field.

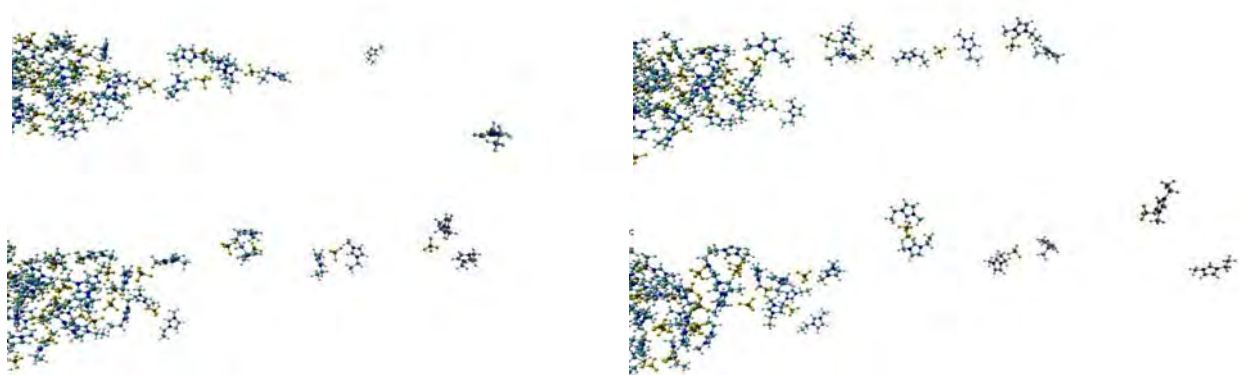


Figure 4.2. This is a sequence of snapshots during emission from a droplet containing 8232 atoms of EMI-BF₄ under an electric field directed to the right. The image order in time is left to right and top to bottom. While many ions are emitted directly from the surface (not

shown), others are emitted slowly as long chains that are stretched until they snap. This bond stretching imparts greater internal energy to the emitted ions than the average; note that this is a relatively extreme case - bond stretching in most cases is less dramatic than this.

The negative dimer fragmentation times indicated that the highest energy ions (5-10 eV energy added during the extraction process) are the most likely to break quickly, regardless of whether an electric field is present or not. However, when an electric field is present, it significantly reduces the fragmentation time at these high energy levels. This is not surprising, but it was more interesting to see that only a negligible fraction of the lowest energy ions fragmented in the 200 ps time of the simulation, even when an electric field was applied - the electric field acts only to accelerate the solvated ion as a whole and has negligible impact on the behavior of its components. This is because the instantaneous force applied by the electric field is not sufficient to pull the individual ions apart - there must be significant separation between the ions to reduce Coulomb attraction before the electric field is capable of separating them and this only occurs to a significant extent at high internal energies. Furthermore, if the internal energy is too high, then separation occurs quickly with or without the electric field.

For intermediate values of internal energy (around 2eV added energy), the electric field had a more significant impact on fragmentation - negligible fragmentation occurred without the field, but significant fragmentation occurred with the field.

In conclusion, fragmentation is likely to occur only in ions to which significant internal energy has been imparted. The electric field is a contributory factor and can increase the rate at which fragmentation occurs within an ion population at a particular internal energy level, but it is a determining factor for whether fragmentation ultimately occurs or not only for intermediate levels of internal energy. The internal energy is always the key deciding factor, as ions with less than 1eV additional internal energy did not fragment at all, even when an electric field was applied.

Mechanism Responsible for Additional Internal Energy

It remains to be explained why some ions are emitted with greater internal energies than others. A relatively extreme example (for ease of illustration) of why this occurs can be seen in figure 4.2; it demonstrates a long chain of ions that is being pulled away from the liquid surface by the electric field - the orientation of the ions in the chain is such that they are attracted strongly to each other. These chains are gradually stretched by the electric field. They are occasionally emitted as complete solvated ions, but often snap if one end remains firmly attracted to the liquid surface and the strain becomes too high. In this case, a number of smaller solvated ions are emitted from the remains of the chain, all at relatively high internal energies because of the bond stretching.

Many emitted ions do not necessarily undergo this stretching process, at least not to the same extent - random motion takes them to the surface of the liquid and they are pulled away at a time when their orientations are such that they are not strongly attracted to their nearest neighbors. No significant internal energy is added to these ions during the emission process and hence they are not likely to fragment.

Trends in Different Liquids

After observing that the internal energy of the emitted ions is crucial to determining fragmentation, consideration can be given to the practical impact on ionic liquid selection. This observation suggests that liquids with relatively large numbers of degrees of freedom may be less susceptible to fragmentation, as there are more modes in which to dissipate excess energy, resulting in reduced risk of moving far enough apart to reduce the Coulomb attraction to the extent that the ions can be completely separated by the electric field. This assumes that the internal energies of emitted ions from different liquids are increased by similar amounts during emission, but this is supported by experimental work in the literature^{45, 49} - energy deficits are generally very similar for different ionic liquids, at least to the same order of magnitude,⁴⁴ where the energy deficit is the difference between the energy required for extraction energy and the kinetic energy, as measured by a retarding potential analyzer (RPA).

To test this hypothesis, molecular dynamics simulations were used to obtain fragmentation statistics for a variety of ionic liquids. For each liquid, the approach described in section 1.1.1 was used. The Canongia Lopes and Padua force field (molecular dynamics parametrization) was used for all ions, as this is the only set of parameters to have been consistently developed for a wide range of ionic liquids. Consistency between energies of different liquids was maintained by using excess energy levels, i.e. internal energy in excess of that of a typical ion in a large equilibrated droplet at 300K. As before, a target temperature was selected for each liquid instead of a target energy, but the resulting energy distributions were confirmed to be similar for all liquids.

The liquids compared all used the EMI cation, as this generally results in the highest conductivity, which gives the highest current and therefore highest thrust from an electrospray. Although the BF_4 anion mentioned earlier is one of the most conductive, BF_4 -based liquids are hydrophilic and hence can easily be contaminated, especially as they tend to hydrolyze when stored in the presence of water for a significant time. The other anions chosen for comparison were as follows:

- Im (also known as Tf_2N or TFSI), bis(trifluoromethanesulfonyl)imide. This is a hydrophobic relatively high-mass anion and is currently one of the most popular ionic liquids for a variety of applications because of its stability and reasonable conductivity.
- FSI, bis(fluorosulfonyl)imide. This is a hydrophobic anion with higher mass than BF_4 , higher conductivity, and a lower melting point. It has not yet been tested in an electrospray.
- FAP (also known as MPI), tris(pentafluoroethyl)trifluorophosphate. This forms some of the most hydrophobic ionic liquids known and has been tested in an electrospray with the C_5MI cation.
- Cl. This was chosen simply for comparison to test the hypothesis, as this is an anion with the smallest number of degrees of freedom.
- Br. As with Cl, this was chosen simply for comparison to test the hypothesis.

The objective here was to compare negative dimer fragmentation probability for liquids with different numbers of degrees of freedom, as determined by the number of atoms. The halides Br and Cl are interesting partly because they have lower numbers of degrees of freedom than the other liquids. It is also worthwhile to note that they have the same number of degrees of freedom (compared to each other, not the other liquids); therefore any significant difference in fragmentation probability between these two liquids would suggest that fragmentation is dependent upon another factor in addition to complexity. Note that these two halides actually melt well above room temperature, yet most ionic liquids exhibit a strong super-cooling tendency down to their low glass temperature temperatures and so it is reasonable to include these halides in a comparison with the others, even though they are unlikely to be of interest in practice.

The simulations were run for 10,000 negative dimer samples with 2 eV excess energy in an electric field of 1 V/nm for 200 ps. Detailed fragmentation time distribution results can be seen in figure 2.3. This number of samples was not sufficient for full convergence, as some noise can be seen in the results. However, this was sufficient to clearly see the trend among these liquids and a few attempts at running simulations with different randomized initial conditions did not significantly change the fragmentation fractions. The results from the simulations are summarized briefly in the table below:

Anion name	# negative dimer atoms	Fragmentation fraction within 200 ps
Br	21	94.6%
Cl	21	98.6%
BF ₄	29	86.3%
FSI	37	72.7%
Im	49	26.7%
FAP	69	3.5%

This supports the hypothesis that an increase in ion complexity results in a significant reduction in fragmentation, as discussed earlier. The results are dramatic, especially for the largest ions. These results are also supported by preliminary data (not shown) for simulations of these ions at various other electric field strengths and internal energies. The fragmentation percentages for the

halides are very similar and, considering that only 10,000 samples were used, are close enough to suggest that complexity may be the only significant factor affecting fragmentation, at least in the negative mode.

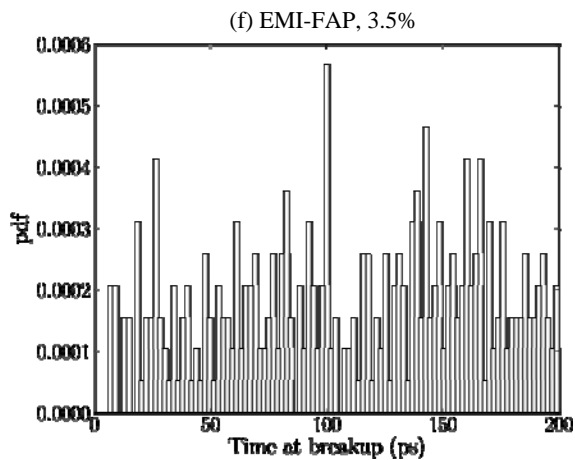
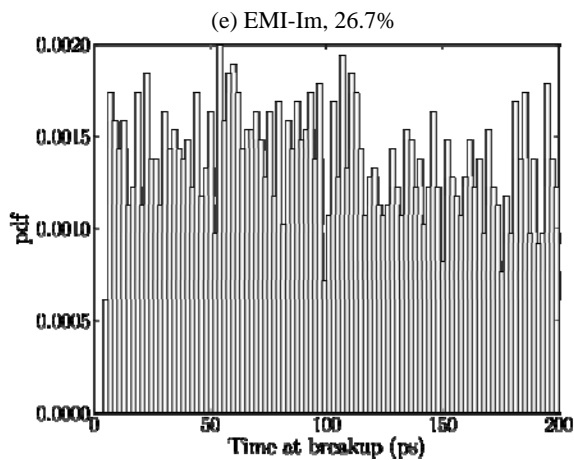
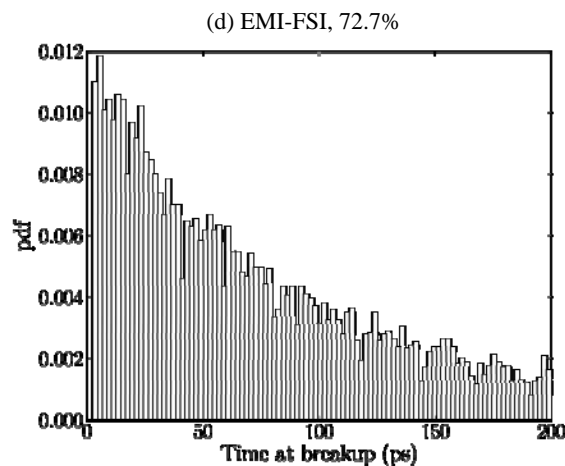
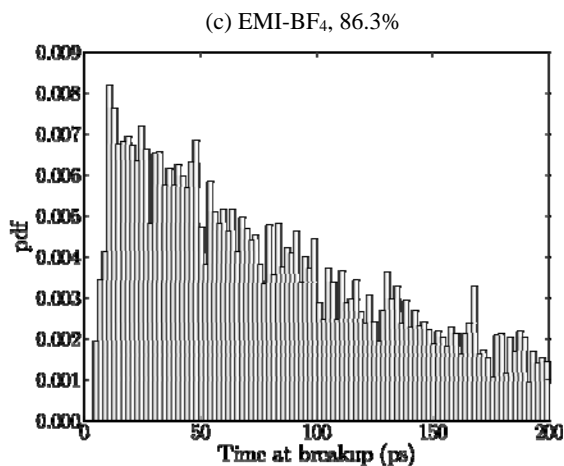
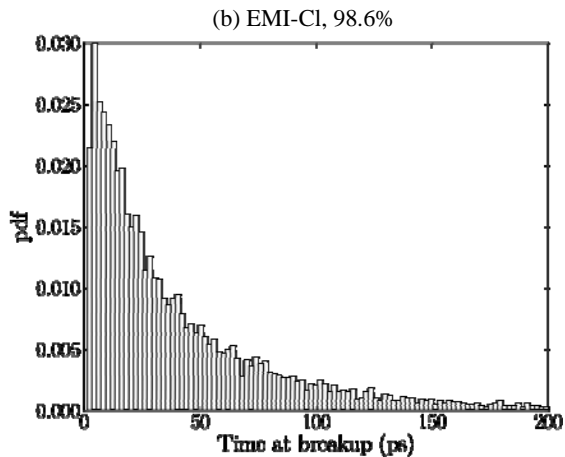
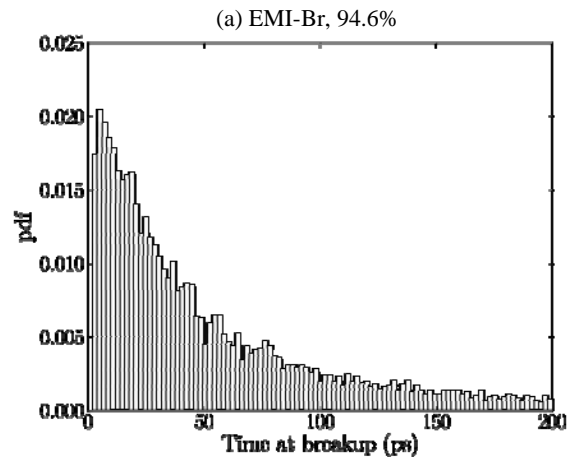


Figure 4.3. Fragmentation time distributions for dimers of various ionic liquids with 10,000 samples at 2eV excess energy with an electric field of 1 V/nm in negative mode. The percentages indicate the portion of samples that fragmented within the 200 ps shown, which is representative of the acceleration region in an electrospray thruster. The considerable noise in the last two plots arose because only a very small number of samples fragmented within 200 ps for these liquids. EMI-Br and EMI-Cl have the same complexity (defined simply as the number of atoms), but then the complexity increases from left to right and top to bottom.

It is important to note again at this point that the chosen electric field is unrealistically strong, given the amount of time for which it is applied. Physically, a field strength of 1 V/nm can be expected only very close to the tip of an electrospray emitter, but 200 ps is sufficient time for an ion to move far away from the tip and so most of this time is spent at much weaker electric field strengths. However, the purpose of these numerical experiments was a comparison between liquids under consistent conditions and the validity of this comparison is not affected; it is just necessary to be aware that the quantitative fragmentation fractions seen in experiments are not as high as those seen here because of the weaker physical electric field for much of the 200 ps.

One factor not explicitly considered here however is the distribution of solvated ion sizes in different liquids; this is an important consideration, as the overall fragmentation fraction depends not only on the probability of fragmentation of dimers, but on the number and type of other solvated ions emitted. As referenced in the introduction to section 1.1, the higher complexity liquids tend to produce the most solvated ions. It is therefore very significant that these offer such dramatically lower fragmentation fractions, as a high degree of fragmentation would result in very substantial efficiency and specific impulse losses for these liquids.

Similar simulations were run for positive dimers, yet the findings were less clear. Further work will be needed to understand the significance of this. Some difference between the positive and negative cases should be expected, as positive dimers differ by only a single anion instead of two anions for negative dimers.

Experimental Consistency

New experimental work is not reported here, but the computational results are consistent with experimental data collected on different occasions in prior work. Figure 2.4 shows retarding potential analyzer (RPA) experimental data for electrospray emissions from three different ionic liquids. Retarding potential analyzer experiments consist of an electrospray source emitting into a collector plate, but with a grid in between. When a potential is applied to the grid, any ions accelerated with less than that potential will be reflected and will no longer reach the collector. If a dimer has fragmented, then the potential required for reflection of the resulting monomer will be significantly reduced because of the reduction in kinetic energy. This allows fragmentation products to be identified in the beam separately from ions that have not fragmented, as those that have not fragmented have not undergone any kinetic energy reduction and can be stopped only by a retarding potential equal in magnitude to the full extraction potential.

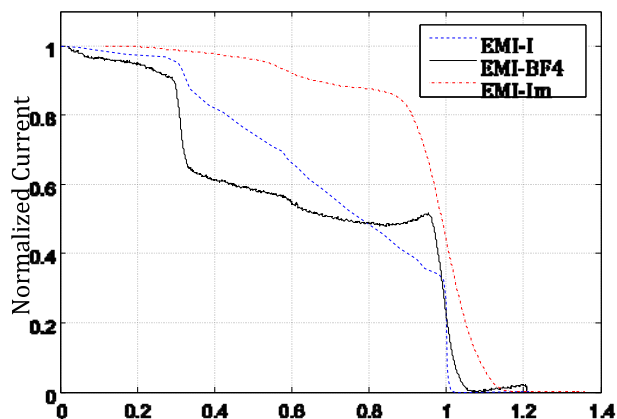


Figure 4.4. Experimental RPA data for three different ionic liquids using data from previous work: the complexity of the liquids increases in the order I, BF₄, Im. The fragmentation current is given by the size of the first step from the left; it clearly significantly decreases as complexity increases.

There is a minimum retarding potential below which no further effect on the current is seen; this minimum is clearly visible in all of the figure 21 plots. It corresponds to fragmentation after complete emission from the thruster; this is the minimum energy that a monomer can have, as it was part of a dimer for all of the time when it was accelerating and hence reached the lowest

possible velocity for an ion emitted from the thruster (when only considering monomers, dimers, and dimer fragmentation products).

There is a discontinuous step after this minimum potential, as all ions fragmenting at any time after acceleration are represented here. However, there is a continuous slope between the step and the full extraction potential because it represents ions fragmenting during acceleration; fragmentation can occur at a continuous range of potential values during acceleration (there does not appear to be any favored position) and hence the corresponding retarding potentials fall within the same continuous range. So the height of this slope on the y-axis indicates the fragmentation current fraction due to fragmentation products. Figure 21 clearly demonstrates a significant decrease in fragmentation as complexity increases.

Note that the experimental data was taken at different times under different conditions and hence cannot be seen as conclusive. However, its consistency with the numerical data lends extra weight to the hypothesis that more complex liquids experience reduced fragmentation, resulting in increased efficiency and improved thrust-Isp trade-offs. A much wider range of ionic liquids is currently being tested experimentally under consistent conditions to more conclusively demonstrate this trend.

4.2 Emission Studies

At the macroscale, the surface of a Taylor cone just before ion emission is an equipotential with a normal electric field strength found from the balance between the electric pressure force and surface tension. This is valid up until emission starts, at which point the cone becomes distorted by space charge effects from the emitted ions.

Macroscale quantities are however only averages over atomic-scale quantities. The electric field strengths responsible for ion emission, which occurs at the atomic scale, are considerably more complicated than can be seen from this simple model. Figure 4.5(a) demonstrates electric field strengths at various distances above the surface of a droplet of 343 ion pairs of EMI-BF₄ well before any emission occurs. This can be contrasted with figure 4.5(b), which shows the electric field for the same droplet, but now just before ion emission occurs in the presence of an external

electric field of strength 1.5 V/nm. Note that the location of ion emission is at approximately $y = -10 \text{ \AA}$, which corresponds to the highest electric field strength in the figure - the electric field appears to be focused at this point just prior to emission.

So ion emission occurs when the electric field is focused, not just over the area of the tip of a Taylor cone, but precisely on specific ions. This has implications for modeling ion emission and particularly the electric field strengths required to overcome the activation energy. Further investigation in this area may also explain why some liquids emit ions more readily than others, as there are likely variations in how effectively the electric field is focused in this manner at the atomic scale, due at least in part to variations in polarizability.

Solvation Energy

A molecular dynamics simulation was used to estimate the solvation energy of an ion in an ionic liquid by removing a surface EMI ion from a large droplet of EMI-BF₄, then calculating the difference between the initial and final configurations. Rather than simply discontinuously moving the ion away from the liquid, which would have neglected any changes to ion internal energy caused by the extraction process, the ion was instead dragged away by a small force. Following extraction, the ion's translational velocity was set to zero and then the difference in energy between the two configurations was calculated. The force was adjusted iteratively until it was too weak to separate the ion - this gave the minimum force for separation. The force giving the minimum extraction energy was expected to be close to the minimum force in magnitude, as much larger forces resulted in considerable disruption to the droplet and the ion, producing relatively large energy changes.

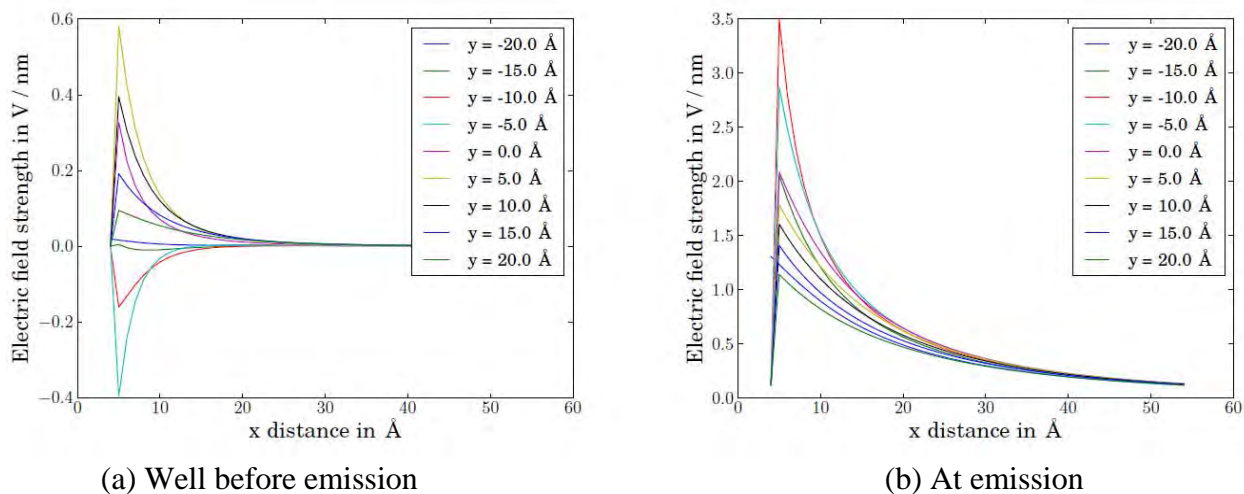


Figure 4.5. These figures show the electric field above the surface of a droplet of ionic liquid along the center in the z direction. The different colored lines represent different positions in the y direction, with the droplet roughly centered at $y = 0$. The x direction is measured from a point just below the surface. The electric field strength is due to the internal field of the droplet only - it does not include the externally applied field of 1.5 V/nm in the positive x direction. The left image demonstrates the somewhat randomized arrangement of low magnitude electric fields at a time well before emission. The right image is just before the first ion emission was detected; it demonstrates that the fields have all aligned and are focused at $y = -10$ Å, which was the location from which the ion was emitted. Note that this focused field is much greater than the applied electric field, which was chosen to mimic the values expected in experiments from continuum arguments balancing electric pressure with surface tension.

Solvation energy calculations were performed in this way on a cation at the surface of a droplet of 343 ion pairs of EMI-BF₄. The force giving the minimum energy change during extraction was found to be 6.95×10^{-11} N, which is within a factor of 2-3 of the force exerted by electric fields used in most simulations in this work (an electric field of 1 V/nm exerts a force of 1.6×10^{-10} N), although a key difference is that the artificial force in solvated ion simulations applies equally to all atoms, whereas that in emission simulations depends upon the partial charges of

the atoms. The solvation energy estimate was 4.64 eV. This is similar to the energy deficit value seen in the literature during ion emission,^{45,49} which is typically 5-6 eV. The discrepancy can be accounted for partly by the limited accuracy of molecular dynamics simulations and partly by the differences in force - the larger electrostatic force is more disruptive and imparts more energy; this additional energy goes into heating the emitted ions, as discussed in section 4.1.

In this minimal energy extraction simulation, the change in internal energy of the emitted ion was negligible, as was the change in internal energy of the droplet. This demonstrates that the solvation energy could in fact have been measured simply by discontinuously removing the ion from the liquid or, equivalently, calculating the potential energy in the Coulomb and Lennard-Jones forces between an ion of interest and the remainder of the liquid.

In the future we plan to compute solvation energies of other liquids and solvation energies of solvated ions, not just monomers. Rather than measuring individual values, distributions of solvation energies are being generated by removing different from different ionic liquid droplets. These solvation energy measurements will allow better interpretation of experimental energy deficits, i.e. for determining how much of the experimental deficit is due only to solvation and how much is due to heating of emitted ions.

4.3 Initial Exploration of New Liquid Types

The ions of ionic liquids tested in the electrospray literature so far have all had only a single charge. However, ionic liquids with multiple charges exist, for example dicationic liquids. The cations in these liquids contain two imidazolium rings bonded by a long chain; each ring has a localized charge of +1, leading to cations with an overall charge of +2. There are typically two anions per cation in these liquids. As an example, the cation 1,8-bis(3-methylimidazolium)octane is shown in Fig. 4.6.

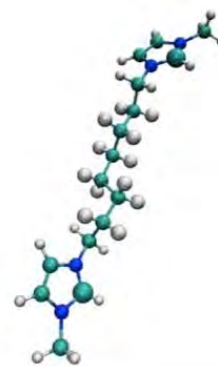


Figure 4.6. 1,8-bis(3-methylimidazolium)octane, which has +1 charge localized to each of the two imidazolium rings.

A droplet of ionic liquid using this cation and the PF_6 anion was created in molecular dynamics simulation and subjected to an electric field in the same way as other liquids considered in this work. Sample images from a simulation of this type can be seen in Fig. 4.7. In the first image, a long chain has started to be emitted because of the localization of negative charge from a cluster predominantly composed of anions. A conventional liquid with only a single disconnected positive charge would tend to undergo solvated ion emission at this point, i.e. when one of the imidazolium rings is so far from the surface. However, that does not happen in this simulation. The second image shows that one of the anions is emitted instead of a solvated ion cluster and then the third image shows another anion also being emitted alone. This happens because the other end of the chain remains anchored relatively securely to the surface, preventing it from being emitted. Ultimately, the final image shows the chain collapsing back toward the surface with no solvated ion emission.

These observations were typical of a number of simulations that were run with various randomized initial coordinates. They do not mean that no solvated ions will ever be emitted, as eventually sufficient negative charge may accumulate around a cation to emit it as a solvated ion, but the frequency of this will likely be significantly lower than in a traditional monocationic liquid. If a solvated ion is emitted, it will have very high mass - at least three anions per cation, which itself is double the mass of a conventional cation. This is important for the focused ion beam application of electrosprays, in which a monodisperse beam is desirable to allow the ions to be focused onto a target. This beam will not be 100% monodisperse, but an occasional very high mass solvated ion can easily be filtered out of the beam. This is also potentially useful if wanting to obtain very high specific impulse at relatively low thrust in an electrospray thruster; efficiency will be affected when solvated ions are released, but not to a significant extent if such emissions are very infrequent.

4.4 Water Contamination of Ionic Liquids

Additional molecular dynamics simulations have been run with water introduced into the ionic liquid. The TIP4P water model was used,⁵⁰ as the OPLS-AA force field⁵¹ (on which the

Canongia Lopes and Padua ionic liquid force field used in this work was based) was designed to be compatible with it. Work involved a high concentration of water with equal numbers of water molecules and ion pairs. Figure 2.8 contains an example image of 250 molecules of water with 250 ion pairs of EMI-BF₄. The simulation was run with the same parameters as the other MD work in this project, but now using the SHAKE algorithm to constrain the water bonds, as required by the TIP4P model. The SHAKE parameters were a tolerance of 0.0001 with the maximum number of SHAKE iterations per time step set to 20. The initial conditions for the simulation involved an inner sphere of water surrounded by ionic liquid, each individually equilibrated at 300 K using an approximate NVT simulation.

The figure shows the separate emission of a water molecule and positive solvated ion. Water molecules tend to evaporate throughout the simulation, regardless of whether an electric field is active or not; this is not surprising, as water does not have zero vapor pressure. Some of the ions extracted by the electric field also have attached water molecules, as shown in the solvated ion in the figure.

This observation could potentially explain spurious signals in RPA data in earlier work,^{45,49} as eventual separation of the water molecules from the ions would result in lost energy by the time of detection with the RPA. More significantly, this water simulation is the first step to larger simulations with water, which will attempt to see if large water bubbles can create a liquid explosion; this is hypothesized to be a cause of thruster short-circuits, which are seen experimentally and may place limits on thruster lifetime.

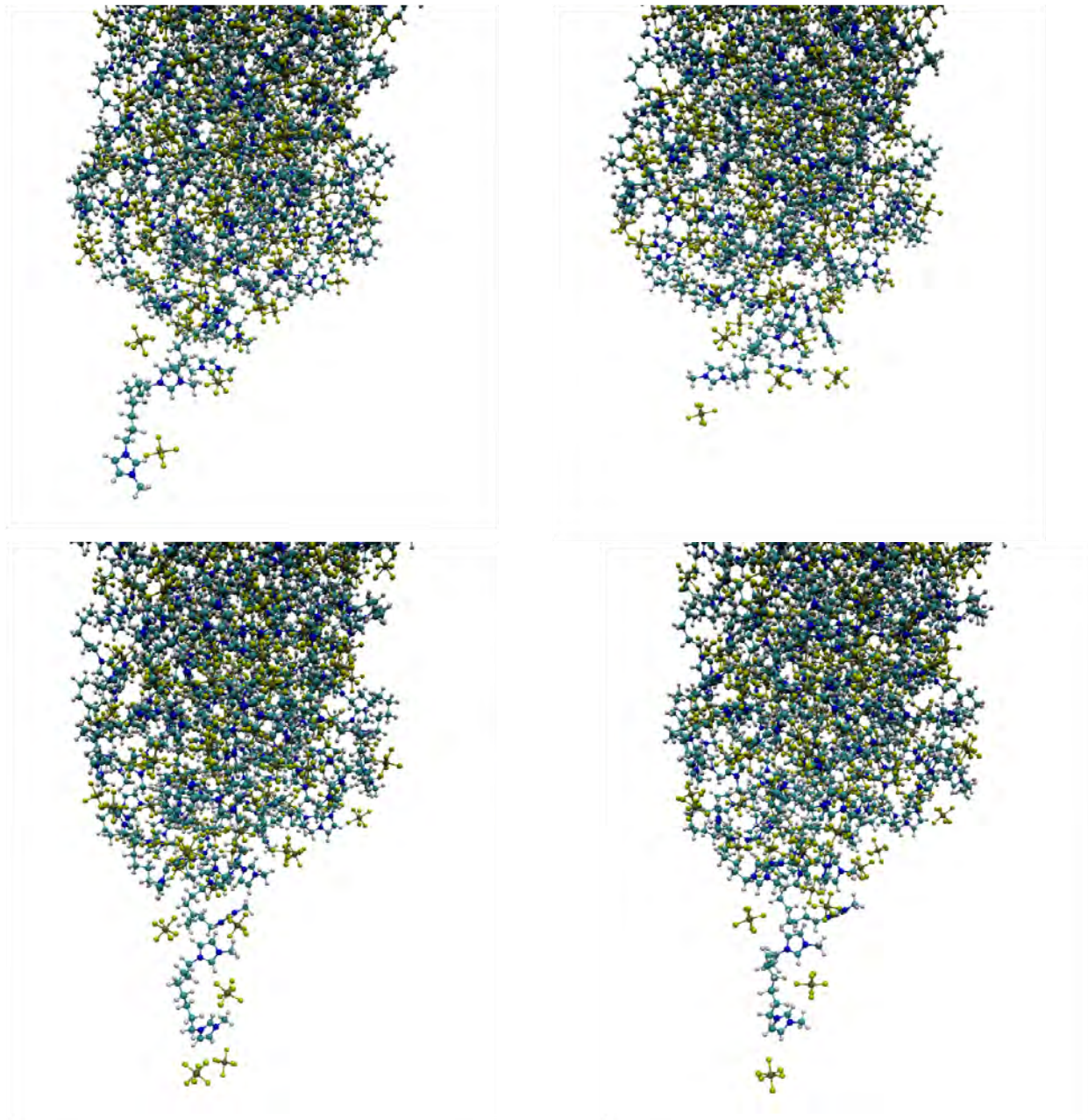


Figure 4.7. Electrospray emissions from the ionic liquid 1,8-bis(3-methylimidazolium)octane hexafluorophosphate; the images are in order of left to right and top to bottom. This dicationic liquid is unlikely to produce significant solvated ion emissions in negative mode, as the chain structure of the cations results in one end being anchored near the liquid surface, preventing the other from being extracted by an electric field. The electric field in these images is oriented with negative down. The images show that a chain starts to be emitted as part of a solvated ion, but ultimately collapses back to the liquid surface. A single anion is emitted between the first and second images, then again between the second and third, but the cation that was initially far from the surface in

the first image has collapsed back to the surface by the time of the fourth image without being emitted.

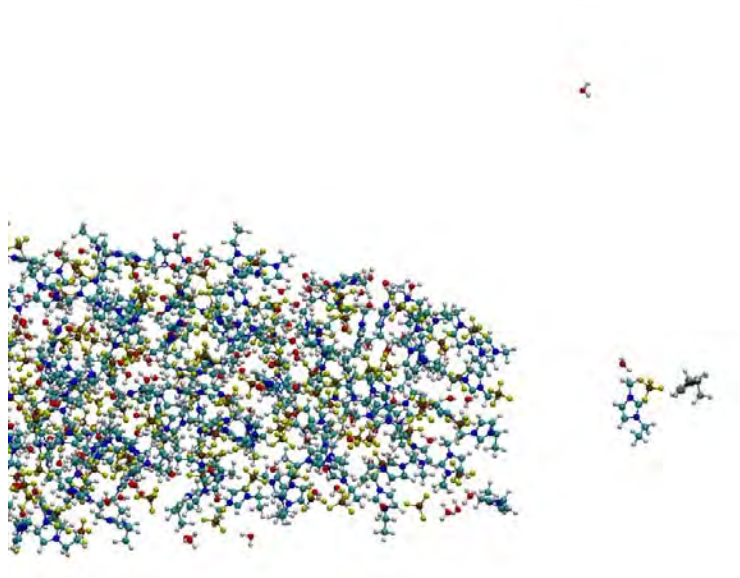


Figure 2.8. Electrospray emission from a droplet of 250 ion pairs of EMI-BF₄ mixed with 250 molecules of water. Some of the water evaporates spontaneously, whether an external electric field is present or not. As seen in this image, some of the emitted ions have attached water molecules.

REFERENCES

- 1 McEwen A. B., Ngo H. L., LeCompte K. & Goldman J. L., “Electrochemical properties of Imidazolium salt electrolytes for electrochemical capacitor applications”. Journal of Electrochemical Society, 1999, 146, pp. 1687-1695.
- 2 M. Gamero-Castaño, Journal of Fluid Mechanics, 604, 339-368 (2008)
- ³ I. Yamada and N. Toyoda, Surf. Coat. Tech. 201, 8579 (2007).
- ⁴ N. Winograd, Z. Postawa, J. Cheng, C. Szakal, J. Kozole, and B. J. Garrison, Appl. Surf. Sci. 252, 6836 (2006).
- ⁵ S. Ninomiya, K. Ichiki, H. Yamada, Y. Nakata, T. Seki, T. Aoki and J. Matsuo, Rapid Commun. Mass Spectrom. 23, 1601 (2009).
- ⁶ D. Asakawa and K. Hiraoka, Surf. Interface Anal. 44, 227 (2012).
- ⁷ J. Samela and K. Nordlund, Phys. Rev. Lett. 101, 027601 (2008).
- ⁸ M. Gamero-Castaño and M. Mahadevan, Appl. Surf. Sci. 255, 8556 (2009).
- ⁹ M. Cloupeau and B. Prunet-Foch, J. Electrostat. 22, 135 (1989).
- ¹⁰ I. Romero-Sanz, R. Bocanegra, J. Fernández de la Mora and M. Gamero-Castaño, J. Appl. Phys. 94, 3599 (2003).
- ¹¹ M. Gamero-Castaño and V. Hruby, J. Propul. Power 17, 977 (2001).
- ¹² Y. Fujiwara, N. Saito, H. Nonaka and S. Ichimura, Surf. Interface Anal. 45, 517 (2013).
- ¹³ A. Zorzos and P. Lozano, J. Vac. Sci. Technol. B 26, 2097 (2008).
- 14 P. Sigmund, Theory of Sputtering. I. Sputtering Yield of Amorphous and Polycrystalline Targets. Physical Review, 184, 383-416 (1969).
- 15 P. Sigmund, Energy density and time constant of heavy-ion-induced elastic-collision spikes in solids. Applied Physics Letters, 25, 169-171 (1974).

- 16 J. Samela and K. Nordlund, Origin of nonlinear sputtering during nanocluster bombardment of metals. *Physical Review B*, 76, 125434 (2007).
- 17 P. Sigmund and C. Claussen, Sputtering from elastic-collision spikes in heavy-ion-bombarded metals. *Journal of Applied Physics*, 52, 990-993 (1981).
- 18 R. Kelly, Thermal effects in sputtering. *Surface Science*, 90, 280-318 (1979).
- 19 M. Medvedeva, I. Wojciechowski, and B.J. Garrison, Effect of mass and incidence angle of keV energy polyatomic projectiles in silicon sputtering. *Surface Science*, 505, 349-357 (2002).
- 20 V. Popok, I. Barke, E. Campbell, and K.H. Meiwes-Broer, Cluster-surface interaction: From soft landing to implantation. *Surface Science Reports*, 66, 347-377(2011).
- 21 I. Yamada and N. Toyoda, Nano-scale surface modification using gas cluster ion beams – A development history and review of the Japanese nano-technology program. *Surface & Coatings Technology*, 201, 8579-8587 (2007).
- 22 N. Winograd, The magic of cluster SIMS. *Analytical Chemistry*, 77, 142A-149A (2005).
- 23 N. Winograd, Z. Postawa, J. Cheng, C. Szakal, J. Kozole, and B. Garrison, Improvements in SIMS continue. Is the end in sight? *Applied Surface Science*, 252, 6836-6843 (2006).
- 24 J.F. Mahoney, Microcluster-surface interactions: a new method for surface cleaning. *International Journal of Mass Spectrometry* 174, 253-265 (1998).
- 25 J.F. Mahoney, J. Perel, S.A. Ruatta, P.A. Martino, S. Husain, T.D. Lee, Massive cluster impact mass-spectrometry - a new desorption method for the analysis of large biomolecules. *Rapid Communications in Mass Spectrometry* 5, 441-445 (1991).
- 26 M. Gamero-Castaño and M. Mahadevan, Sputtering of silicon by a beamlet of electrosprayed nanodroplets. *Applied Surface Science*, 255, 8556-8561 (2009).

- 27 J. Fernández de la Mora and I.G. Loscertales, The current transmitted through an electrified conical meniscus. *Journal of Fluid Mechanics*, 260, 155–84 (1994).
- 28 M. Gamero-Castano and J. Fernández de la Mora, Direct measurement of ion evaporation kinetics from electrified liquid surfaces. *Journal of Chemical Physics*, 113, 815-832 (2000).
- 30 T. Aoki, T. Seki, S. Ninomiya and J. Matsuo, MD simulation study of the sputtering process by high-energy gas cluster impact. *Applied Surface Science* 255, 944-947 (2008).
- 31 S. Ihara, S. Itoh, and J. Kitakami, Mechanisms of cluster implantation in silicon: A molecular-dynamics study. *Physical Review B* 58, 10736 (1998).
- 32 J. Samela and K. Nordlund, Classical molecular dynamics simulations of hypervelocity nanoparticle impacts on amorphous silica. *Physical Review B* 81, 054108 (2010).
- 33 J. Samela, K. Nordlund, J. Keinonen, and V. N. Popok, Comparison of silicon potentials for cluster bombardment simulations. *Nuclear Instruments and Methods in Physics Research Section B: Beam Interactions with Materials and Atoms* 255, 253-258 (2007).
- 34 S. Plimpton, Fast parallel algorithms for short-range molecular-dynamics. *Journal of Computational Physics* 117, 1-9 (1995).
- 35 F. Saiz and M. Gamero Castaño, Amorphization of silicon induced by nanodroplet impact: A molecular dynamics study. *Journal of Applied Physics*, 112, 054302 (2012).
- 36 R. Borrajo-Pelaez, E. Grustan-Gutierrez, and M. Gamero-Castaño, Sputtering of Si, SiC, InAs, InP, Ge, GaAs, GaSb, and GaN by electrosprayed nanodroplets. *Journal of Applied Physics*, 114, 184304 (2013).
- 37 F. H. Stillinger and T. A. Weber, Computer-simulation of local order in condensed phases of silicon. *Physical Review B* 31, 5262-5271 (1985).

- 38 J. F. Ziegler, J. P. Biersack, and U. Littmark, *The Stopping and Range of Ions in Solids*, Volume 1. Pergamon Press, New York, 1985.
- 39 V. G. Sevast'yanov, P. Ya. Nosatenkob, V. V. Gorskiib, Yu. S. Ezhovc, D. V. Sevast'yanova, E. P. Simonenkoa, and N. T. Kuznetsova, Experimental and Theoretical Determination of the Saturation Vapor Pressure of Silicon in a Wide Range of Temperatures. *Russian Journal of Inorganic Chemistry*, 55, 2073–2088 (2010).
- 40 D. V. Makhov and L. J. Lewis, Isotherms for the liquid-gas phase transition in silicon from NPT Monte Carlo simulations. *Physical Review B* 67, 153202 (2003).
- 41 E. G. Ponyatovsky and O. I. Barkalov, Pressure-induced amorphous phases. *Materials Science Reports* 8, 147-191 (1992).
- 42 B. M. French, *Traces of Catastrophe A Handbook of Shock-Metamorphic Effects in Terrestrial Meteorite Impact Structures*, Lunar and Planetary Institute - Houston, 1998.
- 43 F. Saiz, R. Borrajo-Pelaez, M. Gamero Castaño, The influence of the projectile's velocity and diameter on the amorphization of silicon by electrosprayed nanodroplets, *Journal of Applied Physics*, 114, 034304 (2013).
- 44 Timothy Fedkiw and Paulo Lozano. Efficiency Measurements of an Ionic Liquid Ion Source Thruster. In *Space Propulsion*, San Sebastian, Spain, 2010.
- 45 Paulo C Lozano. Energy Properties of an EMI-Im Ionic Liquid Ion Source. *Journal of Physics D: Applied Physics*, 39:126–134, January 2006.
- 46 I. Romero-Sanz, R. Bocanegra, J. Fernandez de la Mora, and M. Gamero-Castano. Source of Heavy Molecular Ions Based on Taylor Cones of Ionic Liquids Operating in the Pure Ion Evaporation Regime. *Journal of Applied Physics*, 94(5):3599–3605, 2003.
- 47 C. Larriba, S. Castro, J. Fernandez de la Mora, and Paulo C. Lozano. Monoenergetic Source of Kilodalton ions from Taylor Cones of Ionic Liquids. *Journal of Applied Physics*, 101:084303, 2007

- 48 Robert S. Legge and Paulo C. Lozano. Electrospray Propulsion Based on Emitters Microfabricated in Porous Metals. *Journal of Propulsion and Power*, 27(2):485–495, March 2011
- 49 Paulo C. Lozano and Manuel Martinez-Sanchez. Efficiency Estimation of EMI-BF₄ Ionic Liquid Electrospray Thrusters. In *The 41st AIAA/ASME/SAE/ASEE Joint Propulsion Conference & Exhibit*, Tucson, Arizona, 2005.
- 50 William L. Jorgensen, Jayaraman Chandrasekhar, Jeffry D. Madura, Roger W. Impey, and Michael L. Klein. Comparison of Simple Potential Functions for Simulating Liquid Water. *The Journal of Chemical Physics*, 79(2):926–935, 1983.
- 51 Edward K. Watkins and William L. Jorgensen. Perfluoroalkanes: Conformational Analysis and Liquid-State Properties from ab Initio and Monte Carlo Calculations. *The Journal of Physical Chemistry A*, 105(16):4118–4125, 2001.

Appendix. Copies of Publications

- F. Saiz and M. Gamero-Castaño, “Atomistic modeling of the sputtering of silicon by electrosprayed nanodroplets”, *Journal of Applied Physics*, 116, 054303 (2014).
- R. Borrajo-Pelaez, E. Grustan-Gutierrez, and M. Gamero-Castaño, “Sputtering of Si, SiC, InAs, InP, Ge, GaAs, GaSb, and GaN by electrosprayed nanodroplets”, *Journal of Applied Physics*, 114, 184304 (2013).
- F. Saiz, R. Borrajo-Pelaez, and M. Gamero-Castaño, “The Influence of the Projectile’s Velocity and Diameter on the Amorphization of Silicon by Electrosprayed Nanodroplets, *Journal of Applied Physics* 114, 034304 (2013)
- F. Saiz, M. Gamero Castaño, “Amorphization of silicon induced by nanodroplet impact: A molecular dynamics study”, *Journal of Applied Physics*, 112(5), 054302/1-6 (2012).
- R. Borrajo-Pelaez and M. Gamero-Castaño, “The Effect of the Molecular Mass on the Sputtering by Electrosprayed Nanodroplets”, Submitted to *Applied Surface Science*.
- M. Gamero-Castaño, A. Torrents, R. Borrajo-Pelaez, J.G. Zheng, “Amorphization of Hard Crystalline Materials by Electrosprayed Nanodroplet Impact”, Submitted to *Applied Surface Science*.
- C. Perez-Martinez and P. Lozano, “Visualization of beams from ionic liquid ion sources for focused ion beam applications”, *J. Vac. Sci. Technol. B* 30(6) (2012)
- T. Coles and P. Lozano, “Investigating efficiency losses from solvated ion fragmentation in electrospray thruster beams”, *Joint Propulsion Conference*, AIAA-2013-4033, July 14-17, 2013, San Jose, CA.

Atomistic modeling of the sputtering of silicon by electrospayed nanodroplets

Fernan Saiz and Manuel Gamero-Castaño^{a)}

Department of Mechanical and Aerospace Engineering, University of California, Irvine, California 92697, USA

(Received 20 May 2014; accepted 26 July 2014; published online 5 August 2014)

The hypervelocity impact of electrospayed nanodroplets on single-crystal silicon ejects a large number of atoms. Although sputtering by atomic, molecular, and gas cluster ions has been thoroughly studied, the significantly larger size of nanodroplets prevents a straightforward extrapolation of the physics governing the impact of these smaller projectiles. This motivates the present molecular dynamics simulations of nanodroplet impact on silicon, aimed at resolving the mechanisms and the effect of the projectile's size and velocity on sputtering. We find that both collision cascades and thermal sputtering contribute to the overall atom ejection, the former being active during the initial stages of the impact characterized by strong interactions between the molecules of the projectile and the atoms of the target, and the absence of partial thermodynamic equilibrium. In addition, for sufficiently large projectile diameters and impact velocities, conglomerates of atoms are ejected by hydrodynamic forces. The sputtering yield, defined as the average number of target atoms ejected per projectile's molecule, increases monotonically with the kinetic energy of the molecules and, at constant molecular kinetic energy, slightly decreases with projectile diameter as a result of enhanced backscattering of the ejected atoms by the projectile's molecules. For the ionic liquid considered in this study, sputtering is first observed at molecular energies near 12.7 eV and, at the highest energy simulated of 73 eV, the sputtering yield averages to 0.37. © 2014 AIP Publishing LLC. [<http://dx.doi.org/10.1063/1.4892442>]

I. INTRODUCTION

Physical sputtering is a fundamental phenomenon with a wide range of applications in surface engineering and surface elemental analysis. Although sputtering by light particles is well understood on the basis of Sigmund's collision cascade linear model,¹ this theory underestimates the sputtering by larger projectiles like heavy atoms, molecular ions, and gas cluster ions.^{2,3} Instead, other mechanisms such as thermal spikes caused by high density collision cascades and thermal evaporation are known to control the sputtering by these larger projectiles.^{4,5} The former is a prototypical non-equilibrium process, while the latter is formulated within the confines of partial thermodynamic equilibrium.

The dependence of the sputtering yield on the nuclearity of molecular and gas cluster ions is superlinear (e.g., the sputtering yield of a cluster ion made of n argon atoms is higher than n times the sputtering yield of an argon atom having the same impact velocity as the cluster) and,⁶ as a result of the sputtering yield enhancement, the use of these large projectiles has proliferated and become an active area of research in ion beams.⁷ Besides enhanced sputtering, the impact phenomenology exhibits unique characteristics, such as shallow implantation, surface smoothing, the ability to desorb intact macromolecules, etc., making large projectiles especially interesting for surface engineering and secondary ion mass spectrometry.^{8,9} These advantageous properties are associated with the short penetration range of a massive

projectile, which transfers its kinetic energy and momentum within a thin surface layer. Dissipation is then concentrated in a small volume of the target, resulting on high energy densities and the maximization of the number of atoms that can overcome the surface binding potential.

The beneficial features of molecular and gas cluster ions are correlated with their size.¹⁰ Until recently, gas cluster ions were the largest projectiles available for ion beams, their low charging level limiting effective diameters to a few nanometers. This obstacle has disappeared with the introduction of electrospayed nanodroplets, which are readily generated with sizes ranging from a few nanometers to tens of microns. Energetic electrospays of glycerol droplets were used in the past to clean surfaces and for secondary ion mass spectrometry,^{11,12} but only recently electrospayed nanodroplets were proven to be efficient sputtering projectiles.¹³ The origin of this development can be traced to advancements in the theory of electrohydrodynamic atomization,¹⁴ which provided a path for the electrospaying of monodisperse and controllable beams of highly charged nanodroplets.¹⁵ Despite the experimental demonstration of nanodroplet sputtering, the associated physics are not yet understood, motivating the present molecular dynamics simulations. More specifically, this article models the impact of a nanodroplet of the ionic liquid 1-ethyl-3-methylimidazolium bis(trifluoromethylsulfonyl) imide,¹⁶ Emi-Im, on a [100] single-crystal silicon target, and resolves the sputtering mechanisms and the effects of the diameter and the velocity of the projectile on the sputtering yield.

The molecular dynamics technique is frequently used to study sputtering by molecular and gas cluster ions

^{a)}Author to whom correspondence should be addressed. Electronic mail: mgamero@uci.edu

because of the accuracy of interacting potentials, and the detailed information on the positions and interactions of all projectile and target atoms. Molecular dynamics has been used to determine the sputtering mechanisms of small nanopropiles;¹⁷ surface amorphization and smoothing;¹⁸ the transition from atomistic to macroscopic behavior exhibited in the collisions of nanopropiles;¹⁹ the effect of the interaction potential of the target's atoms on the sputtering yield,²⁰ etc.

This article is organized as follows: after this introduction, Sec. II explains the simulation technique. Section III presents the main results including a description of the dynamics of the impact, the sputtering mechanisms, and the determination of the sputtering yield as a function of projectile diameter and velocity. Previous simulations for gas cluster ions have shown that the ejection of target atoms is caused by both collisional and thermal sputtering, and our simulations confirm that the same mechanisms drive the sputtering by nanodroplets. Finally, Sec. IV summarizes the main findings.

II. SIMULATION METHODS

We use the open-source program LAMMPS to simulate the impact of a nanodroplet on a [100] silicon wafer.^{21,22} The droplet is built as a hexagonal-closed-packaging arrangement of spheres with masses of 391.31 amu. Each sphere represents a molecule of the ionic liquid Emi-Im, a material that we have used extensively in experiments.²³ The radius of the spheres is set to 0.42 nm to match the density of the liquid, 1520 kg/m³. The parametrical range of the simulations includes projectile diameters of 5, 10, 20, and 30 nm, and impact velocities between 1 and 6 km/s. In this velocity range, the kinetic energy of the projectile varies between 2.0 and 73 eV per molecule. The molecular formulae for the Emi cation and the Im anion are C₆H₁₁N₂ and C₂F₆NO₄S₂, and the kinetic energy per atom, thus, ranges between 0.059 and 2.1 eV. At these relatively low energies, the anion and cation of the Emi-Im molecules may separate upon impact, but otherwise they should remain intact as further dissociation into atomic components is highly unlikely. For example, atomic dissociation in the covalently bonded fullerene projectile, C₆₀, only starts at impact energies exceeding 8.3 eV per atom.²⁴

The dimensions of the silicon slab are adjusted with the droplet's diameter to minimize boundary effects. The target for the 5 nm droplet is a 32.59 nm × 32.59 nm × 24.44 nm parallelepiped (1, 303, 200 Si atoms, the shorter dimension is in the direction of the impact), while the target for the 30 nm droplet is a larger 130.34 nm × 130.34 nm × 97.76 nm slab (83, 059, 200 Si atoms). A Berendsen thermostat at 293 K is applied to the sides and the bottom of the slab to prevent the reflection of the shock wave triggered by the impact, and to enable the cooling of this region.^{25,26} In all simulations, the thermostat has a thickness of 2.17 nm at the sides and 8.69 nm at the bottom, and a time constant of 2 fs. After several tests with the smaller slabs, these values were found to effectively eliminate the reflection of the shock wave at the boundaries, and to dissipate away the energy of

the impact. The 2 fs time constant is significantly smaller than the characteristic times of the dynamics of the impact which, combined with the large sizes of the slabs, produce a quasi-isothermal boundary condition. For reference, the Berendsen thermostat used in Ref. 26 to simulate the impact of Xe ions on Au has a thickness of the order of 0.6 nm and a time constant between 20 and 2000 fs, and is applied to slabs with linear dimensions between 7 and 38 nm.

The forces between silicon atoms are modeled with the Stillinger-Weber (SW) potential,²⁷ while the universal Ziegler-Biersack-Littmark potential is used for the interaction between the projectile's molecules, and between the projectile's molecules and Si atoms.²⁸ This simple, two-body repulsive potential does not reproduce chemical interactions during the impact, nor does it take into account the internal degrees of freedom of the molecule, which is in any case modeled as one large pseudo atom. The ZBL potential has the following form:

$$U(r) = \frac{Z_1 Z_2 e^2}{4\pi\epsilon_0 r} \phi(r), \quad (1)$$

where Z_1 and Z_2 are the atomic numbers of the interacting particles ($Z = 198$ for Emi-Im, computed as the aggregate atomic numbers of its atoms), r is the interatomic distance, and $\phi(r)$ is the screening potential function approximated by

$$\phi(r) = \sum_{i=1}^4 a_i e^{-b_i r/a_U} \quad (2)$$

with coefficients $a_1 = 0.1818$, $a_2 = 0.5099$, $a_3 = 0.2802$, $a_4 = 0.02817$, $b_1 = 3.2$, $b_2 = 0.9423$, $b_3 = 0.4028$, and $b_4 = 0.2016$. a_U is defined as

$$a_U = \frac{0.8854 a_B}{Z_1^{0.23} + Z_2^{0.23}}, \quad (3)$$

where a_B is the Bohr radius (0.539177 Å). The cutoff distance for the interactions between molecule-molecule and silicon-molecule is set to 0.803 nm, i.e., at 95% of the diameter of the Emi-Im molecule. The equations of motion of the constitutive particles are integrated with a timestep of 1 fs, for long enough times to capture all atom ejections (all run times exceed 30 ps).

We will frequently refer to the temperature field in the target when analyzing the simulations. Regardless of whether partial thermodynamic equilibrium is reached, a pseudo local temperature can always be defined at a point as the average of the kinetic energies of N atoms enclosed in a spherical control volume centered at that point

$$T = \frac{m \sum_{i=1}^N (\mathbf{v}^i - \langle \mathbf{v}^i \rangle)^2}{3k_B N}, \quad (4)$$

where k_B is the Boltzmann's constant, m is the mass of a silicon atom, and \mathbf{v}^i is the velocity vector of the i -atom. We will also refer to the thermal energy of an atom, defined as $3k_B T/2$, where the temperature is evaluated at the position of the atom.

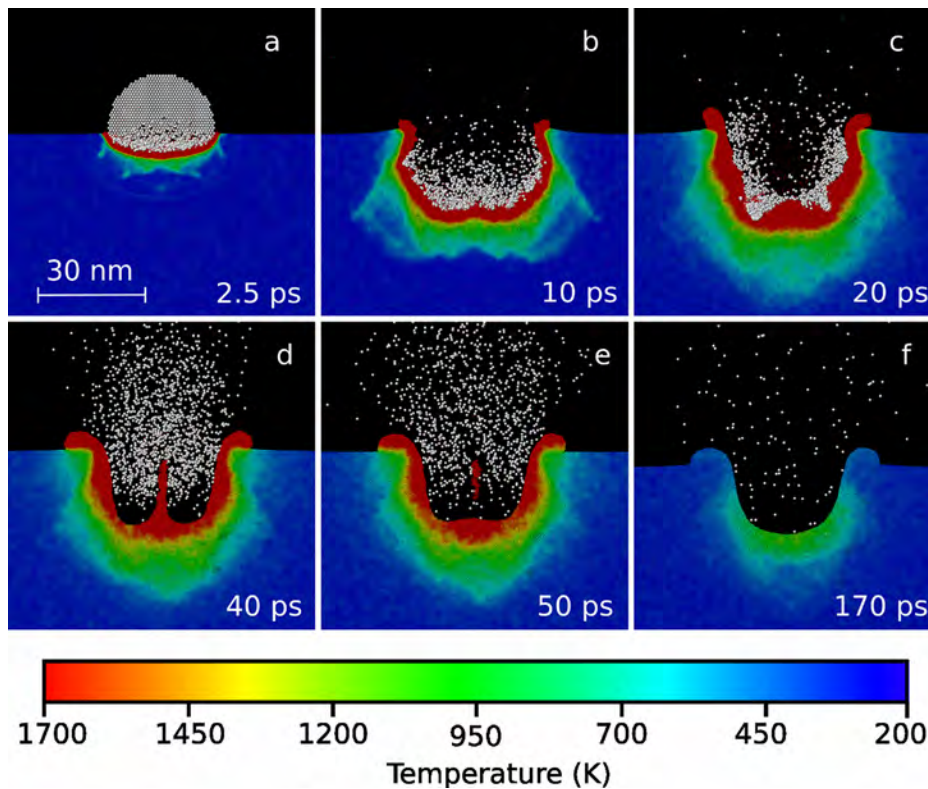


FIG. 1. Impact of 30 nm droplet at 6 km/s. The cross sections include the axis of impact, and show the temperature field in the target. A total of 10 805 Si single atoms are sputtered.

III. SPUTTERING PHENOMENA

Thermal spikes caused by high density collision cascades and thermal evaporation are the dominant sputtering mechanisms for molecular and gas cluster ions, and we expect them to control sputtering by nanodroplets as well. The energy distributions of the atoms sputtered by these two mechanisms are

$$F_C(E) = \frac{2UE}{(E+U)^3}, \text{ and} \quad (5)$$

$$F_{Th}(E) = \frac{E}{(k_B T)^2} \exp\left(-\frac{E}{k_B T}\right), \quad (6)$$

where E is the kinetic energy of the ejected atom, U is the surface binding energy, and T refers to the temperature of the surface from which atoms are evaporated. When comparing the simulation data to these two expressions, we will approximate the surface binding energy by the standard enthalpy of formation of Si(g), $h_f^0 = 4.67$ eV,²⁹ and use the critical temperature of silicon as an upper limit for the temperature of the evaporating surface, $T_{cr} = 7925$ K (or 0.68 eV).³⁰

Figures 1 to 5 illustrate a typical impact, in this case, a 30 nm droplet with a velocity of 6 km/s. Figure 1 shows the evolution of a thin cross section of the target and projectile including the axis of impact. The molecules of the projectile are shown in white, while the color graduation of the target renders the temperature field. At 6 km/s, the projectile has enough energy to penetrate the target a distance comparable to its diameter, leaving behind a crater. As the projectile penetrates a fraction of its kinetic energy is dissipated into a thin layer of silicon generating temperatures well above the melting point (which at 1 atm has a value of 1685 K), and a

substantial region melts and remains liquid for several picoseconds. This phase transition is facilitated by the reduction of the silicon's melting point with pressure.³¹ While the center of the crater reaches its maximum depth of 22.7 nm at 14 ps and begins to unload thereafter, a fraction of the projectile's molecules continues penetrating forming two lobes around the axis of the impact. The higher pressure in the lobes pushes a jet of fluid upward, which, at 48 ps, breaks apart from the target as two large conglomerates of 411 and 1337 Si atoms. These axial uplifts are also observed during the impact of macroprojectiles,³² and appear in our simulations at projectile diameters and velocities of, and exceeding, 20 nm and 5.5 km/s. The

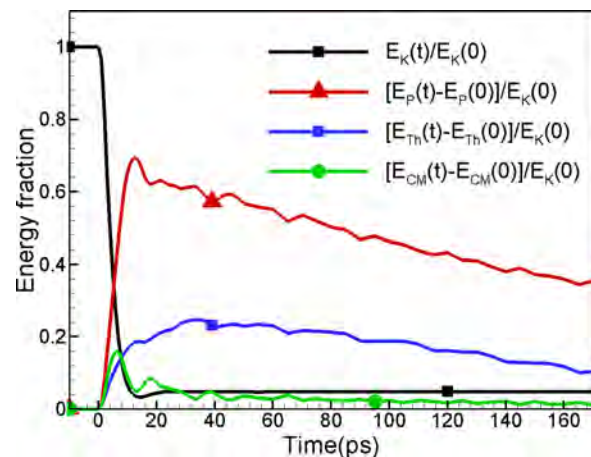


FIG. 2. Impact of 30 nm droplet at 6 km/s: evolution of the projectile's kinetic energy, $E_K(t)$, and the target's potential $E_P(t)$, thermal $E_{Th}(t)$, and kinetic energy of the average velocity field $E_{CM}(t)$. All energies are normalized with the initial kinetic energy of the projectile and, in the case of the target's, offset with their initial values.

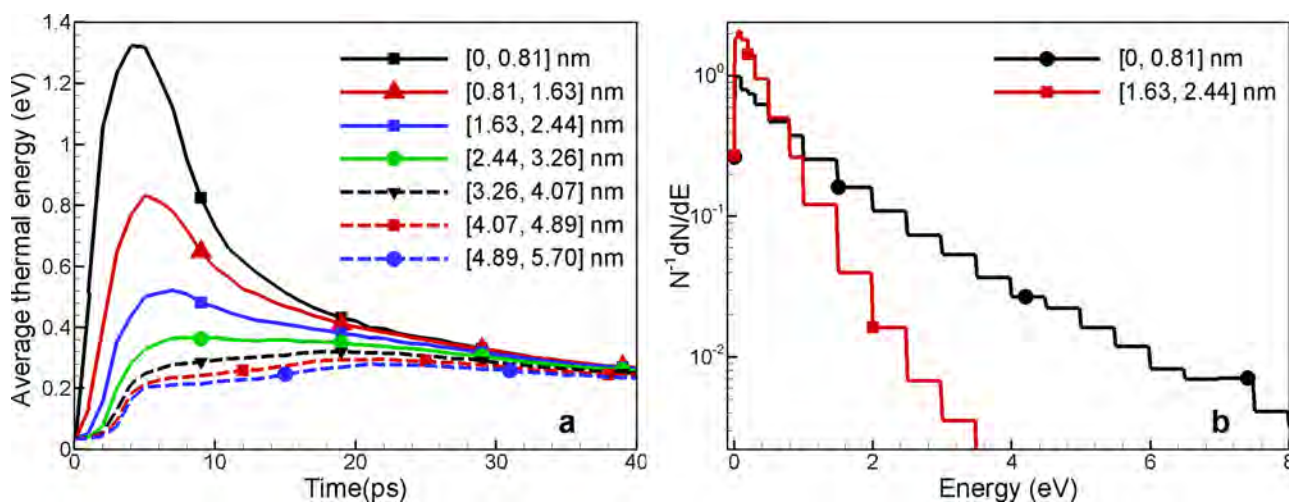


FIG. 3. Impact of 30 nm droplet at 6 km/s: (a) evolution of the atomic average thermal energy as a function of distance from the surface of the crater; (b) distributions of thermal energy for the atoms positioned within [0, 0.81] nm and [1.63, 2.44] nm from the surface of the crater; 4.50% and 0.067% of the atoms exceed the surface binding energy of 4.67 eV, respectively.

surface of the crater stabilizes at about 100 ps, while the temperature field continues its equilibration with the thermal bath. In addition to the conglomerates of 411 and 1337 atoms, 10 805 Si single atoms escape from the target, most of them during the first few picoseconds.

Figure 2 illustrates how the kinetic energy of the projectile, $E_K(t)$, is transferred to the target and converted into thermal and potential energies, $E_{Th}(t)$ and $E_P(t)$, and kinetic energy of the average velocity field, $E_{CM}(t)$. The energies in Fig. 2 are offset with their initial values and normalized with the initial kinetic energy of the projectile. The impact is characterized by a brief period of intense collisionality, the projectile losing 93.4% of its kinetic energy within 10 ps. By this time 16.6%, 65.1%, and 8.9% of the projectile's energy have been transferred to the target in the form of thermal, potential, and average kinetic energies, respectively. The molecules of the projectile retain only 4.8% of their initial kinetic energy as they recoil out of the target. The thermal energy continues increasing after the projectile stops transferring energy to the target, due to the dissipation of the average velocity field and across the shock wave moving away

from the impact. By the end of the simulation, 49.6% of the kinetic energy of the projectile is transferred away from the slab by the thermostat, while 35.4% remains in it as potential energy mostly associated with the formation of the amorphous phase surrounding the impact, and 10.2% as an increase of thermal energy with respect to the initial state.²²

The density of thermal energy near the surface is more relevant to sputtering than the total value deposited in the target because, due to the lack of penetration of the projectile's molecules, it is the energetic state of the outermost silicon atoms what drives sputtering. Figure 3(a) shows the average thermal energy of the atoms located within a thin layer surrounding the crater, as a function of both time and distance from the surface of the crater. The average energy of the outermost atoms peaks 4 ps after the impact, at a value of 1.33 eV. For reference, if the atoms were in equilibrium, the associated temperature would be 10 280 K, i.e., well above the critical temperature. The average thermal energy decreases rapidly with distance from the surface, and at depths

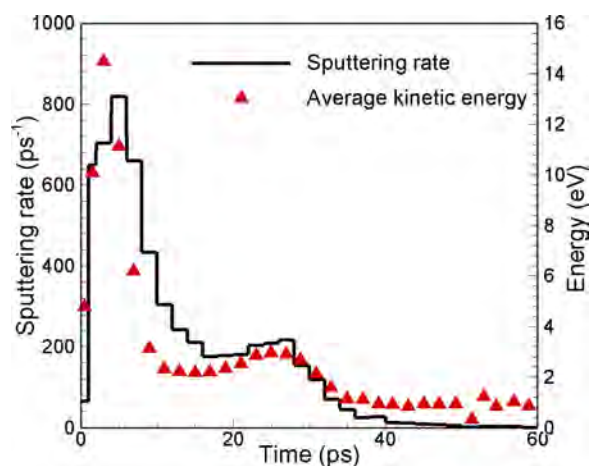


FIG. 4. Impact of 30 nm droplet at 6 km/s: sputtering rate and average kinetic energy of the sputtered atoms over time.

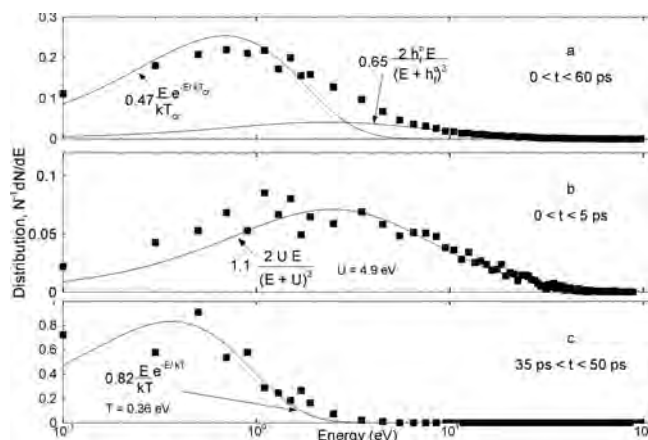


FIG. 5. Impact of 30 nm droplet at 6 km/s: kinetic energy distributions of atoms sputtered in three different periods: (a) within 0 and 60 ps; (b) within 0 and 5 ps; and (c) within 35 and 50 ps. Collision cascades dominate the sputtering during the initial phase of the impact, while atoms are evaporated at latter times.

exceeding 3 nm, the position of the energy maximum shifts towards the 20–30 ps window due to diffusion from the outermost atoms towards the bulk. Note that the large gradients of thermal energy are significantly reduced within this time window, suggesting that the surface approaches partial thermal equilibrium at about 25 ps. Figure 3(b) shows the distribution of thermal energy for the atoms in the [0, 0.81] nm and [1.63, 2.44] nm layers, at 4 ps. 4.50% of the atoms in the outermost layer have energies exceeding the surface binding energy of 4.67 eV, while the same fraction in the [1.63, 2.44] nm layer is only 0.067%. Clearly, the fraction of atoms that are likely to be ejected is significant in the first atomic layer, and decreases rapidly with distance from the crater's surface.

Figure 4 shows the rate at which single Si atoms are sputtered and the average kinetic energy of the ejecta as a function of time, for the 30 nm and 6 km/s projectile. The sputtering rate has a bimodal distribution with a dominant peak associated with the collisional phase of the impact, and a lower second peak centered at 27 ps and coinciding with the onset of partial thermal equilibrium observed in Fig. 3(a). The total number of sputtered atoms is 10 805, with 55.1% of them being ejected within the initial 10 ps. The average kinetic energy of these atoms is high: for example, 13.0% of the sputtered atoms are released between 2 and 4 ps with an average kinetic energy of 14.5 eV. If the ejected atoms followed the thermal evaporation distribution (6), the associated temperature would be 84 000 K. This value, which would correspond to the temperature of the surface from which the atoms are evaporated, greatly exceeds the critical temperature of silicon and therefore a sputtering mechanism other than thermal evaporation must be controlling the ejection of these energetic atoms. Furthermore, the profiles in Fig. 3(a) suggest that the surface is far from partial thermodynamic equilibrium during these early stages. On the other hand, 2.53% of the atoms are ejected after 35 ps from the impact, at a time when the collisions between projectile molecules and target atoms have long subsided (see Fig. 2). The average kinetic energy of these atoms is 0.91 eV, and the corresponding temperature for a thermal evaporation distribution is 5275 K, a value more in sync with the target's temperature field and which makes thermal evaporation the likely sputtering mechanism at these latter times.

The energy distributions in Fig. 5 provide a better deconvolution of the sputtering mechanisms. The distributions are for atoms ejected within three different periods: (a) the overall interval of 60 ps including all sputtered atoms; (b) the initial interval between 0 and 5 ps characterized by intense collisionality; and (c) a period between 35 and 50 ps in which the geometry of the crater has become stationary, there is local thermodynamic equilibrium, and the temperature field relaxes towards the temperature of the bath. The overall distribution (a) decays slowly at high energies, similarly to the E^{-2} decay of collisional sputtering, ruling out thermal evaporation as the only acting mechanism. Conversely, the significant fraction of atoms at low energies is indicative of thermal evaporation, and prevents a good overall fitting to the collision cascade model. Since it is apparent that both mechanisms are contributing to the overall sputtering, we fit the data to a collision cascade model with a

value of h_f^0 for the surface binding energy, and to a thermal evaporation function with the maximum possible temperature $T = T_{cr}$, to estimate the relative importance of each mechanism. The fittings, shown in Fig. 5(a), suggest that about 65% of the sputtered atoms are ejected by collision cascades, and that a maximum of 47% of the atoms can be evaporated. The distribution in Fig. 5(b) follows more closely the collisional sputtering scenario, the interaction between projectile and target being most intense during this initial period of the impact. In this case, we fit the distribution to a collisional model with two free parameters, the surface binding energy and a proportionality constant, obtaining values of 4.9 eV and 1.1, respectively. The fitting yields a good physical value for U and slightly over predicts the area of the distribution, suggesting that collision cascades are indeed the sputtering mechanism acting in the early stages of the impact. Finally, to probe thermal sputtering, we use the energy distribution of atoms emitted between 35 and 50 ps, a period characterized by the absence of direct interaction between the projectile and the target. In this case, a fitting to the evaporation model yields a temperature of 0.36 eV (4200 K) and a distribution that accounts for 82% of the atoms. The temperature of the fitting is significantly lower than the critical temperature of Si, but higher than the temperature of the crater's surface. However, it is worth pointing out that the temperature is not constant nor homogeneous, but varies over time and location in the crater's surface, and therefore the fitting of the actual distribution to the thermal evaporation model with a unique temperature is inappropriate. In any case, the sharp drop of the distribution at increasing energy, its Gaussian shape and the concentration of particles at relatively low energies are indicative of thermal sputtering during this late stage of the process.

The artificial quasi-isothermal boundary condition imposed by the Berendsen thermostat does not introduce spurious effects on the sputtering due to the large sizes of the slabs, and the characteristic times of the sputtering mechanisms. First, for droplets with high enough velocity, sputtering by collision cascades occurs during the period of intimate interaction between the projectile and the substrate, which is of the order of the ratio between the projectile's diameter and its velocity. For example, for the 30 nm and 6 km/s droplet, this characteristic time is 5 ps, which compares well with the 10 ps width of the collision cascades peak in Fig. 4. The impact region is too far from the boundaries to receive information from them within this short 5–10 ps period: even if shock waves were reflected from the boundaries, which they are not because they are eliminated by the thermostat, it would take approximately 20 ps for the shock wave generated by the impact to first reach the boundary, and for its reflected wave to arrive back to the impact region (the speed of sound in Si is 8430 m/s).²² Second, thermal sputtering occurs during a period much shorter than the thermal relaxation time constant of the slab. For example, most of the thermal sputtering for the 30 nm and 6 km/s droplet occurs within 35 ps from the impact (see Fig. 4). The thermal relaxation time constant can be estimated from the decay of the thermal energy curve in Fig. 2, which is 174 ps (obtained by fitting the data to an exponential decay); alternatively, the

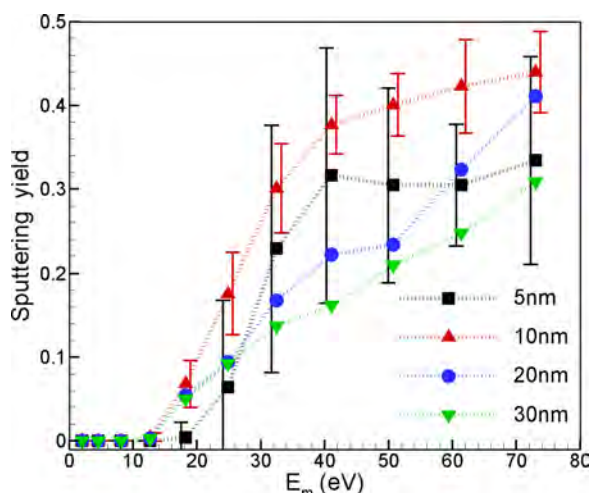


FIG. 6. Sputtering yield as a function of molecular kinetic energy and drop-let diameter. The error bars for the smaller projectiles are indicative of the randomness of the sputtering yield associated with the arbitrariness of the initial atomic configurations.

time constant can be estimated as the characteristic time in the diffusion equation, given by $\rho c_p L^2 / k_{Th} \cong 186$ ps (we use $L = 130$ nm, and the physical properties of silicon $\rho = 2329$ kg m $^{-3}$, $c_p = 706$ J kg $^{-1}$ K $^{-1}$, $k_{Th} = 149$ W m $^{-1}$ K $^{-1}$). In either case, the thermal relaxation time constant of the slab is significantly larger than the period during which thermal evaporation occurs.

Figure 6 shows the sputtering yield (average number of Si atoms ejected per projectile's molecule) as a function of the projectile's size and molecular kinetic energy. One half of the error bars for the 5 nm and 10 nm projectiles represents the standard deviations of the sputtering yield for 10 simulations, each one calculated with a different set of initial conditions for the target atoms and the point of impact. The ratio between the standard deviations and the sputtering yields average to 0.62 and 0.14 for the 5 nm and the 10 nm projectiles, respectively. The fast reduction of the variation of the sputtering yield at increasing projectile diameter makes it unnecessary to simulate the much more computationally expensive impacts of the 20 and 30 nm projectiles with multiple initial conditions. The emission of Si atoms starts between 2.5 and 3.0 km/s (12.7 and 18.3 eV), a range that coincides with the beginning of the melting of the target's surface.³³ Above this threshold, the sputtering yield increases monotonically with the kinetic energy of the projectile, almost linearly for the 20 and 30 nm projectiles, reaching an average value of 0.37 at 73 eV. The sputtering yield at constant impact velocity is maximum for the 10 nm projectile, and decreases with diameter for the 20 and 30 nm projectiles. The main reason for this is the backscattering of ejected Si atoms by collisions with molecules of the nanodroplet and other sputtered Si atoms, and the redeposition of some of the backscattered atoms. For example, for the 30 nm projectile impacting at 6 km/s we count a total of 32 470 Si atoms having at some time a coordination number of zero, i.e., which at some point are detached from the target. But only 10 805 of them escape away from the target and are counted as sputtered atoms; the rest, i.e., more than twice the final number of sputtered atoms, come back to the surface of the crater because either their escape trajectories intersects it,

or because they are backscattered. This reduction of the sputtering yield increases with projectile diameter as the length of the region with a high density of Emi-Im molecules and which the ejected Si atom must cross, and therefore the likelihood for backscattering, is proportional to the diameter of the projectile. The experimental sputtering yields at the highest studied energies are about a factor of 2 larger than in our simulations.²³ The difference between the experimental and numerical results may be due to several reasons: first, the experimental data are generated by a beam of nanodroplets with a distribution of diameters and velocities, which introduces uncertainty in the comparison; and second, the simulations consider the impact of a single projectile on a perfect Si surface, while the experimental data are the result of multiple impacts on the same target area. It is likely that the state of the surface left after each impact in the experiments (a thin layer surrounding the crater melts and quenches to form and amorphous phase, probably generating a zone with high stresses) is weaker and conducive to the formation and propagation of cracks, or to other phenomena that favors sputtering and which are not accounted for in our isolated impact simulations.

IV. CONCLUSIONS

Molecular dynamics simulations show that the impact of a nanodroplet on silicon can eject a large number of atoms. For the Emi-Im liquid considered in this study, the threshold impact velocity for sputtering is 2.5 km/s, or equivalently a molecular kinetic energy of 12.7 eV. Both collision cascades and thermal evaporation contribute to the overall sputtering: collisional sputtering dominates during the initial phase of the impact, while thermal sputtering takes over during the relaxation phase. Although collisional sputtering is the larger contributor, both mechanisms release comparable numbers of atoms. In addition, for projectile diameters and velocities equal to or exceeding 20 nm and 5.5 km/s, an axial jet surges and detaches from the liquefied surface of the target, ejecting conglomerates of atoms. The sputtering yield increases monotonically with molecular kinetic energy and, at constant impact velocity, is maximum for the 10 nm projectile. The main factor for the decrease of the sputtering yield with projectile diameter is the enhanced backscattering of ejected Si atoms by the molecules of the projectile, which becomes more likely at increasing projectile diameter. The average sputtering yield at the highest simulated velocity of 6 km/s is 0.37, which compares well with the value of 0.83 associated with a high fluence, electro-spray beam experiment.

ACKNOWLEDGMENTS

This work was funded by the Air Force Office of Scientific Research, Grant No. FA9550-11-1-0308. The authors are grateful for the support of the AFOSR Program Manager Dr. Birkan.

¹P. Sigmund, "Theory of sputtering. I. Sputtering yield of amorphous and polycrystalline targets," *Phys. Rev.* **184**, 383–416 (1969).

²P. Sigmund, "Energy density and time constant of heavy-ion-induced elastic-collision spikes in solids," *Appl. Phys. Lett.* **25**, 169–171 (1974).

- ³J. Samela and K. Nordlund, "Origin of nonlinear sputtering during nano-cluster bombardment of metals," *Phys. Rev. B* **76**, 125434 (2007).
- ⁴P. Sigmund and C. Claussen, "Sputtering from elastic-collision spikes in heavy-ion-bombarded metals," *J. Appl. Phys.* **52**, 990–993 (1981).
- ⁵R. Kelly, "Thermal effects in sputtering," *Surf. Sci.* **90**, 280–318 (1979).
- ⁶M. Medvedeva, I. Wojciechowski, and B. J. Garrison, "Effect of mass and incidence angle of keV energy polyatomic projectiles in silicon sputtering," *Surf. Sci.* **505**, 349–357 (2002).
- ⁷V. Popok, I. Barke, E. Campbell, and K. H. Meiwes-Broer, "Cluster-surface interaction: From soft landing to implantation," *Surf. Sci. Rep.* **66**, 347–377 (2011).
- ⁸I. Yamada and N. Toyoda, "Nano-scale surface modification using gas cluster ion beams—A development history and review of the Japanese nano-technology program," *Surf. Coat. Technol.* **201**, 8579–8587 (2007).
- ⁹N. Winograd, "The magic of cluster SIMS," *Anal. Chem.* **77**, 142A–149A (2005).
- ¹⁰N. Winograd, Z. Postawa, J. Cheng, C. Szakal, J. Kozole, and B. Garrison, "Improvements in SIMS continue. Is the end in sight?," *Appl. Surf. Sci.* **252**, 6836–6843 (2006).
- ¹¹J. F. Mahoney, "Microcluster-surface interactions: A new method for surface cleaning," *Int. J. Mass Spectrom.* **174**, 253–265 (1998).
- ¹²J. F. Mahoney, J. Perel, S. A. Ruatta, P. A. Martino, S. Husain, and T. D. Lee, "Massive cluster impact mass-spectrometry—A new desorption method for the analysis of large biomolecules," *Rapid Commun. Mass Spectrom.* **5**, 441–445 (1991).
- ¹³M. Gamero-Castaño and M. Mahadevan, "Sputtering of silicon by a beamlet of electrosprayed nanodroplets," *Appl. Surf. Sci.* **255**, 8556–8561 (2009).
- ¹⁴J. Fernández de la Mora and I. G. Loscertales, "The current transmitted through an electrified conical meniscus," *J. Fluid Mech.* **260**, 155–184 (1994).
- ¹⁵M. Gamero-Castaño and J. Fernández de la Mora, "Direct measurement of ion evaporation kinetics from electrified liquid surfaces," *J. Chem. Phys.* **113**, 815–832 (2000).
- ¹⁶A. McEwen, H. Ngo, K. LeCompte, and J. Goldman, "Electrochemical properties of imidazolium salt electrolytes for electrochemical capacitor applications," *J. Electrochem. Soc.* **146**, 1687–1695 (1999).
- ¹⁷T. Aoki, T. Seki, S. Ninomiya, and J. Matsuo, "MD simulation study of the sputtering process by high-energy gas cluster impact," *Appl. Surf. Sci.* **255**, 944–947 (2008).
- ¹⁸S. Ihara, S. Itoh, and J. Kitakami, "Mechanisms of cluster implantation in silicon: A molecular-dynamics study," *Phys. Rev. B* **58**, 10736 (1998).
- ¹⁹J. Samela and K. Nordlund, "Classical molecular dynamics simulations of hypervelocity nanoparticle impacts on amorphous silica," *Phys. Rev. B* **81**, 054108 (2010).
- ²⁰J. Samela, K. Nordlund, J. Keinonen, and V. N. Popok, "Comparison of silicon potentials for cluster bombardment simulations," *Nucl. Instrum. Methods Phys. Res., Sect. B* **255**, 253–258 (2007).
- ²¹S. Plimpton, "Fast parallel algorithms for short-range molecular-dynamics," *J. Comput. Phys.* **117**, 1–9 (1995).
- ²²F. Saiz and M. Gamero-Castaño, "Amorphization of silicon induced by nanodroplet impact: A molecular dynamics study," *J. Appl. Phys.* **112**, 054302 (2012).
- ²³R. Borrajo-Pelaez, E. Grustan-Gutierrez, and M. Gamero-Castaño, "Sputtering of Si, SiC, InAs, InP, Ge, GaAs, GaSb, and GaN by electrosprayed nanodroplets," *J. Appl. Phys.* **114**, 184304 (2013).
- ²⁴C. Anders, H. Kirihaata, Y. Yamaguchi, and H. Urbassek, "Ranges and fragmentation behavior of fullerene molecules: A molecular-dynamics study of the dependence on impact energy and target material," *Nucl. Instrum. Methods Phys. Res., Sect. B* **255**, 247–252 (2007).
- ²⁵H. J. C. Berendsen, J. P. M. Postma, W. F. van Gunsteren, A. DiNola, and J. R. Haak, "Molecular dynamics with coupling to an external bath," *J. Chem. Phys.* **81**, 3684–3690 (1984).
- ²⁶J. Samela, J. Kotakoski, K. Nordlund, and J. Keinonen, "A quantitative and comparative study of sputtering yields in Au," *Nucl. Instrum. Methods Phys. Res. B* **239**, 331–346 (2005).
- ²⁷F. H. Stillinger and T. A. Weber, "Computer-simulation of local order in condensed phases of silicon," *Phys. Rev. B* **31**, 5262–5271 (1985).
- ²⁸J. F. Ziegler, J. P. Biersack, and U. Littmark, *The Stopping and Range of Ions in Solids* (Pergamon Press, New York, 1985), Vol. 1.
- ²⁹V. G. Sevast'yanov, P. Y. Nosatenkob, V. V. Gorskiib, Y. S. Ezhovc, D. V. Sevast'yanov, E. P. Simonenkoa, and N. T. Kuznetsova, "Experimental and theoretical determination of the saturation vapor pressure of silicon in a wide range of temperatures," *Russ. J. Inorg. Chem.* **55**, 2073–2088 (2010).
- ³⁰D. V. Makhov and L. J. Lewis, "Isotherms for the liquid-gas phase transition in silicon from NPT Monte Carlo simulations," *Phys. Rev. B* **67**, 153202 (2003).
- ³¹E. G. Ponyatovsky and O. I. Barkalov, "Pressure-induced amorphous phases," *Mater. Sci. Rep.* **8**, 147–191 (1992).
- ³²B. M. French, *Traces of Catastrophe: A Handbook of Shock-Metamorphic Effects in Terrestrial Meteorite Impact Structures* (Lunar and Planetary Institute, Houston, 1998).
- ³³F. Saiz, R. Borrajo-Pelaez, and M. Gamero-Castaño, "The influence of the projectile's velocity and diameter on the amorphization of silicon by electrosprayed nanodroplets," *J. Appl. Phys.* **114**, 034304 (2013).

Sputtering of Si, SiC, InAs, InP, Ge, GaAs, GaSb, and GaN by electrospayed nanodroplets

Rafael Borrajo-Pelaez, Enric Grustan-Gutierrez, and Manuel Gamero-Castaño^{a)}

Department of Mechanical and Aerospace Engineering, University of California, Irvine, California 92697, USA

(Received 6 September 2013; accepted 26 October 2013; published online 12 November 2013)

This article presents a characterization of the damage caused by energetic beams of electrospayed nanodroplets striking the surfaces of single-crystal semiconductors including Si, SiC, InAs, InP, Ge, GaAs, GaSb, and GaN. The sputtering yield (number of atoms ejected per projectile's molecule), sputtering rate, and surface roughness are measured as functions of the beam acceleration potential. The maximum values of the sputtering yields range between 1.9 and 2.2 for the technological important but difficult to etch SiC and GaN respectively, and 4.5 for Ge. The maximum sputtering rates for the non-optimized beam flux conditions used in our experiments vary between 409 nm/min for SiC and 2381 nm/min for GaSb. The maximum sputtering rate for GaN is 630 nm/min. Surface roughness increases modestly with acceleration voltage, staying within 2 nm and 20 nm for all beamlet acceleration potentials and materials except Si. At intermediate acceleration potentials, the surface of Si is formed by craters orders of magnitude larger than the projectiles, yielding surface roughness in excess of 60 nm. The effect of projectile dose is studied in the case of Si. This parameter is correlated with the formation of the large craters typical of Si, which suggests that the accumulation of damage following consecutive impacts plays an important role in the interaction between beamlet and target. © 2013 AIP Publishing LLC.

[<http://dx.doi.org/10.1063/1.4829925>]

I. INTRODUCTION

The size of the projectile has important effects on how an ion beam interacts with a target, and extending the range of this parameter beyond atomic dimensions offers opportunities in both research and technological applications. For example, the size of gas cluster ions and their relatively low specific charge compared to atomic ions are credited with the high sputtering yields, dense energy deposition, and shallow surface damage typical of cluster ion beams;¹ large projectile sizes are correlated with the ability to desorb large molecules in secondary ion mass spectrometry;^{2–4} and the theoretical study of the energetic impact of cluster ions and larger nanoparticles has become a problem of interest.⁵ Gas cluster ions are the largest projectiles available but, due to their low charging level (one elementary charge), their effective diameters are limited to a few nanometers (e.g., a large Ar_{2000}^+ gas cluster ion has a diameter of 5.6 nm). This absence of an appropriate particle source has hindered the experimental research with larger projectiles and the development of applications benefitting from them, an obstacle that has now been removed by the introduction of energetic beams of electrospayed nanodroplets.⁶

The electrohydrodynamic atomization of dielectric liquids in the cone-jet mode produces sprays of charged droplets with narrow size distributions.⁷ The average diameter of the droplets is controlled between a few nanometers and macroscopic dimensions by adjusting the flow rate and the physical properties of the liquid and, since many dielectric liquids

are readily electrospayed in vacuum, electrohydrodynamic atomization can be used as a source for nanoparticle beams. Besides enabling research and technological applications in a previously unavailable projectile size range, the electro spray source has some advantageous properties: being a point source, its beamlets can be electrostatically focused into sub-micrometric spots; MEMS techniques can be used to fabricate sources with dense emitter arrays for broad beam applications; and the chemical composition of the projectile can be varied to combine physical sputtering with chemical effects. The introduction by Fernandez de la Mora of ionic liquids as ideal fluids for electro spraying in vacuum has been an important factor in the development of the field.⁸ The low vapor pressures and high electrical conductivities of ionic liquids, combined with the very large number of chemical compounds available, has stimulated the research of ionic liquid-based electro spraying for electric propulsion,⁹ secondary ion mass spectrometry,¹⁰ and ion and nanodroplet beams.^{6,11}

Electrospayed nanodroplets are efficient sputtering projectiles. Sputtering yields of 2.3, 1.5, and 2.3 atoms ejected per projectile molecule have been reported for single-crystal silicon, and poly crystalline silicon carbide and boron carbide, respectively. The associated sputtering rates of 448, 172, and 170 nm/min far exceed the physical sputtering of broad-beam ion sources.¹² Besides sputtering these energetic beamlets are known to amorphatize the surface of single crystal silicon, a phase transition caused by the dissipation of energy in the area surrounding the impact, and the subsequent melting and ultrafast quench of the solid phase.^{13,14} This article extends our initial research on nanodroplet sputtering to other single-crystal semiconductors, including

^{a)}Author to whom correspondence should be addressed. Electronic mail: mgamero@uci.edu

indium arsenide, indium phosphide, germanium, gallium arsenide, gallium antimonide, gallium nitride, and silicon carbide. The article quantifies the sputtering yield, sputtering rate, and surface roughness of these semiconductors as functions of the nanodroplet velocity. Anisotropic etching of single-crystal GaN and SiC at the high rates demonstrated in Si is especially attractive for these technological important wide bandgap semiconductors, due to their remarkable chemical stability and resistance to etching.¹⁵ The article also studies the influence of projectile dose on the sputtering yield and the surface roughness of single-crystal Si.

II. EXPERIMENTAL APPARATUS AND METHODS

The ionic liquid 1-ethyl-3-methylimidazolium bis(trifluoromethylsulfonyl) imide, Emi-Im, is electrosprayed to produce a beam of charged nanodroplets. This liquid has been employed in sputtering research,^{6,12} and its electrosprays have been characterized in vacuum.¹⁶ Figure 1 shows a sketch of the experimental setup. The electrospray source is a platinum tube with an inner diameter of 0.16 mm and an outer diameter of 0.48 mm. The tip is chamfered at an angle of 45° to reduce the base of the Taylor cone down to the tube's inner diameter, which promotes the higher atomization stability associated with a reduced cone volume. The platinum tube is crimped to a fused silica tube that takes the fluid from an external bottle to the emission tip located inside the vacuum chamber, which pressure is kept in the low 10^{-6} Torr range. The fused silica tube, having an inner diameter of 40 μm , also increases the hydraulic impedance so that a conveniently high pressure difference relative to the typical capillary and electrostatic pressures in the Taylor cone, as well as the resolution of the pressure gauge, must be used to drive the flow. The platinum emitter is connected to a high voltage power supply of negative polarity with respect to a grounded extractor electrode. A voltage difference of -2150 V between emitter and extractor, V_E , is used in every experiment to set the electrospray. A fraction of the beam exits through an orifice in the axis of the extractor (0.64 mm

in diameter, 3.0° half-cone angle aperture with respect to the emission point), and this beamlet is directed towards the sputtering target. The target is mounted on an XYZ positioner, its surface is normal to the beamlet axis and placed 4 mm from the extractor during the sputtering experiments, and is connected to a high voltage power supply of positive polarity. The potential of the target V_T can be increased up to 25 kV to accelerate the projectiles. The net acceleration potential V_A of the projectiles is the sum of the emitter and extractor potentials. All experiments are performed under identical electrospraying conditions: the pressure difference driving the flow is 200 Torr, yielding a total beam current I_E of 283 ± 4 nA; the current of the beamlet I_B impacting on the target is 19 nA; the beamlet was characterized via time of flight to measure its mass flow rate, $\dot{m}_B = 1.65 \times 10^{-11}$ kg/s, the percentage of the current carried by the droplets, 84%, and their average specific charge, $\langle \xi \rangle = 971$ C/kg. The estimated droplet average diameter is 27 nm.¹⁷ The average impact velocity is estimated with the average specific charge and the acceleration voltage $v = (2\langle \xi \rangle V_A)^{1/2}$. The typical kinetic energy of an Emi-Im molecule in the nanodroplet is $E_m = m_m \langle \xi \rangle V_A$, where m_m is the molecular mass of Emi-Im, 391.12 amu. The stagnation pressure of the projectile is $P = \rho \langle \xi \rangle V_A$, where ρ is the density of Emi-Im, 1520 kg/m³. The acceleration voltage was varied between 6.1 and 26.6 kV, yielding impact velocity, molecular energy and stagnation pressure ranges of 3.4 to 7.2 km/s, 24 to 105 eV, and 9.1 to 39 GPa.

All targets are single-crystal wafers purchased from El-Cat Inc. The Si, Ge, GaAs, GaSb, InAs and InP targets are 2 in. wafers with [100] orientation. The SiC targets are $10 \times 10 \times 0.43$ mm hexahedrons of the 6H polytype, and [0001] orientation. The GaN target is a 100 μm thick epilayer of the semiconductor with a [0001] orientation, grown on a 2 in. sapphire wafer.

The sputtering yields are calculated with the formula

$$Y = \frac{m_m}{\dot{m}_B \tau} \frac{n_c \rho_C V}{m_C}, \quad (1)$$

where ρ_c is the density of the crystal; V is the volume of the target carved by the beamlet, which is measured with a profilometer; n_c is the number of atoms in the crystal cell, and m_c is the sum of their masses; and τ is the time during which the beam strikes the surface. The sputtering rate is defined by

$$R = \frac{V}{A \tau}, \quad (2)$$

where A is the area of the spot carved by the beamlet. The sputtering yield and rate, as well as the surface roughness, are measured in areas carved by the beamlet during 600 s. The target is repeatedly moved while resetting the target potential, to generate an array of spots carved at different acceleration voltages. In a second type of experiments designed to study the effect of projectile dose, the time of bombardment is varied between 10 s and 600 s.

The roughness of the bombarded surface is measured with an atomic force microscope, AFM. The roughness is

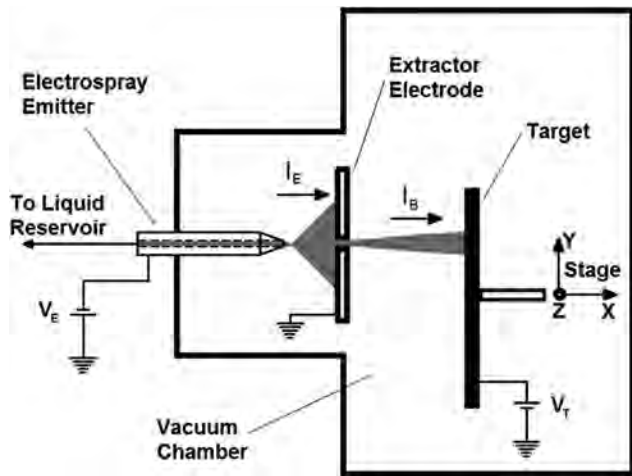


FIG. 1. Diagram of the experimental setup. An electrospray source operating inside a vacuum chamber atomizes a liquid into charged nanodroplets, a fraction of which is accelerated by an electrostatic field and directed against a sputtering target.

computed as the root mean square of the heights of the surface points.

III. RESULTS AND DISCUSSION

Figure 2 shows photographs of the Si, SiC, and Ge targets bombarded at several acceleration potentials, and surface profiles for the Si target. In all cases the beamlet carves a flat circular depression surrounded by a deeper ditch. The diameter of these macroscopic craters decreases at increasing acceleration voltage because the axial electric field between the extractor and the target, being proportional to acceleration voltage, reduces the polar angle of the particle trajectories exiting the extractor orifice. Typical crater diameters for low and high acceleration potentials are 1 mm and 0.3 mm respectively. The depth of the craters augments with acceleration voltage because of the positive correlation between sputtering yield and molecular kinetic energy, and the reduction of the crater area at increasing acceleration potential. For example, the depths of the Si, SiC, and Ge targets are 0.9, 0.7, and 5.6 μm at 14.6 kV acceleration voltage, and 3.7, 5.8, and 22.4 μm at $V_A = 24.6$ kV. Besides these trends common to all target materials there are noticeable differences between the Si surfaces in one hand, and the surfaces of SiC and Ge (all other semiconductors behave like SiC and Ge). First, the Si craters are surrounded by substantial deposits in

the form of circular iridescent rings forming a Newton color series, which are much less visible in other materials. These and similar experiments with other liquids suggest that the projectile's imide group has an affinity for forming charged compounds with the sputtered Si, which are pushed back to the target by the electric field. The roughness of the surfaces is also markedly different. The AFM profiles for Si show surfaces covered by micrometric craters with sizes that increase with the acceleration voltage up to 15 kV. These craters are large, e.g., the typical diameter and depth at $V_A = 14.6$ kV are 2–3 μm and 0.5 μm , respectively, orders of magnitude larger than the average diameter of the nanodroplets. These micrometric and intertwined craters produce very rough surfaces, which manifest in the photographs at 12.1 kV and 14.6 kV by the high scattering of light (the photographed samples are illuminated at a glancing angle). At still higher acceleration potential, the surface of Si becomes specular and is occasionally dotted by very large, isolated craters. The surfaces of all other materials also exhibit craters, but these are significantly smaller, and their sizes and density do not vary with the acceleration voltage as much as in Si.

Figure 3 plots the roughness of the surfaces struck by the beamlet. The roughness of Si increases sharply with acceleration voltage, reaching a maximum value of 69 nm at 14.6 kV; at higher acceleration voltage, the surface becomes much

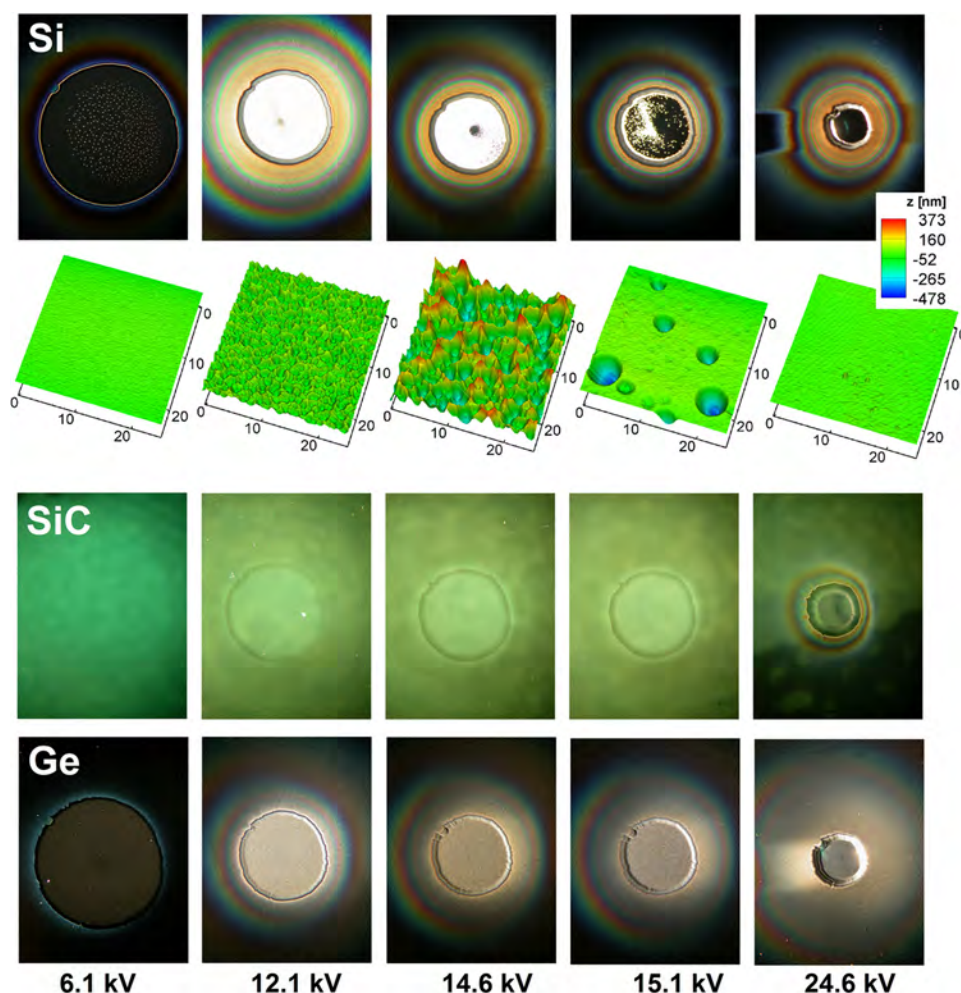


FIG. 2. Photographs of Si, SiC, and Ge targets struck by the beamlet during 600 s, at varying acceleration potential. The Si photographs are complemented with atomic force microscopy of the bombarded surfaces.

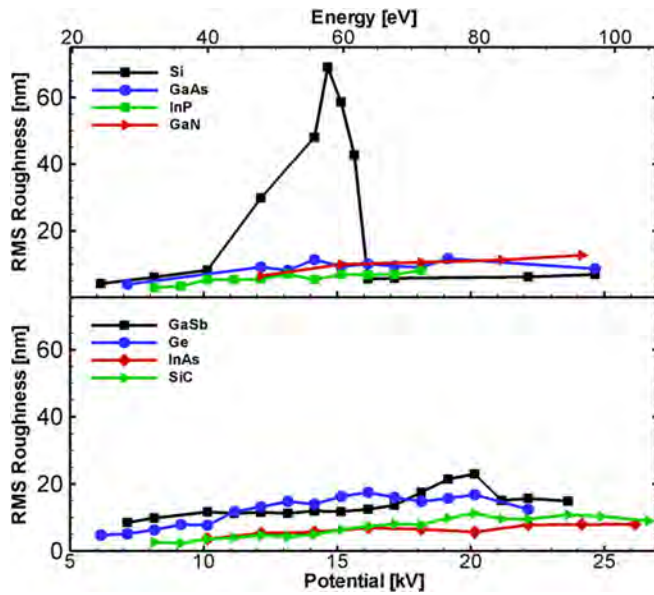


FIG. 3. Roughness of the bombarded samples as a function of acceleration potential. Silicon behaves differently from all other materials.

smoother. The roughness of all other materials increases slowly with acceleration voltage and, in some cases, levels off or slightly decreases at the highest acceleration voltages; the values are substantially lower than the peak roughness for Si. Note that germanium also follows this monotonic trend, despite being a material closely related to silicon. The maximum roughness for GaN, GaAs, GaSb, InP, InAs, Ge, and SiC are 12.7, 11.7, 19.5, 8.1, 7.9, 17.5, and 11.2 nm, respectively. The AFM profiles in Fig. 4 show the patterns of impacts behind the surface roughness of different materials, and the singular behavior of Si. The surfaces of GaN, SiC, and Ge in the bottom row are typical of all semiconductors other than Si: the surfaces have small indentations with diameters of the order of $0.1 \mu\text{m}$ and depths of a few tens of nanometers, and which must be the dimples left by individual

droplets impacting on the surface. The Si targets also display this pattern of small indentations, but at acceleration voltages between 10.1 kV and 15.1 kV, these small marks are superimposed over an additional pattern of much larger craters, which dominate the surface roughness. Each large crater must be produced by the single impact of a projectile that is not much larger than the average droplet (2 orders of magnitude smaller than the large craters): we have never detected large droplets in these beams despite a thoroughly investigation with an induction charge detector;¹⁷ and large droplets, far exceeding the Rayleigh charge limit at the required specific charge, would be unstable.

Figure 5 shows sputtering yields as a function of acceleration voltage, and projectile's molecular kinetic energy. The sputtering yields increase monotonically with molecular energy, leveling off at approximately 70 eV in most materials. The yields for GaAs, InAs, and GaSb decrease slightly at the highest acceleration voltages. The maximum sputtering yields for Si, GaN, GaAs, GaSb, InP, InAs, Ge, and SiC are 2.2, 2.2, 4.2, 4.1, 4.1, 3.6, 4.5, and 1.9, respectively. These values are similar to the maximum sputtering yields of atomic projectiles and significantly higher than those of gas cluster ions. For instance, the sputtering yields of Si and SiC bombarded by atomic argon at normal incidence and 500 eV are 0.4 and 0.8;^{18,19} and the sputtering yields of Si and SiC struck by Ar_{3000}^+ gas cluster ions at 20 kV acceleration potential are 0.008 and 0.013.²⁰ As in the case of the surface roughness, the dependence of the sputtering yield on acceleration voltage differs significantly between Si and other materials. Rather than increasing monotonically with acceleration voltage, the sputtering yield of Si first increases with acceleration voltage, peaks at 12.1 kV, and abruptly decreases at 14.6 kV to remain nearly constant thereafter. The sharp drop in sputtering yield coincides with the drop in surface roughness. Figure 5 also shows that SiC and GaN have substantially higher threshold energies for sputtering than all other semiconductors, which could be expected from the exceptionally

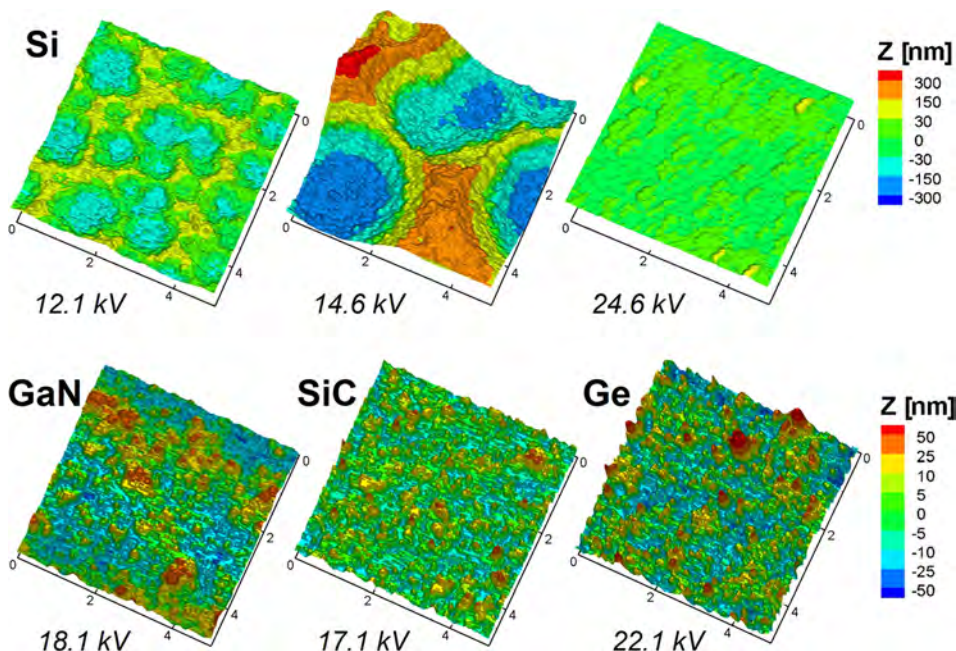


FIG. 4. Atomic force microscope measurements of Si, GaN, SiC, and Ge samples. The impacts of individual droplets produce a pattern of small indentations in all surfaces. In addition, a very few number of impacts produce large craters in Si at acceleration potentials between 10 kV and 15 kV.

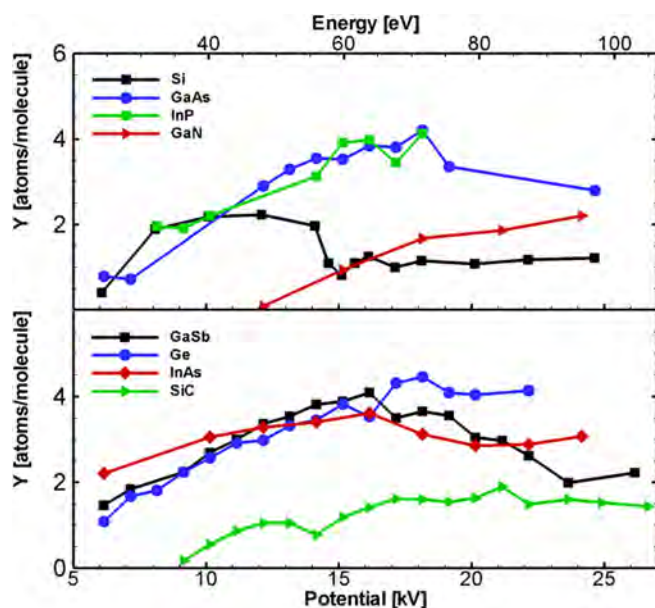


FIG. 5. Sputtering yields as a function of acceleration potential. The maximum sputtering yields of all semiconductors are comparable. The maximum values between 2 and 4 atoms per projectile's molecule are substantially higher than those of gas cluster ions at similar acceleration potentials.

high thermal, mechanical, and chemical stability of these two compounds.

Figure 6 shows sputtering rates, a figure of merit which, being proportional to the particle flux, depends on factors such as beam focusing, emitter density, etc. In our experiments, the flux is only a function of the acceleration voltage, making it possible to compare the sputtering rates on different targets at constant acceleration voltage. The sputtering rate increases monotonically with acceleration voltage because both the particle flux and the sputtering yield increase with this parameter. The sputtering rates for Ge,

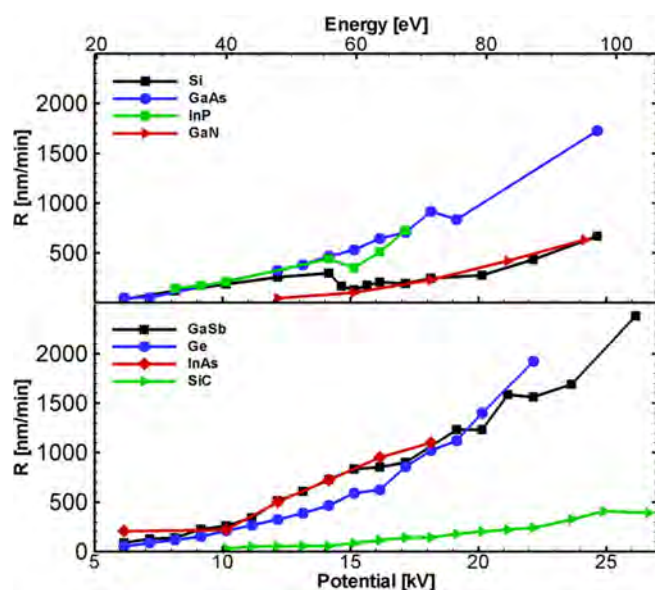


FIG. 6. Sputtering rates versus acceleration potential. The sputtering rates in these experiments are similar to the values yielded by reactive ion etching, and orders of magnitude higher than in the comparable ion beam milling process.

GaSb, and GaAs at 20 kV exceed 1000 nm/min, a value typical of reactive ion etching and orders of magnitude higher than what is achievable with ion beam milling. The maximum sputtering rates for SiC and GaN, 410 and 630 nm/min, are similar to the best rates possible with reactive ion etching (970 nm/min for SiC and 1300 nm/min for GaN), and significantly higher than the rates associated with the more comparable ion beam milling technique (below 10 nm/min for GaN).¹⁵

In an ongoing molecular dynamics study of the impact of a nanodroplet on single-crystal Si we have determined that thermal evaporation is the main sputtering mechanism. The simulations show how a thin layer of Si starts melting at a projectile molecular energy of approximately 18 eV, and that the temperature and thickness of the layer increase with the velocity of the projectile.²¹ The atoms emitted from this molten surface have a Maxwellian distribution, the temperature of the distribution is similar to that of the surface, and the emission rate has the expected exponential dependence on temperature. The role played by thermal evaporation in nanodroplet sputtering and the significantly higher melting points of SiC and GaN (3103 K for SiC and 2400 K for GaN, while Si is the material with the third highest melting point at a distant 1690 K) are consistent with the higher threshold energies for sputtering of these two semiconductors in Fig. 5. In addition to evaporation, other mechanisms are likely contributing to the removal of material observed in our experiments. For example, in the case of Si, we hypothesize that the accumulation of impacts damages the target, until a critical point is reached in which one additional impact carves a crater orders of magnitude larger than the projectile. One such sputtering mechanism dependent on projectile dose could be the nucleation and growth of cracks caused by thermal stresses created by the very fast resolidification of the area surrounding the impact. The large craters in Figures 2 and 4 support this idea: only a small number of impacts generate these large craters because otherwise the sputtering yield would be orders of magnitude higher than what is measured; and, since all projectiles are similar, the conditions of the surface where large craters appear must be substantially different from that of the original target. This difference must result from the accumulation of impacts.

The effect of the projectile dose on the damage exacted on Si is further illustrated in Figure 7. In these experiments, the beamlet strikes a spot during a period, which is varied between 10 s and 600 s. The projectile dose is proportional to this time. The experiments are done at 12.1 kV and 18.1 kV acceleration potentials, to produce conditions that cause intertwined microscopic craters with high surface roughness and a smooth specular surface, respectively (see Fig. 2). The droplet number fluxes are estimated at $3.8 \times 10^{15} \text{ m}^{-2} \text{ s}^{-1}$ and $7.3 \times 10^{15} \text{ m}^{-2} \text{ s}^{-1}$ and, with an average droplet diameter of 27 nm, it takes about 0.47 s and 0.25 s for the beamlet to uniformly strike the surface with at least one impact. The photographed samples are illuminated along the line of sight and, since a rough surface scatters light effectively in all directions, the rougher the surface the darker the bombarded area appears. The photographs and the associated plots show how the surface roughness for the 12.1 kV beamlet increases with dose until it saturates at an exposure time of

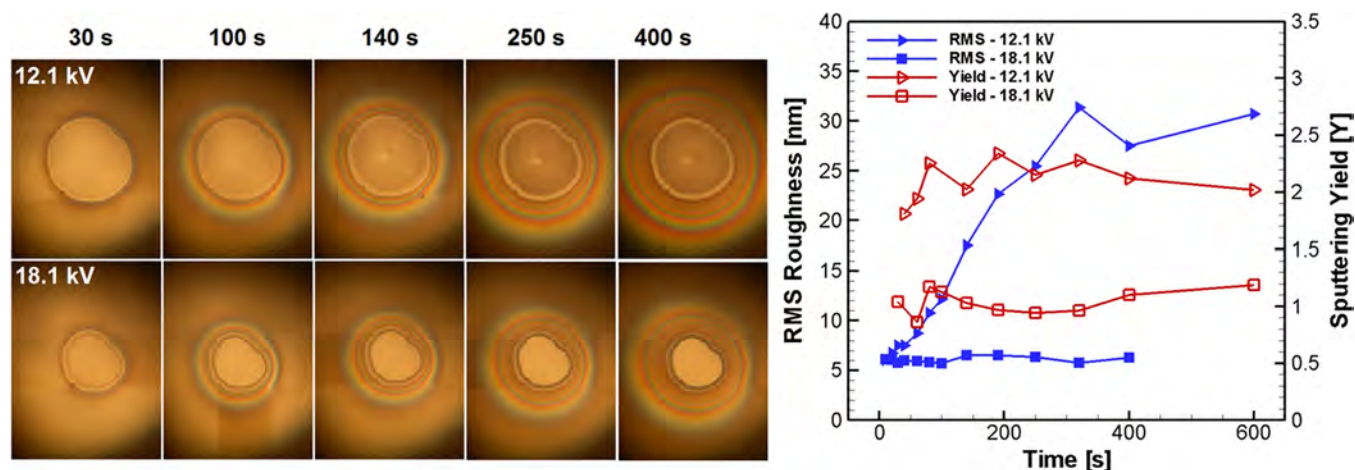


FIG. 7. The effect of projectile dose on the surface roughness and sputtering yield of Si, at 12.1 kV and 18.1 kV beamlet acceleration potentials.

approximately 300 s, i.e., the formation of the large craters typical of Si requires exceeding a critical projectile dose. Conversely, the roughness caused by the 18.1 kV beamlet and the sputtering yields for either acceleration voltage does not depend on the projectile dose. These results suggest a link between the accumulation of damage induced by consecutive impacts, and the formation of the very large craters characteristic of Si, which dominate the surface roughness when present. Also, at high enough projectile energy, the impact modifies the surface in such a way that this accumulation effect disappears. Furthermore, since the ejection of Si from these large craters does not have a significant contribution to the sputtering yield, the frequency at which the large craters form must be much lower than the rate at which the projectiles impact.

IV. CONCLUSION

We have measured the sputtering yield and rate of several single-crystal semiconductors bombarded by a beamlet of electrosprayed nanodroplets at varying acceleration potential. We have also quantified the roughness of the target surfaces, and the effect of projectile dose in the case of Si. The main results are summarized as follows:

- The maximum sputtering yields for Si, SiC, Ge, GaAs, GaSb, GaN, InP, and InAs are 2.2, 1.9, 4.5, 4.2, 4.1, 2.2, 4.1, and 3.6 target atoms per projectile's molecule, respectively. The corresponding sputtering rates are 250, 220, 1020, 920, 850, 630, 390, and 950 nm/min.
- The surface roughness typically increases with the acceleration potential. The variation is gradual and narrow for most of materials, with rms values between 2 nm and 20 nm. Silicon exhibits a singular behavior: the roughness peaks at 69 nm at an intermediate potential and drops sharply at higher potentials; and some impacts produce craters several orders of magnitude larger than the projectiles.

- The formation of the very large crater impacts typical of Si at acceleration potentials between 10 kV and 15 kV requires exceeding a threshold projectile dose. This suggests a link between consecutive projectile impacts and the accumulation of damage in the target.

ACKNOWLEDGMENTS

This work was funded by the Air Force Office of Scientific Research, Grant No. FA9550-11-1-0308. The authors are grateful for the support of the AFOSR Program Manager Dr. Birkan.

- ¹I. Yamada and N. Toyoda, *Surf. Coat. Technol.* **201**, 8579 (2007).
- ²N. Winograd, Z. Postawa, J. Cheng, C. Szakal, J. Kozole, and B. J. Garrison, *Appl. Surf. Sci.* **252**, 6836 (2006).
- ³S. Ninomiya, K. Ichiki, H. Yamada, Y. Nakata, T. Seki, T. Aoki, and J. Matsuo, *Rapid Commun. Mass Spectrom.* **23**, 1601 (2009).
- ⁴D. Asakawa and K. Hiraoka, *Surf. Interface Anal.* **44**, 227 (2012).
- ⁵J. Samela and K. Nordlund, *Phys. Rev. Lett.* **101**, 027601 (2008).
- ⁶M. Gamero-Castaño and M. Mahadevan, *Appl. Surf. Sci.* **255**, 8556 (2009).
- ⁷M. Cloupeau and B. Prunet-Foch, *J. Electrostat.* **22**, 135 (1989).
- ⁸I. Romero-Sanz, R. Bocanegra, J. Fernández de la Mora, and M. Gamero-Castaño, *J. Appl. Phys.* **94**, 3599 (2003).
- ⁹M. Gamero-Castaño and V. Hruby, *J. Propul. Power* **17**, 977 (2001).
- ¹⁰Y. Fujiwara, N. Saito, H. Nonaka, and S. Ichimura, *Surf. Interface Anal.* **45**, 517 (2013).
- ¹¹A. Zorzos and P. Lozano, *J. Vac. Sci. Technol. B* **26**, 2097 (2008).
- ¹²M. Gamero-Castaño and M. Mahadevan, *J. Appl. Phys.* **106**, 054305 (2009).
- ¹³M. Gamero-Castaño, A. Torrents, L. Valdevit, and J. Zheng, *Phys. Rev. Lett.* **105**, 145701 (2010).
- ¹⁴F. Saiz and M. Gamero-Castaño, *J. Appl. Phys.* **112**, 054302 (2012).
- ¹⁵V. Cimalla, J. Pezoldt, and O. Ambacher, *J. Phys. D: Appl. Phys.* **40**, 6386 (2007).
- ¹⁶M. Gamero-Castaño, *Phys. Fluids* **20**, 032103 (2008).
- ¹⁷M. Gamero-Castaño, *Rev. Sci. Instrum.* **78**, 043301 (2007).
- ¹⁸Y. Yamamura and H. Tawara, *Atom. Data Nucl. Data* **62**, 149 (1996).
- ¹⁹T. S. Pugacheva, F. G. Jurabekova, Y. Miyagawa, and S. K. Valiev, *Nucl. Instrum. Methods Phys. Res. B* **127**, 260 (1997).
- ²⁰I. Yamada, *Nucl. Instrum. Methods Phys. Res. B* **148**, 1 (1999).
- ²¹F. Saiz, R. Borrajo-Pelaez, and M. Gamero-Castaño, *J. Appl. Phys.* **114**, 034304 (2013).

The influence of the projectile's velocity and diameter on the amorphization of silicon by electrosprayed nanodroplets

Fernan Saiz, Rafael Borrajo-Pelaez, and Manuel Gamero-Castaño^{a)}

Department of Mechanical and Aerospace Engineering, University of California, Irvine, California 92697, USA

(Received 20 May 2013; accepted 21 June 2013; published online 16 July 2013)

The hypervelocity impact of electrosprayed nanodroplets on single-crystal silicon amorphizes a thin layer of the target. Molecular Dynamics simulations have shown that the amorphization results from the melting of the material surrounding the impact interface, followed by an ultrafast quenching that prevents recrystallization. This article extends this previous work to study the role of the projectile's diameter and velocity on the amorphization phenomena and compares the simulation results with experimental measurements of a bombarded silicon target. In the range of projectile diameter and impact velocity studied (diameter between 5 and 30 nm, and velocity between 1 and 6 km/s), the projectile velocity plays a more relevant role than its diameter. A significant amorphous layer begins to develop at a velocity near 3 km/s, its thickness rapidly increasing with velocity until it plateaus at about 4 km/s. The reduction of the melting temperature with pressure combined with the conversion of kinetic energy into thermal energy are responsible for the melting of silicon starting at an impact velocity of 3 km/s. Once the conditions inducing amorphization are reached, the volume of the generated amorphous phase scales linearly with both the kinetic energy and the volume of the projectile. © 2013 AIP Publishing LLC.
[\[http://dx.doi.org/10.1063/1.4813416\]](http://dx.doi.org/10.1063/1.4813416)

I. INTRODUCTION

Amorphous silicon is commonly prepared into thin films by vapor deposition^{1,2} and has become a material of technological importance in applications such as solar power generation and electronics.^{3–5} Besides vapor deposition, amorphous silicon is also formed by ultrafast quenching of thin layers melted by pulsed laser irradiation,⁶ an amorphization mechanism confirmed by atomistic simulations.^{7,8} Recently, we have reported that the energetic impact of electrosprayed nanodroplets on crystalline silicon also produces thin amorphous layers and modeled the impacts via Molecular Dynamics (MD).^{9,10} The simulations show that a projectile impacting at sufficient velocity is able to melt a thin region surrounding the impact, which then solidifies at cooling rates precluding crystallization.

This article extends our initial MD work by examining the effect of the nanodroplet's size and velocity on the amorphization of silicon. Individual impacts of droplets with diameters between 5 nm and 30 nm, and velocities between 1 km/s and 6 km/s, are numerically simulated, and the results compared with the actual surface damage produced by a beam of nanodroplets impinging on a silicon wafer. In the latter case, the nanodroplets are generated by an electrospray operating in the cone-jet mode, an atomization technique known for producing fine sprays of charged droplets with average diameters as low as a few nanometers. In our experiments, the electrospray source is operated in vacuum and the nanodroplets, with an average charge to mass ratio

of 971 C/kg, readily reach hypervelocity conditions when accelerated by an electrostatic field. For reference, a 971 C/kg particle impacting at 4 km/s requires an acceleration voltage of 8.24 kV. The experimental damage in the silicon surface is the result of multiple impacts by droplets with a narrow size distribution, a circumstance unavoidable in our experiments and which somewhat hinders the comparison with the Molecular Dynamics calculations of isolated impacts in a pristine silicon target.

Molecular Dynamics is a simulation technique for calculating the positions and velocities of all atoms or microscopic particles of a system. The technique is based on the simultaneous integration of the equations of motions of all constituent particles, interacting and coupled through defined potentials. Thermodynamic properties such as temperature, pressure, or density are calculated as ensembles averages of the computed positions and velocities. Structural properties such as the radial distribution function or the static orientation factor can be calculated as ensembles averages of positions. The radial distribution function provides information about the short, medium, and long range orders of a system of particles, and it is used in this study to quantify the extent of the amorphous region produced by the impact.

The article is organized as follows. Section II describes the computational setup for the simulations, the criteria for calculating the extent of the amorphous layers, and the nanodroplet impact experiments. Section III presents the simulations for projectiles with varying velocity and size, analyzes the influence of these parameters in the amorphization, and compares the numerical and experimental data. Finally, Sec. IV summarizes the main findings.

^{a)}Author to whom correspondence should be addressed. Electronic mail: mgamero@uci.edu

II. NUMERICAL AND EXPERIMENTAL METHODS

We use the molecular dynamics package LAMMPS¹¹ to model the impact of a nanodroplet on a (100) silicon target at normal incidence. The projectile is made of identical spheres representing the molecule of the ionic liquid 1-ethyl-3-methylimidazolium bis (trifluoro-methylsulfonyl) imide (Emi-Im, 391.31 amu and 0.42 nm molecular mass and radius), and distributed in a hexagonal centered package lattice. We simulate four projectile diameters: 5, 10, 20, and 30 nm, and impact velocities between 1.0 and 6.0 km/s. The associated kinetic energy varies between 2.0 and 73.0 eV per molecule. The largest simulated droplets and the whole velocity range are comparable to the experimental conditions described later in this section. The target is a silicon slab with dimensions adjusted with increasing projectile diameter to minimize boundary effects. The sides of the target for the 5 nm droplet are 32.59 nm × 32.59 nm × 24.44 nm (1 303 353 Si atoms), where the latter value is the depth of the slab in the direction of impact; the sides for the 30 nm droplet are 130.34 nm × 130.34 nm × 97.76 nm (83 059 200 Si atoms). A thermal bath at 293 K is applied on all faces of the slab except for the impact surface to prevent the reflection of shock waves.¹² The Stillinger-Weber (SW) potential models the forces between silicon atoms.¹³ This potential accurately reproduces the properties of the crystalline and liquid phases, as well as the normal melting point, and has been used to capture the amorphization of silicon by fast quenching of a melt.¹⁴ The interactions between liquid molecules and between liquid molecules and Si atoms are modeled with a repulsive, two-body Ziegler-Biersack-Littmark (ZBL) potential.¹⁵ The equations of motion are integrated with a timestep of 1 fs.

The local temperature is computed using the standard average of the kinetic energies of N atoms enclosed in a control volume

$$T = \frac{m \sum_{i=1}^N (\mathbf{v}^i - \langle \mathbf{v}^i \rangle) \cdot (\mathbf{v}^i - \langle \mathbf{v}^i \rangle)}{3k_B N}, \quad (1)$$

where k_B is the Boltzmann's constant, m is the mass of a silicon atom, and \mathbf{v}^i is the velocity vector of the i -atom. We typically use a spherical control volume with a radius of 1.08 nm and approximately containing 280 atoms.

An analysis of the radial distribution function determines the regions of the substrate amorphized by the impact. Figure 1 contains radial distribution functions obtained from the present simulations, showing the very different structures of the crystalline, amorphous, and liquid phases. The disappearance of all coordination shells beyond the first one at $r = 0.24$ nm and the second one at $r = 0.38$ nm are standard criteria for defining the liquid and amorphous phases, respectively.^{16–18} To create a phase field, a fine square grid with a resolution of 0.86 nm is defined in the silicon substrate, each cubical element typically enclosing 32 atoms. The radial distribution of the element is defined as the average of the radial distributions centered in each atom inside the cubical element. The total volume of the amorphous

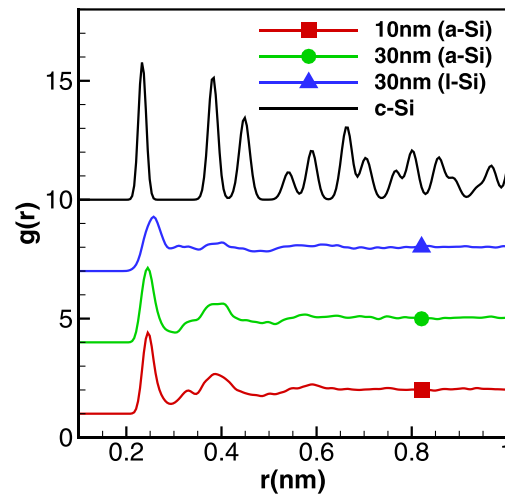


FIG. 1. Radial distribution functions of amorphous (a-Si) and liquid (l-Si) phases produced by the impacts of the 10 and 30 nm droplets at 6.0 km/s. The crystalline pattern (c-Si) is also shown for reference.

phase is obtained by adding the volumes of amorphous elements, and the thickness of the amorphous layer surrounding the crater is calculated by averaging the local thickness of the amorphous phase left by the impact.

The simulations for the 5, 10, and 20 nm projectiles are executed until the temperature throughout the silicon target approaches the bath temperature. For these diameters, integration times under 125 ps suffice to reach the final state. On the other hand, the longer cooling time for the 30 nm projectile and the much larger number of Si atoms in the slab make it very expensive to reach global equilibrium; and for this projectile's size, the simulation is stopped when the local temperature in the target falls everywhere below the glass transition temperature of 1060 K.¹⁸ We have verified that beyond this time, the volume of the amorphous solid phase remains practically constant.

To compare the simulation results with experimental data, a (100) silicon wafer was bombarded with a beam of electrosprayed nanodroplets at varying acceleration voltage, and normal incidence. The resulting surface damage was analyzed via transmission electron microscopy (TEM). The electrospray source, operated in negative mode at -2.15 kV with respect to a grounded extractor/skimmer electrode, and the experimental set up were identical to the one described in Ref. 19. An axial section of the beam was skimmed to produce a beamlet of negatively charged droplets with an average diameter of 26 nm, and an average charge to mass ratio of 971 C/kg. The beamlet transported a current of 19.3 nA. The silicon target was placed 4 mm from the grounded skimmer and connected to a high voltage power supply of positive polarity. The total acceleration voltage of the droplets was varied between 4.65 kV and 18.55 kV, resulting in an impact velocity range between 3.00 km/s and 6.00 km/s. The projectile dose on the target's surface is estimated to be 2.4×10^{16} impacts per square meter or, equivalently, about 4 impacts per target area equal to the cross section of the average droplet. After bombardment, thin cross sectional samples were prepared with a FEI Quanta 3D FEG dual-beam scanning electron microscope/focused ion beam (SEM/FIB), and

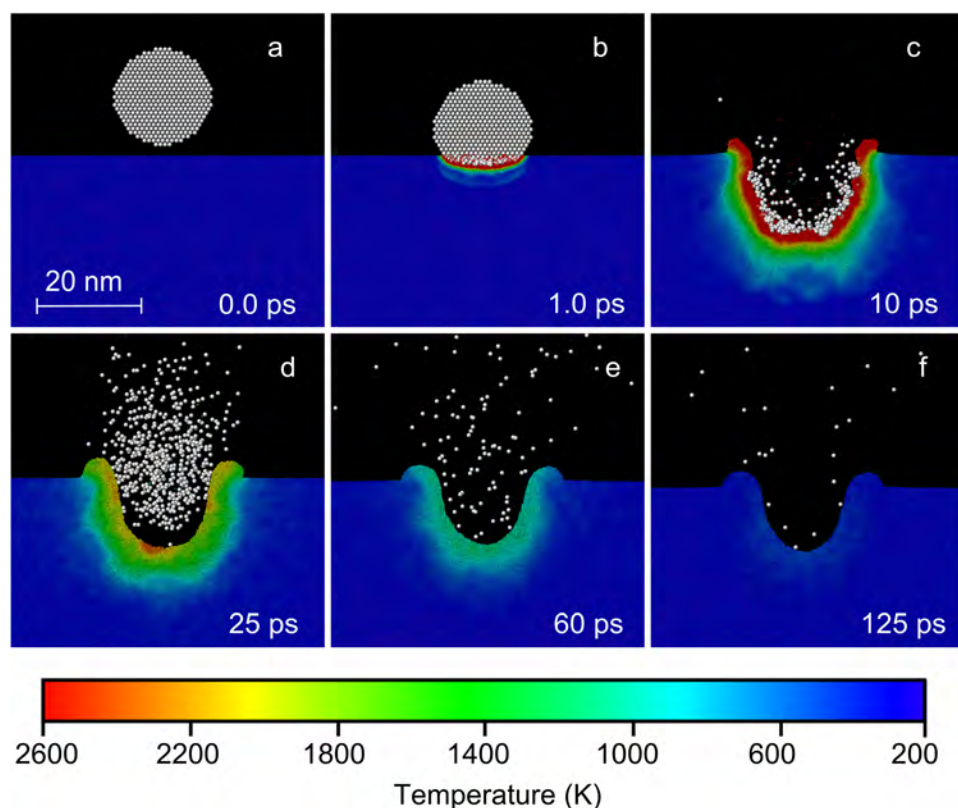


FIG. 2. Impact of a 20 nm projectile at 6 km/s, showing the evolution of the crater and the temperature field in the slab.

examined and digitally photographed with a FEI/Philips CM-20 TEM equipped with a Gatan TEM CCD camera.

III. MOLECULAR DYNAMICS AND EXPERIMENTAL RESULTS

Figure 2 illustrates the evolution of the projectile and the silicon target following the impact of a 20 nm drop at 6 km/s. Each panel shows a slice of atoms in the axis of impact, has a thickness of 0.86 nm, and atoms are colored according to a temperature scale. The projectile penetrates into the substrate producing a crater that reaches a maximum depth of 14 nm at 10 ps, and which stabilizes at a depth of 10.2 nm and diameter of 17.1 nm after several oscillations lasting approximately 35 ps. As the momentum of the projectile's molecules is transferred to the substrate, approximately 97% of its kinetic energy is dissipated within 7.6 ps from impact. During this time, the dissipation is localized in the surrounding area near the crater, increasing the temperature of this region above the melting point (see Fig. 2(c)). This area melts and, due to its very small volume and efficient heat conduction, quenches at a rate near 15.3×10^{12} K/s. At this cooling rate, the liquid phase does not have sufficient time to recrystallize, undergoing a glass transition around 60 ps.

The panels in Fig. 3 show the impact region at the conclusion of the simulations for projectiles with several diameters and velocities. Silicon atoms are colored in red, yellow, and blue to indicate their final phase and phase evolution: red atoms are in the amorphous phase at the end of the simulation; blue atoms are in the crystalline phase at the end of the simulation; yellow atoms are in the crystalline phase at the end of the simulation, but were in the amorphous phase

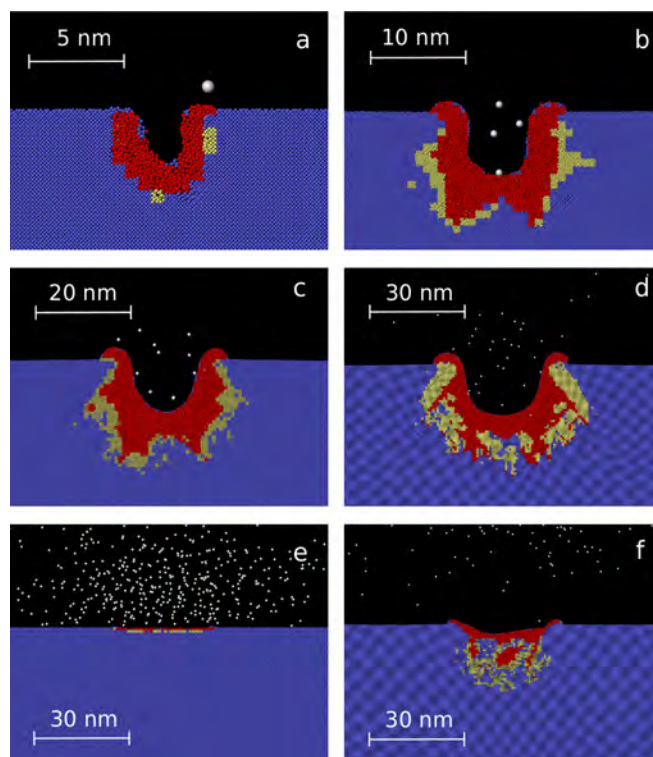


FIG. 3. Cross-sectional images at the end of simulation. Panels (a)–(d) are for projectile diameters of 5 nm, 10 nm, 20 nm, and 30 nm, at impact velocity of 6 km/s. Panels (e) and (f) are for the 30 nm droplet at 2.0 km/s and 3.5 km/s. Projectile molecules are depicted in white; blue atoms represent the Si crystalline phase; red atoms represent amorphous Si areas; and yellow atoms represent crystalline areas that at some previous time were in the amorphous phase.

at some previous time. Panels (a) to (d) show the effect of projectile diameter at an impact velocity of 6 km/s. The impacts produce craters with depths similar to the droplet diameters, and which become more spherical at increasing droplet diameter. At 6 km/s, all projectiles amorphatize a substantial layer surrounding the crater, with average thickness ranging between 2.2 nm and 10.1 nm for the 5 nm and 30 nm droplets, respectively. Panels (e) and (f) are for the 30 nm droplet and velocities of 2.0 and 3.5 km/s. At these lower velocities, the impact produces shallow indentations, and only the first few layers of atoms are rearranged away from the crystalline lattice. In all cases, we observe groups of atoms that at some point, following the impact were in a non-crystalline phase, and which eventually recover the crystalline structure (atoms depicted in yellow). These atoms are located in the interface between the final amorphous and crystalline domains, in regions that during the compression were deformed enough to lose long-range order for a brief period of time but did not melt.

The amorphization of a silicon layer is also observed in nanodroplet impact experiments. Figure 4 shows cross

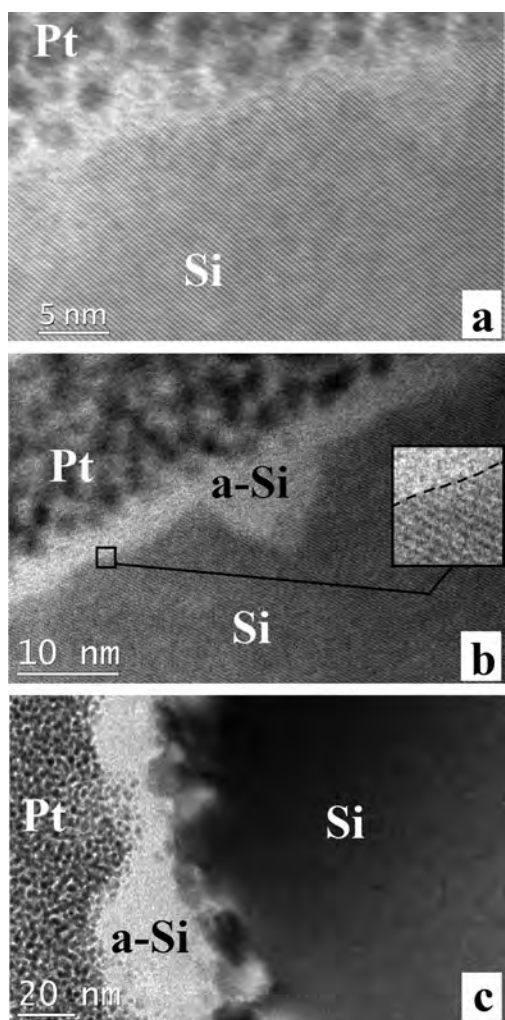


FIG. 4. TEM images of samples bombarded by nanodroplets with acceleration voltages of (a) 4.65 kV, (b) 6.15 kV, and (c) 12.55 kV, and associated impact velocities of 3.00 km/s, 3.45 km/s, and 4.94 km/s. The nanodrops do not significantly alter the crystalline structure at the lowest velocity, and produce amorphous layers at the intermediate and largest velocities.

sectional TEM images of samples bombarded at average velocities of (a) 3.00 km/s, (b) 3.45 km/s, and (c) 4.94 km/s. The spotted regions are platinum layers deposited for protection of the surface during sample processing; crystalline Si shows in the higher magnification images as regions with geometric fringe patterns, and as a dark, homogeneous area at the lowest magnification; and amorphous Si appears as a distinct lighter band sandwiched between the Pt and crystalline Si. The impacts do not significantly alter the crystalline structure at the lowest velocity and produce amorphous layers at the intermediate and largest velocities. The average thickness of the amorphous layer is 3.5 nm at 3.45 km/s, and 25 nm at 4.94 km/s. At 3.45 km/s, the amorphous layer is relatively parallel to the original surface, while it deforms at increasing velocity producing larger amorphous pockets connected by thinner amorphous sections. The increasing surface roughness with impact velocity is consistent with the simulations in Figures 3(d)–3(f), which show how the impact at 2.5 km/s barely modifies the surface of the target, the impact at 3.5 km/s produces a shallow indentation with a thin amorphous layer, and the impact at 6.0 km/s produces a large crater surrounded by an irregular and thick amorphous layer.

Figure 5 shows the dependence of the thickness and volume of the amorphous layer on the projectile's velocity and diameter. Thickness and volume are normalized with the diameter of the projectile and its volume, while a second horizontal axis displays the projectile's molecular kinetic energy, $E_m = m_m v_p^2 / 2$ (m_m is the molecular mass of Emi-Im). The thickness of the amorphous layer is a small fraction of the projectile's diameter for velocities under 3 km/s, it increases to a fraction between 0.29 and 0.34 at 4 km/s, and remains approximately constant at higher velocities. The normalized volume of the amorphous phase is also negligible for impact velocities below 3 km/s, and increases almost linearly with the molecular energy at velocities higher than 3 km/s. The simulations thus indicate that although low velocity impacts randomize the atomic positions in the initial atomic layers of the target, a threshold velocity of approximately 3 km/s is needed to extend the amorphization to atoms that are not in direct contact with the projectile. Furthermore, when the amorphization is significant, the thickness and volume of the amorphous phase scale linearly with the diameter and volume of the projectile. In addition to the simulation results, Fig. 5(a) also displays the thickness of the amorphous layers produced by the beamlet of electro-sprayed nanodroplets (average diameter of 26 nm). The experimental curve matches well the MD simulations: it exhibits a threshold velocity between 3 km/s and 3.45 km/s for triggering the appearance of significant amorphization and shows how the thickness of the amorphous layer increases with impact velocity before settling to a constant value. This constant value is twice as large as what is reproduced by the simulations, a disparity that may be related to the different impact conditions in the experiments: there is a natural variability in the diameter of the electro-sprayed droplets; and the surface of the target in the experiments is modified by multiple impacts with some four droplets typically hitting an area equal to the droplet's cross section. The modeling of the actual, multiple impact problem is not trivial

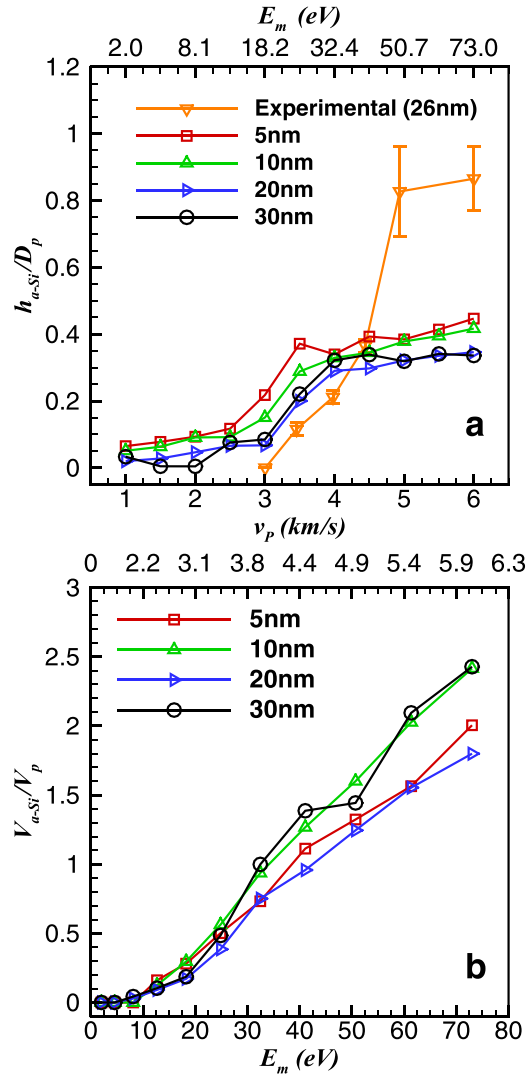


FIG. 5. Thickness of the simulated and experimental amorphous layers, h_{a-Si} , and volume of the simulated amorphous layers, V_{a-Si} , versus projectile diameter and velocity (or equivalently molecular energy). Thickness and volume are normalized with the diameter and volume of the projectile.

because a large number of impacts must be simulated to condition the target. For example, for the 5 and 30 nm projectiles and the targets' dimensions used in this study, we would need to simulate 216 and 96 impacts respectively, randomly distributed throughout the target to reach the experimental projectile dose (our central processing unit (CPU) time for simulating a single impact by a 30 nm droplet exceeds 24 h). In addition, although the SW potential reproduces well the solid and liquid phases of silicon and therefore captures the high pressure melting and the onset of amorphization during quenching, it replicates less accurately the properties of the amorphous phase, and an alternative potential must be used instead to model it.²⁰ We are working on these two issues and plan to discuss the results elsewhere.

During the impact, a fraction of the initial kinetic energy of the projectile is deposited into the target increasing the potential and kinetic energy of the silicon atoms, while the projectile atoms bouncing back from the surface retain the remaining fraction. Furthermore, the kinetic energy of the atoms in the substrate can be decomposed into thermal

and translational components by dividing the target into adjacent cubical volumes (we use a side of 1.69 nm, i.e., three Si unit cell side lengths), computing the average velocity v^k of the atoms for each volume k , and subtracting this average velocity to obtain the temperature T^k , Eq. (1). For a cubical volume with N atoms, its thermal E_{Th}^k and translational energies E_{CM}^k are then given by

$$E_{Th}^k = \frac{3}{2} N k_B T^k, \quad (2)$$

$$E_{CM}^k = \frac{1}{2} N m (v^k)^2. \quad (3)$$

The thermal and translational energies of the target are the sum of E_{Th}^k and E_{CM}^k over all cubical volumes. The energy retained by the projectile molecules and the thermal, translational, and potential energies of the substrate change over time, and a typical evolution can be observed in Fig. 4 of Ref. 10 for a 10 nm projectile impacting at 6.4 km/s. Although near the time of impact the sum of the four energy fractions (that remaining in the projectile molecules, and the thermal, potential, and translational energy of the target) is equal to the initial energy of the system, the total energy of the simulated atoms slowly decays because of thermal conduction with the thermal bath imposed in the boundaries of the target. Figure 4 in Ref. 10 shows how the projectile molecules lose 90% of their initial kinetic energy extremely fast, within 3 ps from the time of impact. By this time, 12%, 18%, and 60% of the projectile's energy has been transferred to the target in the form of translational, thermal, and potential energies, respectively. After peaking at 12 ps, the thermal energy in the slab is gradually lost by heat conduction with the bath, while the potential energy asymptotes to a constant fraction of 24%. The translational energy of the target is only significant during the initial stage of the impact, and becomes negligible by 10 ps. Figure 6 in this article shows the fraction of the projectile's energy transferred to the target, as well as the fraction converted into target's thermal energy, as functions of projectile diameter and velocity. Since the thermal energy and the total energy of the target evolve with time, Fig. 6 plots their maximum values. The diameter of the projectile does not have a significant effect on the total fraction, and has a small influence in the fraction converted into thermal energy (the smaller the diameter, the higher the conversion). On the other hand, the velocity plays a significant role: a mere 15% of the projectile energy is transferred at 1 km/s of which an average of 7% is in the form of thermal energy; both fractions increase with projectile velocity, reaching 70% and 18%, respectively, at 3 km/s; and at velocities beyond 3 km/s, the transferred energy fraction increases asymptotically to a value of 95%, while the fraction converted into thermal energy remains approximately constant at 22%. These results indicate that for impact velocities below 3 km/s, the temperature of the silicon region surrounding the impact increases with the fraction of energy that is transferred. At still higher velocities and as the temperature exceeds the melting point of silicon, the resulting phase change becomes an efficient mechanism for absorbing the energy of the projectile at relatively constant temperature.

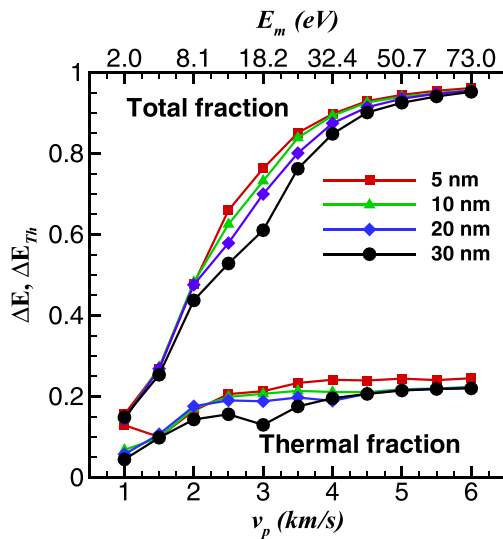


FIG. 6. Total fraction of the projectile's kinetic energy transferred to the target, ΔE , and fraction that is converted into thermal energy, ΔE_{Th} , as functions of the projectile's velocity and diameter.

Since the interactions between liquid molecules, and between liquid molecules and Si atoms, are modeled with a crude two-body ZBL potential, it is worth considering whether the use of a more accurate full atom force field for the interaction between droplet atoms, and between droplet and silicon atoms, would significantly change how much energy of the projectile is transferred to the target. Although we cannot answer this question directly (the number of atoms in the projectiles is too large to consider a full atom force field), we think that the picture described in the previous paragraph is essentially correct. This opinion is based

on: the very large kinetic energy of the projectiles' molecules (e.g., 18.2 eV at 3.0 km/s, 73.0 eV at 6.0 km/s); the comparatively very small value of the ionic bond energy in the molecules of the ionic liquid (a large fraction of the anions and cations are already dissociated at room temperature, and a small fraction of the projectile energy would be needed to dissociate the remaining molecules); and the unlikely generalized decomposition of the covalent bonds joining the atoms in the ions.

Both experiments and simulations show that substantial amorphization only occurs when the impact velocity exceeds a value of approximately 3.0 km/s. The sharp onset of amorphization at this threshold velocity results from the sudden convergence of the temperature and the melting point in the area surrounding the impact. This rapid convergence is caused by the simultaneous increase of the temperature and the reduction of the melting point at increasing impact velocity. To illustrate this, Fig. 7 shows the evolution of the temperature, pressure, melting point, and atomic coordination number near the impact interface, for a 10 nm projectile and four impact velocities. A spherical control volume with a radius of 1.08 nm, containing 280 Si atoms, and centered in the axis of impact 1.2 nm below the surface, is used to compute the thermodynamic paths. All charts show a pressure pulse following the impact with a lag of approximately 1 ps, and with a peak value (4.33 GPa, 6.20 GPa, 10.6 GPa, and 11.23 GPa) correlated with the stagnation pressure of the projectile (3.04 GPa, 4.75 GPa, 6.84 GPa, and 9.31 GPa). The melting point of Si decreases at increasing hydrostatic pressure,^{21,22} and its evolution in Fig. 7 is estimated by inserting the pressure of the control volume in the known relation for the melting curve $T_m(P_H)$.²³ Thus, the impact reduces the

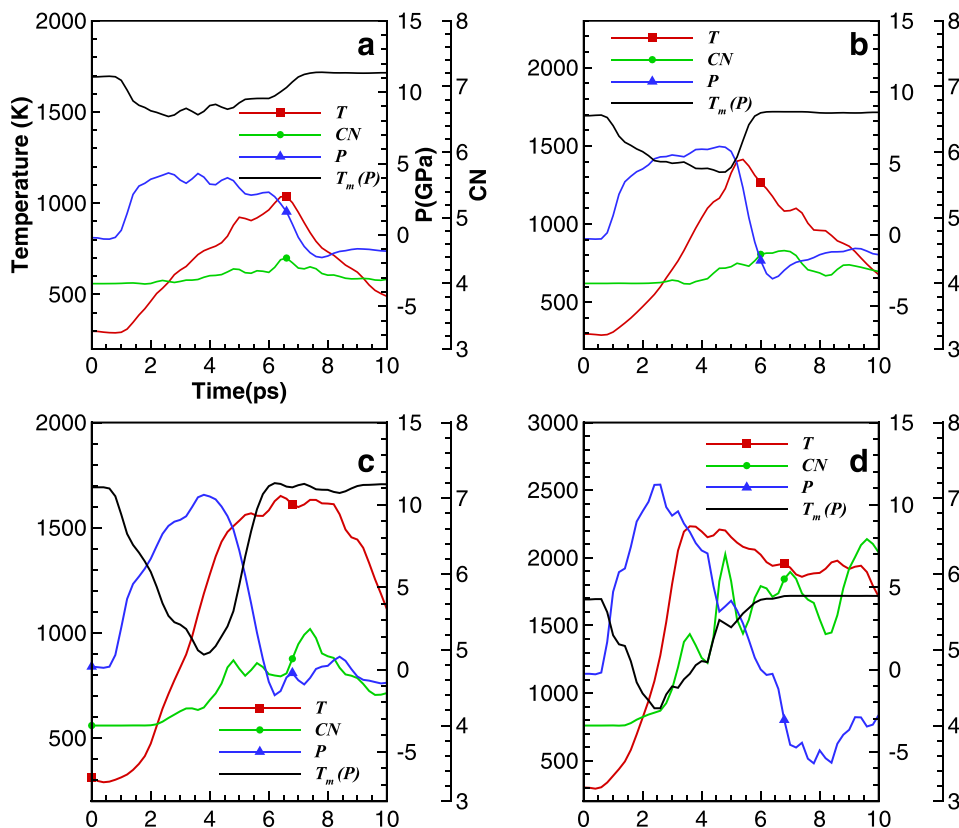


FIG. 7. Evolution of the temperature, coordination number, pressure, and melting point below the surface of impact for the 10 nm projectile at velocities of (a) 2 km/s, (b) 2.5 km/s, (c) 3 km/s, and (d) 3.5 km/s.

melting point from 1685 K to minima of 1475 K, 1332 K, 897 K, and 887 K at increasing impact velocity. At the same time, dissipation and the peak temperature of the control volume increase with impact velocity. Figure 7 illustrates how these two trends sharply reduce the minimum gap between melting point and substrate temperature, finally bringing the temperature above the melting point during an extended period at a velocity of 3.0 km/s. The melting of the solid phase beyond this threshold velocity is most evident in the shift of the coordination number from 4 to a value near 6.5.

IV. CONCLUSION

Molecular Dynamics simulations resolve how the energetic impact of nanodroplets on a silicon target amorphizes the area of impact. The amorphization is a result of the melting and fast quenching of the silicon and is activated at a projectile velocity near 3 km/s. At this velocity, the lowering of the melting point induced by the compression, combined with the increase of the substrate temperature caused by the dissipation of the projectile's energy, trigger the melting of the crystalline phase. As the projectile's velocity exceeds 3 km/s, the thickness of the amorphized layer first increases and then plateaus at about 4 km/s, at a fraction of the projectile's diameter between 0.3 and 0.4, while its volume increases linearly with the projectile's energy. Both the thickness and the volume of the amorphous layer are proportional to the diameter and volume of the projectile. The analysis of experimental samples bombarded with similar electrosprayed nanodroplets confirms the Molecular Dynamics results.

ACKNOWLEDGMENTS

This work was funded by the Air Force Office of Scientific Research, Grant No. FA9550-11-1-0308 and by a

Balsells Fellowship. The authors are grateful for the support of the AFOSR Program Manager Dr. Birkan and the support of Pete J. Balsells.

- ¹D. E. Carlson and C. R. Wronski, *Appl. Phys. Lett.* **28**, 671 (1976).
- ²F. B. Ellis, R. G. Gordon, W. Paul, and B. G. Yacobi, *J. Appl. Phys.* **55**, 4309 (1984).
- ³K. Tanaka, E. Maruyama, T. Shimada, and H. Okamoto, *Amorphous Silicon* (Wiley, New York, 1999).
- ⁴R. A. Street, *Technology and Applications of Amorphous Silicon* (Springer, New York, 2000).
- ⁵J. Yang, A. Banerjee, and S. Guha, *Appl. Phys. Lett.* **70**, 2975 (1997).
- ⁶M. O. Thompson, J. W. Mayer, A. G. Cullis, H. C. Webber, N. G. Chewet, J. M. Poate, and D. C. Jacobson, *Phys. Rev. Lett.* **50**, 896 (1983).
- ⁷W. D. Luedtke and U. Landman, *Phys. Rev. B* **40**, 1164 (1989).
- ⁸M. D. Kluge and J. R. Ray, *Phys. Rev. B* **36**, 4234 (1987).
- ⁹M. Gamero-Castaño, A. Torrents, L. Valdevit, and J.-G. Zheng, *Phys. Rev. Lett.* **105**, 145701 (2010).
- ¹⁰F. Saiz and M. Gamero-Castaño, *J. Appl. Phys.* **112**, 054302 (2012).
- ¹¹S. J. Plimpton, *J. Comput. Phys.* **117**, 1 (1995).
- ¹²J. Samela, J. Kotakoski, K. Nordlund, and J. Keinonen, *Nucl. Instrum. Methods B* **239**, 331 (2005).
- ¹³F. H. Stillinger and T. A. Weber, *Phys. Rev. B* **31**, 5262 (1985).
- ¹⁴J. Q. Broughton and X. P. Li, *Phys. Rev. B* **35**, 9120 (1987).
- ¹⁵J. F. Ziegler, J. P. Biersack, and U. Littmark, *The Stopping and Range of Ions in Solids* (Pergamon Press, New York, 1985).
- ¹⁶S. Ansell, S. Krishnan, J. J. Felten, and D. L. Price, *J. Phys.: Condens. Matter* **10**, L73 (1998).
- ¹⁷T. Moroshita, *Phys. Rev. Lett.* **93**, 055503 (2004).
- ¹⁸S. Sastry and C. A. Angell, *Nature Mater.* **2**, 739 (2003).
- ¹⁹M. Gamero-Castaño and M. Mahadevan, *J. Appl. Phys.* **106**, 054305 (2009).
- ²⁰E. J. Albenze and P. Clancy, *Mol. Simul.* **31**, 11 (2005).
- ²¹*Properties of Crystalline Silicon*, edited by R. Hull (Inspec, London, 1999).
- ²²M. Kaczmariski, O. N. Bedoya-Martínez, and E. R. Hernández, *Phys. Rev. Lett.* **94**, 095701 (2005).
- ²³S. K. Deb, M. Wilding, M. Somayazulu, and P. F. McMillan, *Nature* **414**, 528 (2001).

Amorphization of silicon induced by nanodroplet impact: A molecular dynamics study

Fernan Saiz and Manuel Gamero-Castaño^{a)}

Department of Mechanical and Aerospace Engineering, University of California, Irvine, California 92717, USA

(Received 6 June 2012; accepted 20 July 2012; published online 5 September 2012)

The hypervelocity impact of electrosprayed nanodroplets on crystalline silicon produces an amorphous layer with a thickness comparable to the droplet diameters. The phase transition is puzzling considering that amorphization has not been observed in macroscopic shock compression of silicon, the only apparent difference being the several orders of magnitude disparity between the sizes of the macroscopic and nanodroplet projectiles. This article investigates the physics of the amorphization by modeling the impact of a nanodrop on single-crystal silicon via molecular dynamics. The simulation shows that the amorphization results from the heating and subsequent melting of a thin layer of silicon surrounding the impact area, followed by an ultrafast quenching with cooling rates surpassing 10^{13} K/s. These conditions impede crystalline growth in the supercooled liquid phase, which finally undergoes a glass transition to render a disordered solid phase. The high temperature field near the impact interface is a localized effect. The significantly different temperatures and cooling rates near the surface and in the bulk explain why amorphization occurs in nanodroplet impact, while it is absent in macroscopic shock compression. Since these high temperatures and ultrafast quenching rates are likely to occur in other materials, nanodroplet impact may become a general amorphization technique for treating the surfaces of most crystalline substrates. © 2012 American Institute of Physics. [<http://dx.doi.org/10.1063/1.4748177>]

I. INTRODUCTION

Electrospraying in the cone-jet mode is an atomization technique with a singular ability for producing charged nanodroplets with narrow distributions. This technique is best known for its use in electrospray mass spectrometry.¹ It is also employed in combustion, electric propulsion, nanoparticle generation, and other applications requiring fine atomization.^{2–4} An electrospray can be operated in vacuum and, when complemented with electrostatic acceleration, may be used as a source of energetic projectiles in the size range between approximately 1 nm and 1 μ m. The impact of projectiles larger than 1 μ m (commonly referred to as the hypervelocity impact problem) and that of atomic, molecular, and cluster ions (i.e., sizes below some 3 nm) have been studied in detail.^{5,6} Conversely, the substantial intermediate size range remains largely unexplored due to the absence of projectiles, a problem that can now be resolved with the electrospray source. Recent research has shown that the impact of electrosprayed nanodroplets on materials such as silicon, silicon carbide, and boron nitride is characterized by sputtering yields (number of target atoms ejected per molecule in the projectile) of order one, and by diverse phenomena in the bombarded surface such as the appearance of craters that are orders of magnitude larger than the projectiles, extremely smooth surfaces, and amorphization.^{7,8} These phenomena depend on the projectile's velocity and diameter, the projectile dose, and the nature of the target.

The impact of electrosprayed nanodroplets on single-crystal silicon is known to amorphatize a surface layer of approximately 20 nm.⁸ Using drops with an average diameter of 29 nm, Gamero *et al.* have reported amorphization at projectile velocities exceeding 4.6 km/s. The interface between the amorphous and crystalline phases displays significant roughness in the scale of a few tens of nanometers, likely resulting from the discrete nature of the impacts of similarly sized projectiles. The amorphization of a region comparable in size to the projectile does not occur during the impact of macroprojectiles, which invariably leave the recovered silicon target in a polycrystalline state.⁹ The simplest explanation for the observed amorphization is based on a glass transition: in this scenario, the temperature of the shocked substrate rises above its melting point T_m , which in the case of silicon has the favorable property of decreasing at increasing pressure; the neighborhood of the impact then melts and, given the small thermal diffusion time of this nanometric region, cools down at a rate that prevents the regrowth of the crystalline phase; finally the temperature of the undercooled liquid descends below the glass transition temperature forming an amorphous solid.¹⁰ In fact similar thin amorphous layers have been obtained by melting and fast quenching of crystalline silicon during pulsed laser irradiation.¹¹ However appealing this amorphization mechanism does not seem to be at play during nanodroplet impact, because the temperature of shocked silicon remains well below the melting point. Instead, as the strength of the shock increases, cubic-diamond silicon undergoes a high pressure crystalline transition to its metallic beta-tin phase.¹² With this in mind, and to justify the very different outcomes of macroscopic and nano

^{a)}Author to whom correspondence should be addressed. Electronic mail: mgamero@uci.edu.

projectile impacts, Gamero *et al.* put forward two mechanisms based on pressure-induced amorphization and the very fast pressurization and thermal transients typical of nanodroplet impact.⁸ However, these explanations are hypothetical at best, and solving a first-principles model is needed to understand the physics behind the amorphization.

Molecular dynamics (MD) is a powerful technique for simulating the evolution of small systems, both in thermodynamic equilibrium as well as in non equilibrium situations. It has been used to describe the impact of larger nanopropellers^{13,14} and that of smaller cluster and molecular ions.¹⁵ This computational technique integrates the equations of motion of an ensemble of particles coupled by interacting potentials. The calculated positions and momenta are used to compute ensemble averages such as temperature, pressure, or density and hence to obtain the thermodynamic state of the system. In this work, we use MD to simulate the impact of a nanodroplet on a (100) Si target, modeled by the semi-empirical Stillinger-Weber (SW) potential.¹⁶ This potential reproduces well the solid and liquid phases of silicon and predicts accurately the normal melting point, $T_m = 1690$ K versus an experimental value of 1685 K, an excellent agreement important for this study.¹⁷ Furthermore, the SW potential has reproduced the amorphous state of silicon quenched from its melt¹⁸ and has been used to study its undercooled liquid phases down to the final glassification.¹⁹

The overall goal of this article is to understand the amorphization mechanism in nanodroplet impact. Following this introduction, Sec. II outlines the simulation conditions, introduces formulae for computing thermodynamic parameters of interest, and describes the basic phenomena accompanying the impact of a 10 nm projectile. Section III shows how the projectile, impacting at a velocity of 6.4 km/s, generates an amorphous Si layer with a thickness of approximately 4 nm. The amorphization does follow a glass transition, with the unexpected melting resulting from the significant dissipation of the projectile's mechanical energy preceding the formation of a shock wave.

II. SIMULATION METHODS

We use the large-scale atomic/molecular massively parallel simulator package, LAMMPS,²⁰ to model the impact of a liquid droplet on a (100) Si target. The droplet has a diameter of 10 nm and is made of 1224 identical spheres distributed in a hexagonal close-packed arrangement. Each sphere has a radius of 0.422 nm, a mass of 391.31 amu, and represents a molecule of the ionic liquid 1-ethyl-3-methylimidazolium bis (trifluoro-methylsulfonyl) imide, $C_8H_{11}F_6N_3O_4S_2$, used in the nanodroplet impact research of Ref. 8. The target is a slab 30.55 nm in the impact direction (y), 48.88 nm \times 48.88 nm wide in the lateral directions (x and z), and is filled with 4 390 200 Si atoms in the standard cubic-diamond arrangement. The impact direction is aligned with the [100] direction of the crystal. The interactions between liquid molecules and between liquid molecules and silicon atoms are modeled with a Ziegler-Biersack-Littmark two-body potential,²¹ frequently used in impact problems of dissimilar materials;^{22–24}

$$U(r) = \frac{Z_1 Z_2}{r} \varphi(r), \quad (1)$$

where Z_1 and Z_2 are the atomic number of the sphere (198, computed as the sum of the atomic numbers of its atomic constituents) and silicon, r is the interatomic distance between two particles, and $\varphi(r)$ is the empirical screening potential function

$$\varphi(r) = \sum_{i=1}^4 a_i e^{-b_i r/a_U}, \quad (2)$$

with coefficients $a_1 = 0.1818$, $a_2 = 0.5099$, $a_3 = 0.2802$, $a_4 = 0.02817$, $b_1 = 3.2$, $b_2 = 0.9423$, $b_3 = 0.4028$, $b_4 = 0.201$.²¹ a_U is defined as

$$a_U = \frac{0.854 a_B}{Z_1^{0.23} + Z_2^{0.23}}, \quad (3)$$

where a_B is the Bohr radius (0.539177 Å). The cutoff distance for the interactions between molecule-molecule and silicon-molecule is set to 0.803 nm, i.e., at 95% of the diameter of the ionic liquid molecule. The usual parametrization of the SW potential is used for the interaction between silicon atoms.¹⁶

The droplet is directed towards the target with an initial velocity of 6.4 km/s and a temperature of 0 K. At this velocity, the stagnation pressure and the kinetic energy per molecule are 31.33 GPa and 81.82 eV. The faces of the slab in the y direction are two free surfaces, while periodic boundary conditions are imposed in the x and z directions. All faces of the slab except for the top free surface are in contact with a Berendsen thermostat at 293 K, to help prevent the reflection of shock waves arriving at the domain boundaries.²⁵ The simulation uses a 1 fs integration time step and is run for 70 ps. By the time, the simulation is stopped the dynamic phenomena produced by the impact have died out, and the temperature field of the slab is almost uniform and near the temperature of the thermostat.

Figure 1 shows silicon atoms and liquid molecules in a slice bounded by planes $z = -0.5$ nm and $z = 0.5$ nm, at different times of the simulation. Silicon atoms with a potential energy higher than -4.10 eV are displayed in blue, while those with lower values are shown in red. Since the average atomic potential energy for the cubic-diamond phase is -4.29 eV, the blue areas are indicative of atomic arrangements that significantly depart from the crystalline structure. In fact, the average potential energy for the amorphous phase is -4.10 eV,¹⁸ and therefore blue is indicative of highly disordered, maybe even amorphous configurations. The frames show how the projectile penetrates the target, carving a crater with a maximum volume at about 5 ps. The surface of the crater then contracts and expands several times, relaxing to a final volume with a depth of 9.8 nm and a maximum width of 7.1 nm. A number of Si atoms are ejected from the slab.

The temperature at the position of an atom j is computed by the usual average of the kinetic energies of neighboring atoms

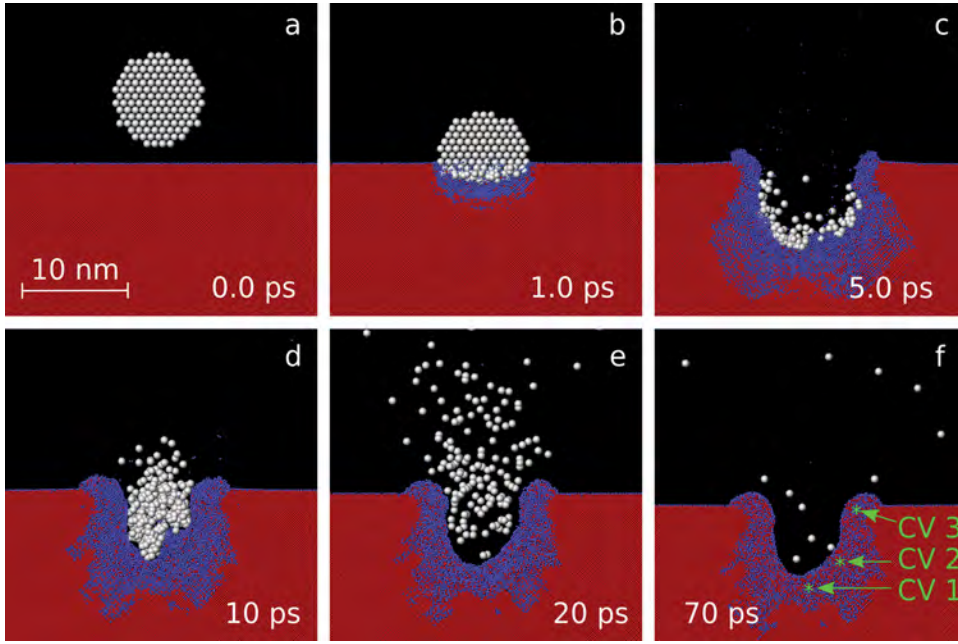


FIG. 1. Cross-sectional images of the impact at 0 ps, 1 ps, 5 ps, 10 ps, 20 ps, and 70 ps. White spheres represent the molecules of the projectile, while silicon atoms are depicted in blue or red depending on whether their potential energies are higher or lower than -4.10 eV.

$$T(\mathbf{x}^j) = \frac{m \sum_{i=1}^N (\mathbf{v}^i - \langle \mathbf{v}^i \rangle) \cdot (\mathbf{v}^i - \langle \mathbf{v}^i \rangle)}{2k_B N}, \quad \|\mathbf{x}^i - \mathbf{x}^j\| \leq 1.08 \text{ nm}, \quad (4)$$

where k_B is the Boltzmann's constant, m is the mass of a silicon atom, and \mathbf{x} and \mathbf{v} are the position and velocity vectors of individual atoms. All N atoms within a spherical control volume with a radius of 1.08 nm and centered in atom j are included in the average. Typically, there are some 280 atoms inside the control volume, a sufficient number to obtain reliable statistics. We have also confirmed that, with the exception of atoms near the moving shock wave generated by the impact, the velocity distributions inside these control volumes do not depart significantly from a Maxwellian, and therefore it is a good approximation to consider that the atoms in the slab are in partial equilibrium. Figure 2 shows

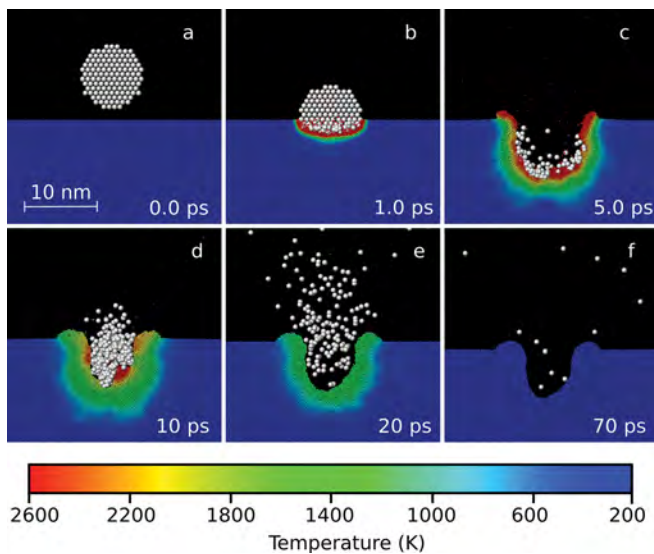


FIG. 2. Temperature field in the slab at 0 ps, 1 ps, 5 ps, 10 ps, 20 ps, and 70 ps. The temperature in an area surrounding the impact remains above the melting point for over 10 ps.

the temperature field in the slab for the frames in Fig. 1. Upon impact, a substantial amount of energy is dissipated in the contact region, raising its temperature above several thousand degrees (see 5 ps frame). This evolving layer surrounding the crater remains above the normal melting point for over 10 ps, before cooling down and equilibrating with its surroundings.

The virial stress for a single atom j is computed by the formula

$$\sigma_{\alpha\beta}^j = m v_{\alpha}^j v_{\beta}^j + \frac{1}{2} \sum_{i \neq j} \left(-\frac{1}{r} \frac{\partial U}{\partial r} \right) r_{\alpha} r_{\beta} \Big|_{r=r_{ji}}, \quad (5)$$

where α and β refer to the x , y , and z Cartesian coordinates. The summation is done over all atoms inside the range of the potential. Similarly to the temperature, we define the stress at the position of atom j as the average of the virial stresses of all atoms within a spherical control volume centered in atom j , divided by the volume of the sphere.¹⁴ Figure 3

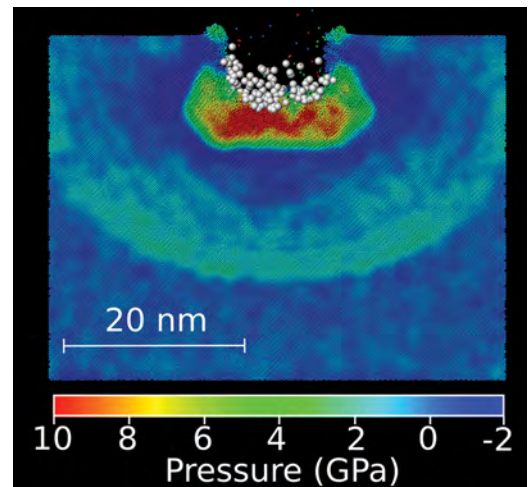


FIG. 3. Pressure field at 3.5 ps. A shock wave moves away from the point of impact at a speed of 8.31 km/s. The front at the axis of impact is located 26 nm below the surface.

shows the pressure field in the slab at 3.5 ps. The area at the bottom of the crater is decelerating the projectile and therefore is highly compressed, while a nearly spherical elastic wave moves away from the point of impact. The velocity of the front along the axis of impact is 8.31 km/s, slightly below the experimental sound speed in the [100] direction (8.43 km/s at room temperature and 1 atm). Although not shown in this figure the jump in temperature across the shock wave averages to 9 K, a marginal increase consistent with the nearly isentropic nature of shock compression.

Figure 4 shows the evolution of the total thermal, translational, and potential energies of the slab, and the total kinetic energy of the projectile, $E_{Th}(t)$, $E_{CM}(t)$, $E_P(t)$, and $E_K(t)$, respectively. They are computed by adding the respective energies of all atoms in the slab and in the projectile; the thermal energy of an atom j is $k_B T(\mathbf{x}^j)$, where the temperature is defined by Eq. (4). The average velocities of the 1.08 nm spherical control volumes are used to compute the translational energy. To illustrate better how the energy is transferred to the slab the thermal, translational, and potential energies are offset by their initial values preceding the impact, and normalized by the initial projectile's energy (1.03×10^5 eV). The projectile molecules lose 90% of their initial kinetic energy within 3 ps. By this time, 12%, 18%, and 60% of the projectile's energy has been transferred to the slab in the form of translational, thermal and potential energies, respectively. After peaking at 12 ps, the thermal energy in the slab is gradually lost by heat conduction with the surrounding thermal bath, while the potential energy asymptotes to a constant fraction of 24%. This potential energy excess is mostly distributed in the region near the impact, where the atomic arrangement is highly disordered by the end of the simulation.

III. AMORPHIZATION MECHANISM

Figure 1(f) shows the centers of three control volumes with radii of 1.08 nm, at the end of the simulation. The control volumes are located near the crater surface, in the layer where the atomic structure clearly departs from the crystal-

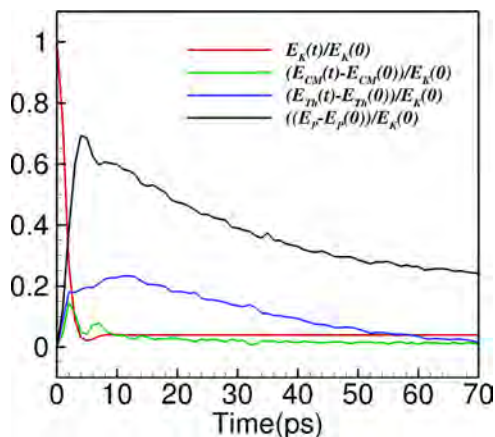


FIG. 4. Total thermal (E_{Th}), translational (E_{CM}) and potential (E_P) energies of the slab, and total kinetic energy of the projectile (E_K), as functions of time. The thermal, translational, and potential energies are offset by their initial values preceding the impact, and normalized by the initial projectile's energy (1.03×10^5 eV).

TABLE I. Thermodynamic and structural information near the point of impact at 70 ps (CV1, CV2 and CV3). T , P_E , ρ , CN , $\langle\theta\rangle$ and $\sigma(\theta)$ stand for temperature, average potential energy, density, average coordination number, average bond angle and standard deviation of the bond angles. a-Si (SW) and g-Si (SW) are amorphous and glassy phases of silicon from molecular dynamics simulations using the Stillinger-Weber potential,¹⁸ a-Si (exp) is for a vapor deposition sample,²³ and c-Si (SW) is for the crystalline phase in the slab before the impact.

Sample	$T(K)$	$P_E(eV)$	$\rho(kg/m^3)$	CN	$\langle\theta\rangle(deg)$	$\sigma(\theta)(deg)$
CV1	376	-4.04	2439	4.49	107.5	19.3
CV2	355	-4.06	2482	4.63	106.5	20.8
CV3	395	-4.05	2456	4.45	107.2	19.6
a-Si (SW)	300	—	2345	4.21	107.8	16.0
g-Si (SW)	300	-4.10	2477.25	4.66	106.6	22.6
a-Si (exp)	300	—	2395.67	3.95	—	—
c-Si (SW)	288	-4.30	2413	4	109.5	2.9

line arrangement. We will compute several parameters for each control volume to prove that a disordered, non-crystalline phase results from the impact. Table I collects the average potential energy, density, average coordination number, and the average and standard deviation of the bond angle distribution of each control volume. These parameters are good indicators of the thermodynamic state and allow a comparison with published values of disordered and crystalline Si phases, also listed in the Table I. The experimental amorphous phase, a-Si (exp), is a sample obtained by vapor deposition.²⁶ The data referred to as a-Si (SW) and g-Si (SW) are for amorphous and glassy phases resulting from fast quenching at different cooling rates and obtained via molecular dynamics using the Stillinger-Weber potential.¹⁸ Further structural information is given in Fig. 5 in the form of radial distribution functions. As can be seen in Table I, and especially in Fig. 5, the control volumes near the area of impact are in a disordered state nearly identical to the glassy g-Si (SW) phase. Although clearly non-crystalline, it was early recognized that the structure of g-Si (SW) differed from that of amorphous silicon in its higher average coordination number, and the appearance of a near-side shoulder on the second peak of the radial distribution (see shoulder at 0.33 nm in the

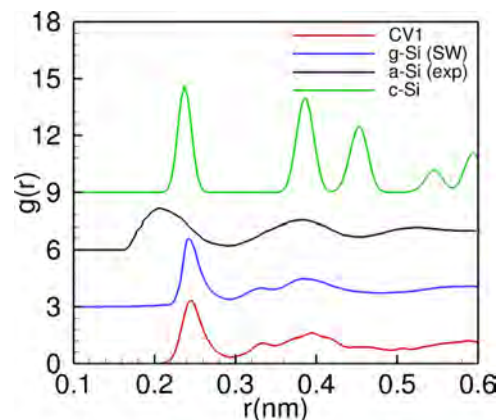


FIG. 5. Radial distribution functions for the atoms in control volume CV1, the glassy state g-Si (SW), the amorphous phase a-Si (exp), and crystalline silicon.

CV1 and g-Si (SW) curves in Fig. 5). Although this disagreement was initially explained in terms of the inadequacy of the SW potential for reproducing the glass transition of silicon, Luedtke and Landman found that it was rooted on kinetics since they were able to obtain a-Si (SW), with properties nearly identical to experimental amorphous phase, by enforcing a slower cooling rate (approximately 2×10^{11} K/s). In the paragraph below we show that the undercooled liquid phase resulting from the impact is quenched at rates exceeding 10^{13} K/s, and therefore it is not surprising that the final solid is in the glassy g-Si (SW) state.

We next follow the trajectory of the central atom in control volume CV1 and quantify the thermodynamic state of the neighborhood of this moving atom to identify the mechanism responsible for the overall crystalline to amorphous phase transition. Figure 6 shows the evolution of the temperature, pressure, and coordination number of the moving control volume. It also displays a melting point curve, which is a function of the hydrostatic pressure, $T_m(P_H)$.²⁷ Although the pressure in the slab is not hydrostatic we will use its value to estimate the melting point. The center of the control volume is initially 7.72 nm below the free surface, and it takes 1.0 ps for changes associated with the impact to reach this position. At this time, the pressure and the temperature start to increase, and rapidly plateau around 5.2 GPa and 350 K at 1.8 ps. During this initial compression, the material remains in the cubic-diamond arrangement, as seen from its constant coordination number of 4. Additional confirmation is provided by the radial distribution function at 1.8 ps in Fig. 7, which has the isolated peaks of the crystalline arrangement.

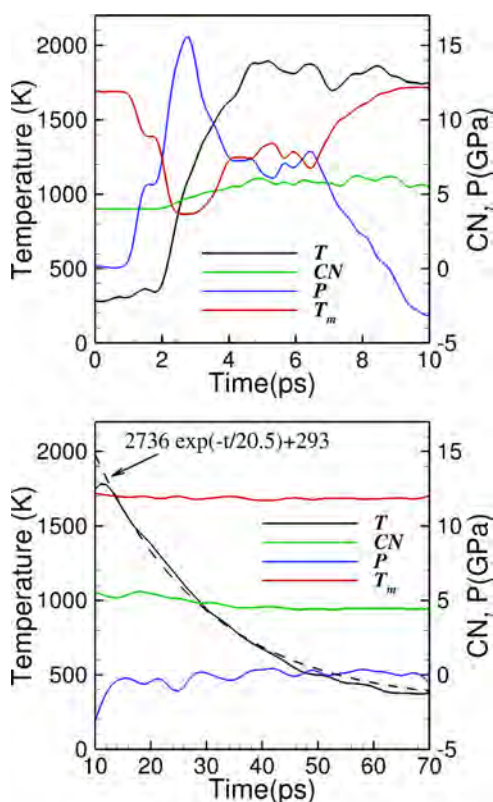


FIG. 6. Temperature, coordination number, pressure, and melting point in the control volume CV1 as functions of time.

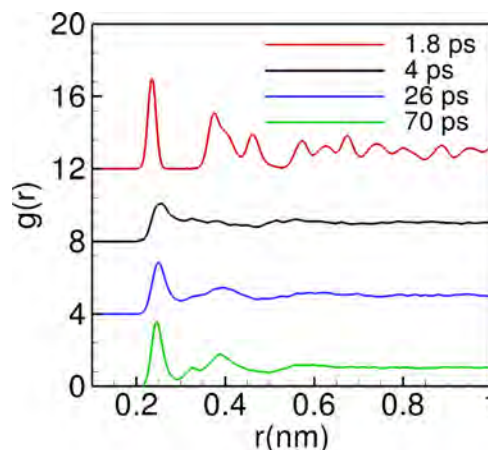


FIG. 7. Radial distribution functions for the atoms in control volume CV1 at 1.8 ps, 4 ps, 26 ps, and 70 ps.

This initial phase is followed by a sustained increase of the temperature, pressure, and coordination number. At about 2.2 ps, the temperature exceeds the melting point, and the control volume starts to undergo a solid to liquid phase transition. This is confirmed by the coordination number fluctuating around a value of 6 and the disappearance of long-range order in the radial distribution function at 4.0 ps. Although not shown in these figures the simulation captures other signs typical of the liquid phase such as the almost complete elimination of shear stresses, and the near hydraulic nature of the pressure. It is worth noting that although the pressure peaks at 15 GPa around 2.3 ps and rapidly decays afterward, the temperature does not reach its maximum value of 1900 K until approximately 8 ps, once the control volume is largely unloaded. From this point on the temperature decays at a rate well fitted by the exponential law $T(K) = 2736 \exp(-t/20.5) + 293$. The cooling rates are as high as 6.8×10^{13} K/s at the normal melting point and 3.7×10^{13} K/s at the glass transition temperature of 1060 K.¹⁹ It is worth noting that these cooling rates exceed by over four orders of magnitude the typical value of 10^9 K/s needed to prevent the regrowth of the crystalline phase.¹¹ As the control volume cools down the second coordination shell at 0.4 nm begins to develop (see radial distribution function at 26 ps, $T = 1060$ K), signaling the onset of glassification. Finally at 70 ps and a temperature of 376 K, the second coordination shell is well resolved, while all other long range peaks remain suppressed, and the radial distribution curve is identical to that of the glassy g-Si (SW) phase.

Although the hypervelocity impacts of a nanodroplet and macroscopic projectiles are similar problems, it is apparent that the steady shock wave theory commonly used to interpret the latter cannot predict the observed amorphization: the temperature increases only modestly behind a steady shock front, e.g., as low as a few tens of degrees for a pressurization of 15 GPa in silicon,²⁸ which is clearly insufficient to melt the solid phase. Figures 3 and 4 offer clues to the unexpected difference. Figure 3 shows how the impact does generate a shock wave, which is fully developed by the time it travels 26 nm into the slab. The changes in thermodynamic variables, particle velocity, and stress across the shock

are consistent with those for an elastic wave. On the other hand, it is apparent that near the impact the standard jump conditions across a steady shock cannot be fulfilled because basic assumptions such as the homogeneity of the material and the existence of a shock wave travelling at constant speed break down. It appears that there is an initial zone in the substrate where the non uniform momentum exchange between projectile molecules and silicon atoms is homogenized, setting up the conditions required for the development of the steady shock wave. Figure 4 indicates that this homogenization is accompanied by the dissipation of approximately 23% of the projectile's kinetic energy into thermal energy, which is ultimately responsible for the melting of the crystal.

In summary, the simulation shows that upon impact of a 10 nm projectile 23% of its kinetic energy is dissipated into the silicon slab near the point of contact, melting a layer with a thickness of a few nanometers. This layer then cools down at rates exceeding 10^{13} K/s, far surpassing the typical value of 10^9 K/s known to prevent recrystallization. Under such quenching conditions, the undercooled liquid must solidify as an amorphous phase, regardless of whether the fast kinetics prevent the Stillinger-Weber potential from reproducing a physical amorphous phase. The high dissipation of kinetic energy within a short distance from the impact and the ultrafast quenching phenomena are not restricted to silicon substrates, and therefore this technique should be able to amorphatize thin surface layers in other crystalline materials having lower or similar melting points, under cold bulk conditions.

ACKNOWLEDGMENTS

This work was supported by the Air Force Office Of Scientific Research, Grant No. FA9550-11-1-0308, and by a Balsells Fellowship. The authors are grateful for their support.

- ¹J. B. Fenn, M. Mann, C. K. Meng, S. K. Wong, and C. M. Whitehouse, *Science* **246**, 64 (1989).
- ²I. G. Loscertales, A. Barrero, I. Guerrero, R. Cortijo, M. Marquez, and A. M. Gañán-Calvo, *Science* **295**, 1695 (2002).
- ³D. C. Kyritsis, S. Roychoudhury, C. S. McEnally, L. D. Pfefferle, and A. Gomez, *Exp. Thermal Fluid Sci.* **28**, 763 (2004).
- ⁴M. Gamero-Castaño, *J. Propul. Power* **20**, 736 (2004).
- ⁵I. Yamada and N. Toyoda, *Surf. Coat. Technol.* **201**, 8579 (2007).
- ⁶L. D. Libersky, A. G. Petschek, T. C. Carney, J. R. Hipp, and F. A. Allahdadi, *J. Comput. Phys.* **109**, 67 (1993).
- ⁷M. Gamero-Castaño and M. Mahadevan, *J. Appl. Phys.* **106**, 054305 (2009).
- ⁸M. Gamero Castaño, A. Torrents, L. Valdevit, and J.-G. Zheng, *Phys. Rev. Lett.* **105**, 145701 (2010).
- ⁹H. Kishimura and H. Matsumoto, *J. Appl. Phys.* **103**, 023505 (2008).
- ¹⁰D. Turnbull, *Contemp. Phys.* **10**, 473 (1969).
- ¹¹M. O. Thompson, J. W. Mayer, A. G. Cullis, H. C. Webber, N. G. Chewet, J. M. Poate, and D. C. Jacobson, *Phys. Rev. Lett.* **50**, 896 (1983).
- ¹²D. C. Swift, G. J. Ackland, A. Hauer, and G. A. Kyrala, *Phys. Rev. B* **64**, 214107 (2001).
- ¹³J. Samela and K. Nordlund, *Phys. Rev. Lett.* **101**, 027601 (2008).
- ¹⁴P. S. Branicio, R. K. Kalia, A. Nakano, P. Vashishta, F. Shimajo, and J. P. Rinob, *J. Mech. Phys. Solids* **56**, 1955 (2008).
- ¹⁵N. Winograd, Z. Postawa, J. Cheng, C. Szakal, J. Kozole, and B. J. Garrison, *Appl. Surf. Sci.* **252**, 6836 (2006).
- ¹⁶F. H. Stillinger and T. A. Weber, *Phys. Rev. B* **31**, 5262 (1985).
- ¹⁷J. Q. Broughton and X. P. Li, *Phys. Rev. B* **35**, 9120 (1987).
- ¹⁸W. D. Luedtke and U. Landman, *Phys. Rev. B* **40**, 1164 (1989).
- ¹⁹S. Sastry and C. A. Angell, *Nature Mater.* **2**, 739 (2003).
- ²⁰S. J. Plimpton, *J. Comput. Phys.* **117**, 1 (1995).
- ²¹J. F. Ziegler, J. P. Biersack, and U. Littmark, *The Stopping and Range of Ions in Solids* (Pergamon, New York, 1985).
- ²²S. Valkealahti and R. M. Nieminen, *Nucl. Instrum. Methods B* **18**, 365 (1986).
- ²³E. Holmström, J. Samela, and K. Nordlund, *Europhys. Lett.* **96**, 16005 (2011).
- ²⁴T. Aoki, T. Seki, S. Ninomiya, and J. Matsuo, *Surf. Coat. Technol.* **201**, 8427 (2007).
- ²⁵J. Samela, J. Kotakoski, K. Nordlund, and J. Keinonen, *Nucl. Instrum. Methods B*, **239**, 331 (2005).
- ²⁶P. Evans, G. Devaud, T. Kelly, and Y.-W. Kim, *Acta Metall. Mater.* **38**, 719 (1990).
- ²⁷E. G. Ponyatovsky and O. I. Barkalov, *Mater. Sci. Rep.* **8**, 147 (1992).
- ²⁸S. D. Gilev and A. M. Trubachev, *J. Phys.: Condens. Matter* **16**, 8139 (2004).

The Effect of the Molecular Mass on the Sputtering by Electrospayed Nanodroplets

Rafael Borrajo-Pelaez and Manuel Gamero-Castaño[†]

*Department of Mechanical and Aerospace Engineering, University of California, Irvine,
California, 92697, USA*

ABSTRACT

Energetic bombardment of covalently bonded materials by electrospayed nanodroplets causes sputtering and topographic changes on the surface of the target. This work investigates the influence of the projectile's molecular mass on these phenomena by sputtering single-crystal silicon wafers with a variety of liquids and acceleration voltages. In particular we electro spray formamide and the ionic liquids ethylammonium nitrate (EAN), 1-ethyl-3-methylimidazolium tetrafluoroborate (EMI-BF₄), 1-ethyl-3-methylimidazolium bis(trifluoromethylsulfonyl) imide (EMI-Im), triethylsulfonium bis(trifluoromethylsulfonyl) imide (TES), and trihexyltetradecylphosphonium bis(2,4,4-trimethylpentyl) phosphinate (TPP), which have molecular masses of 45.0, 108.1, 198.0, 391.3, 399.4 and 773.3 amu respectively. The electrospays are characterized via time of flight to determine the charge to mass ratio of the nanodroplets which, together with the acceleration voltage, yield the impact velocity, the stagnation pressure, and the molecular kinetic energy of the projectile. The estimated range of

[†] Corresponding author, mgameroc@uci.edu

droplet diameters is 20-79 nm, while the impact velocity, the stagnation pressure and the molecular kinetic energy range between 2.9-10 km/s, 4.7-63 GPa, and 2.1-98 eV. The damage on the surface of the targets strongly depends on the molecular mass of the projectile: the formamide and EAN nanodroplets, having the lowest molecular masses, sputter significantly less and produce nanometric indentations and low surface roughness, the latter increasing moderately with stagnation pressure; in contrast, the roughness caused by the impacts of droplets with larger molecular mass exhibits a characteristic non-monotonic behavior. In the latter case the roughness increases with stagnation pressure up to values several times larger than for formamide and EAN, and the surface is dominated by micron-sized craters orders of magnitude larger than the projectiles; furthermore the roughness peaks at a critical stagnation pressure and decreases sharply beyond this point. The sputtering yield by nanodroplets with high molecular mass follows a similar trend, with a maximum located at the same critical stagnation pressure. The maximum sputtering yields for formamide, EAN, EMI-BF₄, EMI-Im, TES, and TPP are 0.20, 0.75, 1.20, 2.80, 4.00 and 2.90 silicon atoms per molecule in the projectile. These trends indicate that despite their rather large diameters, the sputtering by electrosprayed nanodroplets is intrinsically a molecular scale phenomenon not amenable to modeling with a continuum formulation.

I. INTRODUCTION

Physical sputtering is used in surface engineering and surface analysis applications such as ion beam milling, focused ion beams, sputtered deposition, ion etching and secondary ion mass spectrometry. The mass of an atomic ion plays an important role in determining the sputtering yield, and generally on the phenomenology of the impact.¹ Light projectiles directed towards a strongly bonded material penetrate deep into the target, exchanging momentum with the atoms encountered along its path which in turn interact with other atoms. These collisions may transfer enough energy to near-surface atoms to overcome the surface binding potential, ultimately escaping the surface. Light projectiles interact with few of the atoms in the neighborhood of its track, giving rise to the so-called linear collision cascade sputtering.² In contrast the penetration range of heavy atomic ions, molecular ions and gas cluster ions is much shorter, producing shallow layers of atoms with high energy densities, larger numbers of atoms capable of overcoming the surface potential, and ultimately non-linear and enhanced sputtering.³ Besides enhanced sputtering yield, the distinct phenomenology derived from the short penetration range and high energy density deposition includes surface cleaning and smoothing, low energy ion implantation, and the ability to desorb intact macromolecules from organic samples for secondary ion mass spectrometry.^{4,5} Although these beneficial features are correlated with the size of the projectile, the study of size effects has been restricted to diameters below a few nanometers, i.e. to the largest gas cluster ions that can be accelerated to hypervelocities by practical acceleration voltages. For example, the diameter of a large Ar_{2000}^+ gas cluster ion is 5.6 nm.

The recent introduction of electrosprayed nanodroplets has extended the diameter range of projectiles for ion beam applications.⁶ The electrohydrodynamic atomization of liquids into charged nanodroplets generates projectiles with narrow diameter distributions, average diameters controllable from a few nanometers to tens of microns, and charging levels near the maximum set by the Rayleigh limit.⁷ In addition, a great variety of liquids with different chemical compositions and molecular masses can be electrosprayed to produce nanodroplets. No other ion source provides comparable control of both the projectile size and the molecular mass. Nanodroplets of the ionic liquid EMI-Im have been used to sputter a variety of semiconductor materials such as single crystal Si, SiC, InAs, InP, Ge, GaAs, GaSb and GaN, and polycrystalline B₄C.^{8,9} The associated sputtering yields, defined as the average number of target atoms ejected per projectile's molecule, depend on the velocity of the projectile and the composition of the target. Values as high as 2.2 and 1.9 were recorded for GaN and SiC, two materials notoriously hard and inert. The associated sputtering rates of 630 and 220 nm/min are significantly higher than what is possible with ion beam milling, and similar to reacting ion etching rates for Si and SiC.^{10,11} In addition, nanodroplet bombardment is known to amorphize the surface of silicon targets.¹² The amorphization results from the melting and fast quench of a thin layer surrounding the impact area.¹³ The influence of the projectile's diameter and velocity on the amorphization phenomenon has been studied with molecular dynamics, and its results compared with experimental measurements, showing that the velocity plays a more relevant role than the diameter.¹⁴

The diameters of the EMI-Im nanodroplets used in the research referenced above range between 24 and 35 nm. Given the much smaller size of the EMI-Im molecule and the large number of them present in the projectile (e.g. 52,500 molecules in a 35 nm projectile), it is worth

considering whether nanodroplet sputtering is the result of large-scale continuum phenomena or, alternatively, is intrinsically tied to molecular collisions and can only be described by atomistic models. For example, it is well-known that the simultaneous and associated phenomenon of cratering undergoes the transition from atomistic to macroscopic behavior at relatively small projectile diameters, e.g. between 3 and 7 nm in the case of gold on gold impact.¹⁵ This article will address this question, which is important for both obtaining a good understanding of the physics of this problem and to decide what type of model, continuum or atomistic, is most effective to simulate it.

The main goal of this article is to study the effect of the nanodroplet's molecular mass on the sputtering of single-crystal silicon, and on the topography of the resulting surfaces. We cover a broad range of molecular masses, between 45 and 773 amu, by electrospraying formamide and the ionic liquids ethylammonium nitrate (EAN), 1-ethyl-3-methylimidazolium tetrafluoroborate (EMI-BF₄), 1-ethyl-3-methylimidazolium bis(trifluoromethylsulfonyl) imide (EMI-Im), triethylsulfonium bis(trifluoromethylsulfonyl) imide (TES), and trihexyltetradecylphosphonium bis(2,4,4-trimethylpentyl) phosphinate (TPP). After this introduction Section II describes the experimental setup, the time-of-flight technique used to characterize the beams, and the relevant beam parameters. Section III presents the experimental results, namely the sputtering, surface roughness and surface features caused by the bombardment of single-crystal silicon by the nanodroplets of the different liquids in a wide range of impact velocities. The discussion of the experimental results is presented in Section IV, and a brief summary of the main findings is given in Section V.

II. EXPERIMENTAL SETUP AND BEAM CHARACTERIZATION

The experimental setup is shown in Fig. 1. An electrospray source is operated inside a vacuum chamber with a background pressure of 8×10^{-6} Torr. The emitter is a chamfered platinum tube with a longer fused silica capillary inserted in the opposite end. The lengths, inner diameters and outer diameters of these tubes are 1.2 and 31.3 cm, 160 and 40 μm , and 480 and 150 μm respectively. The liquid to be electrosprayed is kept in a bottle outside the vacuum chamber, and fed to the chamfered tip through the fused silica line. The flow rate is controlled by adjusting the pressure in the bottle. A voltage difference $-V_E$ is applied between the emitter and a facing extractor electrode to set the electrospray, which is operated in the cone-jet mode producing negatively charged nanodroplets. The total current of the electrospray is I_E , of which a small fraction I_B passes through a pinhole perforated in the center of the extractor. This beamlet is directed towards a [1 0 0] single-crystal silicon wafer mounted on an XYZ stage; during the sputtering experiments this target is placed 4 mm from the extractor. The target is electrified at a potential V_T , and the nanodroplets are accelerated by a combined acceleration voltage $V_A = V_T + V_E$. The temperature of the electrospray source is adjusted with an electrical heater and a thermocouple inserted in the extractor electrode, and connected to a digital controller.

The beamlet is characterized with a time-of-flight setup.¹⁶ To obtain a spectrum the electrospray is suddenly interrupted by shorting the potential of the emitter with an ultrafast switch, and the current reaching a collector at a distance L_{TOF} from the emitter is measured over time. The time-varying signal $I_B(t)$ is integrated to compute the mass flow rate of the beamlet:

$$\dot{m} = \frac{4V_A}{L_{TOF}} \int_0^\infty I_B(t) dt \quad (1)$$

We use the mass flow rate and the current of the beamlet to define an average charge to mass ratio for the droplets, $\langle \xi \rangle = I_B / \dot{m}$. The velocity of a projectile with this charge to mass ratio is $\langle v \rangle = \sqrt{2 \langle \xi \rangle V_A}$.

The typical droplet diameter is estimated with the average charge to mass ratio, and the assumption that it is charged at 68% of its Rayleigh limit, or maximum charge that a stable droplet can hold:

$$\langle d \rangle = 0.68^{2/3} \left(\frac{288 \gamma \epsilon_0}{\rho^2 \langle \xi \rangle^2} \right)^{1/3} \quad (2)$$

γ and ρ stand for the surface tension and the density of the liquid, while ϵ_0 is the permittivity of the vacuum. The 0.68 factor has been confirmed experimentally with electrosprayed nanodroplets of EMI-Im and propylene carbonate.¹⁷

In a typical experiment the beamlet carves an array of points in the target. Each point is struck for 600 seconds at fixed target potential. The settings of the electrospray source (liquid, flow rate, emitter potential and temperature) are kept constant throughout the experiment, while the potential of the target and therefore the acceleration voltage of the beamlet is changed for each point in the array. The topography of the sputtered surface is measured with an atomic force microscope, AFM, and its roughness computed as the root-mean-square of the heights of the measured points. The volume of silicon carved by the beamlet is measured with a mechanical profilometer. We use the following figures of merit to analyze the sputtering results: the sputtering yield Y , or average number of silicon atoms ejected per molecule in the projectile; the

sputtering per unit area Y_Ω , or number of atoms sputtered by the droplet of average diameter divided by its cross section; the kinetic energy of a molecule E_m ; the kinetic energy per unit area E_Ω , or kinetic energy of the average droplet divided by its cross section; and the stagnation pressure of the projectile P_s . These parameters are defined in terms of experimental measurements and physical properties as follows:

$$Y = \frac{\rho_{Si} \Lambda m_l}{m_{Si} \dot{m} \tau}, \quad Y_\Omega = \frac{2}{3} \frac{\rho_{Si} \Lambda \rho < d >}{m_{Si} \dot{m} \tau} \quad (3, 4)$$

$$E_m = m_l < \xi > V_A, \quad E_\Omega = \frac{2}{3} \rho < \xi > V_A < d >, \quad P_s = \rho < \xi > V_A \quad (5-7)$$

where Λ is the volume of silicon sputtered by the beamlet; ρ_{Si} and m_{Si} are the density and atomic mass of silicon; m_l is the molecular mass of the nanodroplet; and τ is the exposure time to the beamlet. The sputtering yield and the molecular kinetic energy are better suited to describe molecular processes, while the sputtering per unit area, the kinetic energy per unit area and the stagnation pressure are the natural variables in a continuum treatment of the impact. The choice of stagnation pressure versus kinetic energy per unit area to represent the energy of the impact is somewhat arbitrary. The stagnation pressure is the standard parameter in hypervelocity impact of macroprojectiles and was used in previous nanodroplet work to present the data; impact phenomena that scale with the volume of the projectile such as crater formation and amorphization should correlate better with the stagnation pressure, which is the ratio between the kinetic energy of the projectile and its volume. On the other hand phenomena restricted to a few atomic layers near the surface such as sputtering may correlate better with the kinetic energy transferred to the target per unit area.

Table I summarizes the physical properties of the liquids. The broad range of molecular masses, varying between 45 amu for formamide and 773 amu for TPP, should reveal any potential dependence of the sputtering phenomena on this parameter. All electrical conductivities are measured at room temperature. This parameter must be of the order of 1 S/m to produce the nanodroplets required for sputtering.¹⁸ This condition is satisfied at room temperature by all ionic liquids except TPP, which we electrospray at 254°C to increase its conductivity and therefore the charge to mass ratio of its droplets. The electrical conductivity of pure formamide is also insufficient for this study, and the desired level near 1 S/m is obtained by adding a small amount of EAN (4% vol. concentration). All other values in Table I are from published work.

Table II collects beamlet and impact parameters. Each liquid is electrosprayed in a single operational point except formamide, which is electrosprayed at three different currents to characterize the effect of the droplet diameter. The two values of the molecular kinetic energy, stagnation pressure and impact velocity correspond to the minimum and maximum acceleration voltages used for each liquid. Table II illustrates the main singularity of these projectiles: all droplets have diameters of tens of nanometers and include tens of thousands of molecules, i.e. they are extremely large projectiles compared to atomic and molecular ions; yet, the high charging level imparted by the electrospraying technique (nearly as high as the theoretical Rayleigh limit) makes it possible to accelerate them with relative ease into the hypervelocity regime of macroscopic impact or, equivalently, into the lower end of the molecular energy range of ion beams.

III. EXPERIMENTAL RESULTS

Figure 2(a) shows the sputtering per unit area as a function of the projectile's kinetic energy per unit area for all liquids. The curves follow one of two distinct patterns depending on the molecular mass. While the sputtering of the lighter formamide and EAN increases monotonically with energy, the sputtering curves of the liquids with heavier molecules EMI-BF₄, EMI-Im and TES display a maximum: the sputtering first increases with energy, peaks at values of 24, 37 and 53 atoms/nm² at 697, 659 and 589 eV/nm², and sharply decreases thereafter to settle around 15, 17 and 28 atoms/nm² respectively. In addition, the sputtering levels of the liquids with lighter molecules are much lower overall. Note also that the sputtering at low energy is ordered according to molecular weights. For example, at 620 eV/nm², the sputtering per unit area of TES, EMI-Im, EMI-BF₄, EAN and formamide are 48, 37, 19, 8 and 3 atoms/nm² respectively. Figure 2(b) shows the same data in the form of sputtering yield versus molecular kinetic energy. The sputtering yield of formamide stays below 0.08 in all cases, while TES exhibits the highest yield, 3.97 at 43.9 eV. In the new abscissa scale the low sputtering yields of the lighter liquids, especially formamide, have correspondingly low molecular kinetic energies while TPP, TES, EMI-Im, and EMI-BF₄ combine higher molecular kinetic energies with higher sputtering yields. Finally, Fig. 2(c) plots the data in terms of sputtering yield versus the stagnation pressure of the projectile. Just like in Fig. 2(a), impacts with identical energy densities (see for example formamide and TES at 15 GPa) have very different sputtering yields.

The molecular mass of the nanodroplet also has a major effect on the topography of the surface. Figure 3 shows photographs of bombarded areas for different liquids and stagnation pressures, together with surface maps measured with an AFM. The beamlet carves a circular depression surrounded by a thin layer of deposits. The photographs provide a qualitative estimation of the roughness: because the samples are illuminated along the line of sight, a rough surface scattering

light in all directions reduces the intensity that comes back to the camera, and appears darker than a smooth, specular surface. At similar stagnation pressures the surfaces bombarded by liquids with high molecular mass appear dark and are therefore rough, while those bombarded by EAN and formamide are bright and hence smooth. The AFM measurements are more quantitative: the top row shows the original surface of the target, which has a roughness of 1.2 nm, and three surfaces bombarded by formamide at fixed stagnation pressure and increasing droplet diameter. The surfaces bombarded by formamide are covered by indentations with diameters from tens to a few hundred nanometers, which must be the sign of individual impacts. The depths and diameters of the indentations augment with the size of the nanodroplets, and the roughness increases from 7.5 nm to 14 nm as the droplet diameter increases from 37 to 59.5 nm. The surfaces bombarded by the ionic liquids are displayed in the bottom row. The EAN nanodroplets, which have the smallest average diameter, produce the smoothest surface with a roughness of 1.7 nm, while the surfaces bombarded by TES, EMI-Im and EMI-BF₄ display a double pattern of indentations different from the formamide and EAN cases: the nanometric craters produced by individual impacts are superimposed over much larger craters with diameters of several microns. The high roughness of these three surfaces, 43.5, 46.9 and 47.9 nm respectively, is mostly the result of these micron-sized craters.

Figure 4 plots the roughness as a function of the projectile's stagnation pressure. We omit the representation in terms of the molecular kinetic energy because the roughness of the surface is dominated by cratering, a phenomenon associated with the energy density of the impact. Initially the roughness for any liquid increases moderately with the stagnation pressure and is correlated with the average droplet diameter, ranging between 0.4 and 17 nm. In this low energy region the roughness is caused by indentations of the order of the size of the projectile. This trend changes

at about 11 GPa for the liquids with high molecular mass, when the roughness of EMI-BF₄, EMI-Im and TES starts to increase until they peak at 79.8, 46.9 and 43.5 nm respectively. The increase in roughness is caused by the presence of craters almost two orders of magnitude larger than the projectiles, which only appear in the surfaces bombarded by EMI-BF₄, EMI-Im, TES and TPP. These micron-sized craters are always absent in the formamide and EAN samples. After peaking between 14.4 and 20.2 GPa, the roughness of EMI-BF₄, EMI-Im and TES decreases sharply down to values near 7 nm. The presence of a maximum in the roughness curves and the sharp decrease thereafter are analogous to the evolution of the sputtering curves in Fig. 2. In addition, for each one of these three liquids, the roughness and sputtering curves peak at the same values of the stagnation pressure. The scanning electron micrographs in Fig. 5 provide a visual description of the evolution of the patterns of craters. The top row shows the small indentations produced by the formamide beamlets, which only increase moderately in size with the energy of the nanodroplets. Conversely the variation of the diameters of the craters caused by the EMI-BF₄ and EMI-Im nanodroplets is much more substantial in the same range of stagnation pressures. As the energy of these droplets increases, the nanometric indentations gradually give rise to larger and deeper craters with sizes of several microns in the case of EMI-BF₄, and of tens of microns for EMI-Im. At even higher energies these large craters are suppressed, and only the initial pattern of nanometric indentations remains.

Although experimental limitations restricted the characterization of TPP to a narrow range of kinetic energies, it is apparent that this liquid behaves like the heavy molecular weight EMI-BF₄, EMI-Im and TES. Besides the high roughness measured in the samples bombarded by TPP, the SEM image in Fig. 6 shows that TPP nanodroplets produce the micron-sized craters only observed in the bombardment by liquids of high molecular mass.

IV. DISCUSSION

A key question in nanodroplet sputtering is whether the processes leading to the ejection of atoms can be modeled as a continuum, macroscopic problem or necessarily require an atomistic formulation. The large diameter of the nanodroplet compared to the size of its molecules and the large number of molecules in the nanodroplet suggest that the ejection should exhibit macroscopic behavior. Examples of macroscopic mechanisms that could be responsible for the ejection are thermal evaporation from the surface melted by the impact, and the release of clusters of atoms from this liquid phase by hydrodynamic instabilities. However, the experimental results do not support the macroscopic ejection hypothesis. This is best observed in Fig. 2(a), where projectiles that are macroscopically similar sputter very different numbers of atoms. For example, the average EMI-Im and formamide ($I_E = 330$ nA) nanodroplets have similar diameters, 34.6 and 37.0 nm respectively, yet their sputtering per unit area are 37 and 3 atoms/nm² when a similar energy density of 650 eV/nm² is transferred to the target. Although the projectile diameters of other liquids fall within a broader range, the normalization of the sputtering and the kinetic energy with the cross section of the projectile should reduce size effects. Thus, the disparities between the different curves in Fig. 2(a) indicate that the molecular properties of the projectile must have an important effect in sputtering.

The observation in Fig. 2(a) that at energies below the maxima the sputtering increases with the molecular mass suggests that this parameter plays an important role. We can think of two reasons explaining this correlation between sputtering and molecular mass. First, the energy transferred by a molecule to those few atoms affected by knock-on collisions is proportional to its mass.

Thus, the heavier the molecule the lower the velocity that is required to produce target atoms with sufficient energy to overcome the surface binding potential, i.e. to be sputtered by knock-on collisions. Second, we expect a rise of the temperature of the surface, and hence of thermal sputtering, with increasing molecular mass at constant stagnation pressure: the larger energy transferred to the knock-on atoms and the greater separation between these points of contact in the case of heavier molecules, should translate into a higher spatial unevenness of the energy density in the target. Upon local equilibration the higher unevenness will cause higher dissipation, a more elevated temperature field, and ultimately lead to a higher evaporation rate.

The different response of formamide and EAN compared to EMI-BF₄, EMI-Im and TES could also be due to chemically enhanced sputtering, rather than to the disparity in molecular masses. Unlike formamide and EAN, fluorine is present in EMI-BF₄, EMI-Im and TES. This chemical element is highly reactive with silicon, and is widely used in reactive ion etching of this semiconductor.¹⁹ TPP was included in this study to test whether the enhancement of sputtering in the case of EMI-BF₄, EMI-Im and TES is a molecular mass or a chemical effect, since TPP does not contain fluorine and has a molecular mass that nearly doubles that of TES. Although we could not characterize this liquid in a broad range of energies due to difficulties associated with its electrospraying and limitations of our experimental setup, the three TPP points in Fig. 2 show that this liquid, despite lacking fluorine, has the high sputtering efficiency typical of EMI-BF₄, EMI-Im and TES. That is, the enhancement of sputtering is likely due to the molecular mass effect. Besides this direct evidence there are other arguments against the importance of chemical sputtering: first, it is unlikely that a significant number of the strong covalent B-F and C-F bonds present in EMI-BF₄, EMI-Im and TES will break upon impact under our experimental conditions. For example, atomic dissociation in the covalently bonded fullerene projectile, C₆₀,

only starts at impact energies exceeding 8.3 eV per atom,²⁰ while this number is only 1.5, 1.4 and 1.2 eV for EMI-BF₄, EMI-Im and TES at the sputtering maxima. Second, the sharp drop in the sputtering yield of EMI-BF₄, EMI-Im and TES at increasing energy is at odds with chemical sputtering, because the fraction of broken B-F and C-F bonds should correlate with the molecular kinetic energy.

The sharp drop of the sputtering yields for EMI-BF₄, EMI-Im and TES at projectile energies exceeding a critical value is surprising. This behavior was previously reported in experiments with EMI-Im nanodroplets impacting on silicon. Although the sputtering yields of GaAs, GaSb, and InAs bombarded by EMI-Im also display maxima, these are much less pronounced and the sharp drops observed in Fig. 2 are unique to silicon. Furthermore, we are unaware of a similar behavior when silicon is bombarded by either molecular ions or gas cluster ions. From previous experimental and molecular dynamics work on the Si/EMI-Im pair we know that the impact velocity at which the sharp drop occurs coincides with the formation of a substantial amorphous layer, and we think that this amorphous layer is reducing the sputtering efficiency of the nanodroplets. Although an amorphous layer of a few atoms is formed by EMI-Im nanodroplets at stagnation pressures below 9 GPa, its thickness only starts increasing at this point, becoming nearly constant and comparable to the diameter of the projectile at stagnation pressures exceeding 18 GPa,¹⁴ a value that coincides with the sputtering and roughness maxima in figures 2(c) and 4. Thus the immediate cause for the sharp drop of the sputtering yield probably is the new atomic ordering of the region affected by the impact. The amorphization results from the dissipation of a fraction of the projectile's kinetic energy in the region of the target surrounding the impact, the melting of this area, and a subsequent quench that prevents the resolidification in crystalline form. The association of the sharp drop in sputtering yield with projectiles of heavy

molecules is consistent with the expected correlation between dissipation and temperature on the target, and the molecular mass: although we have not characterized the atomic arrangement of the bombarded targets, it appears that in the velocity range of our experiments only the heavier molecules are able to dissipate enough energy to melt a substantial layer of the target, and therefore to produce the amorphous region of sufficient thickness able to reduce the sputtering efficiency of the nanodroplets.

The roughness is a measure of the craters left by the impacts. Molecular dynamics simulations have shown that the impact of an EMI-Im nanodroplet on single-crystal silicon produces a spherical-cup crater with a diameter similar to that of the projectile, and a depth that increases with its velocity.¹⁴ This is consistent with the present results at low energy, where the roughness is caused by indentations with dimensions of the order of the diameter of the projectiles, and moderately increases with the velocity and the diameter of the droplets. This situation changes at higher energy for the liquids with heavier molecules, when much larger craters appear in addition to the projectile-sized indentations. These large craters were discussed in previous sputtering work based on the EMI-Im/Si pair,⁹ and the present data show that they are only produced by projectiles with high molecular mass. Each micron-sized crater is carved by a single nanodroplet on a surface modified by a large number of previous impacts. The accumulation of impacts damages the target (e.g. by sputtering atoms, creating grain boundaries and dislocations, inducing thermal stresses that may contribute to the nucleation and growth of cracks, etc.) until a critical point is reached in which one additional impact carves a crater orders of magnitude larger than the projectile. At still higher energies the formation of a thick amorphous layer apparently eliminates the conditions leading to micron-sized craters, just like it changes the resistance of the surface to sputtering.

V. CONCLUSIONS

The molecular mass of a nanodroplet has a strong effect on how its energetic impact modifies the surface of a silicon target. Liquids with high molecular mass like EMI-BF₄, EMI-Im, TES and TPP sputter significantly more atoms than formamide and EAN, which have much lighter molecules; a few of their projectiles are able to carve craters orders of magnitude larger than their diameters; and their sputtering yields and associated surface roughness exhibit sharp maxima. The strong dependence on the molecular mass is rationalized in terms of the increased kinetic energy of heavy molecules. Having more energy to transfer in the first few collisions with target atoms, heavier molecules generate more knock-on atoms able to overcome the surface binding potential. A second molecular-size effect driving thermal sputtering is the higher energy dissipation and increased target temperatures caused by the impact of heavier molecules. This effect may also be responsible for the presence of maxima in the roughness and sputtering curves, through the melting and subsequent resolidification in amorphous form of a thick layer that responds differently to the impact of the nanodroplets.

The very different sputtering by droplets that are macroscopically similar (i.e. droplets that have the same diameters and kinetic energies), and the strong dependence of the effects of the impact on molecular mass, indicate that nanodroplet sputtering is intrinsically a molecular phenomenon, dominated by the transfer of energy under non equilibrium conditions. Therefore a continuum formulation is ill-suited for the modeling of this problem.

ACKNOWLEDGMENTS

This work was funded by the Air Force Office of Scientific Research, Grant No. FA9550-11-1-0308. The authors are grateful for the support of the AFOSR Program Manager Dr. Birkan.

Table I. Physical properties of liquids: molecular formula; molecular mass, m_l (amu); estimated molecular diameter, d_m (nm); density, ρ (kg/m³); surface tension, γ (N/m) and conductivity, K (S/m).

Liquid	<i>Formula</i>	m_l	d_m	ρ	γ	K^{**}
FM	CH ₃ NO	45.0	0.45	1130	0.058 ²¹	0.96
EAN	C ₂ H ₈ N ₂ O ₃	108.1	0.58	1261	0.047 ²²	2.03
EMI-BF₄	C ₆ H ₁₁ BF ₄ N ₂	198.0	0.71	1294	0.054 ²³	1.31
EMI-Im	C ₈ H ₁₁ F ₆ N ₃ O ₄ S ₂	391.3	0.84	1520	0.035 ²⁴	0.77
TES	C ₈ H ₁₅ F ₆ NO ₄ S ₃	399.4	0.86	1470	0.030 ^{*,25}	0.64
TPP	C ₄₈ H ₁₀₂ O ₂ P ₂	773.3	1.26	895	0.029 ²⁶	0.02

* No surface tension data was found for TES in the literature. This value corresponds to a liquid with identical anion as TES but different cation: tri-(1-butyl)methylammonium bis(trifluoromethylsulfonyl)imide.

** Conductivity was measured at room temperature for all liquids.

Table II. Properties of the electrospray beams: electrospray current, I_E (nA); beamlet current, I_B (nA); beamlet mass flow rate, \dot{m} (kg/s); average charge to mass ratio of droplets, $\langle \xi \rangle$ (C/kg); average droplet diameter, $\langle d \rangle$ (nm); number of molecules in the average droplet, N_d ; acceleration potential, V_A (kV); average droplet velocity, $\langle v \rangle$ (km/s); molecular energy, E_m (eV); kinetic energy per unit area E_Ω (eV/nm²); and stagnation pressure $\langle P_s \rangle$ (GPa). The last four parameters correspond to the minimum and maximum values of their ranges.

Liquid	I_E	I_B	\dot{m}	$\langle \xi \rangle$	$\langle d \rangle$	N_d	V_A	$\langle v \rangle$	E_m	E_Ω	P_s
FM	330	46.5	4.54×10^{-11}	1024	37.0	400,804	8.0/24.0	4.0/7.0	4.2/12.7	357/1076	9.3/28.0
	485	32.0	5.17×10^{-11}	618	51.9	1,106,188	8.2/24.2	3.2/5.5	2.5/7.5	311/918	5.8/17.0
	700	27.5	5.47×10^{-11}	503	59.5	1,666,778	8.2/24.2	2.9/4.9	2.1/7.0	291/856	4.7/13.8
EAN	895	14	6.81×10^{-12}	2054	20.1	29,849	3.5/24.5	6.3/10.0	21.9/56.4	190/1328	24.7/63.5
EMI-BF₄	1350	17.5	1.47×10^{-11}	1194	29.9	55,048	8.5/24.5	4.5/7.6	20.1/60.0	408/1177	13.1/37.9
EMI-Im	285	14	2.13×10^{-11}	656	34.6	59,031	8.2/25.2	3.3/5.8	21.9/67.2	297/911	8.3/25.3
TES	240	10.8	1.84×10^{-11}	585	36.3	55,474	8.1/26.1	3.1/5.5	19.7/63.3	264/848	7.0/22.5
TPP	54	6.7	2.30×10^{-11}	292	79.0	179,811	33.9/41.9	4.5/4.9	88.8/98.2	771/900	9.9/10.9

Figure 1. Schematic of the experimental setup. A variety of liquids are electrosprayed inside a vacuum chamber, and their beamlets are accelerated towards a sputtering target. The facility includes diagnostics for characterizing the beams.

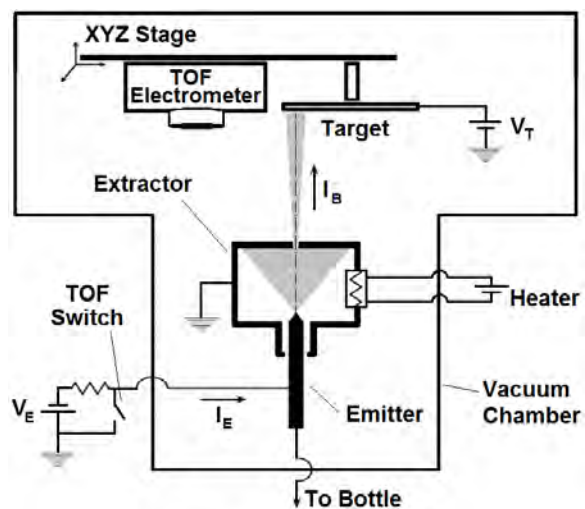


Figure 2. Sputtering of silicon by nanodroplets of formamide (FM), EAN, EMI-BF₄, EMI-Im, TES and TPP. The data are presented in the form of (a) sputtering per unit area vs. kinetic energy per unit area; (b) sputtering yield vs. molecular kinetic energy; and (c) sputtering yield vs. stagnation pressure.

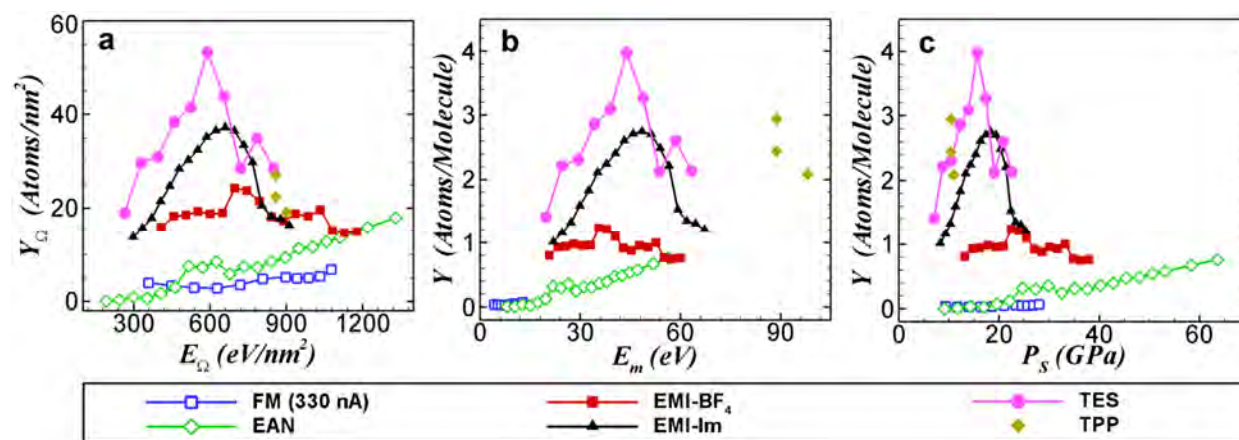


Figure 3. Photographs of silicon targets bombarded by formamide (FM), EAN, EMI-BF₄, EMI-Im and TES, together with AFM measurements of typical 5×5 μm patches. An AFM characterization of the original silicon surface is included for reference.

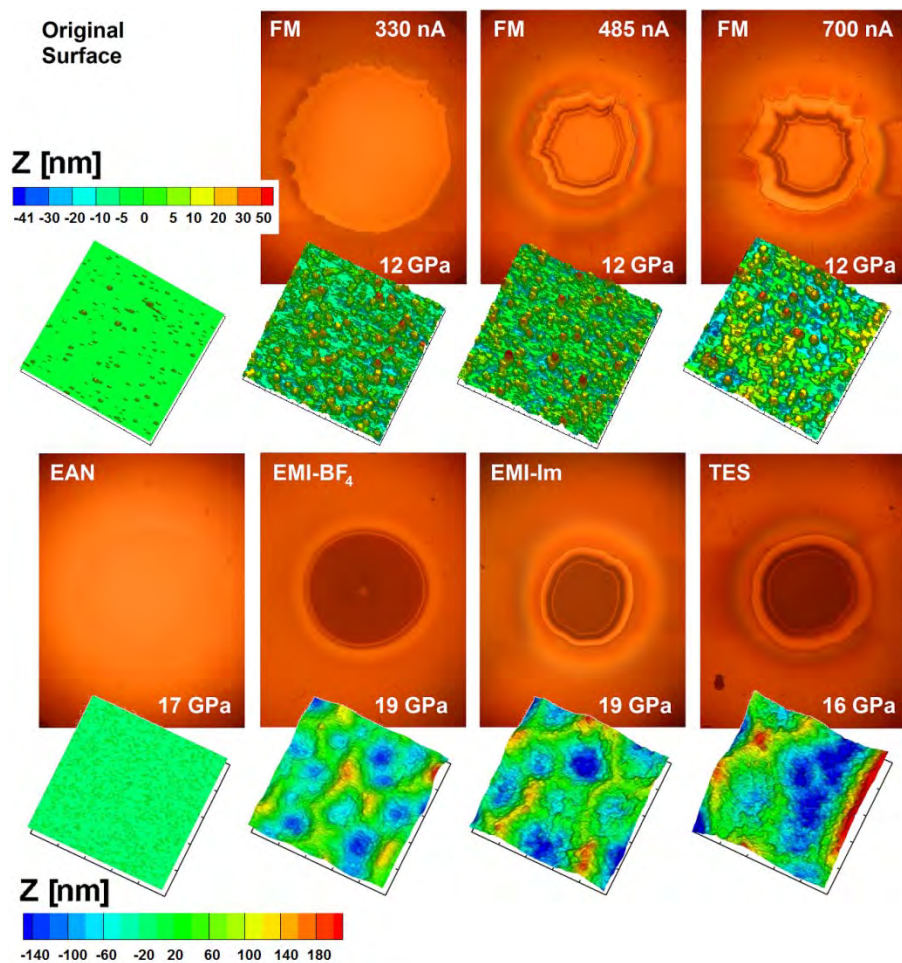


Figure 4. Roughness of the silicon surfaces as a function of the projectile's stagnation pressure.

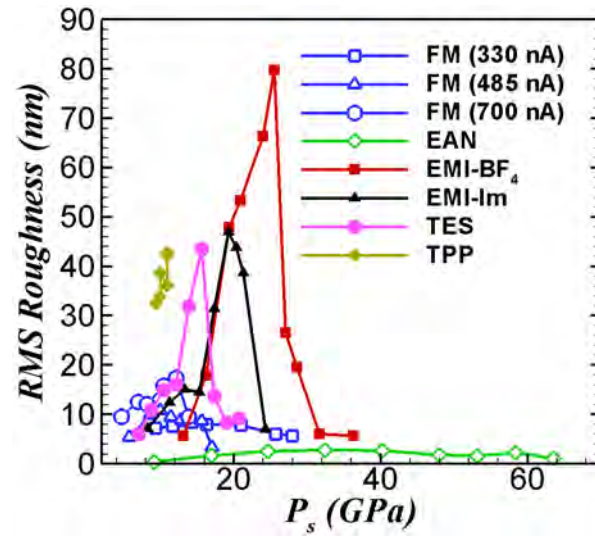


Figure 5. SEM images of silicon surfaces sputtered by formamide (FM), EMI-BF₄ and EMI-Im droplets, at overlapping ranges of stagnation pressure within 14 and 32 GPa. Formamide creates a pattern of nanometric marks with sizes that have a small dependence on droplet energy. EMI-BF₄ and EMI-Im, with molecular masses approximately 4 and 8 times higher than formamide respectively, carve larger craters with diameters increasing with stagnation pressure. These large craters disappear at high enough impact velocity.

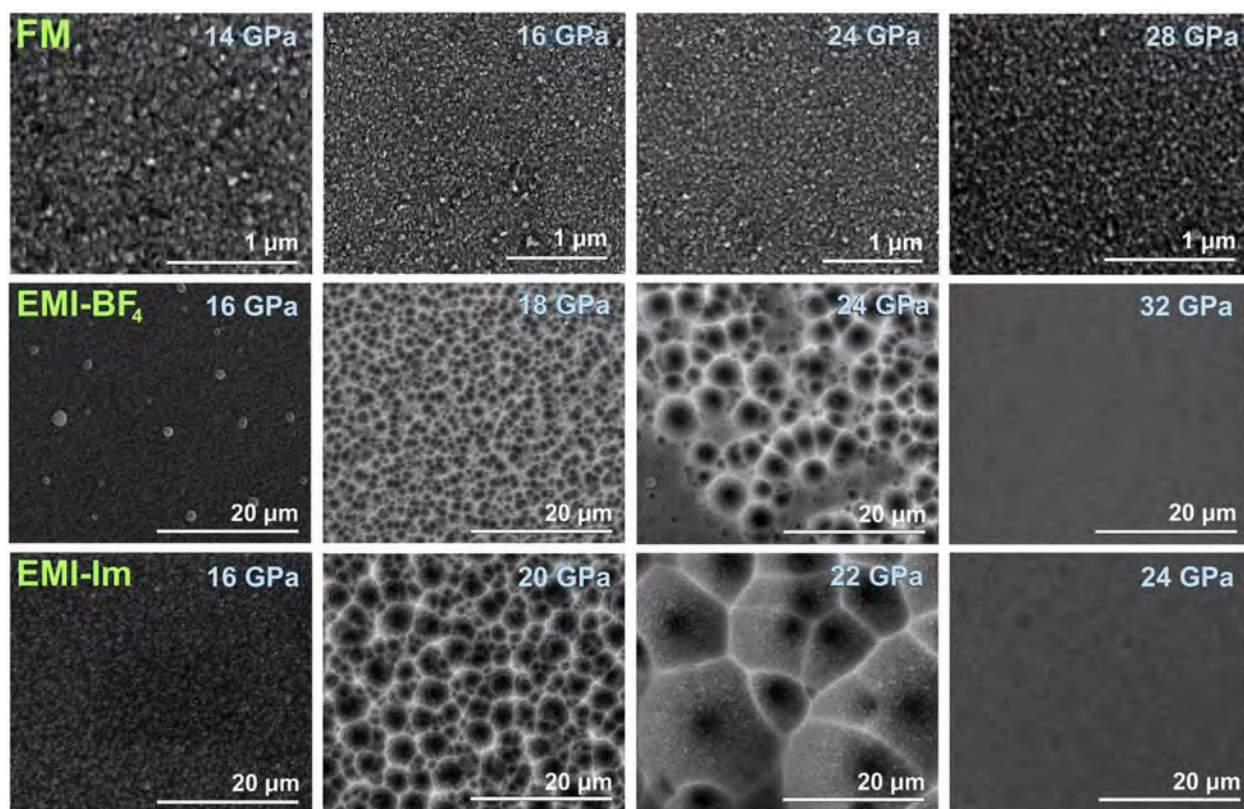
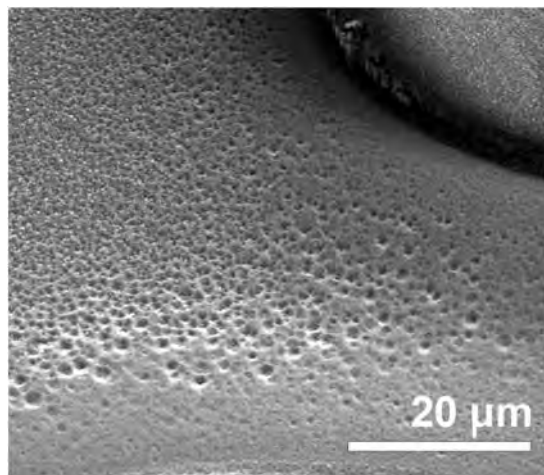


Figure 6. SEM images of a silicon target bombarded by TPP droplets, at a stagnation pressure of 11 GPa. This liquids produces a pattern of micron-sized indentations similar to that observed in EMI-BF₄, EMI-Im and TES, and absent in formamide and EAN.



REFERENCES

- ¹ Y. Yamamura and H. Tawara, Energy dependence of ion-induced sputtering yields from monatomic solids at normal incidence, *Atom. Data Nucl. Data* 62 (1996) 149-253.
- ² P. Sigmund, Theory of Sputtering. I. Sputtering Yield of Amorphous and Polycrystalline Targets, *Phys. Rev.* 184 (1969) 383.
- ³ J. Samela and K. Nordlund, Emergence of non-linear effects in nanocluster collision cascades in amorphous silicon, *New J. Phys.* 10 (2008) 023013.
- ⁴ I. Yamada and N. Toyoda, Nano-scale surface modification using gas cluster ion beams—A development history and review of the Japanese nano-technology program, *Surf. Coat. Tech.* 201 (2007) 8579-8587.
- ⁵ N. Winograd, The magic of cluster SIMS, *Anal. Chem.* 77 (2005) 142A-149A.
- ⁶ M. Gamero-Castaño and M. Mahadevan, Sputtering of silicon by a beamlet of electrosprayed nanodroplets, *Appl. Surf. Sci.* 255 (2009) 8556-8561.
- ⁷ J. Fernández de la Mora and I.G. Loscertales, The current emitted by highly conducting Taylor cones, *J. Fluid Mech.* 260 (1994) 155-184.
- ⁸ M. Gamero-Castaño and M. Mahadevan, Sputtering yields of Si, SiC, and B₄C under nanodroplet bombardment at normal incidence, *J. Appl. Phys.* 106 (2009) 054305.

- ⁹ R. Borrajo-Pelaez, E. Grustan-Gutierrez and M. Gamero-Castano, Sputtering of Si, SiC, InAs, InP, Ge, GaAs, GaSb, and GaN by electrosprayed nanodroplets, *J. Appl. Phys.* 114 (2013) 184304.
- ¹⁰ H. Cho, P. Leerungnawarat, D. C. Hays, S. J. Pearton, S. N. G. Chu, R. M. Strong, C.-M. Zetterling, M. Östling, and F. Ren, Ultradeep, low-damage dry etching of SiC, *Appl. Phys. Lett.* 76 (2000) 739-741.
- ¹¹ J. Sugiura, W. J. Lu, K. C. Cadien and A. J. Steckl, Reactive ion etching of SiC thin films using fluorinated gases, *J. Vac. Sci. Tech. B*, 4 (1986) 349-354.
- ¹² M. Gamero-Castano, A. Torrents, L. Valdevit and J. G. Zheng, Pressure-Induced Amorphization in Silicon Caused by the Impact of Electrosprayed Nanodroplets, *Phys. Rev. Lett.* 105 (2010) 145701.
- ¹³ F. Saiz and M. Gamero-Castaño, Amorphization of silicon induced by nanodroplet impact: A molecular dynamics study, *J. Appl. Phys.* 112 (2012) 054302.
- ¹⁴ F. Saiz, R. Borrajo-Pelaez and M. Gamero-Castaño, The influence of the projectile's velocity and diameter on the amorphization of silicon by electrosprayed nanodroplets, *J. Appl. Phys.* 114 (2013) 034304.
- ¹⁵ J. Samela and K. Nordlund, Transition from atomistic to macroscopic cluster stopping in Au, *Nucl. Instrum. Meth. B* 267 (2009) 2980-2986.
- ¹⁶ M. Gamero-Castaño and V. Hruby, Electrospray as a Source of Nanoparticles for Efficient Colloid Thrusters, *J. Propul. Power* 17 (2001) 977-987.

- ¹⁷ M. Gamero-Castaño, Retarding potential and induction charge detectors in tandem for measuring the charge and mass of nanodroplets, *Rev. Sci. Instrum.* 80 (2009) 053301.
- ¹⁸ J. Fernandez de la Mora, The Fluid Dynamics of Taylor Cones, *Annu. Rev. Fluid Mech.* 39 (2007) 217-243.
- ¹⁹ D. L. Flamm, Mechanisms of silicon etching in fluorine- and chlorine-containing plasmas, *Pure App. Chem.* 62 (9) (1990) 1709-1720.
- ²⁰ C. Anders, H. Kirihaata, Y. Yamaguchi, H. Urbassek, Ranges and fragmentation behavior of fullerene molecules: A molecular-dynamics study of the dependence on impact energy and target material, *Nuclear Instr. and Meth. in Phys. Res. B* 255 (2007) 247-252.
- ²¹ Polymer Interface and Adhesion, Souheng Yu, Marcel Dekker, New York, NY, 1982, p. 151.
- ²² D. Fennell Evans, A. Yamauchi, R. Roman and E. Casassa, Micelle formation in ethylammonium nitrate, a low-melting fused salt, *J. Colloid Interface Sci.* 88 (1) (1982) 89-96.
- ²³ M. Martino, J. Fernandez de la Mora, Y. Yoshida, G. Saito and J. Wilkes, Surface tension measurements of highly conducting ionic liquids, *Green Chem.* 8 (2006) 390-397.
- ²⁴ D. Garoz, C. Bueno, C. Larriba, S. Castro, I. Romero-Sanz, J. Fernandez de la Mora, Y. Yoshida and G. Saito, Taylor cones of ionic liquids from capillary tubes as sources of pure ions: The role of surface tension and electrical conductivity, *J. Appl. Phys.* 102 (2007) 064913.
- ²⁵ Y. Pan, L.E. Boyd, J.F. Kruplak, W.E. Cleland Jr., J.S. Wilkes and C.L. Hussey, Physical and Transport Properties of Bis(trifluoromethylsulfonyl)imide-Based Room-Temperature Ionic

Liquids: Application to the Diffusion of Tris(2,2'-bipyridyl)ruthenium(II), J. Electrochem. Soc. 158 (1) (2011) F1-F9.

²⁶ H. Almeida, J. Lopes-da-Silva, M. Freire and J. Coutinho, Surface tension and refractive index of pure and water-saturated tetradecyltriethylphosphonium-based ionic liquids, J. Chem. Thermodyn. 57 (2013) 372-379.

Amorphization of Hard Crystalline Materials by Electrosprayed Nanodroplet Impact

Manuel Gamero-Castaño^{†*}, Anna Torrents[†], Rafael Borrajo-Pelaez[†], Jian-Guo Zheng[‡]

[†]Department of Mechanical and Aerospace Engineering, University of California, Irvine,
California 92697

[‡]Materials Characterization Center, Calit2, University of California, Irvine

ABSTRACT

A beam of electrosprayed nanodroplets impacting on a single-crystal silicon wafer amorphatizes a thin surface layer under, of a thickness comparable to the diameter of the drops. The phase transition occurs at projectile velocities exceeding a threshold, and results from the quenching of material melted by the impacts. This article demonstrates that the amorphization of silicon is a general phenomenon, as nanodroplets impacting at sufficient velocity also amorphatize other covalently-bonded crystals. In particular we bombard single-crystal wafers of Si, Ge, GaAs, GaP, InAs and SiC in a range of projectile velocities, and characterize the samples via electron backscatter diffraction and transmission electron microscopy to determine the aggregation state under the surface. InAs requires the lowest projectile velocity to develop an amorphous layer, followed by Ge, Si, GaAs and

* Corresponding author, mgameroc@uci.edu

GaP. SiC is the only semiconductor that remains fully crystalline, but this is likely due to the relatively low velocities of the beamlets used in this study. The resiliency of each crystal to amorphization correlates well with the specific energy needed to melt it except for Ge, which requires projectile velocities higher than expected.

I. INTRODUCTION

Beams of electrosprayed droplets have been used in applications such as surface cleaning,¹ secondary ion mass spectrometry and electric propulsion for spacecraft,^{2,3} and research in this area has now been extended to activities like sputtering and surface amorphization requiring higher projectile velocities.⁴ Several features of electrosprayed nanodroplets make them unique projectiles for ion beam applications: they are naturally charged near the maximum stability level set by the Rayleigh limit,⁵ and therefore have top impact velocities for a given acceleration voltage; they are formed in the capillary breakup of a steady jet, an atomization mechanism that yields a continuous stream of drops with a narrow distribution of diameters;⁶ the average diameter can be controlled from a few nanometers to hundreds of microns which, together with the high charge state, makes it possible to extend the research and applications of particle beams to diameters exceeding the few nanometers that are currently possible with the largest gas cluster ions;^{7,8} the molecular mass and chemistry of the nanodroplet's liquid can be extensively varied to research and optimize the effects of these parameters on the impact, which are relevant because the impact initially proceeds in the absence of partial thermodynamic equilibrium and thus has a phenomenology intrinsically tied to the molecules' nature; electrospray emitters can be

miniaturized and, using microfabrication techniques, multiplexed in the form of a broad-beam particle source for batch fabrication;⁹ and being a point source, an electrospray emitter is also suitable to electrostatic focusing for applications similar to those of Liquid Metal Ion Sources-Focused Ion Beams.

A high velocity nanodroplet impacting on crystalline silicon amorphatizes a region of comparable volume,¹⁰ a phase transformation ultimately produced by quenching. The initial stages of the impact are characterized by the low penetration of the projectile's molecules and by knock-on and non-linear cascade collisions, which deposit high energy densities in a shallow region under the surface. A fraction of this energy is thermalized, melting the area near the impact when the projectile exceeds a threshold velocity. The thermal energy is then conducted away at cooling rates far exceeding the value preventing recrystallization, and the undercooled liquid solidifies as an amorphous phase.^{11,12} Since a substantial fraction of the projectile's kinetic energy is directly dissipated within a few nanometers below the surface, a nanodroplet with sufficient energy will melt a thin layer of any material. Furthermore the thinness of the layer creates a temperature gradient of the order of $(10^3 \text{ K}/10^{-8} \text{ m}) \sim 10^{11} \text{ K/m}$ and, in the case of silicon, a heat flux $f = -K(\partial T / \partial x)$ and a cooling rate $f / \rho c_p \Delta x$ of the order of 10^{13} W/m^2 and 10^{14} K/s . The latter estimate compares well with value of $6.8 \times 10^{13} \text{ K/s}$ at the normal melting point computed via molecular dynamics for a typical nanodroplet impact.¹¹ The very high cooling rates and the capacity to melt any material provide extreme conditions for surface amorphization, exceeding what is possible in laser processing,¹³ and the main goal of this research is to confirm that nanodroplet impact can indeed amorphatize any semiconducting material besides silicon. To prove this we bombard single-crystal wafers of Si, Ge, GaAs, GaP, InAs and SiC, and characterize the modified surfaces using electron backscatter diffraction and

transmission electron microscopy to determine whether they are amorphatized, and the impact velocity needed for the phase transformation.

II. EXPERIMENTAL PROCEDURES

Fig. 1(a) is a sketch of the experimental setup. The nanodroplets are electrosprayed and electrostatically accelerated in a vacuum chamber kept at a pressure below 10^{-5} Torr with a turbomolecular and a mechanical forepump. The electrospray emitter is a chamfered platinum tube 1.2 cm long with outer and inner diameters of 480 and 150 μm . A fused silica capillary inserted in the non-chamfered end feeds the ionic liquid EMI-Im,¹⁴ stored in a reservoir outside of the chamber. The length and inner diameter of the capillary are 31.3 cm and 40 μm . The pressure inside the reservoir is adjusted to drive the desired flow rate. The electrospray source is operated in negative mode, i.e. a negative potential $-V_E$ between the emitter and a facing extractor electrode sets a cone-jet and atomizes the liquid into negatively charged nanodroplets. The total current of the electrospray is I_E , of which a small fraction I_B passes through a pinhole perforated in the center of the extractor and is directed towards the target. All experiments are carried out with identical source settings: $V_E = 2150$ V, $I_E = 283 \pm 4$ nA, and $I_B = 19$ nA. The mass flow rate of the beamlet, $\dot{m} = 1.65 \times 10^{-11}$ kg/s, was measured with the time-of-flight technique.³ The average charge to mass ratio of the nanodroplets, $\langle \xi \rangle = 971$ C/kg, is approximated by the ratio I_B / \dot{m} . The typical diameter of the droplets is 27 nm, a value estimated with the average charge to mass ratio and the assumption that the droplet is charged at 68% of its Rayleigh limit:

$$\langle d \rangle = 0.68^{2/3} \left(\frac{288 \gamma \epsilon_0}{\rho^2 \langle \xi \rangle^2} \right)^{1/3} \quad (1)$$

where γ and ρ stand for the surface tension and the density of EMI-Im, and ϵ_0 is the permittivity of the vacuum. The 68% charging level was determined in a previous experimental characterization of similar electrosprays.¹⁵

The beamlet is directed towards a single-crystal wafer mounted on an XYZ stage. The potential of the target is set at V_T , resulting in a combined acceleration voltage $V_A = V_T + V_E$ and a projectile velocity $\langle v \rangle = \sqrt{2 \langle \xi \rangle V_A}$. The maximum and minimum acceleration voltages used in this study are 25.65 and 4.15 kV, and the associated projectile velocities are 7.06 and 2.84 km/s. For reference, the stagnation pressures of the nanodroplet at these velocities are 37.9 and 6.12 GPa; the energy densities are 681 and 110 J/m²; the power densities are 1.78×10^{14} and 1.16×10^{13} W/m²; and the kinetic energies of each EMI-Im molecule are 101 and 16.3 eV. In a typical experiment the target is moved with the XYZ positioner, and the beamlet strikes a series of parallel lines at increasing acceleration voltage, as illustrated in Fig. 1(b). The width of these lines decreases with the acceleration voltage due to focusing effects, varying between 0.30 and 1.14 mm for acceleration voltages between 25.65 and 4.15 kV (the distance between the target and the extractor is kept at 4 mm in all experiments). The target is moved at a speed of 4.4×10^{-4} m/s, resulting in an impact density between 8.2×10^{15} and 2.1×10^{15} droplets/m². The average number of impacts in an area equal to the cross section of a 27 nm droplet is between 4.6 and 1.2, i.e. any point in the path of the beam is struck by nanodroplets multiple times. All targets are single-crystal wafers purchased from El-Cat Inc. The Si, Ge, GaAs, GaP, and InAs targets are 2'' wafers with [100] orientation, and the SiC targets are 10x10x0.43 mm hexahedrons of the 6H polytype, and [0001] orientation.

The bombarded samples were analyzed using electron backscatter diffraction (EBSD) and transmission electron microscopy (TEM). The EBSD measurements were performed with a

Zeiss UltraPlus scanning electron microscope (SEM) equipped with an Oxford's EBSD detector and HKL Channel 5 Flamenco software. Thin cross sectional samples for TEM were prepared with a FEI Quanta 3D FEG dual-beam scanning electron microscope/focused ion beam, and examined and digitally photographed with a FEI/Philips CM-20 TEM equipped with a Gatan TEM CCD camera.

III. RESULTS AND DISCUSSION

Figure 2 shows the paths of the beamlet on InAs and GaP at acceleration voltages between 6.65 and 15.75 kV, as both SEM images and EBSD crystal orientation maps. In the SEM images the paths are typically brighter than the surrounding surface, and the contrast augments with acceleration voltage. Since the depth of sputtered material is only a few nanometers, the strong contrast in the SEM image cannot be caused by the the shape of the path but must be due to enhanced secondary electron emission from the ridges of the nanocraters carved by the projectiles, or from a modified atomic arrangement under the surface of the target. Each pixel in the crystal orientation maps corresponds to an electron backscatter pattern (EBSP) taken at 20 micron intervals. The patterns indexed as zinc blende crystals are assigned a color according to crystallographic orientation, in particular a red pixel indicates that the analyzed point is a crystal with the [100] direction along the surface normal, while an EBSP that cannot be indexed and which therefore is likely to be amorphous is depicted as a black pixel. The crystal orientation map is superimposed to a grayscale band-contrast map indicative of the surface's topography, which darkens the shade of red inside the beamlet's path. The crystal orientation maps show that the crystalline order is progressively eliminated as the impact energy of the nanodroplets increases: in the case of InAs only 1.3% of the pixels fail to be indexed at an acceleration voltage

of 6.65 kV, i.e. the surface bombarded by the beamlet remains uniformly crystalline; this fraction increases moderately to 6.3% at the acceleration voltage of 8.65 kV; a further increase of 2 kV brings the likely amorphatized area to 65.6%; and at the two largest acceleration voltages, 12.65 and 15.65 kV, 85.7% and 91.8% of the path fail to be indexed. The trend for GaP is similar, but the acceleration voltage required by a given fraction of the path to fail the indexing test is higher. For example, the acceleration voltage associated with 50% indexation is 13.2 kV for GaP, and 9.9 kV for InAs. In summary, the crystal orientation maps indicate that beamlets with high enough acceleration voltage are likely amorphatizing the surface of InAs and GaP, and that GaP is more resilient than InAs to the phase transformation.

Failure to be indexed as a crystal does not necessarily imply that the measured point is amorphous. An EBSP may display crystalline features, but if these are faint or distorted and the comparison with a standard pattern does not surpass an operator-chosen quality factor, the point will not be indexed. But, regardless of whether the crystal orientation map is a precise amorphization test, direct inspection of the EBSPs shows that the crystalline features progressively fade with increasing acceleration voltage, disappearing in most semiconductors at sufficiently high impact energy. This is illustrated in Fig. 3, which contains three EBSPs for each semiconductor: a reference pattern for the pristine crystalline structure and two patterns generated at an intermediate and the highest acceleration voltage used in each case. The sharp Kikuchi bands in the reference patterns, which are reflections of the crystallographic planes, become diffuse and in some cases darker than the background at the intermediate acceleration voltages, and are barely discernible at the highest acceleration voltages. The only exceptions are the EBSPs of SiC which, although somewhat blurred, retain the crystalline features at all voltages investigated. Since the backscattered electrons forming the EBSP come from depths of

up to some 50 nanometers inside the sample, the blurring and final disappearance of the crystalline features demonstrate that the most energetic beamlets amorphatize layers of a few tens of nanometers in Si, Ge, GaAs, GaP and InAs. The contrast reversal of some Kikuchi bands may be another sign of the presence of a thin amorphous layer. For example, a similar phenomenon occurs in crystalline samples when the source of backscattered electrons is deep under the surface, because of the strong absorption of backscattered electrons by the atomic positions in the crystallographic planes between the source and the surface.¹⁶ In the case of a thin amorphous layer a fraction of the incident electron beam will go through the amorphous phase and reach the crystalline region below, and the resulting backscattered electrons should form Kikuchi bands in the EBSP. The contrast reversal must be due to the interaction of the backscattered electron with a media other than the original crystal in its way towards the surface, and the amorphous layer could be this new media.

The thickness of the amorphous layer may be inferred from the EBSPs using a dynamical simulation of the electron diffraction phenomena,¹⁶ but such exercise is beyond the scope of this article. Instead we compare the EBSPs of the bombarded samples with the EBSP of the pristine crystal to rank the semiconductors according to their resistance to amorphization. To quantify the modification of a crystal we measure a series of 56 EBSPs traversing the beamlet's path at 20 micron intervals, and compute the correlation of each EBSP with the first one in the series. The latter, measured outside of the area bombarded by the beamlet, is the pattern of the pristine crystal. We then average the correlations for the 10 points nearer the center of the path, and use this value to describe the atomic arrangement: a value of 1 indicates that the surface remains a pristine crystal, while a value of 0 indicates that the substrate has become amorphous within the penetration range of the electron beam. Figure 4 illustrates this analysis with two GaAs samples

bombarded at 7.65 and 19.65 kV. The average correlation for the samples are 0.76 and 0.033 respectively, i.e. the nanodroplets have enough energy to modify the crystalline arrangement in both cases, but only the more energetic beamlet produces extensive amorphization. Note that the boundaries of the paths are sharp, extending only about three pixels or equivalently 60 microns. Figure 5 shows the correlation of the EBSPs as a function of the acceleration voltage, for all semiconductors. SiC is the material most resilient to amorphization, its bombarded surface departing little from the pristine crystal even at the highest impact velocity employed in the experiments. All other semiconductors are amorphatized by the beamlet: InAs requires the lowest impact velocity, Si and Ge behave similarly and rank second weakest, GaAs follows them, and GaP is the most resilient. In all cases the elimination of the crystalline features in the EBSPs increases monotonically with acceleration voltage. Molecular dynamics simulations of the impact of a nanodroplet on single-crystal Si have shown that the amorphization is caused by the melting of the region surrounding the impact, followed by an ultrafast quench that solidifies the melt through a glass transition.¹¹ Although fast quenching is a general amorphization mechanism, the present case is unique due to the high dissipation of energy and the concentration of the dissipation within a layer a few nanometers thick below the surface, which combine to produce quenching rates exceeding 10^{13} K/s. Since these cooling rates are much higher than the minimum ones preventing recrystallization, e.g. Si recrystallizes at cooling rates below 10^9 K/s,¹⁷ the major factor determining the resiliency of these semiconductors to amorphization must be the specific energy needed to melt them. To test this hypothesis we use the thermal properties and calculations listed in Table I. The impact of a nanodroplet compresses the substrate underneath, lowering the melting point T_m due to the negative pressure coefficients dT_m/dp of these materials. Table I lists the melting points at both atmospheric pressure and 10 GPa, the latter being a typical

condition for melting under nanodroplet impact based on molecular dynamics simulations of the amorphization of Si.¹² We could not find the pressure coefficient of GaP and SiC, and cannot estimate their melting points at 10 GPa. With these values and the dependence of the specific heat with temperature (values at 273K are listed for reference), we estimate the energy per atom required to elevate the temperature from 273K to the melting point, $Q_{Tm} = \int_{273K}^{Tm} C_p(T) dT$; SiC is the crystal that requires the most energy to reach the melting point, more than doubling the values for GaP, GaAs and Si, and almost quadrupling the values for InAs and Ge. Table I also lists the heats of fusion, ΔH_m : they are nearly identical for GaP and SiC, followed by the values of Si and GaAs, while the heats of fusion for InAs and Ge are the lowest. The last row of Table I shows the total energy per atom needed to melt the crystals which, with the exception of the value for Ge, follow the same order as the resiliency to amorphization. SiC with a value of 1.47 eV/atom requires the most energy, followed by GaP at 0.98 eV/atom. GaAs and Si are in third place at 0.88 eV/atom, while InAs is the easiest crystal to melt and amorphatize at a distant 0.65 eV/atom. Germanium is the only exception to the good correlation, requiring an energy similar to that of InAs for melting but amorphatizing at a projectile velocity comparable to that of Si. When compared to Si, which has the same crystalline structure as Ge, the reason for the latter needing an unexpectedly high impact velocity to amorphatize may be a dependence of dissipation on the atomic mass of the substrate. In related experiments and molecular dynamics simulations we have observed that the mass of the projectile's molecule plays an important role in the sputtering of Si, heavier molecules producing more energetic atoms by knock-on collisions and dissipating a higher fraction of their kinetic energies, and consequently elevating more the temperature of the target's surface, than lighter molecules at the same impact velocity. Conversely, it is likely

that at fixed projectile's molecular mass the heavier Ge atom will require a higher impact velocity to dissipate the same energy than the lighter Si atom.

Finally, the cross-sectional TEM images of Si, GaAs, GaP and InAs samples in Fig. 6 directly show the extent and structure of the amorphous layers. All micrographs present a similar sequence of bands: a spotted region formed by a protective layer of platinum deposited on the surface during sample preparation; a bright and thin layer corresponding to the amorphatized surface of the target; and the crystalline substrate which, in the vicinity of the amorphous layer, displays sharp contrast variations due to the distortion of the lattice and twin defects. The higher resolution micrograph for each material directly shows the diffuse features characteristic of the amorphous phase versus the periodic patterns of the crystalline substrate. The amorphous layer is undulated: at these impact velocities the nanodroplets carve craters with diameters and depths of the order of their diameters, and the ripples on the surface are due to the intertwinement of these nanocraters. The amorphous layer has a thickness of several tens of nanometers in the case of Si, and is thinner for the other three semiconductors.

IV. CONCLUSIONS

Electrosprayed nanodroplets impacting at sufficient velocity amorphatize thin surface layers on Si, Ge, GaAs, GaP and InAs. They also distort the crystalline arrangement of SiC, but not enough to amorphatize it at the impact velocities used in this article (7.06 km/s is the highest value). The melting of a thin surface layer by the impact and the subsequent quenching is the amorphization mechanism, and the specific energy needed to melt each semiconductor correlates well with their resiliency to amorphization. The capacity for melting any material and the ultrafast cooling rates associated with the low penetration of the projectiles are ideal for testing

the limits of surface amorphization, and we plan to investigate whether some elemental metals can be amorphatized using this technique.

ACKNOWLEDGMENTS

This work was funded by the Air Force Office of Scientific Research, Grant No. FA9550-11-1-0308. The authors are grateful for the support of the AFOSR Program Manager Dr. Birkan.

Table I. Relevant thermal parameters for InAs, Ge, Si, GaAs, GaP and SiC: atomic density d_{at} (10^{28} m^{-3}); melting point at 1 atm and 10 GPa, T_{m} (K); heat capacity per atom at constant pressure and 273 K, C_{p} (10^{-4} eV/at K); energy needed to rise the temperature from 273 K to the melting point Q_{Tm} (eV/at); heat of fusion ΔH_{m} (eV/at); and total energy needed to melt the crystal at 273 K, $\Delta H_{\text{m}} + Q_{\text{Tm}}$ (eV/at). The parameters are taken from references [18,19,20].

	InAs		Ge		Si		GaAs		GaP		SiC	
d_{at}	3.60		4.42		4.99		4.43		4.94		9.66	
T_{m}	1210	780	1210	830	1685	1105	1513	1173	1730		2810	
C_{p}	2.41		2.22		2.31		2.38		2.21		3.47	
Q_{Tm}	0.26	0.13	0.23	0.13	0.37	0.20	0.33	0.23	0.37		0.87	
ΔH_{m}	0.39		0.38		0.52		0.55		0.61		0.6	
$\Delta H_{\text{m}} + Q_{\text{Tm}}$	0.65	0.52	0.61	0.51	0.89	0.72	0.88	0.78	0.98		1.47	

FIGURE CAPTIONS

Figure 1. a) Sketch of the experimental setup; b) path traced on a silicon wafer by the beamlet, operated at increasing acceleration voltage from left to right. The first of 23 vertical lines is traced at $V_A = 9.75$ kV, and successive lines at 400 V increments.

Figure 2. SEM images of paths traced by the beamlet on InAs and GaP at increasing acceleration voltage, together with EBSD crystal orientation maps of the surfaces. Red pixels indicate that the material is crystalline InAs or GaP with the [100] direction along the surface normal, while black pixels correspond to points that cannot be indexed as crystalline.

Figure 3. EBSPs of Si, Ge, GaAs, GaP, InAs and SiC samples for the pristine surfaces, and after nanodroplet bombardment at intermediate and high acceleration voltages. The impacts reduce and in some case eliminate the crystalline features of the EBSPs.

Figure 4. Correlation between the EBSPs along a line traversing the beamlet path and the EBSP of the pristine GaAs crystal, for two acceleration voltages.

Figure 5. Correlation between the EBSPs of bombarded samples and their pristine crystals, as a function of the acceleration voltage and the velocity of the droplets. InAs requires the lowest impact velocity to develop an amorphous layer, followed by Ge, Si, GaAs and GaP. The crystalline structure of SiC remains relatively unchanged at these projectile velocities.

Figure 6. Cross-sectional TEM images of bombarded Si, GaAs, GaP and InAs substrates, showing the extent and structure of the amorphous layers.

Figure 1. a) Sketch of the experimental setup; b) path traced on a silicon wafer by the beamlet, operated at increasing acceleration voltage from left to right. The first of 23 vertical lines is traced at $V_A = 9.75$ kV, and successive lines at 400 V increments.

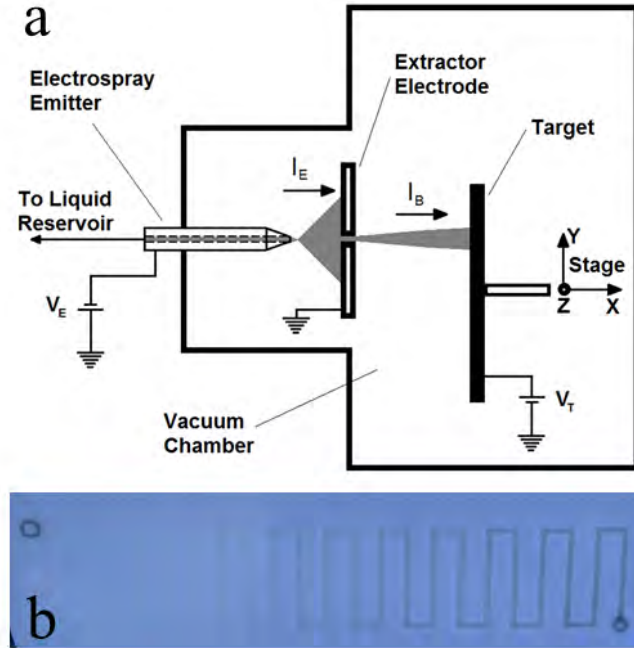


Figure 2. SEM images of paths traced by the beamlet on InAs and GaP at increasing acceleration voltage, together with EBSD crystal orientation maps of the surfaces. Red pixels indicate that the material is crystalline InAs or GaP with the [100] direction along the surface normal, while black pixels correspond to points that cannot be indexed as crystalline.

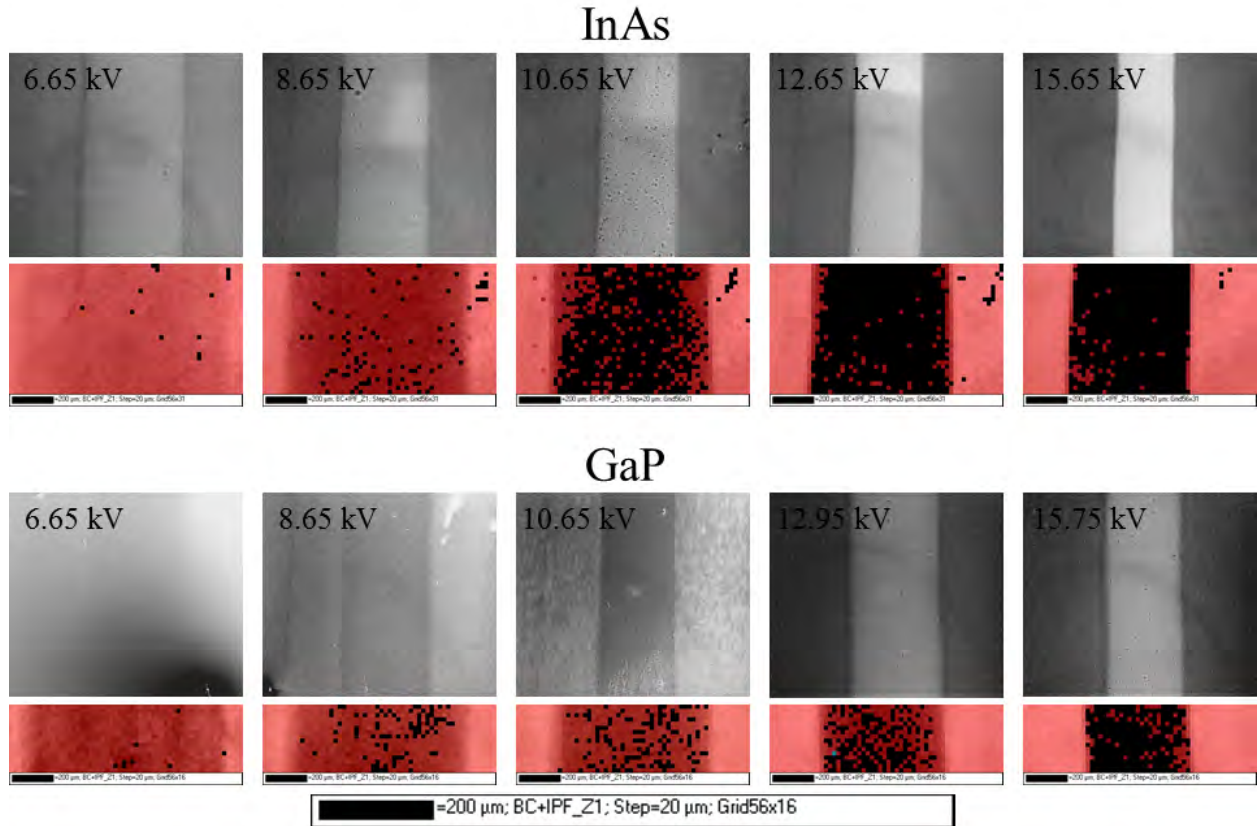


Figure 3. EBSPs of Si, Ge, GaAs, GaP, InAs and SiC samples for the pristine surfaces, and after nanodroplet bombardment at intermediate and high acceleration voltages. The impacts reduce and in some case eliminate the crystalline features of the EBSPs.

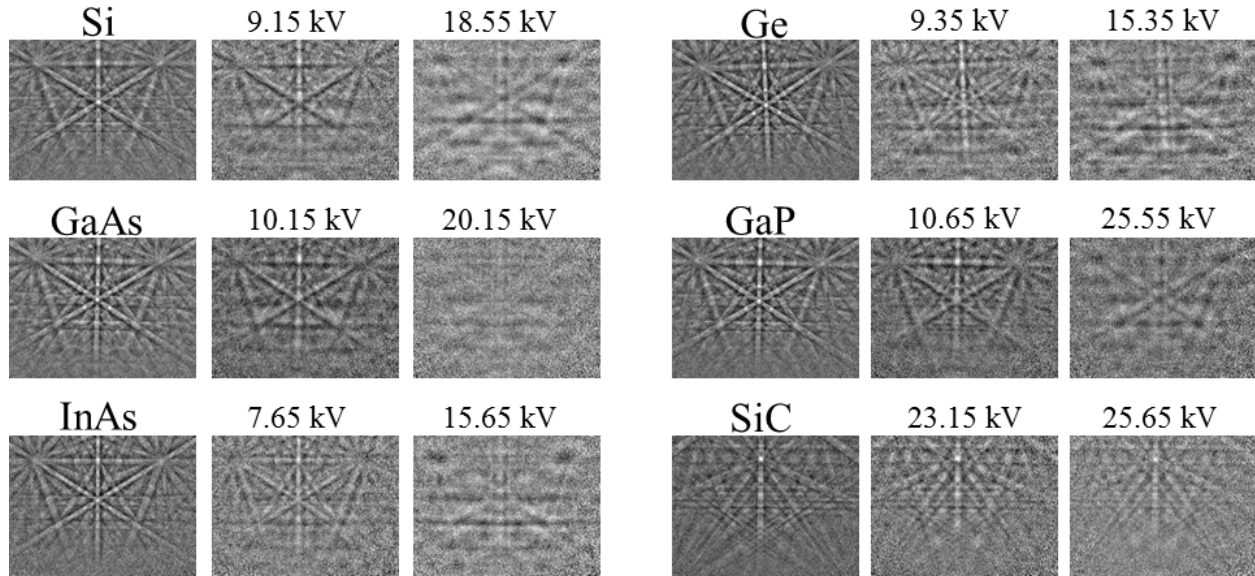


Figure 4. Correlation between the EBSPs along a line traversing the beamlet path and the EBSP of the pristine GaAs crystal, for two acceleration voltages.

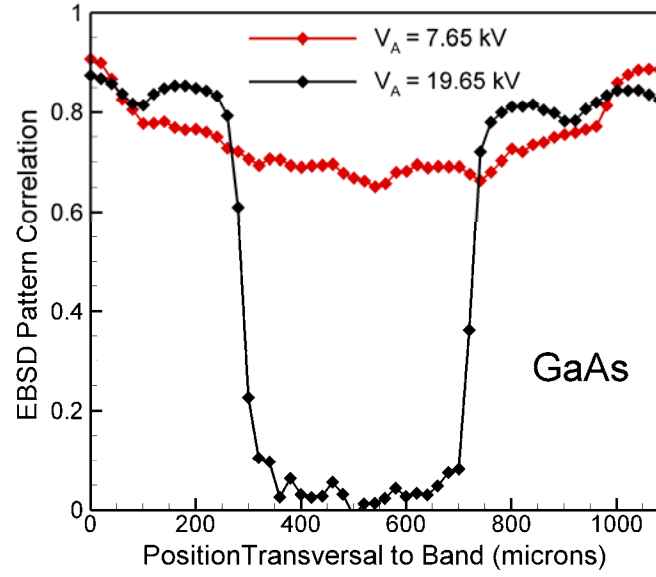


Figure 5. Correlation between the EBSPs of bombarded samples and their pristine crystals, as a function of the acceleration voltage and the velocity of the droplets. InAs requires the lowest impact velocity to develop an amorphous layer, followed by Ge, Si, GaAs and GaP. The crystalline structure of SiC remains relatively unchanged at these projectile velocities.

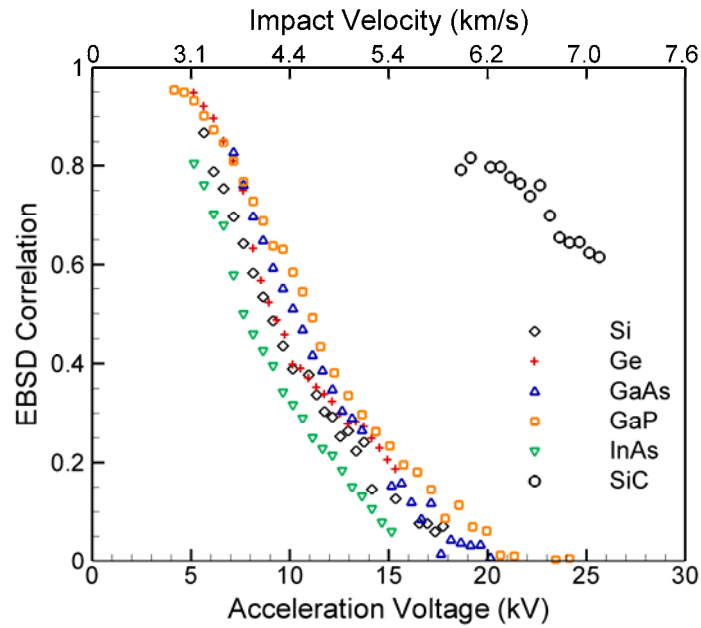
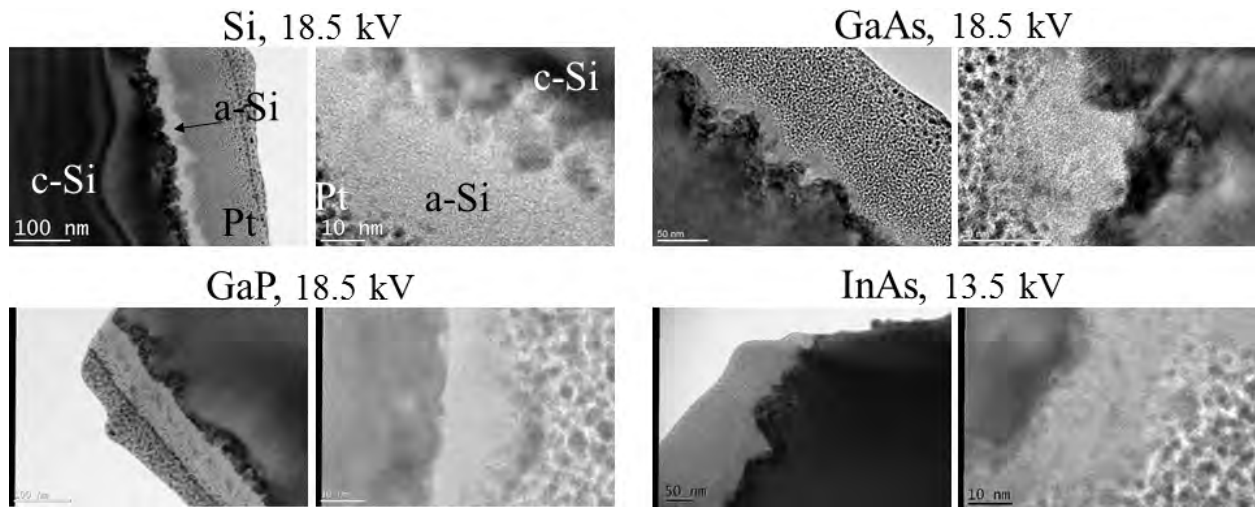


Figure 6. Cross-sectional TEM images of bombarded Si, GaAs, GaP and InAs substrates, showing the extent and structure of the amorphous layers.



REFERENCES

- ¹ J.F. Mahoney, Microcluster-surface interactions: a new method for surface cleaning. *International Journal of Mass Spectrometry* 174, 253-265 (1998).
- ² J.F. Mahoney, J. Perel, S.A. Ruatta, P.A. Martino, S. Husain, T.D. Lee, Massive cluster impact mass-spectrometry - a new desorption method for the analysis of large biomolecules. *Rapid Communications in Mass Spectrometry* 5, 441-445 (1991).
- ³ M. Gamero-Castaño & V. Hruby, Electrospray as a source of nanoparticles for efficient colloid thrusters. *Journal of Propulsion and Power*, 17, 977-987 (2001).
- ⁴ M. Gamero-Castaño and M. Mahadevan, Sputtering of silicon by a beamlet of electrosprayed nanodroplets. *Applied Surface Science*, 255, 8556-8561 (2009).
- ⁵ L. de Juan and J. Fernández de la Mora, *J. Colloid Interface Sci.* 186, 280 (1997).
- ⁶ M. Gamero-Castaño & V. Hruby, Electric measurements of charged sprays emitted by cone-jets. *Journal of Fluid Mechanics*, 459, 245-276 (2002)
- ⁷ J. Fernández de la Mora and I.G. Loscertales, The current transmitted through an electrified conical meniscus. *Journal of Fluid Mechanics*, 260, 155–84 (1994).
- ⁸ I. Yamada and N. Toyoda, Nano-scale surface modification using gas cluster ion beams – A development history and review of the Japanese nano-technology program. *Surface & Coatings Technology*, 201, 8579–8587 (2007)
- ⁹ R. Krpoun and H.R. Shea, Integrated out-of-plane nanoelectrospray thruster arrays for spacecraft propulsion. *Journal of Micromechanics and Microengineering*, 19, 045019 (2009).
- ¹⁰ M. Gamero Castaño, A. Torrents, L. Valdevit, and J.-G Zheng, *Phys. Rev. Lett.* 105, 145701 (2010)

- ¹¹ F. Saiz and M. Gamero Castaño, Amorphization of silicon induced by nanodroplet impact: A molecular dynamics study. *Journal of Applied Physics*, 112, 054302 (2012).
- ¹² F. Saiz, R. Borrajo-Pelaez, M. Gamero Castaño, The influence of the projectile's velocity and diameter on the amorphization of silicon by electrosprayed nanodroplets, *Journal of Applied Physics*, 114, 034304 (2013).
- ¹³ J.D. Majumdar and I. Manna, Laser material processing. *International Materials Reviews*, 56, 341-388 (2011).
- ¹⁴ A. McEwen, H.L. Ngo, K. LeCompte and J.L. Goldman, Electrochemical properties of imidazolium salt electrolytes for electrochemical capacitor applications. *Journal of The Electrochemical Society*, 146, 1687-1695 (1999).
- ¹⁵ M. Gamero-Castaño, Retarding potential and induction charge detectors in tandem for measuring the charge and mass of nanodroplets. *Review of Scientific Instruments*, 80 053301 (2009).
- ¹⁶ A.J. Schwartz, M. Kumar, B.L. Adams and D.P. Field, Editors. *Electron Backscatter Diffraction in Materials Science*, 2nd Ed. Chapter 2. Springer, New York, 2009.
- ¹⁷ A. Hedler, S.L. Klaumünzer and W. Wesch, Amorphous silicon exhibits a glass transition. *Nature Materials*, 3, 804-809 (2004)
- ¹⁸ *Handbook on Physical Properties of Semiconductors, Volume 1 Group-IV Semiconductors*, S. Adachi Editor. Kluwer Academic Publishers 2004.
- ¹⁹ *Handbook on Physical Properties of Semiconductors, Volume 2 III-V Compound Semiconductors*, S. Adachi Editor. Kluwer Academic Publishers 2004

- ²⁰ R. Devanathan, F. Gao and W.J. Weber, Atomistic modeling of amorphous silicon carbide using a bond-order potential. Nuclear Instruments and Methods in Physics Research B, 255, 130–135 (2007).

Visualization of beams from ionic liquid ion sources for focused ion beam applications

Carla S. Perez-Martinez^{a)} and Paulo C. Lozano

Department of Aeronautics and Astronautics, Massachusetts Institute of Technology, Cambridge, Massachusetts 02139

(Received 29 June 2012; accepted 26 July 2012; published 10 August 2012)

Ionic liquid ion sources (ILIS) share qualities with liquid metal ion sources necessary for focused ion beams (FIB) operation, such as pure ion emission and low energy spreads. These sources work at lower currents, room temperature, and are able to produce both positive and negative ions from a large number of ionic liquids. The influence of the applied voltage on the beam emitted from the ILIS based on the liquid EMI-BF₄ (1-ethyl 3-methyl imidazolium tetrafluoroborate) is characterized by using a beam visualization system. As the applied voltage is increased, the source transitions from single to multiple beam emission. The visualization tool is also used to determine the spatial distribution of the neutral particle population contained within the beam emitted from ILIS. Cluster ions can break during flight, yielding a new ion and neutral particles. This neutral population can be highly energetic, and might be of interest for material treatment applications where charging of targets is undesirable. For FIB applications, these neutrals could lead to undesired effects in the sample, and so it is necessary to know the distribution of the neutrals within the beam in order to specify the filtering and optics required to implement an ILIS-based FIB. It is found that 20% of the ion beam results from fragmentation events, and that the neutral population is concentrated at the center of the beam. © 2012 American Vacuum Society. [<http://dx.doi.org/10.1116/1.4745187>]

I. INTRODUCTION

Focused ion beams (FIB) are an important tool in micro and nanofabrication for microscopy, spectroscopy, micromachining, and lithography. Traditionally, FIB technology has relied on liquid metal ion sources (LMIS), of which the most developed and widely used is the gallium source,¹ although other elements like Au, Cs, or In can be produced. LMIS are also capable of providing elements like As, B, Bi, and Si if an alloy source is used.² Recently, the addition of high brightness helium and neon beams through the advancements in field ionization sources has provided more high-resolution tools for microscopy and lithography.^{3,4} Nonetheless, there is still a need for ion sources capable of delivering heavy ion species as well as negatively charged ions, which would diversify the number of FIB applications.

Ionic liquid ion sources (ILIS) have been recently proposed as a new tool for FIB.^{5,6} ILIS are very similar to LMIS, but they rely instead on the field evaporation from room-temperature molten salts, or ionic liquids. These substances are a mixture of complex organic and inorganic ions, which have negligible vapor pressures, making them apt for operation in vacuum. In addition, ionic liquids have high conductivities and low surface tensions, which make them capable of being electrostatically stressed to obtain ion evaporation.

The ILIS consists of an electrochemically treated tungsten needle—the emitter—coated with an ionic liquid (Fig. 1). The emitter is placed in front of a downstream metallic extractor, and a potential difference of 1–2 kV is applied between the emitter and the extractor in order to electrostatically stress the liquid meniscus. Once the electrostatic traction due to the

applied voltage exceeds the liquid surface tension, the liquid at the tip develops into a Taylor cone. At the apex of the cone, the electric field could reach values of a few V/nm, which allows ion evaporation; the ions could then be directed to an optics column for focusing and, subsequently, to a substrate for patterning. Since the ionic liquid contains both cations and anions, it is possible to obtain positive or negative beams by simply reversing the polarity of the power supply. In addition, the variety of available ionic liquids is immense, which could allow obtaining many different ion species that could be tailored for a particular application. Some ionic liquids have ions with reactive species and could be used for etching applications; it has been shown that ILIS are capable of etching silicon at rates faster than those of LMIS, since the ions from ILIS likely react with the surface and create volatile species that aid in material removal.⁷ It is then, of interest, to study the applicability of these versatile sources in a focused ion beam column.

The beams obtained from ILIS have several characteristics that make them suitable for FIB operation. In FIB, a figure of merit is the probe size (the size of the beam after focusing), which is limited by chromatic and spherical aberrations of the optical system. ILIS are capable of stable operation at currents as low as a few nA, thus lessening chromatic and spherical aberrations. Currents this low are generally not stable with LMIS, as the Taylor cone cannot be maintained at the reduced potentials due to the higher surface tension of liquid metals. Furthermore, the beams obtained from ILIS contain highly monoenergetic populations with energy spreads of a few eV,^{8,9} which are required to reduce chromatic aberrations in an optical column.

In order to implement ILIS in FIB applications, it is required to characterize the source behavior under different

^{a)}Electronic mail: carlita@mit.edu

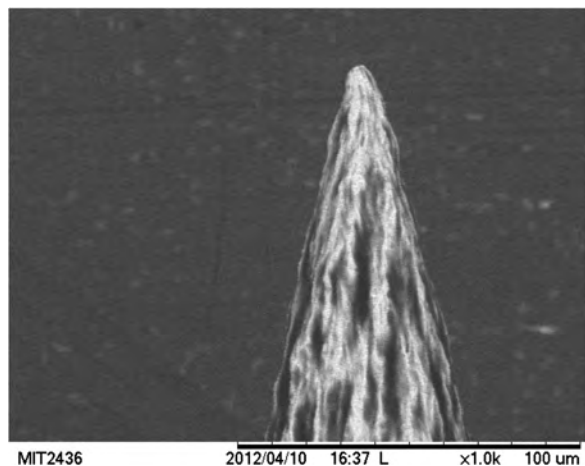


FIG. 1. Scanning electron micrograph of the tip of an ILIS emitter wetted by the liquid EMI-BF₄.

conditions as well as the different particle populations within the beam. An ionic liquid composed of anions (A⁻) and cations (C⁺) will produce ion species (AC)_nA⁻ or (AC)_nC⁺, for the negative and positive extraction polarity, respectively, and where n , the degree of solvation, is the number of neutral clusters attached to the ion ($n=0, 1$, and sometimes 2). These clusters of ions are metastable, and they can break during flight, yielding neutrals and a new ion. From experimental observations, it is known that breakup can happen in regions of zero potential as well as in the acceleration zone between the emitter and the extractor.^{9,10} This work aims at identifying the spatial distribution of the neutral particles within the beam.

A beam visualization system (BVS) is used to characterize the shape of the beam produced by an ILIS based on the liquid EMI-BF₄ (1-ethyl 3-methyl imidazolium tetrafluoroborate, C₆H₁₁N₂⁺-BF₄⁻) as the applied potential is modified. Retarding potential analyzer (RPA) measurements are performed to estimate the breakup rate of particles within the beam, and the visualization system is used to determine the spatial distribution of the neutral particles within the beam.

II. ION FRAGMENTATION

As mentioned in Sec. I, the beams obtained from ILIS have several ion species. Previous time-of-flight mass spectrometry indicates that the current in the beam for the liquid EMI-BF₄ is roughly equally divided between the $n=0$ and $n=1$ degrees of solvation,⁵ with some minor contribution of larger species. It is found that the heaviest species ($n \geq 1$) are metastable, and a fraction of them breakup during flight. Evidence for the occurrence of breakup events is found in the retarding energy spectra for the full beam.

A large fraction of the emitted current is indeed a highly monoenergetic population with an energy close to the applied potential, but there is also a population of ions coming with a continuum of energies below the main energy peak, since these ions are the result of breakup of larger species.⁸ Ideally, all ions should have a final kinetic energy $K = qV_{\text{app}}$, where V_{app} is the applied potential. However, if

an ion with degree of solvation n and mass m_n breaks into a neutral and an ion with degree of solvation m ($m < n$) and mass m_m , at a region with potential V_b , the final kinetic energy of the ion resulting from breakup is given by

$$K_m = qV_b + \frac{m_m}{m_n}q|V_{\text{app}} - V_b|. \quad (1)$$

The resulting neutral has an energy given by

$$K_{\text{neutral}} = \frac{m_n - m_m}{m_n}q|V_{\text{app}} - V_b|. \quad (2)$$

If ions break up in the acceleration zone, they can have energies anywhere between $m_m q V_{\text{app}} / m_n$ (if breakup occurs after the heavy ion is fully accelerated, $V_b = 0$) and up to $K = qV_{\text{app}}$ (if fragmentation occurs soon after emission, $V_b = V_{\text{app}}$). Notice that the neutrals resulting from breakup can have energies of hundreds of electron volts if they are the result of breakup late in the acceleration zone. Then, the beams obtained from ILIS have a population of highly energetic neutrals, which could be of interest in applications like etching of dielectric materials, where charging leads to undesired features in the substrate.¹¹ For FIB applications, it would be necessary to deflect the beam to prevent neutrals, which cannot be focused, from provoking any undesired effects in the sample. Therefore, it is of interest to determine the neutral population distribution within the ion beam.

III. EXPERIMENTAL METHODS

The emitter is a 0.5 mm diameter tungsten wire, treated electrochemically to produce a tip with a 5 μm radius of curvature (Fig. 1). In order to facilitate wetting by the ionic liquid, the emitter was micro roughened in a hot solution of NaOH (1 N) and K₃Fe(CN)₆. The fabrication procedure is similar to the one described in Ref. 5, although we have skipped the emitter annealing step. The emitter is held in place by a copper clamp; the copper piece has a 2.54 mm diameter stainless steel cylinder filled with ionic liquid, which serves as a liquid reservoir, located approximately 3 mm away from the emitter tip.

The extractor consists of a grounded stainless steel plate with a 1.6 mm diameter aperture, followed by another grounded stainless steel plate with a 4.76 mm diameter aperture; this second plate functions as a shield, and holds a small magnet which traps any secondary electrons produced if ions impact components of the experimental setup.

A signal generator (Agilent 33220 A) connected to a high voltage power supply (Matsusada AMS-5B6) is used to direct the voltage applied to the tip. The current emitted by the source is determined by measuring the voltage drop across a 1 M Ω resistor placed in series with the power supply. All tests are conducted at room temperature at pressures below 1.3×10^{-4} Pa.

A. Retarding potential analyzer

In order to estimate the percentage of the beam current that results from breakup for the operating conditions used

for the visualization experiments, we fire the ion source toward a retarding potential analyzer. The RPA is composed of five grids, followed by a Faraday cup detector. All grids are 90% transparent tungsten mesh. The entrance grid is grounded and located 26 mm downstream of the extractor. The next three grids serve as the retarding grids, and are followed by a secondary electron retarding grid, set to -15 V. The Faraday cup functions as a collector, and is connected to an oscilloscope through a high impedance electrometer (Keithely 6514). A high voltage triangular wave is applied to the retarding grids while the ILIS is emitting, and the collected current signal is processed using a low pass filter.

B. Beam visualization system

The BVS setup is shown in Fig. 2. The copper clamp is placed on a triaxial stage with submicron resolution, while the extractor is held fixed. In this way, we can adjust the emitter position with respect to the extractor *in situ*. The stage and extractor are placed in a vacuum chamber, so that the beam is directed toward a visualization system located at the side of the chamber. The extractor is placed 77 mm away from the entrance of the viewing system, which is composed by a microchannel plate (MCP) detector and a phosphor screen. When a sufficiently energetic particle hits the surface of one of the channels in the plate, electrons will be emitted from the surface and be driven toward the back of the microchannel plate by the applied potential V_{MCP} . The electrons then hit the phosphor screen, biased at V_P . The phosphor screen will glow when impacted by electrons, and the image is recorded with a CCD camera.

In order to visualize only the neutral population within the beam, we have installed two stainless steel deflector plates 7 mm downstream from the extractor exit. One of the plates is biased to a potential V_{def} while the other is kept grounded. The deflector plates produce a uniform electric field along 12.7 mm of the path of the beam, and thus deviate the charged particles from their normal trajectory, but do not affect the neutral particle trajectory. Then, the image produced in the BVS corresponds only to the impact from the neutral particles. For these tests, we apply a square wave signal to the emitter from $-V_{app}$ to V_{app} with a period of 10 s. A 1.5 kV voltage is applied to the biased plate of the deflector every other period of the emitter in such a way that we can

image the full beam in one period and the neutral particles over the next period.

IV. RESULTS AND DISCUSSION

A. Retarding potential analyzer

For these tests, the ILIS start-up potential was found to be close to ± 1.38 kV, with the source positioned approximately 1 mm away from the extractor. The emitted currents by this particular source were found to be in the order of a few nA.

We measure the energy of the full beam emitted at $V_{app} = 1.4$ kV, and the collected current as a function of the retarding potential is shown in Fig. 3. This energy curve is a low-resolution measure of the beam energy distribution as there are two artifacts in the data provoked by the instrument: (1) artificial spreading in the energy signal due to beam divergence and (2) potential *sagging*, explained below. The purpose of this experiment is not to determine the precise energy characteristics of our source, but rather to estimate the level of ion fragmentation (hence, neutral production) for a source operating in the conditions used for the visualization experiments, which is possible despite these effects.

(1) *Spreading*. Previous studies indicate that the beam emitted from an EMI-BF₄-based ILIS has a half aperture angle of approximately 18° ,¹² i.e., an ion can approach the retarding grids at an angle θ between 0° and 18° with respect to the axis. An ion with energy qV_0 should ideally be stopped by a potential barrier $V_{RP} = V_0$. However, an ion coming at an angle θ will be deflected by a potential $V_{RP} = V_0 \cos^2 \theta$. Then, since the RPA instrument is capturing the whole beam, it should be expected to see current decreases for a range of energies even if the ions come with a sharp energy distribution. In Fig. 3, we do not observe a sharp drop in beam current close to the applied potential, but rather a gradual decrease; the actual energy spread of the population coming close to the applied potential is sharper than what is measured, as was shown before.¹²

(2) *Sagging*. It can be observed that the amplitude of the measured current does not drop to zero for retarding potentials exceeding the applied potential; the emission potential must be exceeded by roughly 100 V before no current passes. The retarding grids should create deep equipotential regions

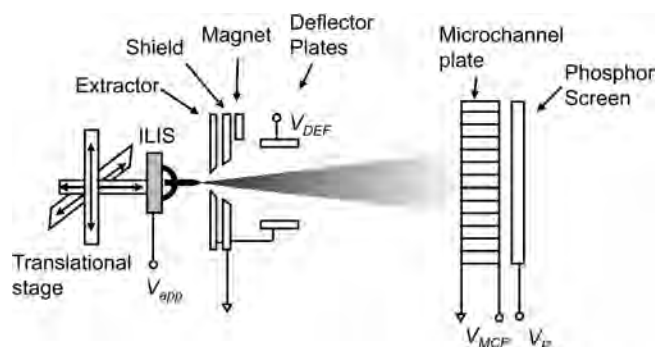


FIG. 2. Experimental setup for the beam visualization experiments.

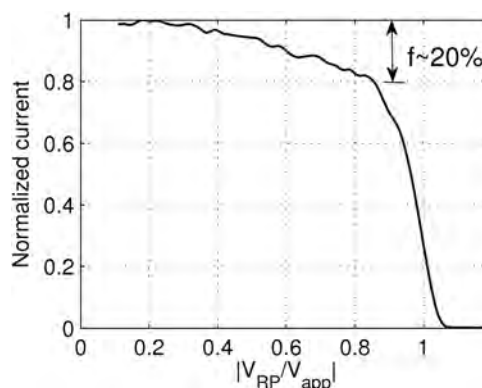


FIG. 3. Coarse RPA signal for $V_{app} = 1.4$ kV.

along the path of the beams, but this RPA uses coarse grids that do not provide a uniform potential. Then, even if the grid material is at the retarding potential, some intermediate regions can be at lower voltages, which allow some of the ions to leak to the collector even if they have energies less than V_{RP} .

Using the RPA data, it is estimated that 20% of the current is a result from breakup events. For an emitted current of 3 nA, the source produces 1.88×10^{10} ions per second and 3.75×10^9 neutral particles per second. From Fig. 3, it can be seen that the ions resulting from breakup have an approximately uniform energy distribution between $0.3V_{app}$ and V_{app} , as judged from the nearly linear slope in the energy spectra. Assuming most fragmentation events are from the $n = 1$ to the $n = 0$ degree of solvation, this energy range is to be expected, as the ratio of masses of the EMI+ molecule to the (EMI- BF_4)EMI+ molecule is 0.36 and Eq. (2) dictates the resulting EMI+ ion will have an energy of $0.36V_{app}$ if breakup occurs after the $n = 1$ ion is fully accelerated. In the same way, the neutrals produced have a uniform distribution of energies between a few eV (if they are produced soon after the ion is emitted) and approximately two thirds of the applied potential (if the neutral results from $n = 1$ to $n = 0$ breakup after the $n = 1$ ion has been fully accelerated).

B. Beam distribution

1. Influence of the applied voltage

We determine the change in behavior of the beam as the applied voltage is increased. For the beam visualization

experiments, the startup potential is found to be close to 1 kV. We increase the voltage gradually up to 1.5 kV while recording the emitted current and beam profile; for imaging, the BVS conditions are set to $V_{MCP} = 1.5$ kV and $V_P = 4.3$ kV. Figure 4 shows the beam contour and extracted current I for different applied potentials in the positive polarity. Each image corresponds to a snapshot of the BVS signal.

It had previously been determined that the beam profile is a parabolic function of the aperture angle.^{5,12,13} At the given gain set by the conditions of the BVS, the profiles for the lower voltages follow this shape, but at as the potential is increased, the current emitted and the intensity of the profile also increase, and the viewing system becomes saturated. Then, it is not possible to distinguish the shape of the beam in the center of the impacts in Figs. 4(d)–4(f), although the shape should remain parabolic as established by previous measurements at higher currents.¹³ In addition, the BVS has a limited detection efficiency that depends on its gain and the particle flux and energy. If the voltages of the MCP and phosphor screen are increased, the gain of the detector increases, and the detected profiles become wider as the particles coming at the edge of the beam, which have lower flux and lower energies, can be detected. The measurements presented here are a qualitative description of beam profiles, as they do not capture the full beam behavior; nevertheless, they provide the spatial distribution information required to complement electrical measurements and determine the basic trajectories of the beam.

For voltages close to the onset potential and up to 1.4 kV, the source has a single emission site as shown by the single

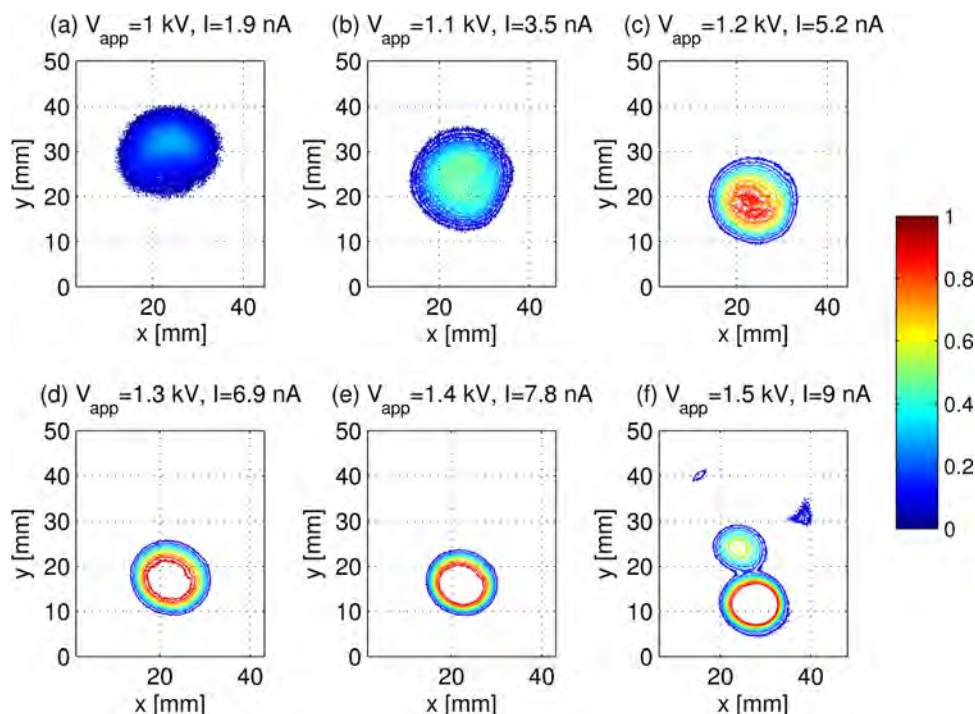


FIG. 4. (Color online) (a)–(f) Beam distributions as the applied potential is increased. The applied voltage and measured current for each case are indicated at the top of each panel. The x and y coordinates are the spatial coordinates of the image captured. The regions outside the profile contours correspond to zero intensity, while regions inside the contours that appear white have an intensity of one, since the BVS has become saturated. Slight distortion of the beam is produced by imperfections in the MCP used in these experiments.

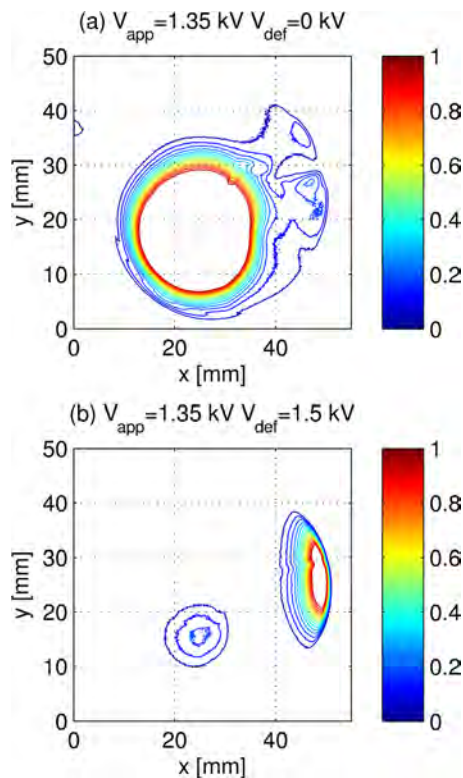


FIG. 5. (Color online) (a) Full beam distribution for $V_{\text{app}} = 1.35$ kV; irregular contour lines appearing for $x > 40$ mm are due to defects of the MCP that are attenuated at the higher gain conditions used for this trial. (b) Neutral beam distribution and deflected beam for $V_{\text{app}} = 1.35$ kV. Note that the deflected beam appears rounded off since the BVS has a circular imaging area and the deflected beam is directed toward the edge.

impact in the BVS. The beam changes direction as the applied potential is increased. If we exceed 1.5 kV, the source becomes unstable, and more emission sites can be obtained [Fig. 4(f)]. For this test, we have operated at low gain conditions, in order to be able to capture the behavior of the beam before reaching saturation—however, it was not possible to operate at lower gains without losing too much signal close to the startup potentials.

2. Neutral particle visualization

To determine the neutral population distribution, we operate the source at $V_{\text{app}} = \pm 1.35$ kV, and increase the gain of the viewing system by setting $V_{\text{MCP}} = 1.8$ kV and $V_p = 5$ kV. The full beam profile and neutral profile for the positive mode are shown in Figs. 5(a) and 5(b), respectively. Each image is the average of 20 frames taken every 0.2 s in order to reduce noise.

The width of the full beam profile and the saturation are greater for the higher gain conditions. In Fig. 5(a), the features to the side of the beam are due to MCP imperfections. From Fig. 5(b), we note that the charged particles in the beam have been redirected due to the deflector action, and that the impact observed must correspond to neutral particles that were unaffected by the applied electric field. The neutral population profile is centered at the same position as the non-deflected beam. This indicates that neutral particles are being

generated close to the center of the beam. The distributions might not be complete due to reduced detection efficiency, but they give us a qualitative idea of how particles propagate downstream.

V. SUMMARY AND CONCLUSIONS

The behavior of the beam as the applied potential is increased was determined, and the source operates stably close to the emission onset potential. The neutral particle distribution is concentrated toward the center of the beam and appears to have a smaller footprint than the ion beam.

ILIS operation in a single polarity is limited by the electrochemical decomposition of the liquid, as the accumulation of the counter ions on the surface of the electrode leads to the formation of a charge double layer across which electron transfer can occur, leading to reactions and emission degradation within a few minutes. The decomposition of the liquid can be avoided by alternating the polarity of the source to avoid the formation of the charged layer. It has been shown that the ILIS can operate stably for >200 h with voltage alternation frequency of 1 Hz.⁶ Current work is underway with different emitter configurations with the goal of minimizing or eliminating the requirement of voltage alternation.

ILIS have characteristics that make them apt for FIB operation, and could expand the capabilities of this technique thanks to the possibility of extracting negative ions and providing more ion species. To realize an ILIS-based FIB with the smallest probe size possible, it would be required to select the highly monoenergetic component of the beam and eliminate the neutral particles using an ExB filter. ILIS can also be used as a source of highly energetic neutrals containing reactive species, applicable in material treatment where charging is not acceptable; in order to implement this idea, further work would study the neutral particle interaction with materials. By providing not only beams suitable for FIB applications, but also by serving as a source of neutral particles, ILIS are an interesting tool for micro and nanofabrication.

ACKNOWLEDGMENTS

Partial funding for this work was provided by the National Science Foundation and by an AFOSR grant monitored by Mitat Birkan. C.P.-M. would like to thank the MIT Office of the Dean of Graduate Education and the MIT Department of Aeronautics and Astronautics for funding for this work. The authors wish to thank J. Gierak and S. Guilet (CNRS-LPN), and M. Martinez-Sanchez (MIT) for useful suggestions in this study.

¹J. Gierak, *Semicond. Sci. Technol.* **24**, 043001 (2009).

²J. Orloff, L. W. Swanson, and M. Utlaut, *High Resolution Focused Ion Beams: FIB and its Applications* (Springer, New York, 2002).

³B. W. Ward, J. A. Notte, and N. P. Economou, *J. Vac. Sci. Technol. B* **24**, 2871 (2006).

⁴D. Winston *et al.*, *Nano Lett.* **11**, 4343 (2011).

⁵P. Lozano and M. Martinez-Sanchez, *J. Colloid Interface Sci.* **280**, 149 (2004).

⁶P. Lozano and M. Martinez-Sanchez, *J. Colloid Interface Sci.* **282**, 415 (2005).

- ⁷C. Perez-Martinez, S. Guilet, N. Gogneau, P. Jegou, J. Gierak, and P. C. Lozano, *J. Vac. Sci. Technol. B* **28**, L25 (2010).
- ⁸P. Lozano, *J. Phys. D: Appl. Phys.* **39**, 126 (2006).
- ⁹T. P. Fedkiw and P. C. Lozano, *J. Vac. Sci. Technol. B* **27**, 2648 (2009).
- ¹⁰T. P. Fedkiw, "Characterization of an iodine-based ionic liquid ion source and studies on ion fragmentation," SM thesis (MIT, 2010).
- ¹¹D. Economou, *J. Phys. D: Appl. Phys.* **41**, 024001 (2008).
- ¹²P. Lozano and M. Martinez-Sanchez, "Efficiency estimation of EMI-BF₄ ionic liquid electrospray thrusters," in Proceedings of the 41st AIAA/ASME/SAE/ASEE Joint Propulsion Conference and Exhibit, Tucson, Arizona, 2005 (unpublished).
- ¹³C. Perez-Martinez, S. Guilet, J. Gierak, and P. C. Lozano, *Microelectron. Eng.* **88**, 2088 (2011).

Investigating Efficiency Losses from Solvated Ion Fragmentation in Electrospray Thruster Beams

Thomas M. Coles*, and Paulo C. Lozano†

Massachusetts Institute of Technology, Cambridge MA 02139

Electrospray thrusters use ionic liquids (room temperature molten salts) as propellants. When operating in ionic mode, these thrusters emit either individual ions or small ion clusters, typically comprised of 3 or sometimes 5 individual ions. These clusters are known as solvated ions. If these ions fragment into smaller clusters before complete emission from the thruster, efficiency and specific impulse can be significantly reduced because neutral anion-cation pairs can no longer be accelerated by the electric field. This work uses molecular dynamics simulations to compare emissions from a number of different ionic liquids to identify trends in solvated ion fragmentation to provide a new metric to consider when selecting a propellant for electrospray thrusters. It has been found that solvated ions from relatively complex ionic liquids (i.e. those with a large number of atoms per ion) are less likely to fragment than simpler ones, as there are more degrees of freedom in which to dissipate energy without fragmenting.

Nomenclature

η_p	Polydispersive efficiency
f_0	Current fraction due to directly emitted monomer ions
f_1	Current fraction due to directly emitted dimer ions
f_f	Current fraction due to fragmentation product monomer ions
q	Charge of an ion
m_n	Mass of a neutral cation-anion pair
m_0	Mass of a monomer ion
I_0	Beam current due to directly emitted monomer ions
I_1	Beam current due to dimer ions
I_f	Beam current due to fragmentation product monomer ions
I_T	Total beam current
RPA	Retarding Potential Analyzer

I. Introduction

ELECTROSPRAY thrusters are electrostatic propulsion devices that operate by using an electric field to extract ions or charged droplets from an electrically stressed conductive surface.¹ When an electric field is applied across a liquid surface between electrodes above and below it, the balance between surface tension and electric pressure results in the formation of a conical structure called a Taylor Cone.² The electric field is focused by the tip of the cone, rising to local values around 10^9 V/m when the applied field is only around 10^6 V/m. This strong electric field at the tip of the cone is sufficient to extract ions or charged droplets from the liquid surface. These ions or charged droplets are then accelerated by the electric field until passing through an aperture in the electrode above the liquid surface, thereby providing thrust.

Early work on electrosprays used a variety of solvents, including glycerol, formamide, and tributyl phosphate with the salts NaI and LiCl.^{3,4} However, these evaporate slowly under vacuum and generally result

*PhD Candidate, Department of Aeronautics and Astronautics, 77 Massachusetts Ave 37-438, AIAA Member

†Associate Professor, Department of Aeronautics and Astronautics, 77 Massachusetts Ave 37-401, AIAA Member

in the emission of charged droplets rather than ions. Due to a low charge to mass ratio, the specific impulse from this charged droplet emission is relatively low - no more than hundreds of seconds. However, a specific impulse of at least 3000s is attainable when operating in purely ionic mode,¹ which can be achieved when using ionic liquids as propellants.^{1,5,6} Ionic liquids are salts that are liquid at room temperature. The most common families of these liquids are comprised of complex organic cations with inorganic anions.

A key advantage of ionic liquids over other propellants is that they have zero vapor pressure and hence do not evaporate in vacuum - there is therefore no need for any pressurization when storing them onboard a spacecraft. There is also no need for active flow control, as emitters can be constructed from porous materials that feed the propellant passively through capillarity.⁷⁻⁹ Furthermore, the ions are complex in the sense that they consist of a large number of atoms and hence have high mass compared to the simple ions found in hall thrusters, ion engines, and liquid metal ion sources (LMIS). As a result of this high mass, the space charge considerations inherent in the design of some other electric propulsion systems are much less significant for electrosprays - high thrust density can be achieved well before reaching the space charge limit.

The first ionic liquid to be tested in an electrospray was EMI-Im (also known as EMI-TFSI, EMI-Tf₂N, or 1-ethyl-3-methylimidazolium bis(trifluoromethanesulfonyl)imide).³ Initial work was unable to achieve purely ionic mode emission with this liquid, but experiments with EMI-BF₄ (1-ethyl-3-methylimidazolium tetrafluoroborate) were able to demonstrate purely ionic emission.⁵ The later development of needle Ionic Liquid Ion Sources (ILIS) has enabled purely ionic emission of EMI-Im and most other ionic liquids of interest.^{6,10-12}

The thrust from an individual ionic electrospray emitter is in the nN range,¹¹ which is ideal for very precise station-keeping and formation flight. However, this technology can be scaled to much higher thrust by clustering large numbers of emitters together. Thrust areal density up to 0.5N/m² has been achieved with microfabricated arrays^{7-9,13} and an order of magnitude improvement should easily be attainable. When considering the mass of the thruster alone, the thrust mass density achieved by these thrusters is 0.05 N/kg. Individual thrusters can be manufactured with an area as small as 1 cm², requiring no more than 1 W of power. These characteristics are particularly beneficial for cubesat applications and it is significant that no pressurization or chemical energy is required, as cubesats typically share rides to orbit with much more expensive payloads and hence are prohibited from any significant energy storage so that there is no risk of damage.

Although cubesats are the initial application for this technology, it is also scalable to much higher power levels and larger spacecraft, not only because of the characteristics mentioned so far, but also because of high efficiency. Due to precise alignment of the emitters with the extractor apertures, beam interception is negligible. Heating of the thruster is also believed to be negligible. No energy is required for ionization, as the liquid already exists in ionic state. Some energy is required for extraction of the ions from the liquid surface to overcome the solvation energy, but this does not significantly affect thruster performance. However, one remaining consideration is efficiency losses in the acceleration of the thruster beam; these losses arise both from polydisperse effects (accelerating ions to different velocities) and the fragmentation of ion clusters after emission, forming neutral clusters that cannot be accelerated. A study of these efficiency losses is the focus of the molecular dynamics simulations carried out in this work; in particular, the effect of ionic liquid propellant selection is considered.

Section I.A provides more background on ionic liquids, then section II provides more detailed motivation for this work. Details of molecular dynamics simulations are provided in section III. A reader interested in the contribution of this work rather than this background information may wish to skip to the introductory paragraphs in section III and then from there skip directly to section IV.

A. Ionic Liquids

Ionic liquids typically consist of organic cations with inorganic anions, where the cations are generally based on aromatic rings (imidazolium, pyrrolidinium, or pyridinium) with the addition of hydrocarbon chains of various lengths, sometimes also incorporating various functional groups - commonly allyl, hydroxyl or methoxy. The emission rate from electrospray thrusters depends on the conductivity of the liquid, so a high conductivity liquid is desirable to give high thrust. Of the common ionic liquids that exist in liquid state at room temperature, the highest conductivities are typically achieved with the cation EMI (1-ethyl-3-methylimidazolium) and hence most ionic electrospray thruster work in the past has used liquids based on this. This cation can be seen in figure 1.

A vast variety of ionic liquids can be created and the field is rapidly growing every year with many new liquids being developed for a wide range of applications.¹⁴ Although the BF_4 anion is one of the most conductive, other anions are also worthy of consideration for use in electrospray thrusters. In particular, selection of liquids with different ion masses allows for a trade-off between thrust and specific impulse, as explained in section II.B. Furthermore, BF_4 -based liquids are highly hydrophilic^{14–16} and hence can easily be contaminated, especially as they tend to hydrolyze when stored in the presence of water for a significant time;^{17,18} this suggests that an alternative propellant would be preferable. Some other anions of interest are shown in figure 2 and are described below:

- Im (also known as Tf_2N or TFSI), bis(trifluoromethanesulfonyl)imide. This is a hydrophobic relatively high-mass anion and is currently one of the most popular ionic liquids for a variety of applications because of its stability and reasonable conductivity.
- FSI, bis(fluorosulfonyl)imide. This is a hydrophobic anion with higher mass than BF_4 , higher conductivity, and a lower melting point.^{19,20} However, it has not yet been tested in an electrospray.
- FAP (also known as MPI), tris(pentafluoroethyl)trifluorophosphate. This forms some of the most hydrophobic ionic liquids known²¹ and has been tested in an electrospray with the C_5MI cation.^{11,13}

The melting point of EMI-BF_4 is high (12°C) and hence heating may be required for use in space propulsion. Some of the other anions have somewhat lower melting temperatures (for example, -15°C for EMI-Im), but significantly lower melting temperature can be attained by using cations with long side chains. However, the conductivity decreases dramatically by using significantly larger ions because ion mobility is reduced, so cations larger than BMI (1-butyl-3-methylimidazolium) in the imidazolium family are unlikely to be of interest. Cations with symmetric side chains (for example, 1-ethyl-3-ethylimidazolium) are also of little interest for this application because the smaller number of possible conformations results in much higher melting temperatures.²²

II. The Impact of Thruster Beam Composition

The emissions from an ionic mode electrospray are typically comprised not only of individual ions, but also of small clusters, known as solvated ions. These solvated ions typically consist of an ion with attached neutral clusters. For example, when operating in ionic mode with positive polarity and the liquid EMI-BF_4 , the beam consists of $(\text{EMI-BF}_4)_n \text{EMI}^+$. For many liquids, the beam contains mostly $n = 0$ ions (known as monomers) and $n = 1$ ions (known as dimers).^{5,10,23} The $n = 0$ fraction is typically between 30% and 50%. A small proportion of $n = 3$ ions are also found. For more complex liquids, such as EMI-Beti and $\text{C}_5\text{MI-FAP}$, somewhat higher proportions of $n = 3$ and even $n = 4$ ions are found,^{11,13} but the largest constituents of the beam are still $n = 0$ and particularly $n = 1$.

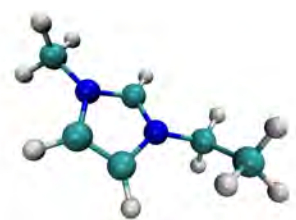


Figure 1. The EMI cation with net charge $+1$: white is H, green is C, blue is N.

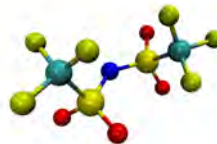
(a) BF_4



(b) FSI



(c) Im (TFSI)



(d) FAP (MPI)

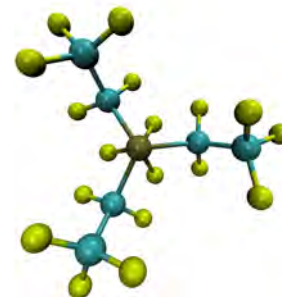


Figure 2. A selection of the inorganic anions forming ionic liquids discussed in this work. All have net charge of -1 . Green is carbon, blue is nitrogen, red is oxygen, dark brown is boron, light brown is phosphorous, small darker yellow if fluorine, and large lighter yellow (only on the central atoms of FSI and TFSI) is sulphur.

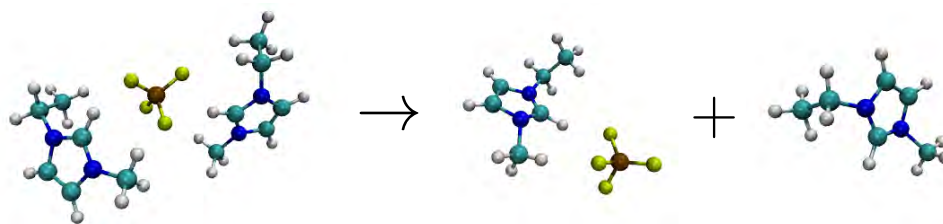


Figure 3. The ion fragmentation process illustrated for a positive dimer emitted from the liquid EMI-BF₄. The dimer on the left has +1 charge and fragments into a cation-anion pair with zero net charge and a cation monomer with +1 charge. The neutral pair can no longer be accelerated by the electric field and hence fragmentation is a cause of inefficiency if it occurs before the dimer is fully emitted from the thruster. Atom color descriptions are given in the captions to figures 1 and 2.

After extraction, these solvated ions can fragment, typically forming neutrals and ions with lower n .¹⁰ This process is illustrated for a dimer in figure 3. Occasional complete fragmentation into individual ions has been seen in computational models, but this effect is not believed to be significant; in this case, the ions of opposite polarity return to the liquid surface.²⁴ When fragmentation occurs after the ion has been completely emitted from the thruster, there is no impact on performance. However, fragmentation that occurs while the ion is still accelerating can significantly affect efficiency and specific impulse, as the neutral clusters formed during fragmentation cannot be accelerated by the electric field; if this fragmentation occurs before the neutrals have reached high speed, they drift out of the thruster slowly and provide only a negligible contribution to thrust, although this is partially compensated by the increased speed of the ion product, which accelerates faster at lower mass. An understanding of the factors affecting fragmentation is therefore important when selecting a particular ionic liquid as the propellant.

An additional factor affecting efficiency is polydispersity; this refers to the different sizes of ions present in the beam. When a given amount of energy is available for accelerating particles to provide thrust, it is always most efficient to use that energy to accelerate particles to the same size, as explained in section A. The presence of ions with various different n therefore causes efficiency losses because different mass implies different speed. Furthermore, fragmentation contributes to the distribution of particle sizes and so also affects these polydispersity losses.

A. A Simple Model of Efficiency for an Ionic Electrospray

To illustrate the impact of polydispersive efficiency quantitatively and further motivate the need to study fragmentation, a simple model is developed here as an expansion to the model reported in Ref 23, which in turn was a further development of the expression for polydispersive efficiency in the absence of fragmentation, as found in Ref 25.

Efficiency losses in space propulsion generally refer to wasted electrical power in the sense of conversion of electrical energy into a form other than useful kinetic energy in the thruster beam. However, a polydispersive efficiency loss is subtly different, as it does not refer to any loss in the conversion of electrical power into beam power. Indeed, a highly polydispersively inefficient system can still transfer its electrical power into beam power without loss of any energy into other forms. Instead, polydispersive efficiency is a measure of the effectiveness with which beam power contributes to thrust. For a given thrust and mass flow, the minimum beam power requirement occurs when all of the emitted particles have the same velocity. This can be shown by solving a simple constrained optimization problem with Lagrange multipliers; it arises from the presence of speed as a linear term in momentum, but as a squared term in kinetic energy. The polydispersive efficiency is then defined as the ratio of this minimum power requirement to the actual beam power.

The following expression for polydispersive efficiency in the presence of fragmentation is derived in appendix A, under the assumption that only $n = 0$ and $n = 1$ ions are emitted from the surface:

$$\eta = \frac{\beta^2}{1 + (\xi - 1)f_0} \quad (1)$$

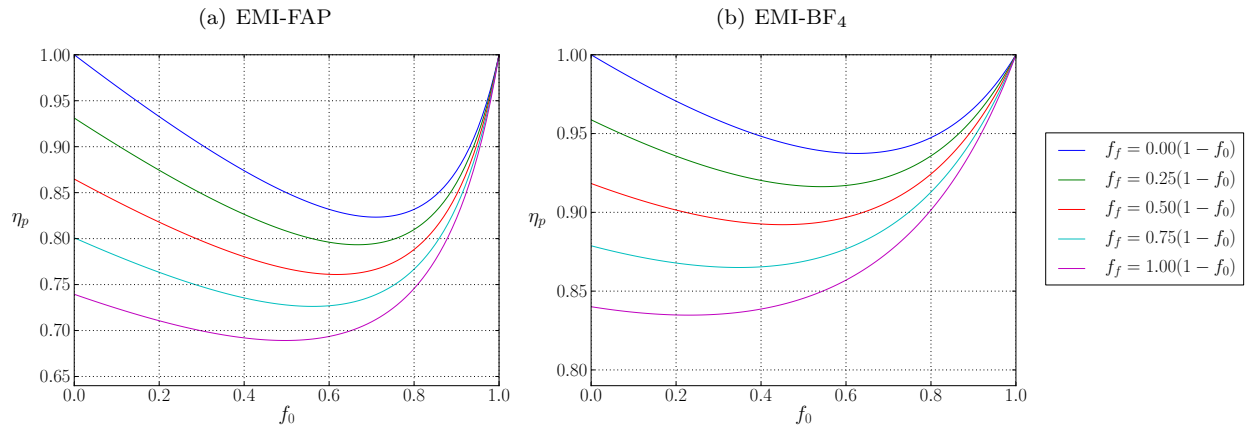


Figure 4. Polydisperse efficiency from equation (1) for two ionic liquids in negative mode under the assumption of predominantly $n = 0$ and $n = 1$ emissions. f_f refers to the current fraction due to dimer fragmentation and f_0 refers to monomer current fraction. Each line corresponds to a different level of fragmentation, ranging from total fragmentation to no fragmentation.

where:

$$\beta = 1 + (\sqrt{\xi} - 1)f_0 + \frac{1}{3}f_f \left[2\sqrt{\xi} \frac{1 - \sqrt{\xi}}{1 - \xi} - 1 \right] \quad (2)$$

$$\xi = \frac{m_0}{m_0 + m_n} \quad f_0 = \frac{I_0}{I_T} \quad f_f = \frac{I_f}{I_T} \quad (3)$$

with m_0 as the mass of a monomer, m_n as the mass of a neutral comprised of a single cation-anion pair, I_0 as the monomer current directly emitted from the liquid, I_T as the total current, and I_f as the monomer current resulting from dimer fragmentation.

Figure 4 shows the theoretical impact of fragmentation from equation (1) on the polydisperse efficiency of two different ionic liquids: EMI-FAP and EMI-BF₄. For both liquids, the effect of fragmentation is to decrease the polydisperse efficiency. For FAP, complete fragmentation with a 50% monomer fraction results in an additional efficiency loss of approximately 17% compared to no fragmentation. For BF₄, the additional efficiency loss is approximately 10%. The difference in behavior for the two liquids results from differences in ion mass: the EMI cation mass is 111.2 amu, FAP anion mass is 445.0 amu, and the BF₄ anion mass is 86.8 amu. Increased inequality in mass results in increased inequality in velocity when accelerating all particles with the same potential, so the greater $n = 0$ and $n = 1$ mass disparity for FAP is responsible for the more serious polydisperse losses, both with and without fragmentation.

The sizes of these numbers indicate that polydisperse efficiency losses do not detract from the utility of electrospray propulsion technology, yet the impact of fragmentation is sufficient to require further study.

B. Thrust and Specific Impulse

Efficiency losses can perhaps be understood more clearly in terms of their impact on thrust and specific impulse, which are considered in this section. An expression for the thrust follows immediately from some of the working for the efficiency calculation in appendix A:

$$F = \sqrt{\frac{2V_0(m_0 + m_n)}{q}} I_T \beta \quad (4)$$

It is more interesting to consider the thrust to power ratio:

$$\frac{F}{I_T V_0} = \sqrt{\frac{2(m_0 + m_n)}{q V_0}} \beta \quad (5)$$

where the leading coefficient indicates that the highest thrust is obtained by using high mass liquids at low voltage; these two factors together give high mass flow. This is a well-known result and occurs because mass contributes linearly to kinetic energy when velocity contributes as a quadratic term. The factor β is of greater interest here to show the effects of polydispersity and fragmentation. This can be contrasted with the expression for specific impulse:

$$g I_{sp} = \frac{F}{\dot{m}_T} = \sqrt{\frac{2qV_0}{m_0 + m_n}} \frac{\beta}{1 + (\xi - 1)f_0} \quad (6)$$

where the effect of mass and voltage is reversed with respect to the thrust in equation (5). This is again a well-known and obvious result, but is augmented by the new term for polydisperse efficiency with fragmentation.

Clearly the Isp and thrust can be adjusted by changing the voltage, but this is generally not practical in existing thruster designs, as the voltage is set according to the electric field strength required to extract ions from the ionic liquid surface in a given configuration. The required voltage varies for different liquids, but the variations are relatively small. Designs decoupling the acceleration potential from the extraction potential have not yet been implemented. Instead of varying the potential, propellant mass can be used to trade between Isp and thrust. Figure 5 compares thrust and Isp for an EMI cation with a range of different anion masses for fixed monomer fraction f_0 . The impact of fragmentation is clear - for fixed thrust, there is an Isp loss of around 10% between the no fragmentation and total fragmentation cases. Similarly, there is a thrust loss of around 10% when the specific impulse is fixed. The conclusion is the same as in the efficiency discussion above: these numbers indicate that polydisperse efficiency losses do not detract from the utility of electrospray propulsion technology, yet the impact of fragmentation is sufficient to require further study.

Note that figure 5 still uses the assumption of only $n = 0$ and $n = 1$ ions. Furthermore, f_0 is fixed at 0.5 in this case. Real thrust vs Isp curves will therefore deviate significantly from this, as changing the propellant will change f_0 and the range of ion types found in the beam. This image is nevertheless sufficient to give a reasonable indication of the impact of fragmentation, but it must be remembered that it is not possible to move precisely along any of these lines because the degree of fragmentation, ion mass, f_0 , and ion types in the beam cannot each be independently fixed.

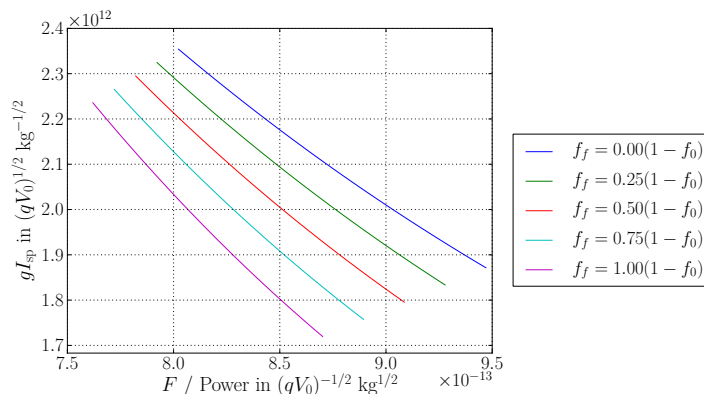


Figure 5. Thrust vs specific impulse for EMI-based ionic liquids in negative mode from equations (5) and (6) under the assumption of predominantly $n = 0$ and $n = 1$ emissions. f_f refers to the current fraction due to dimer fragmentation, f_0 refers to monomer current fraction and is set to 0.5 here. The mass range for this plot was from the lowest to highest mass anions of potential interest, with the lowest being Cl and the highest being FAP - tris(pentafluoroethyl)trifluorophosphate.

III. Molecular Dynamics

Our earlier work²⁴ on ion fragmentation demonstrated that there are two significant factors determining ion fragmentation: the electric field strength and the internal ion energy. In particular, solvated ions are unlikely to fragment at even the strongest anticipated electric field strengths unless significant additional internal energy is imparted by the electric field during the emission process. The electric field is found to be only a secondary factor in the emission process; this is because the electric field strength is not sufficient

to overcome Coulomb attraction unless the ions first move apart to a significant distance due to oscillations that occur when internal energy is high. One cause for this high internal energy in some ions was found to be bond stretching during extraction - some solvated ions remain temporarily attracted to the liquid surface at one end while being electrostatically pulled in the opposite direction.

This observation that fragmentation depends upon internal energy suggests that liquids with more degrees of freedom may be less susceptible to fragmentation, as there are more modes in which to dissipate excess energy, resulting in reduced oscillations in the distance between the ions and therefore reduced risk of moving far enough apart to be completely separated by the electric field. This hypothesis is explored in this work with molecular dynamics simulations of a number of different ionic liquids. Section A introduces general concepts of ionic liquid simulation with molecular dynamics, while section B provides further details on this work.

A. Implementation Details

Intra-molecular forces are modeled with simple harmonic terms for angles and bonds, along with cosine series for dihedrals. There are also Coulomb forces and Van der Waals forces (modeled with the Lennard-Jones approximation) between atoms. These are only simple approximations to the complex underlying quantum mechanics and hence can only offer limited quantitative accuracy, but they are nevertheless sufficient to examine mechanisms and trends.

In molecular dynamics, a parametrization of the forces for a particular molecule is known as a force field. Force fields also include partial charges assigned to each individual atom. A number of ionic liquid force fields have been proposed (see Ref 26 for a good recent review) and these have generally been based on two of the earlier more popular force fields for general organic molecules, known as OPLS-AA²⁷⁻²⁹ and AMBER.³⁰ OPLS-AA is derived from AMBER, yet includes more cosine terms for greater accuracy in dihedral calculations. Although these force fields treat a wide variety of organic molecules, they require modification for use in ionic liquids because their parametrization of aromatic rings with symmetric side chains is not suitable for use in ionic liquids with asymmetric cations, such as EMI and BMI. Furthermore, they did not include suitable parametrizations for the inorganic anions found in ionic liquids.

Initial work by our group³¹⁻³³ used the early EMI-BF₄ force field of de Andrade,³⁴ but this was only a minor modification to AMBER. Our more recent work²⁴ used the Liu³⁵ force field, which was derived more rigorously and found to give greater accuracy. However, a key shortcoming was the small number of ions that were parametrized. For this work, we have instead adopted the force field of Canongia Lopes and Padua,³⁶⁻⁴³ which is based on OPLS-AA. This force field encompasses a very wide variety of different ionic liquids and hence is ideal for a comparison between liquid types. It should be noted that it does not predict quantitatively accurate transport properties, yet is nevertheless superior to Liu in this regard.⁴⁴ This is not an issue for this study, which is aimed at identifying trends and mechanisms rather than attempting to precisely measure quantitative values.

The Lennard-Jones and Coulomb forces can theoretically act at any distance. However, Lennard-Jones forces become negligible for the atoms of interest at a distance of around 9 Å; these forces are therefore evaluated only at distances below that. Coulomb forces do not become negligible until very large distances, but a cut-off at 100 Å was found to be reasonable in most cases. As this is the same order as the size of the droplet simulations in this work, the Coulomb forces result in a scaling of computational time with N^3 , where N is the number of atoms. Faster methods exist for the evaluation of Coulomb forces, but existing implementations are efficient only when periodic boundary conditions are present; ion extraction from a liquid is clearly not a periodic process.

The simulations themselves are carried out using the molecular dynamics software LAMMPS⁴⁵ and NAMD,⁴⁶ with visualizations created using VMD.⁴⁷ The hardware used is a cluster with an infiniband network and AMD K10 processors, arranged in nodes with 8 or 12 cores. An OpenMP shared memory approach was used as much as possible droplet simulations, as this resulted in a significant performance improvement over MPI-style message passing; this is because of the high degree of inter-dependency resulting from the long-range Coulomb forces.

B. Simulation Setup

The overall goal was to simulate a large number of solvated ions from different ionic liquids to determine the likelihood of fragmentation. The first step in analyzing these ions was to determine the range of energies

of interest. For this, electric fields were applied to droplets of ionic liquid. This resulted in the emission of ions and the distribution of these ions' energies could then be determined. The droplets were created using the following process, which is similar to that reported previously:^{24,33}

1. Stack the desired number of ion pairs in a spherical grid with spacing of 10 Å. No algorithm exists for the creation of a sphere with a fixed number of equally-spaced ions, but a sphere of approximately correct size can be created by estimating the required volume. This must be a slight over-estimate so that excess ions can be removed at random to give a final droplet with the required total number of ions.
2. A molecular dynamics simulation is run for 100 ps with a 1 fs timestep to allow the ions to collapse into a droplet; this process is assisted by a weak radially inward force of 3.5×10^{-13} N to ensure that the ions do not escape before coalescing. The initial temperature is 300 K. The Coulomb force cut-off can be reduced to only 20 Å at this point, as the objective is simply to assemble the ions into a droplet and the dynamics need not be completely physically realistic. Physical realism is more significant in later stages when the droplet is equilibrated at a desired temperature.
3. The reduction in potential energy of the droplet after ions coalesce results in a significant increase in temperature, so the temperature is reset to 300 K and the simulation is run for another 50 ps, now with a more realistic Coulomb cut-off of 100 Å.
4. The droplet is equilibrated at 300 K for another 50 ps using an approximation to an NVT (i.e. constant temperature) simulation carried out by rescaling the temperature every 250 fs. This is effectively an energy minimization step.
5. The droplet is simulated for a further 1 ps without temperature rescaling to confirm that it is in an equilibrium state by checking that the temperature does not deviate significantly from 300 K during this time.

After creating droplets at 300 K, electric fields were applied to simulate ion emission from an electrospray. In a physical experiment, electric fields of the order 10^6 V/m are imposed externally. Due to the focusing effect of the Taylor cone formed from the liquid meniscus in these fields, this external field is sufficient to generate fields of the order 10^9 V/nm at the tip of the cone, resulting in ion emission. However, the droplets used in this simulation are only approximately 15 nm in diameter and this has proved to be insufficient for Taylor cone formation. As a result, ion emission can be achieved only by directly applying an external electric field of the order 10^9 V/nm to simulate the field at the tip of a Taylor cone. Ion emission is then seen in both directions from the droplets and so the droplet remains approximately charge neutral. The two sides can be analyzed individually to see the different effects of each polarity.

A droplet with 4913 pairs of ions of EMI-BF₄ was simulated to gather statistics on ion energies during the emission process. Figure 6 is an image of the negative side of such a droplet undergoing ion emission. The range of internal energies from emitted ions in the negative mode was consistent with those seen in Ref 24; note that internal here means potential energy and kinetic energy in each ion's individual rest frame.

Unfortunately, such a simulation is computationally expensive without a fast method for evaluating long-range Coulomb forces. The simulation in the figure took almost one month to emit 1000 ions when running on 50 AMD K10 processor cores. It was therefore not practical to simulate multiple liquids in this

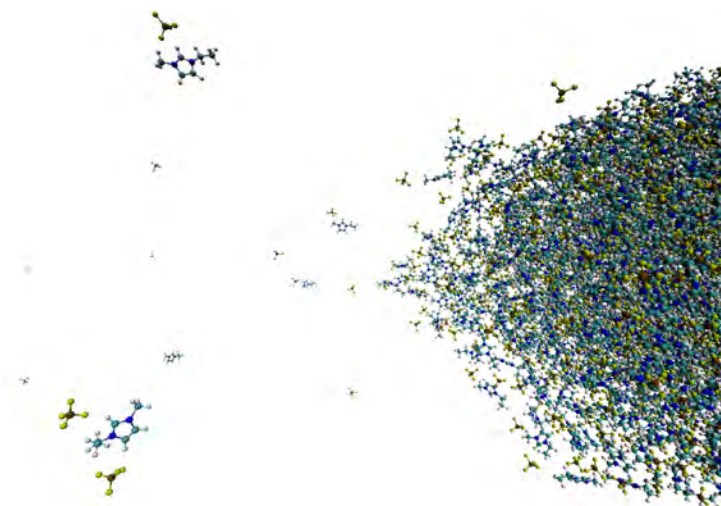


Figure 6. The negative side of a droplet of 4913 pairs of ions of EMI-BF₄ undergoing electrospray emission in an electric field of 1.5 V/nm. Emissions in this image consist of negative monomers, negative dimers, and neutral fragmentation products. The colors are as described in figures 1 and 2.

manner. Smaller droplets could be used, but only a small number of ions could then be emitted before the droplet starts to disintegrate, invalidating results of further ion emission. Instead, dimers were sampled independently at an energy level representative of those seen in emission from the droplet. The same energies were used for each liquid; this is justifiable because differences in solvation energy among the ionic liquids are small compared to the energies under consideration here.⁵ The procedure for sampling individual dimers was as follows, now with a 0.5 fs timestep:

1. For liquids other than EMI-BF₄, sample coordinates of a stable dimer were obtained from the emission of small droplets consisting of 250 ion pairs.
2. 10,000 copies of the stable dimer are made, each with different random velocities on every atom at 298 K.
3. A simulation of each dimer is run for 10 ps with a N se-Hoover thermostat⁴⁸ to bring the temperature from 298 K to a temperature corresponding to the desired internal energy. The thermostat's damping parameter is set to 500 fs. The thermostat then serves to equilibrate the dimer in an approximate NVT simulation - this ensures that the velocity changes are consistent with the potential energy configuration.
4. If desired, a constant electric field is applied and then an NVE (i.e. constant energy) molecular dynamics simulation is run for 200 ps or until dimer fragmentation occurs.
5. Histograms are made to show the distribution of fragmentation events within this 200 ps interval.

Note that the use of an NVT thermostat above results in a range of different internal energies rather than just one fixed value. However, this range was examined and found to be similar for all liquids; the comparison is therefore still fair. The advantage of this approach is that an NVT thermostat prevents any individual ion from moving at a significant velocity relative to any of the others. Without this, the dimers could fragment during the equilibration step, thereby complicating the generation of suitable initial conditions for the production phase of the simulation.

The energy levels described here are excess energy levels, i.e. the additional internal energy in emitted ions above the average internal energy of ions in the liquid state. When the same energy is added to all liquids in the steps above, it refers to excess energy defined in this way.

IV. Results

A range of EMI-based liquids was tested with molecular dynamics simulations because the EMI cation results in the highest conductivity, as discussed in section I.A. The anions are those mentioned in section I.A with the addition of two halides: Br and Cl. The objective here was to compare dimer fragmentation probability for liquids with different numbers of degrees of freedom, as determined by the number of atoms. The halides are interesting partly because they have smaller degrees of freedom than the other liquids and also because they share the same number of degrees of freedom; therefore any significant difference in fragmentation probability between these two liquids would suggest that fragmentation is dependent upon another factor in addition to complexity. Note that these two halides actually melt well above room temperature, yet most ionic liquids exhibit a strong super-cooling tendency down to their low glass temperature temperatures²² and so it is reasonable to include these halides in a comparison with the others, even though they are unlikely to be of interest in practice.

The simulations were run for 10,000 negative dimer samples with 2 eV excess energy (as defined in section III.B) in an electric field of 1.5 V/nm for 200 ps. Detailed fragmentation time distribution results can be seen in figure 7. This number of samples was not sufficient for full convergence, as some noise can be seen in the results. However, it was sufficient to clearly see the trend among these liquids. A few attempts at running simulations with different randomized initial conditions did not significantly change the fragmentation fractions. The results from the simulations are summarized briefly in the table below:

Anion name	# negative dimer atoms	Fragmentation fraction within 200 ps
Br	21	94.6%
Cl	21	98.6%
BF ₄	29	86.3%
FSI	37	72.7%
Im	49	26.7%
FAP	69	3.5%

This supports the hypothesis that an increase in ion complexity results in a significant reduction in fragmentation, as discussed in the introduction to section III. The results are dramatic, especially for the largest ions. These results are also supported by preliminary data (not shown) for simulations of these ions at various other electric field strengths and internal energies. The fragmentation percentages for the halides are very similar and, considering that only 10,000 samples were used, are close enough to suggest that complexity may be the only significant factor affecting fragmentation, at least in the negative mode.

It is important to note at this point that the chosen electric field is unrealistically strong, given the amount of time for which it is applied. Physically, a field strength of 1 V/nm can be expected only very close to the tip of an electrospray emitter, but 200 ps is enough time for an ion to move far away from the tip and almost be emitted completely from the thruster; most of this time is therefore spent at much weaker electric field strengths. However, the purpose of these numerical experiments was a comparison between liquids under consistent conditions and the validity of this comparison is not affected; it is just necessary to remember that the quantitative fragmentation fractions seen in experiments are not as high as those seen here because of the weaker physical electric field for most of the 200 ps.

One factor not explicitly considered here however is the distribution of solvated ion sizes in different liquids; this is an important consideration, as the fragmentation current fraction depends not only on the probability of fragmentation, but on the number of dimers (or higher degree solvated ions) emitted. As referenced in section II, the higher complexity liquids tend to produce the most solvated ions. It is therefore very significant that these offer such dramatically lower fragmentation fractions, as a high degree of fragmentation would result in very substantial efficiency and specific impulse losses for these liquids.

Similar simulations were run for positive dimers, yet the findings were less clear. Further work will be needed to understand the significance of this. Some difference between the positive and negative cases should be expected, as positive dimers differ by only a single anion instead of two anions for negative dimers.

A. Experimental Consistency

New experimental work is not reported here, but the computational results are consistent with experimental data collected at different times in prior work. Figure 8 shows retarding potential analyzer (RPA) experimental data for electrospray emissions from three different ionic liquids. Retarding potential analyzer experiments consist of an electrospray source emitting into a collector plate, but with a grid in between. When a potential is applied to the grid, any ions accelerated with less than that potential will be reflected and will no longer reach the collector. If a dimer has fragmented, then the potential required for reflection of the resulting monomer will be significantly reduced because of the reduction in kinetic energy.¹⁰ This allows fragmentation products to be identified in the beam separately from ions that have not fragmented, as ions that have not fragmented have not undergone any kinetic energy reduction and can be stopped only by a retarding potential equal in magnitude to the full extraction potential.

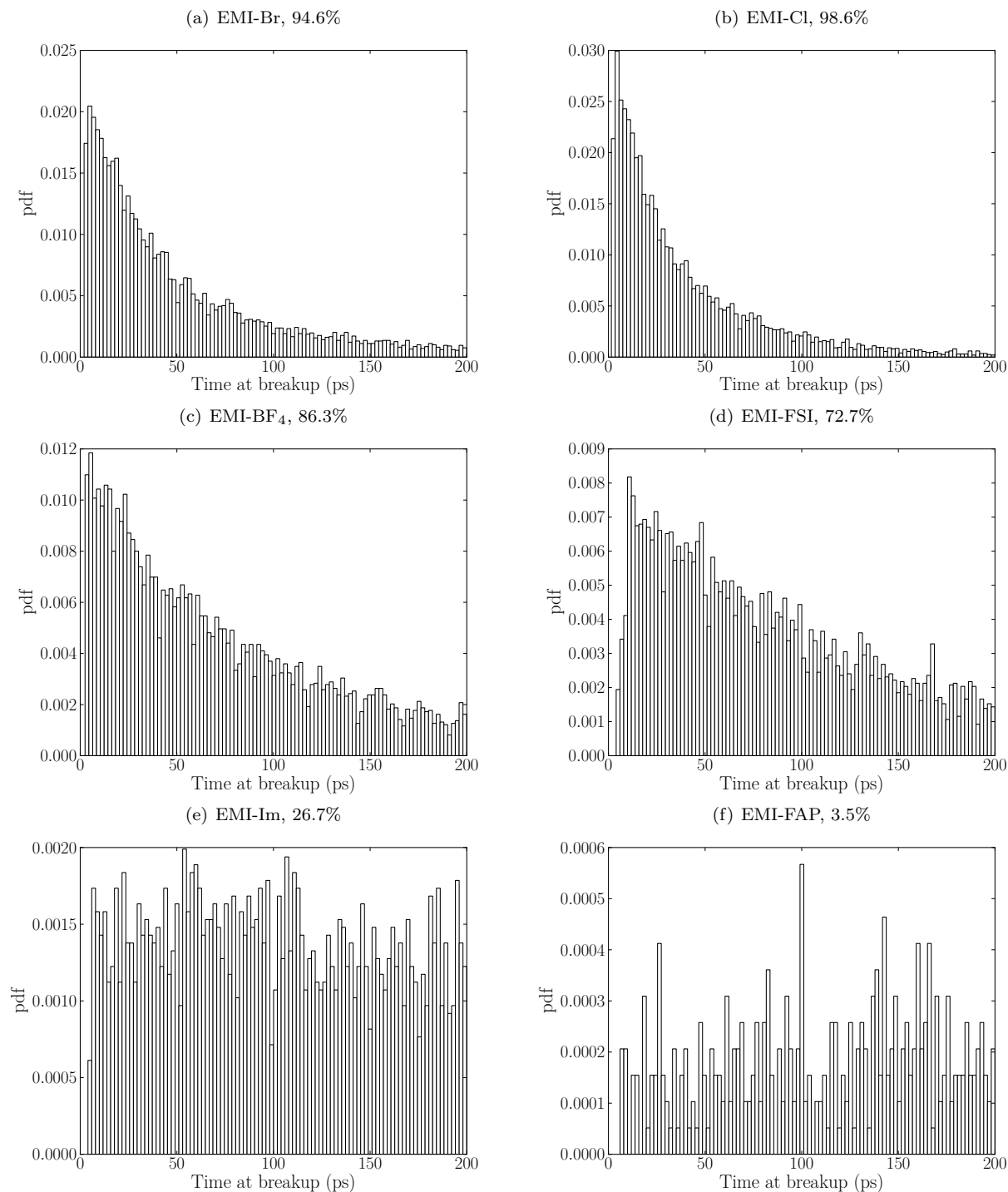


Figure 7. Fragmentation time distributions for dimers of various ionic liquids with 10,000 samples at 2eV excess energy with an electric field of 1 V/nm in negative mode. The percentages indicate the portion of samples that fragmented within the 200 ps shown, which is representative of the acceleration region in an electrospray thruster. The considerable noise in the last two plots arose because only a very small number of samples fragmented within 200 ps for these liquids. EMI-Br and EMI-Cl have the same complexity (defined simply as the number of atoms), but then the complexity increases from left to right and top to bottom.

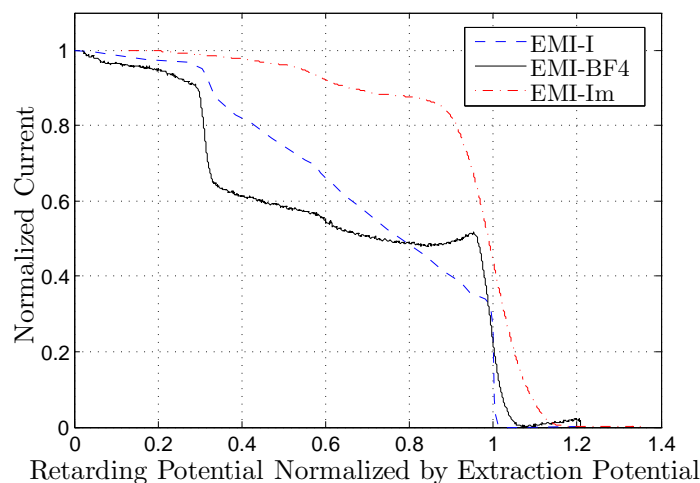


Figure 8. RPA data for three different ionic liquids; the complexity of the liquids increases in the order I, BF_4 , Im, but the fragmentation current fraction significantly decreases. The BMI-I data is from Ref 49, the EMI- BF_4 data is from Ref 24, and the EMI-Im data is from Ref 10, but plotted differently.

There is a minimum retarding potential below which no further effect on the current is seen; this minimum is clearly visible in all of the figure 8 plots. It corresponds to fragmentation after complete emission from the thruster; this is the minimum energy that a monomer can have, as it was part of a dimer for all of the time when it was accelerating and hence reached the lowest possible velocity for an ion emitted from the thruster (when only considering monomers, dimers, and dimer fragmentation products).

There is a discontinuous step after this minimum potential, as all ions fragmenting at any time after acceleration are represented here. However, there is a continuous slope between the step and the full extraction potential because it represents ions fragmenting during acceleration; fragmentation can occur at a continuous range of potential values during acceleration (there does not appear to be any favored position) and hence the corresponding retarding potentials fall within the same continuous range. So the height of this slope on the y -axis indicates the fragmentation current fraction due to fragmentation products. Figure 8 clearly demonstrates a significant decrease in fragmentation as complexity increases.

Note that the experimental data was taken at different times under different conditions and hence cannot be seen as conclusive. However, its consistency with the numerical data lends extra weight to the hypothesis that more complex liquids experience reduced fragmentation, resulting in increased efficiency and improved thrust-Isp trade-offs.

V. Summary and Future Work

An expression for efficiency loss in the presence of fragmentation was given in equation (1). It was then demonstrated via molecular dynamics simulations that the fragmentation probability depends upon ion complexity, which had been predicted because higher complexity results in more effective dissipation of internal energy added to ions during the extraction process. With higher internal energy in each degree of freedom, ions would be more likely to oscillate slightly apart and then be more easily separated by the electric field because of the reduction in Coulomb attraction from the increased distance. This observation was supported by past experimental data. However, this experimental data was taken at different times and under different conditions, so it will be important to perform new consistent experimental work with a wide range of liquids to confirm this cause of fragmentation. Further molecular dynamics simulations will also be run under different conditions and for even more liquids.

Acknowledgments

Funding for this work was provided by an AFOSR grant monitored by Dr. Mitat Birkan.

Appendix

A. Efficiency Calculation

The efficiency expression given earlier in equation (1) is derived in this section. The thrust from an electrospray with N different particle types in the beam is given by:

$$F = \sum_{i=1}^N \dot{m}_i v_i \quad (7)$$

where the individual particle types (defined as particles with different mass and/or velocity) have emission speed v_i and mass flow \dot{m}_i . To calculate the polydisperse efficiency, the equivalent emission speed from a monodisperse thruster producing the same thrust with the same mass flow must be found; this is because, as described in section II.A, the minimum power for given thrust occurs when all particles are accelerated to the same speed. If this speed is denoted by c , the expression is:

$$c = \frac{1}{\dot{m}_T} \sum_{i=1}^N \dot{m}_i v_i \quad \text{where} \quad \dot{m}_T = \sum_{i=1}^N \dot{m}_i \quad (8)$$

The power input to an electrospray beam (after losses) is given by $I_T V_0$, where I_T is the total beam current and V_0 is the full potential between the emitter and extractor. The polydisperse efficiency is the ratio of the minimum required beam power for given thrust to this actual input power for the same thrust, where the minimum beam power is the rate of change of beam kinetic energy for the equivalent monodisperse thruster.

$$\eta_P = \frac{\frac{1}{2} \dot{m}_T c^2}{I_T V_0} \quad (9)$$

Now substitute for c :

$$\eta_P = \frac{1}{2} \frac{1}{\dot{m}_T} \frac{\left(\sum_{i=1}^N \dot{m}_i v_i \right)^2}{I_T V_0} \quad (10)$$

For an ion that has been accelerated with the full potential V_0 , the resulting speed can be found easily from energy considerations:

$$v_i = \sqrt{2 \frac{q}{m_i} V_0} \quad (11)$$

The analysis becomes more complicated when fragmentation occurs. If we assume that a single fragmentation event occurs after acceleration through a potential V_1 and that the products are a neutral of mass m_{a_i} and an ion of mass m_{b_i} , then the speed v_{a_i} of the neutral and the speed of v_{b_i} of the ion at emission are again found from energy considerations:

$$v_{a_i} = \sqrt{2 \frac{q}{m_{a_i} + m_{b_i}} V_1} \quad (12)$$

$$v_{b_i} = \sqrt{2 \frac{q}{m_{a_i} + m_{b_i}} V_1 + 2 \frac{q}{m_{b_i}} (V_0 - V_1)} \quad (13)$$

To simplify the analysis, we will consider the case of relatively low complexity liquids that typically emit negligible fractions of $n = 2$ or higher solvated ions, so only $n = 0$ and $n = 1$ ions need to be considered for a good approximation. The following notation will be used for the different ions in the beam:

- \dot{m}_0, v_0 for directly emitted monomer ions (all have same speed).
- \dot{m}_1, v_1 for directly emitted dimer ions that do not fragment prior to emission (all have same speed).

- $\dot{m}_{0_i}, \dot{m}_{n_i}, v_{0_i}, v_{n_i}$ for the products of the fragmentation of dimers, where the 0_i terms refer to monomer fragmentation products and n_i terms refer to neutral fragmentation products. Note that an i suffix is required to indicate different velocities, as the velocities of fragmentation products vary depending on the local value of V_1 .

where the term *directly emitted* refers to ions emitted from the liquid surface and not to ions that are the products of fragmentation events. These terms can now be used in equation (10):

$$\eta = \frac{1}{2\dot{m}_T I_T V_0} \left(\dot{m}_0 \sqrt{2 \frac{q}{m_0} V_0} + \dot{m}_1 \sqrt{2 \frac{q}{m_0 + m_n} V_0} + \sum_i \left[\dot{m}_{0_i} \sqrt{2 \frac{q}{m_0 + m_n} V_1 + 2 \frac{q}{m_0} (V_0 - V_1)} + \dot{m}_{n_i} \sqrt{2 \frac{q}{m_0 + m_n} V_1} \right] \right)^2 \quad (14)$$

where m_0 denotes monomer mass, m_n denote the mass of a neutral consisting of a single cation-anion pair, and the summation is now over all of the fragmentation products at different velocities (i.e. different V_1 potentials). Note that neutrals and dimers are created in equal numbers by fragmentation events, so the fragmentation product mass flows are related by:

$$\dot{m}_{n_i} = \frac{m_n}{m_0} \dot{m}_{0_i} \quad (15)$$

This can be substituted into the efficiency expression. As fragmentations occur over an effectively continuous range of velocities, it is appropriate to replace the summation with an integral over all of the possible values of the potential V_1 . The individual mass flows \dot{m}_{0_i} are now replaced by a distribution function $\dot{m}_{0_f}(V_1)$:

$$\eta = \frac{1}{2\dot{m}_T I_T V_0} \left(\dot{m}_0 \sqrt{2 \frac{q}{m_0} V_0} + \dot{m}_1 \sqrt{2 \frac{q}{m_0 + m_n} V_0} + \int_0^{V_0} \dot{m}_{0_f}(V_1) \left[\sqrt{2 \frac{q}{m_0 + m_n} V_1 + 2 \frac{q}{m_0} (V_0 - V_1)} + \frac{m_n}{m_0} \sqrt{2 \frac{q}{m_0 + m_n} V_1} \right] dV_1 \right)^2 \quad (16)$$

Experimental data is expressed more directly in terms of current rather than mass flows, so the individual mass flow terms are now converted to currents (or a current distribution function in the case of $I_f(V_1)$) using appropriate q/m ratios:

$$\eta = \frac{1}{2\dot{m}_T I_T V_0} \left(I_0 \sqrt{2 \frac{m_0}{q} V_0} + I_1 \sqrt{2 \frac{m_0 + m_n}{q} V_0} + \sqrt{\frac{2}{q}} \int_0^{V_0} I_f(V_1) \left[\sqrt{m_0} \sqrt{V_0 - \frac{m_n}{m_0 + m_n} V_1} + \sqrt{\frac{m_n^2}{m_0 + m_n} V_1} \right] dV_1 \right)^2 \quad (17)$$

where q and V_0 have now been separated, even though they may be negative. This is justifiable if the absolute values are used for convenience, which is reasonable when noting that qV_0 is always positive because q and V_0 always have the same sign. The total mass flow rate can be converted to a current as follows, where I_f in this context is total fragmentation current:

$$\dot{m}_T = \frac{1}{q} (m_0 I_0 + (m_n + m_0) I_1 + (m_n + m_0) I_f) \quad (18)$$

The fragmentation current distribution still remains to be determined. Although not yet explained by theory, linear data in experimental results obtained from retarding potential analyzers in prior work suggests that V_1 is, at least for some liquids, uniformly distributed between 0 and V_0 ;^{23, 24, 49} this can be seen in figure 8.

This information can now be used to compute the integral:

$$\begin{aligned}
\eta &= \frac{\left(I_0 \sqrt{m_0 V_0} + I_1 \sqrt{(m_0 + m_n) V_0} + \frac{2}{3} I_f \sqrt{V_0} \left[\sqrt{m_0} \frac{m_0 + m_n}{m_n} \left(1 - \left(1 - \frac{m_n}{m_0 + m_n} \right)^{3/2} \right) + \sqrt{\frac{m_n^2}{m_0 + m_n}} \right] \right)^2}{(m_0 I_0 + (m_n + m_0)(I_1 + I_f)) I_T V_0} \\
&= \frac{\left(I_0 \sqrt{m_0} + I_1 \sqrt{(m_0 + m_n)} + \frac{2}{3} I_f \left[\sqrt{m_0} \frac{m_0 + m_n}{m_n} - \frac{m_0^2}{m_n \sqrt{m_0 + m_n}} + \frac{m_n}{\sqrt{m_0 + m_n}} \right] \right)^2}{(m_0 I_0 + (m_n + m_0)(I_1 + I_f)) I_T} \\
&= \frac{\left(I_0 \sqrt{m_0} + I_1 \sqrt{(m_0 + m_n)} + \frac{2}{3} I_f \left[\sqrt{m_0} \frac{m_0 + m_n}{m_n} + \sqrt{m_0 + m_n} \frac{m_n - m_0}{m_n} \right] \right)^2}{(m_0 I_0 + (m_n + m_0)(I_1 + I_f)) I_T} \tag{19}
\end{aligned}$$

Now define a non-dimensional mass fraction and non-dimensional current fractions:

$$\xi = \frac{m_0}{m_0 + m_n} \quad f_0 = \frac{I_0}{I_T} \quad f_1 = \frac{I_1}{I_T} \quad f_f = \frac{I_f}{I_T} \tag{20}$$

Note that the following relationship exists between the current fractions:

$$1 = f_0 + f_1 + f_f \tag{21}$$

The efficiency expression can now be re-written as:

$$\begin{aligned}
\eta &= \frac{\left(\sqrt{\xi} f_0 + f_1 + \frac{2}{3} f_f \left[\sqrt{\frac{m_0}{m_n}} \frac{1}{\sqrt{1-\xi}} + 1 - \frac{m_0}{m_n} \right] \right)^2}{\xi f_0 + f_1 + f_f} \\
&= \frac{\left(\sqrt{\xi} f_0 + f_1 + \frac{2}{3} f_f \left[\sqrt{\frac{\xi}{1-\xi}} \sqrt{\frac{1}{1-\xi}} + 1 - \frac{\xi}{1-\xi} \right] \right)^2}{1 + (\xi - 1) f_0} \\
&= \frac{\left(1 + (\sqrt{\xi} - 1) f_0 + \frac{1}{3} f_f \left[2\sqrt{\xi} \frac{1 - \sqrt{\xi}}{1 - \xi} - 1 \right] \right)^2}{1 + (\xi - 1) f_0} \tag{22}
\end{aligned}$$

which is equivalent to equation (1).

References

- ¹Lozano, P. C., *Studies on the Ion-Droplet Mixed Regime in Colloid Thrusters*, PhD thesis, Massachusetts Institute of Technology, 2003.
- ²Taylor, G., "Disintegration of Water Drops in an Electric Field," *Proceedings of the Royal Society. Series A, Mathematical and Physical Sciences*, Vol. 280, No. 1382, 1964, pp. 383–397.
- ³Gamero-Castano, M. and Hruby, V., "Electrospray as a Source of Nanoparticles for Efficient Colloid Thrusters," *Journal of Propulsion and Power*, Vol. 17, No. 5, 2001, pp. 977–987.
- ⁴Fernández de la Mora, J. and Loscertales, I. G., "The Current Emitted by Highly Conducting Taylor Cones," *Journal of Fluid Mechanics*, Vol. 260, 1994, pp. 155–184.
- ⁵Romero-Sanz, I., Bocanegra, R., Fernández de la Mora, J., and Gamero-Castano, M., "Source of Heavy Molecular Ions Based on Taylor Cones of Ionic Liquids Operating in the Pure Ion Evaporation Regime," *Journal of Applied Physics*, Vol. 94, No. 5, 2003, pp. 3599–3605.
- ⁶Lozano, P. C. and Martínez-Sánchez, M., "Ionic Liquid Ion Sources: Characterization of Externally Wetted Emitters," *Journal of Colloid and Interface Science*, Vol. 282, No. 2, Feb. 2005, pp. 415–21.
- ⁷Courtney, D. G., *Ionic Liquid Ion Source Emitter Arrays Fabricated on Bulk Porous Substrates for Spacecraft Propulsion*, PhD thesis, Massachusetts Institute of Technology, 2011.
- ⁸Courtney, D. G., Li, H. Q., and Lozano, P., "Emission Measurements from Planar Arrays of Porous Ionic Liquid Ion Sources," *Journal of Physics D: Applied Physics*, Vol. 45, Dec. 2012, pp. 485203.
- ⁹Courtney, D. G., Li, H., and Lozano, P. C., "Electrochemical Micromachining on Porous Nickel for Arrays of Electrospray Ion Emitters," *Journal of Microelectromechanical Systems*, Vol. 22, No. 2, 2013, pp. 471–482.
- ¹⁰Lozano, P. C., "Energy Properties of an EMI-Im Ionic Liquid Ion Source," *Journal of Physics D: Applied Physics*, Vol. 39, Jan. 2006, pp. 126–134.
- ¹¹Larriba, C., Castro, S., Fernández de la Mora, J., and Lozano, P. C., "Monoenergetic Source of Kilodalton ions from Taylor Cones of Ionic Liquids," *Journal of Applied Physics*, Vol. 101, 2007, pp. 084303.

- ¹²Castro, S., Larriba, C., Fernández de la Mora, J., Lozano, P. C., Sumer, S., Yoshida, Y., and Saito, G., "Effect of Liquid Properties on Electrospays from Externally Wetted Ionic Liquid Ion Sources," *Journal of Applied Physics*, Vol. 102, No. 9, 2007, pp. 094310.
- ¹³Legge, R. S. and Lozano, P. C., "Electrospray Propulsion Based on Emitters Microfabricated in Porous Metals," *Journal of Propulsion and Power*, Vol. 27, No. 2, March 2011, pp. 485–495.
- ¹⁴Hallett, J. P. and Welton, T., "Room-Temperature Ionic Liquids: Solvents for Synthesis and Catalysis. 2." *Chemical reviews*, Vol. 111, May 2011, pp. 3508–3576.
- ¹⁵Kuboki, T., Okuyama, T., Ohsaki, T., and Takami, N., "Lithium-Air Batteries Using Hydrophobic Room Temperature Ionic Liquid Electrolyte," *Journal of Power Sources*, Vol. 146, 2005, pp. 766–769.
- ¹⁶Cuadrado-Prado, S., Domínguez-Pérez, M., Rilo, E., García-Garabal, S., Segade, L., Franjo, C., and Cabeza, O., "Experimental Measurement of the Hygroscopic Grade on Eight Imidazolium Based Ionic Liquids," *Fluid Phase Equilibria*, Vol. 278, 2009, pp. 36–40.
- ¹⁷Lu, Y., King, F. L., and Duckworth, D. C., "Electrochemically-Induced Reactions of Hexafluorophosphate Anions with Water in Negative Ion Electro spray Mass Spectrometry of Undiluted Ionic Liquids," *Journal of the American Society for Mass Spectrometry*, Vol. 17, 2006, pp. 939–944.
- ¹⁸Freire, M. G., Neves, C. M. S. S., Marrucho, I. M., Coutinho, J. a. A. P., and Fernandes, A. M., "Hydrolysis of Tetrafluoroborate and Hexafluorophosphate Counter Ions in Imidazolium-Based Ionic Liquids," *The Journal of Physical Chemistry A*, Vol. 114, 2010, pp. 3744–3749.
- ¹⁹Ishikawa, M., Sugimoto, T., Kikuta, M., Ishiko, E., and Kono, M., "Pure Ionic Liquid Electrolytes Compatible with a Graphitized Carbon Negative Electrode in Rechargeable Lithium-Ion Batteries," *Journal of Power Sources*, Vol. 162, No. 1, 2006, pp. 658–662.
- ²⁰Matsumoto, H., Sakaebe, H., Tatsumi, K., Kikuta, M., Ishiko, E., and Kono, M., "Fast cycling of Li/LiCoO₂ cell with low-viscosity ionic liquids based on bis(fluorosulfonyl)imide [FSI]," *Journal of Power Sources*, Vol. 160, No. 2, 2006, pp. 1308–1313.
- ²¹Ignat'ev, N. V. and Welz-Biermann, U., "New Hydrophobic Ionic Liquids (Molten Salts) with Highly Fluorinated Anions. Synthesis and Properties," *Molten Salts XIV*, The Electrochemical Society, Honolulu, Hawaii, 2004, pp. 353–358.
- ²²Zhang, S., Sun, N., He, X., Lu, X., and Zhang, X., "Physical Properties of Ionic Liquids: Database and Evaluation," *Journal of Physical and Chemical Reference Data*, Vol. 35, No. 4, 2006, pp. 1475–1517.
- ²³Fedkiw, T. and Lozano, P., "Efficiency Measurements of an Ionic Liquid Ion Source Thruster," *Space Propulsion*, San Sebastián, Spain, 2010.
- ²⁴Coles, T. M., Fedkiw, T. P., and Lozano, P. C., "Investigating Ion Fragmentation in Electro spray Thruster Beams," *The 48th AIAA/ASME/SAE/ASEE Joint Propulsion Conference & Exhibit*, Atlanta, Georgia, 2012.
- ²⁵Khayms, V., *Advanced Propulsion for Microsatellites*, PhD thesis, Massachusetts Institute of Technology, 2000.
- ²⁶Dommert, F., Wendler, K., Berger, R., Delle Site, L., and Holm, C., "Force Fields for Studying the Structure and Dynamics of Ionic Liquids: A Critical Review of Recent Developments," *Chemphyschem*, Feb. 2012.
- ²⁷Jorgensen, W. L., Maxwell, D. S., and Tirado-Rives, J., "Development and Testing of the OPLS All-Atom Force Field on Conformational Energetics and Properties of Organic Liquids," *Journal of the American Chemical Society*, Vol. 118, No. 45, 1996, pp. 11225–11236.
- ²⁸Mcdonald, N. A. and Jorgensen, W. L., "Development of an All-Atom Force Field for Heterocycles. Properties of Liquid Pyrrole, Furan, Diazoles, and Oxazoles," *The Journal of Physical Chemistry B*, Vol. 102, 1998, pp. 8049–8059.
- ²⁹Watkins, E. K. and Jorgensen, W. L., "Perfluoroalkanes: Conformational Analysis and Liquid-State Properties from ab Initio and Monte Carlo Calculations," *The Journal of Physical Chemistry A*, Vol. 105, No. 16, 2001, pp. 4118–4125.
- ³⁰Cornell, W. D., Cieplak, P., Bayly, C. I., Gould, I. R., Merz, K. M., Ferguson, D. M., Spellmeyer, D. C., Fox, T., Caldwell, J. W., and Kollman, P. A., "A Second Generation Force Field for the Simulation of Proteins, Nucleic Acids, and Organic Molecules," *Journal of the American Chemical Society*, Vol. 117, No. 19, May 1995, pp. 5179–5197.
- ³¹Takahashi, N. and Lozano, P. C., "Computational Investigation of Molecular Ion Evaporation in Electro spray Thrusters," *The 44th AIAA/ASME/SAE/ASEE Joint Propulsion Conference & Exhibit*, Hartford, Connecticut, 2008.
- ³²Takahashi, N. and Lozano, P. C., "Atomistic Numerical Approach to Ion Evaporation from a Tungsten Surface for Electro spray Thrusters," *The 45th AIAA/ASME/SAE/ASEE Joint Propulsion Conference & Exhibit*, Denver, Colorado, 2009.
- ³³Takahashi, N., *Molecular Dynamics Modeling of Ionic Liquids in Electro spray Propulsion*, Master's thesis, Massachusetts Institute of Technology, 2010.
- ³⁴de Andrade, J., Bo, E. S., and Stassen, H., "Computational Study of Room Temperature Molten Salts Composed by 1-Alkyl-3-methylimidazolium Cations - Force-Field Proposal and Validation," *Journal of Physical Chemistry B*, Vol. 106, 2002, pp. 13344–13351.
- ³⁵Liu, Z., Huang, S., and Wang, W., "A Refined Force Field for Molecular Simulation of Imidazolium-Based Ionic Liquids," *The Journal of Physical Chemistry B*, Vol. 108, 2004, pp. 12978–12989.
- ³⁶Canongia Lopes, J. N., Deschamps, J., and Padua, A. A. H., "Modeling Ionic Liquids Using a Systematic All-Atom Force Field," *The Journal of Physical Chemistry B*, Vol. 108, 2004, pp. 2038–2047.
- ³⁷Canongia Lopes, J. N., Deschamps, J., and Padua, A. A. H., "Additions and Corrections for Modeling Ionic Liquids Using a Systematic All-Atom Force Field," *The Journal of Physical Chemistry B*, Vol. 108, 2004, pp. 11250.
- ³⁸Canongia Lopes, J. N. and Padua, A. A. H., "Molecular Force Field for Ionic Liquids Composed of Triflate or Bistriflylimide Anions," *The Journal of Physical Chemistry B*, Vol. 108, 2004, pp. 16893–16898.
- ³⁹Canongia Lopes, J. N. and Padua, A. A. H., "Molecular Force Field for Ionic Liquids III: Imidazolium, Pyridinium, and Phosphonium Cations; Chloride, Bromide, and Dicyanamide Anions," *The Journal of Physical Chemistry B*, Vol. 110, No. 39, Oct. 2006, pp. 19586–92.
- ⁴⁰Canongia Lopes, J. N., Shimizu, K., Pádua, A. a. H., Umebayashi, Y., Fukuda, S., Fujii, K., and Ishiguro, S.-i., "Potential Energy Landscape of Bis(fluorosulfonyl)amide," *The Journal of Physical Chemistry B*, Vol. 112, No. 31, Aug. 2008, pp. 9449–55.

- ⁴¹Canongia Lopes, J. N., Padua, A. A. H., and Shimizu, K., "Molecular Force Field for Ionic Liquids IV: Trialkylimidazolium and Alkoxy carbonyl-Imidazolium Cations; Alkylsulfonate and Alkylsulfate Anions," *The Journal of Physical Chemistry B*, Vol. 112, 2008, pp. 5039–46.
- ⁴²Shimizu, K., Almantariotis, D., Costa Gomes, M. F. ., Padua, A. A. H., and Canongia Lopes, J. N., "Molecular Force Field for Ionic Liquids V: Hydroxyethylimidazolium, Dimethoxy-2-Methylimidazolium, and Fluoroalkylimidazolium Cations and Bis(Fluorosulfonyl)Amide, Perfluoroalkanesulfonylamide, and Fluoroalkylfluorophosphate Anions," *The Journal of Physical Chemistry B*, Vol. 114, 2010, pp. 3592–3600.
- ⁴³Canongia Lopes, J. N. and Pádua, A. A. H., "CL&P: A Generic and Systematic Force Field for Ionic Liquids Modeling," *Theoretical Chemistry Accounts*, Vol. 131, No. 3, Feb. 2012.
- ⁴⁴Dommert, F., Schmidt, J., Qiao, B., Zhao, Y., Krekeler, C., Delle Site, L., Berger, R., and Holm, C., "A Comparative Study of Two Classical Force Fields on Statics and Dynamics of [EMIM][BF₄] Investigated via Molecular Dynamics Simulations," *The Journal of Chemical Physics*, Vol. 129, No. 22, 2008, pp. 224501.
- ⁴⁵Plimpton, S., "Fast Parallel Algorithms for Short-Range Molecular Dynamics," *Journal of Computational Physics*, Vol. 117, 1995, pp. 1–19.
- ⁴⁶Phillips, J. C., Braun, R., Wang, W., Gumbart, J., Tajkhorshid, E., Villa, E., Chipot, C., Skeel, R. D., Kalé, L., and Schulten, K., "Scalable Molecular Dynamics with NAMD," *Journal of Computational Chemistry*, Vol. 26, No. 16, Dec. 2005, pp. 1781–802.
- ⁴⁷Humphrey, W., Dalke, A., and Schulten, K., "VMD – Visual Molecular Dynamics," *Journal of Molecular Graphics*, Vol. 14, 1996, pp. 33–38.
- ⁴⁸Martyna, G. J., Tobias, D. J., and Klein, M. L., "Constant Pressure Molecular Dynamics Algorithms," *The Journal of Chemical Physics*, Vol. 101, No. September, 1994, pp. 4177–4189.
- ⁴⁹Fedkiw, T. P. and Lozano, P. C., "Development and Characterization of an Iodine Field Emission Ion Source for Focused Ion Beam Applications," *Journal of Vacuum Science & Technology B: Microelectronics and Nanometer Structures*, Vol. 27, No. 6, 2009, pp. 2648–2653.